THE UNIVERSITY *of* EDINBURGH

Effects of High Pressure on the Electronic Spectra and Crystal Structure of Molecular Materials

Alif Nur Patriya Sussardi

A thesis submitted in fulfilment of the requirements for the degree of

Doctor of Philosophy to the School of Chemistry

The University of Edinburgh

2020

for Ibu

the invincible under the sun

ᬓᬶᬢᭀᬢᭀᬲᬸᬭᬬᬸᬦᬶᬯᬶᬲᬶᬬᬦᬶᬫᭀᬦᬶᬓᬸᬫᬸᬦᬶᬓᬸᬫᬸᬦᬶᬓᬸᬫᬸ

Abstract

The fluorescence of solid-state molecular materials is a field of growing research interest, stimulated by technological applications, such as organic light-emitting diodes and optical sensing. Investigation of the relationship between pressure-induced changes in the structure and electronic spectra of such materials offers opportunities for understanding the influence of intermolecular interactions and conformational changes on optical properties. However, there have been few studies that directly correlate the results of high-pressure X-ray crystallography and high-pressure optical spectroscopy.

An apparatus for the *in situ* measurement of UV-visible absorption and fluorescence emission spectra of crystals in a diamond anvil cell (DAC) has been developed. The effects of pressure (up to several GPa) on the structure and spectra of metal-organic frameworks (MOFs), molecular rotors, conjugated aromatic molecules and thermally activated delayed-fluorescence (TADF) materials have been studied.

A Luminescent MOF material, Hf-peb, was studied. Hf-peb MOF is a MOF with two-fold interpenetrated linker, 1,4-phenylene-bis(4-ethynylbenzoate) (peb^{2-}). X-ray crystallography reported in this thesis showed that the linker exists in two conformational states at ambient pressure (and room temperature), one in which the central phenyl ring is coplanar with the two terminal phenyl rings, and the second is the newly reported twisted conformer, where the central phenyl ring is perpendicular to the terminal phenyls. The fractional population of the twisted conformer increased with increasing pressure, from 28% at ambient pressure to 100% at 2.1 GPa. Both the absorption spectrum and the emission spectrum shifted to longer wavelength with increasing pressure. It was also found that the observed emission spectra, across the pressure range, can be well-fitted by linear combinations of the 2.1 GPa spectrum, assigned to the twisted conformer, and the ambient pressure spectrum. The fractional population of the twisted conformer at each pressure estimated in this manner was in good agreement with the values determined from the X-ray diffraction data. The close correlation indicates that the contribution of each conformer to the observed emission

spectrum is determined by its ground-state population, and hence the two conformers must have very similar fluorescence brightness.

A combined high-pressure UV-vis absorption spectroscopy and computational study on Zr-abdc MOF, a MOF containing an azobenzene dicarboxylate ($abdc^{2-}$) linker has been carried out. It is revealed the effect of pressure on the absorption spectra in penetrating (methanol) and non-penetrating (FC-70) pressure media. Penetration of methanol into the porous MOF framework resulted in a hypsochromic shift that can be attributed to solvent-induced stabilisation of the more polar the ground state. In the non-penetrating FC-70 medium, pressure-induced compression of the unit cell volume caused a decrease in length of the $abdc^{2-}$ linker. DFT calsculations predicted a consequent bending of the linker structure with increasing pressure. TDDFT calculations then predicted a decrease in the energy of the transition to the nπ* state, with increased bending. The TDDFT-predicted trend was in good agreement with the experimentally observed spectral shift.

The effects of pressure on the fluorescence properties of two related molecular rotors, *sym*-pentaphenylcyclopentadiene (Ph_5C_5H) and *sym*-heptaphenylcycloheptatriene (Ph_7C_7H), have also been studied. The redshift in UV-vis absorption and emission spectra with increasing pressure on Ph_5C_5H could be attributed to stronger interphenyl interactions, which are already present at ambient pressure. On the other hand, X-ray crystallography on Ph_7C_7H demonstrated the influence of specific interphenyl interactions, both intramolecular and intermolecular, on the optical spectra. For Ph_7C_7H at high pressures, interphenyl interactions that closely resemble effective displaced-stacked benzene dimers can be identified. The observed fluorescence spectra could be interpreted in terms of relaxed excimer emission from these dimer-like species which occur only at high pressure. These observations elucidate the interactions that lead to aggregation-induced emission in molecular rotors of this type.

The 1,4-bis(4-carbomethoxyphenylethynyl)benzene (BCPEB) is an example of a linear π-conjugated system, and also a molecular rotor, with three phenyl rings connected by acetylene linkers. The latter chromophore, commonly known as bis(phenylethynyl)benzene (BPEB), is considered to be a model system for one-dimensional molecular wires that have numerous applications in optoelectronics. The

photophysical properties of BPEB are known to be strongly influenced by torsional isomerism. The solution phase and low-temperature fluorescence measurements showed very similar photophysical properties of both BPEB and BCPEB. The structure of BCPEB was investigated as a function of pressure, by single-crystal X-ray diffraction in a DAC, using synchrotron radiation. The pressure-induced hypsochromic shift and spectral profile evolution with decreasing pressure in the UV-vis absorption and emission spectrum can be related to decrease in intermolecular stacking interaction and increase in torsional movement, due to less restricted molecular movement in the crystal.

Pressure-dependent properties were also studied for the well-known TADF material of 1,2,3,5-tetrakis(carbazol-9-yl)-4,6-dicyanobenzene (4CzIPN) and its derivative, 4CzIPN-$^{t}Bu_8$. Single-crystal X-ray diffraction of 4CzIPN, obtained up to 4.16 GPa, showed a decrease in the intermolecular inter-carbazole distance with increasing pressure. In addition to steady-state UV-vis and fluorescence spectroscopy, time-resolved measurements of delayed fluorescence were conducted as a function of pressure. Both 4CzIPN and 4CzIPN-$^{t}Bu_8$ show different response to pressure on the steady-state electronic spectra and its emission kinetics, in which the 4CzIPN-$^{t}Bu_8$ experienced change in singlet-triplet energy gap at pressures higher than ~0.8 GPa. The observed pressure-dependence of the delayed fluorescence lifetime can be interpreted in terms of the effect of intermolecular interaction between the carbazole groups on the TADF process in the two systems.

In summary, this thesis reports the relation between the crystal structure and the electronic spectra of photo-active materials, using a custom made high-pressure optical spectroscopy measurement system to elucidate various photophysical processes under high-pressure conditions.

Lay Summary

Solid-state fluorescent materials, especially those based on organic molecules, are exciting candidates for light-emitting diodes (LEDs) and optical sensing. Most of these luminescent molecules are conjugated aromatic molecules, which can produce various colours and brightness. In solution-phase, these molecules are moving freely, which makes it difficult to assign the absorption or emission of light to a particular molecular structure. In solid phase, however, the movement of the molecules is restricted, and the absorption or emission phenomena can be directly related to specific molecular structures and interactions.

In this work, fluorescence measurement techniques have been combined with single-crystal X-ray diffraction to understand the direct relation between molecular structure and fluorescence phenomena. Fluorescence techniques are some of the most powerful methods to study molecular dynamics and intermolecular interactions due to their selectivity and high sensitivity. On the other hand, single-crystal X-ray diffraction technique allows us to determine the structure of a molecule directly, along with its surrounding environment in the crystal.

Applying pressure on the gigapascal (GPa) scale, 10,000 times atmospheric pressure, to a solid material squeezes the molecules and changes the molecular structure and arrangement. This can be achieved using a diamond anvil cell (DAC). The change of molecular structure causes changes in the absorption and emission spectra. However, different molecules responded differently to the high-pressure environment. In this work, several molecules, such as metal-organic frameworks (MOFs), molecular rotors and molecules that show thermally activated delayed fluorescence (TADF) have been studied to investigate the change in light absorption and emission at different pressures.

Declaration

I declare that the work contained within this thesis is my own, except where otherwise stated and indicated with a reference.

Work from Chapter 4 of this thesis is published in the paper entitled “Correlating Pressure-Induced Emission Modulation with Linker Rotation in a Photoluminescent MOF” A. Sussardi, C. L. Hobday, R. J. Marshall, R. S. Forgan, A. C. Jones and S. A. Moggach, *Angew. Chem. Int. Ed.*, 2020, 59, 8112–8122.

No part of this thesis has been submitted for any other degree or professional qualification.

Signed:

_____

Date:

14/10/2020

Acknowledgement

This space is not long enough to thank everyone who helped me during the last four years in Edinburgh, but I will try anyway.

Firstly, I would like to thank my supervisor, Prof Anita Jones, for all her support and guidance throughout my PhD, and taught me about photophysics, grammar and solar eclipse. I really have learned a lot from her, and for that, I am grateful. Also, my former co-supervisor, Dr Stephen Moggach, who taught me crystallography and let me join him to the Synchrotron. Moreover, the Indonesia Endowment Fund for Education (LPDP) for allowing me to pursue my PhD.

Secondly, I would like to thank Dr Marc Etherington of the University of Northumbria for all his help and advice for the TADF part and also Prof Andy Monkman of Durham University, for the discussion and for letting me use the time-resolved fluorescence equipment and fun and pleasant time during my visit in Durham. Also, Prof Ross Forgan of Glasgow University, who provided me with the MOFs samples. Furthermore, I would like to thank Prof Simon Parson, who let me use the DAC loading and pressure measurement facility in Lab 83. Charlie, Claire, Jonny, and Gemma for the training with the DAC and discussions about crystallography.

I would also like to thank my friends in the department. All the past and current members of the Jones Group for their productive chats, particularly Rachel, who showed how the lab worked when I first arrived. Ahmad “the royal”, who was friendly, supportive, and encouraging. Kyle, with his wit and “interesting” conversations about crimes, politics, and culture. Sergio, the bouldering, climbing, walking and road trip pal, the dude who distracted me from work whenever and wherever possible. Additional thanks to Kostas, Lavrentis, Viona and everyone else: you have made my PhD a lot more fun!

To my mother, father and my brothers who have supported me unconditionally in pretty much everything I have ever done. Last, but certainly not least, to Nesya my truly best friend ever, thank you for your encouragement and support over the last wee while. It just would not have been the same without you.

Contents

Chapter 1
Introduction

1.1 Purpose and Context of Thesis

The utilisation of X-ray radiation to characterise materials has been known since the early discovery of the X-ray by Wilhelm Röntgen in 1895 and the observation of the diffraction of X-rays by crystalline solids by Paul Ewald in 1912, with notable contributions of many scientists, including Max von Laue and William Bragg.[1] It is still the most reliable and well-established method for crystal structure elucidation, from simple minerals to more complicated molecules such as DNA and proteins.[2-4] The X-ray diffraction measurement setup can also be modified and adapted to various measurement environment such as temperature, humidity and pressure.[5,6]

Research activity in X-ray diffraction measurements at high pressure, in the realms of gigapascal (GPa), has intensified since the development of the miniaturised diamond anvil cell (DAC) by Merrill and Bassett.[7] Pressures in the GPa range can change the molecular conformation and intermolecular interactions within the unit cell.[8-11] A more moderate pressure apparatus, within the range of kPa has also been developed, to observe gas intake within porous materials.[12-14] The applications of the DAC, however, are mainly concentrated in X-ray diffraction, high-pressure synthesis, infrared spectroscopy and Raman spectroscopy.[7] The utilisation of the DAC for UV-vis absorption and fluorescence spectroscopy have also been carried out, but to a lesser extent than the other applications.[15-17]

UV-vis absorption spectroscopy is a useful technique to measure the energy that is needed to promote a molecule from the ground electronic state to the excited state. This method is sensitive to the molecular structure and intermolecular interactions in the ground-state. On the other hand, fluorescence emission spectroscopy has a much higher detection sensitivity than UV-vis absorption, and the emission spectrum is more sensitive in its response to the local molecular environment. Fluorescence measurements can also provide information about the evolution of the molecule and

its interactions in the excited state. The combination of both UV-vis absorption and fluorescence emission spectroscopy techniques is powerful approach to study molecular photophysics and photochemistry.

Moreover, combining solid-state electronic spectroscopy with single-crystal X-ray diffraction technique has the potential to give detailed information about the relationship between the optical spectra, molecular structure and intermolecular interactions.[18] Implementation of both of these techniques in a DAC could reveal evolution of optical spectra with increasing pressure and directly link this to the pressure-induced change in molecular structure and intermolecular interactions.

This thesis will describe the development of an experimental system for the measurement of UV-vis absorption and fluorescence spectra of crystals at high pressure, in a DAC. The use of this measurement setup to correlate pressure-induced changes in the optical spectra of a variety of molecular system to their crystal structures is then reported. The molecular systems that have been studied include metal-organic frameworks (MOFs), molecular rotors and thermally activated delayed fluorescence (TADF) materials. The measurement of UV-vis absorption and fluorescence spectra in relation to the changes in unit cell volume, molecular structure and intermolecular distances is a common theme throughout this thesis.

1.2 Structure of Thesis

This section outlines the structure of the thesis, presenting a summary of the content of each chapter.

Chapter 2 provides the fundamental theory relevant to the optical spectroscopy, fluorescence-based techniques, single-crystal X-ray diffraction and high-pressure techniques used in this work. Moreover, some examples of the pressure-induced response of materials, such as MOFs and aromatic molecular crystals, are considered. Further theoretical considerations and reviews of the literature specific to each study are presented in the Introduction section of the relevant chapter.

The following chapter, Chapter 3, discusses the experimental techniques that are commonly used throughout this thesis, such as high-pressure single-crystal X-ray diffraction technique. The design and development of the apparatus for high-pressure UV-vis absorption and fluorescence spectroscopy, utilised throughout this thesis, are

also described in this chapter. Specific experimental details relating to a particular study are given in the Experimental section in the relevant chapter.

Chapter 4 mainly discusses the effect of pressure on the crystal structure and optical spectroscopy of a Hf-based MOF, with two-fold interpenetrated 1,4-phenylenebis(4-ethynylbenzoate) (peb^{2-}) ligand, Hf-peb MOF. The crystal structure at various pressures, up to 2.1 GPa, has been measured in detail, with two conformations of the ligand being identified, in which the relative populations depended on pressure. The absorption and emission spectra were measured as a function of pressure and changes in the emission spectrum as a function of pressure could be linked directly to the change in conformational populations.

Chapter 5 discusses the pressure-induced shift of the UV-vis absorption spectrum of a MOF containing the azobenzene dicarboxylate ($abdc^{2-}$) ligand, Zr-abdc MOF. The study was conducted using both an interpenetrating pressure-transmitting medium (PTM), methanol, and a non-interpenetrating PTM, FC-70. It was known from previous work that the unit cell volume decreases with increasing pressure in FC-70, with a consequent bending (decrease in length) of the ligand.[20] TDDFT calculations were performed to investigate the correlation between the shift of UV-vis absorption spectrum and pressure-induced bending of the azobenzene ligand.

Chapter 6 discusses the effect of pressure on the crystal structure of molecular rotors; *sym*-pentaphenylcyclopentadiene (Ph_5C_5H) and *sym*-heptaphenylcycloheptatriene (Ph_7C_7H). These molecules are known to exhibit aggregation-induced emission (AIE), a phenomenon where a molecule becomes more fluorescent upon aggregation, in contrast to the more common aggregation-caused quenching (ACQ).[21] UV-vis absorption and fluorescence emission spectra were collected for both Ph_5C_5H and Ph_7C_7H as a function of pressure. Changes in absorption and emission spectra of Ph_5C_5H and Ph_7C_7H could be linked directly to changes in specific inter-phenyl interactions in the crystal.

Chapter 7 discusses the investigation of the photophysical properties of the linearly conjugated rigid molecular rod, 1,4-bis(4-carbomethoxyphenylethynyl)benzene (BCPEB) in solution phase, in a frozen matrix at 77 K, and as a function of pressure in its crystal form. The photophysical properties of BCPEB in solution-phase were

found to closely resemble those reported previously for the well-known analogue, 1,4-bis(phenylethynyl)benzene (BPEB).[23] High-pressure solid-state X-ray diffraction was used in combination with high-pressure UV-vis absorption and fluorescence spectroscopy to investigate the effect of intermolecular interactions and the restriction of torsional mobility on the electronic spectra of the molecule.

Chapter 8 discusses the effect of pressure on the well-known TADF material 1,2,3,5-Tetrakis(carbazol-9-yl)-4,6-dicyanobenzene (4CzIPN) and its derivative, 4CzIPN-$^{t}Bu_8$. In addition to steady-state spectroscopic measurements, time-resolved fluorescence emission spectroscopy was carried out as a function of pressure, in collaboration with Dr Marc Etherington of Northumbria University and Prof Andrew Monkman of Durham University. The differing responses to pressure of 4CzIPN and 4CzIPN-$^{t}Bu_8$, in terms of both the steady-state spectra and the lifetime of TADF, can be interpreted in terms of the shift in relative energies of the singlet and triplet energy levels.

Finally, Chapter 9 summarises the most significant conclusions from earlier chapters and draws some general conclusions from the studies. Suggestions are made for future work that could be carried out to reinforce and extend the present studies, and some proposals are made for possible future directions in the research.

1.3 References

1. Hargittai, I. ; Hargittai, B., *Science of crystal structures: highlights in crystallography*. Springer International Publishing, Switzerland, **2015**.
2. D. Watson, J.; C. Crick, F. H., Molecular Structure of Nucleic Acids: A Structure for Deoxyribose Nucleic Acid. *Nature* **1953,** *171* (4356), 737-738.
3. Tulinsky A., *Chapter 35: The Protein Structure Project, 1950–1959: First Concerted Effort of a Protein Structure Determination in the U.S. In Annual Reports in Medicinal Chemistry*, Elsevier: 1996; pp 357-366.
4. Blundell, T. L., *IUCrJ* **2017,** *4* (4), 308-321.
5. Hashizume, H.; Shimomura, S.; Yamada, H.; Fujita, T.; Nakazawa, H.; Akutsu, O., *Powder Diffr.* **1996,** *11* (4), 288-289.
6. Piermarini, G. J., *J. Res. Natl. Inst. Stand. Technol.* **2001,** *106* (6), 889-920.
7. Merrill, L.; Bassett, W. A., *Rev. Sci. Instrum.* **1974,** *45* (2), 290-294.

8. Boldyreva, E. V., *J. Mol. Struct.* **2003,** *647* (1-3), 159-179.
9. Boldyreva, E. V.; Ahsbahs, H.; Weber, H. P., *Z. Kristallogr.* **2003,** *218* (3), 231-236.
10. Hobday, C. L.; Woodall, C. H.; Lennox, M. J.; Frost, M.; Kamenev, K.; Duren, T.; Morrison, C. A.; Moggach, S. A., *Nat. Commun.* **2018,** *9* (1), 1429.
11. McKellar, S. C.; Sotelo, J.; Greenaway, A.; Mowat, J. P. S.; Kvam, O.; Morrison, C. A.; Wright, P. A.; Moggach, S. A., *Chem. Mater.* **2016,** *28* (2), 466-473.
12. McMonagle, C. J.; McKellar, S. C.; Sotelo, J.; Warren, M. R.; Allan, D. R.; Moggach, S. A., *Acta Crystallogr. A* **2015,** *71*, S84-S84.
13. Yufit, D. S.; Howard, J. A. K., *Acta Crystallogr. A* **2005,** *61*, C468-C468.
14. Yufit, D. S.; Howard, J. A. K., *J. Appl. Crystallogr.* **2005,** *38*, 583-586.
15. Drickamer, H. G., *J. Lumin.* **1991,** *48-9*, 11-17.
16. Drickamer, H. G., *Annu. Rev. Mater. Sci.* **1990,** *20*, 1-17.
17. Drickamer, H. G., *Acc. Chem. Res.* **1986,** *19* (11), 329-334.
18. Wright, J. D., *Molecular Crystals*. Second ed.; Cambridge University Press: Cambridge, **1995**.
19. Sussardi, A.; Hobday, C. L.; Marshall, R. J.; Forgan, R. S.; Jones, A. C.; Moggach, S. A., *Angew. Chem. Int. Ed.* **2020,** *59* (21), 8118-8122.
20. Hobday, C. L.; Marshall, R. J.; Murphie, C. F.; Sotelo, J.; Richards, T.; Allan, D. R.; Düren, T.; Coudert, F.-X.; Forgan, R. S.; Morrison, C. A.; Moggach, S. A.; Bennett, T. D., *Angew. Chem. Int. Ed.* **2016,** *128* (7), 2447-2451.
21. Sturala, J.; Etherington, M. K.; Bismillah, A. N.; Higginbotham, H. F.; Trewby, W.; Aguilar, J. A.; Bromley, E. H. C.; Avestro, A. J.; Monkman, A. P.; McGonigal, P. R., *J. Am. Chem. Soc.* **2017,** *139* (49), 17882-17889.
22. Field, L. D.; Hambley, T. W.; Lindall, C. M.; Masters, A. F., *Inorg. Chem.* **1992,** *31* (12), 2366-2370.
23. Roy, K.; Kayal, S.; Kumar, V. R.; Beeby, A.; Ariese, F.; Umapathy, S., *J. Phys. Chem. A* **2017,** *121* (35), 6538-6546.

Chapter 2
Background Theory

This chapter will discuss the general theory that underlies the work of this thesis. It starts with a description of the principles of UV-vis absorption and fluorescence spectroscopy. The chapter then will discuss the X-ray diffraction technique, the method to generate a high-pressure environment and some cases of materials' response to pressure. Much of the content of this chapter is derived from Lakowicz, Atkins and De Paula, Hollas, Birks and Wright.[1-5]

2.1 Fluorescence Spectroscopy

2.1.1 Electromagnetic Absorption

This thesis is concerned with the electronic transitions of organic molecules that occur in the ultraviolet (UV) and visible regions (100–780 nm) of the electromagnetic spectrum. During absorption of UV-visible light by a molecule, an electron is promoted from its lowest energy state, known as the ground state, to a higher energy state, known as the excited state, as depicted in **Figure 2.1**. The wavelength, λ, of the electromagnetic radiation that absorbed is directly related to the energy difference between the ground state, E_i, and the excited state, E_f, by **Equation 2.1**.

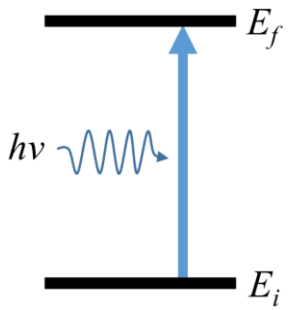

Figure 2.1. Schematic diagram of the absorption of a photon (hv).

$$E_{fi} = \frac{hc}{\lambda}$$

Equation 2.1

where h is Planck's constant and c is the speed of light in a vacuum.

Electromagnetic radiation consists of perpendicular magnetic and electric fields oscillating at some frequency. For a molecule to be able to absorb or emit a photon of frequency, *v*, it must possess, if only transiently, a dipole oscillating at the same frequency. This transition dipole is expressed quantum mechanically in terms of the transition dipole moment, μ_{fi}. The transition dipole moment is described in **Equation 2.2**.

$$\mu_{fi} = \int \Psi_f \hat{\mu} \Psi_i d\tau$$

Equation 2.2

where Ψ_f and Ψ_i are the vibronic wavefunction of the upper and lower states, respectively. The $\hat{\mu}$ is the dipole moment operator and $d\tau$ is the integration component of space. The $d\tau$ could be separated into x, y and z components where only one of these needs to be non-zero in order for a transition to be symmetry-allowed. The size of the transition dipole can be regarded as a measure of the charge distribution that accompanies a transition. When the $\mu_{fi} = 0$, the transition is symmetry-forbidden, and no absorption or emission will be observed.

The intensity of the transition is proportional to the square of μ_{fi} and is related to the Einstein coefficient for induced absorption (B) as expressed in **Equation 2.3**.

$$B = \frac{2\pi^2}{3\varepsilon_0 h^2} \left| \mu_{fi} \right|^2$$

Equation 2.3

where the ε_0 is the vacuum permittivity. The absorption experiment is illustrated in **Figure 2.2**, where radiation intensity, I_0, passed through the absorption cell of length *l* containing absorbing material of concentration *C* in the liquid phase. Upon passing through the liquid, the radiation is absorbed in a specific frequency, *v*, and the remaining intensity, *I*, could be detected by the detector. The absorption spectrum, typically measured as absorbance, *A*, as expressed in **Equation 2.4**.

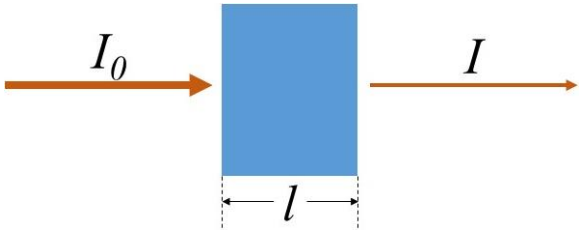

Figure 2.2. Simplified schematic of an absorption experiment.

$$A(\nu) = -\log_{10}\frac{I}{I_0} = \varepsilon(\nu)\, C\, l$$

Equation 2.4

where $A(\nu)$ is the absorbance at a wavenumber of ν, $\varepsilon(\nu)$ is the molar absorption coefficient which has a dimension of (concentration × length)$^{-1}$ and the unit is commonly known as mol^{-1} dm^3 cm^{-1}. Absorbance is related to the concentration of absorbing species with their specific molar absorption coefficient. The molar absorption coefficient is a measurable property of a molecule, and it represents the strength of absorption by a molecule at a specific wavelength. The spectral profile of ε as a function of ν can vary, which affects the area under the spectrum, as shown in **Figure 2.3**.

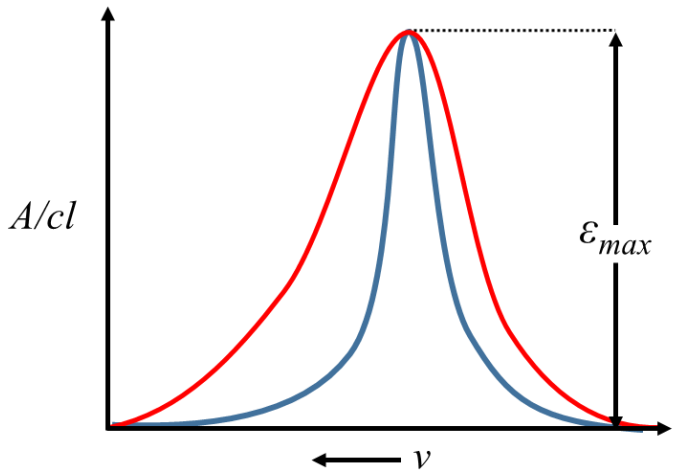

Figure 2.3. The absorption spectra where the spectrum profile is narrow (blue) and broader (red).

It is shown in **Figure 2.3**, that both spectra have the same ε_{max}, but the blue spectrum has a much lower integrated intensity, illustrating the problem of using ε_{max}. It is best to integrate the area under the ε spectrum of ν, as expressed in **Equation 2.5**, provided

that the population molecules in the excited state N_f is much smaller than the population at the ground state N_i.

$$\int_{\nu_1}^{\nu_2} \varepsilon(\nu)\mathrm{d}\nu = \frac{N_A h \nu_{fi} B}{ln\ 10}$$

Equation 2.5

where ν_{fi} is the average wavenumber of the absorption and N_A is the Avogadro constant. The oscillator strength, f_{fi} is often used to quantify the intensity which is related to the area under the curve as expressed in **Equation 2.6**.

$$f_{fi} = \frac{4\varepsilon_0 m_e c^2 ln10}{N_A e^2} \int_{\nu_1}^{\nu_2} \varepsilon(\nu)\mathrm{d}\nu$$

Equation 2.6

where m_e and e are the rest mass of an electron and the charge of an electron, respectively. The f_{fi} is dimensionless and is the ratio between the strength of the transition to that of an electric dipole transition between two states of an electron oscillating in three dimensions in a simple harmonic way. The quantity of the f_{fi} can vary between zero and one. The direct correlation of the f_{fi} and the μ_{fi} can be obtained and is shown in **Equation 2.7**.

$$f_{fi} = \frac{8\pi^2 m_e c^2}{3he^2} \nu_{fi} \left| \mu_{fi} \right|^2$$

Equation 2.7

In 1925, James Franck put a qualitative argument to explain the various types of intensity distributions found in vibronic (vibrational and electronic) transitions. His conclusion was based on an appreciation that an electronic transition takes place more rapidly compared to the vibrational transition so that in a vibronic transition, the nuclei have nearly the same position and velocity before and after the transition.

In 1928, Edward Condon treated the intensities of vibronic transitions quantum mechanically. The vibronic wavefunction, Ψ,(see **Equation 2.2**) can be factorised into the electronic component, ψ^{elec}, and the nuclear component, ψ^{nucl}, as shown in **Equation 2.8.**

$$\mu_{fi} = \iint \psi_f^{elec} \psi_f^{nucl} \hat{\mu}\, \psi_i^{elec} \psi_i^{nucl} d\tau_{elec}\ dr$$

Equation 2.8

The Born-Oppenheimer approximation, which assumes that the nuclei can be regarded as stationary in relation to the much more fast-moving electrons, allows the integration of the electronic component over electron coordinates τ_{elec} and independent of nuclear coordinate, *r*, as shown in the **Equation 2.9**.

$$\mu_{fi} = \mu^{elec} \int \psi_f^{nucl}\, \psi_i^{nucl}\ dr$$

Equation 2.9

The quantity of the $\int \psi_f^{nucl}\, \psi_i^{nucl}\ dr$ is called the vibrational overlap integral, as it is a measure of the degree to which the two vibrational wave functions overlap. Its square is known as the Franck-Condon factor to which the intensity of the vibronic transition is proportional. The nuclear coordinates, *r*, is required to remain constant during the integration.

Figure 2.4 depicts the case where the maximum of the $\upsilon' = 4$ wave function near to the classical turning point is vertically above the $\upsilon'' = 0$ wave function. The most significant contribution to the vibrational overlap integral is marked by the upward arrow with a solid line. A more appreciable contribution extends to values of *r* within the dashed line. The schematic in **Figure 2.4** is quite a typical case for the transition of an electron where the ground state is bonding, and the upper state is antibonding, where the bond length is weaker and more extended. Reversibly for the case where the electron in ground state occupy the antibonding excited to the bonding molecular orbital, then the $r' < r''$.

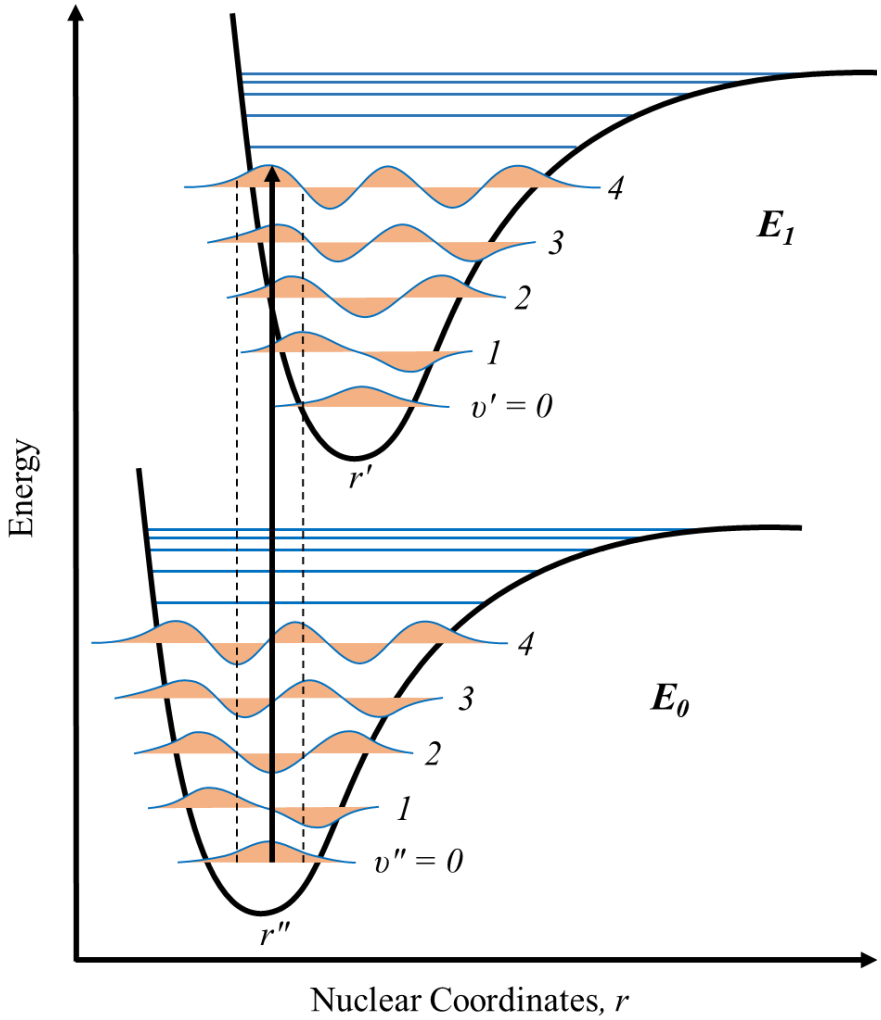

Figure 2.4. Franck-Condon principle applied to a case which $r' > r''$ and the 4-0 transition is the most probable. Adapted from Hollas.[3]

Apart from the symmetry-forbidden transition, an electronic transition can also be spin-forbidden. Electronic states can be described by the symbol L_n where the L represents the multiplicity of the vibronic state, and the n is integer represents the electronic energy level. The letter L can be obtained from the formula of $2\boldsymbol{S}+1$ where the $\boldsymbol{S}$ is the total spin angular momentum quantum number. When electrons are paired, and the spins are antiparallel to each other (+½ and -½), this gives $\boldsymbol{S}$ equal to zero, making the multiplicity of one, hence this is called a singlet state, and assigned to letter S. When the electrons are parallel to each other (+½ and +½), the total angular momentum is one, making the multiplicity of three, hence a triplet state, assigned to letter T. A transition from a singlet ground state to a singlet upper state is typically denoted as $S_0 \rightarrow S_1$. The transition between a singlet and a triplet state is spin-forbidden due to the violation of the Pauli Exclusion Principle. Thus, in most absorption or

excitation processes, the transition typically occurs for the S→S or T→T. However, it is common to observe the transition from singlet to triplet and triplet to the singlet, known as intersystem crossing (ISC), as a result of spin-orbit coupling.

2.1.2 Radiative and Non-radiative Decay

A molecule in the excited state will eventually return to its ground state by discarding its excitation energy to the environment. The release of the energy can come in the form of radiative and non-radiative processes. The radiative process, also called radiative decay, involves the emission of light, while any processes that do not result in the emission of light are classified as non-radiative decay. The most common fate of molecules after experiencing irradiation is following the non-radiative decay pathways. The remaining molecules follow the radiative decay with the mechanism of the photon emission occurring either by fluorescence or phosphorescence.

For fluorescence, the emission of electromagnetic radiation occurs immediately after the excitation has occurred, typically on the nanosecond time scale. In phosphorescence, however, the spontaneous emission may persist for a prolonged time, usually longer than milliseconds, since this is a spin-forbidden transition. The processes that occur following absorption of a photon are represented by the Jablonski diagram, as shown in **Figure 2.5**.

In 1950, Michael Kasha proposed a rule that in a polyatomic molecule, luminescence with appreciable yield only occurs from the lowest excited state of a given multiplicity.[6] A consequence of Kasha's rule is that the emission spectra are independent of the excitation wavelength. Kasha's rule is the consequence of the process of rapid internal conversion and vibrational relaxation, as shown in **Figure 2.5**, following absorption, to reach the lowest vibrational state of given electronic state. From this state, several processes can occur. Fluorescence (green arrows in **Figure 2.5**) is the spin-allowed radiative transition from the excited state (S_1) to the ground state, S_0, which usually occurs in about 10^{-8} s.

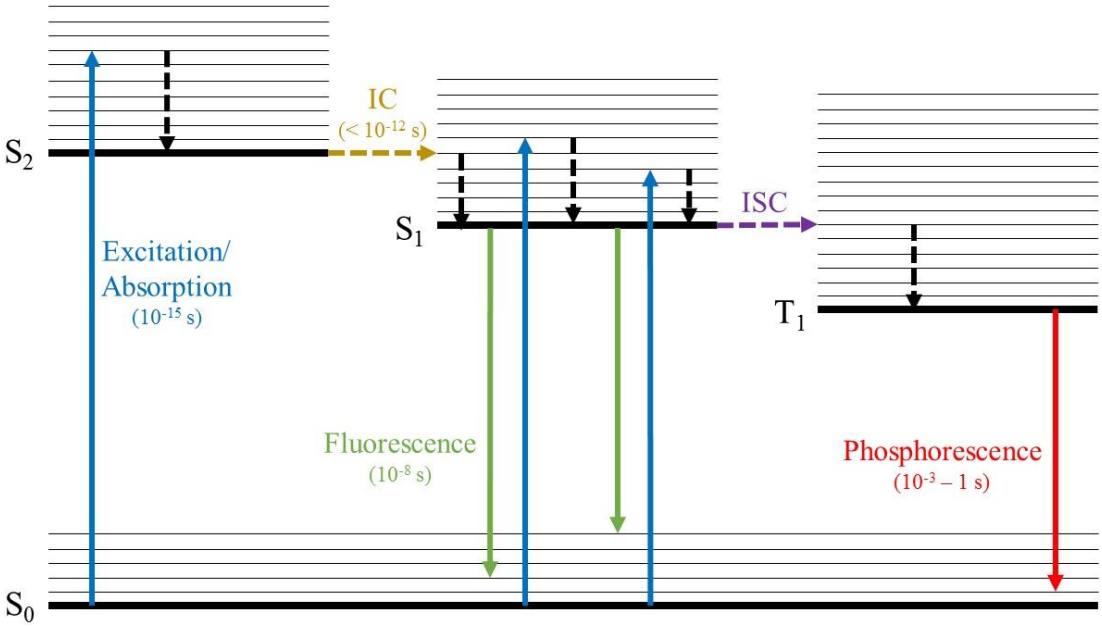

Figure 2.5. Jablonski diagram illustrating excitation and decay processes, where IC and ISC stand for internal conversion and intersystem crossing, respectively.

Non-radiative decay from S_1, competing with fluorescence, occurs by internal conversion (IC) to S_0 or intersystem crossing (ISC) to the triplet manifold. ISC leads to populate the lowest triplet state T_1, which can result in phosphorescence when T_1 decays radiatively to S_0. Phosphorescence can be identified by its low its long lifetime, in the scale of milliseconds (10^{-3} s). When the T_1 and S_1 energy levels have a small energy gap, the reverse intersystem crossing (rISC) may occur and could lead to delayed fluorescence, that will be discussed further in **Chapter 8**.

The fluorescence process can be compromised, resulting in the decrease of its intensity, called fluorescence quenching. Fluorescence quenching can occur in several ways, for example, collisional quenching when an excited fluorophore collides with another molecule, the so-called a quencher. Quenching involves the conversion of the electronic energy of the excited fluorophore into vibrational energy, which can be lost to the surroundings as heat. Some examples of common collisional quenchers are molecular oxygen, halogens, and amines. Other quenching processes include excited state reactions, energy transfer and complex formation.[9] An example of complex formation in the excited state is the formation of an excited dimer, known as excimer, which will be discussed in **2.1.6**.

According to Jablonski diagram (**Figure 2.5**), the transition energy of the emission is typically lower (i. e. longer wavelength) than of the absorption. This phenomenon was first observed by Stokes in 1852, hence is named Stokes shift. The most common reason for this phenomenon is the loss of the vibrational energy from the excited molecule to the surroundings, known as vibrational relaxation, before emission, so that emission occurs from the υ'=0 level (See **Figure 2.4**) to higher ground state vibrational levels ($\upsilon'' > 0$). The 0–0 transition ($\upsilon' = 0 \rightarrow \upsilon'' = 0$) will have the same energy in both the emission and absorption spectra, and corresponds to the point of intersection between the absorption and emission spectra, as shown in **Figure 2.6**. Other factors may contribute to the Stokes shift such as solvent effects and complex formation, and these may cause the emission origin to be shifted to longer wavelengths than the excitation origin.

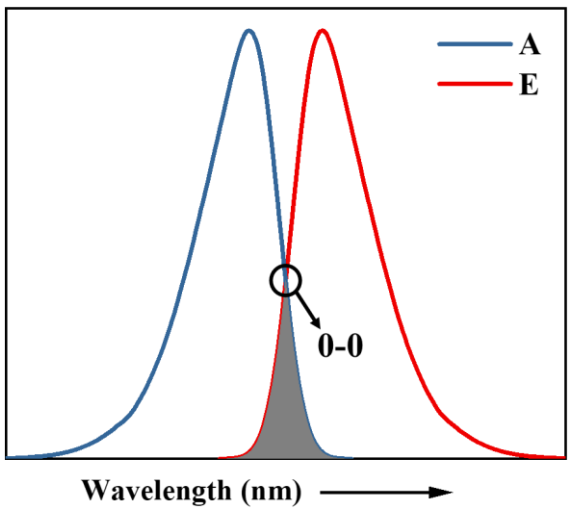

Figure 2.6. The overlap between absorption (blue line) and emission (red line) spectra, showing the wavelength range (shaded area) where reabsorption can occur.

The molecules or solvent that surround the fluorescent molecule can have a significant effect on both fluorescence quantum yield and the spectral profile. This is caused by the stabilisation of the excited state by reorientation of the solvent in response to the change in electronic structure (dipole moment) of the fluorophore on excitation. When the lifetime is long enough, the polarity of the excited state and the solvent molecule can collaborate to achieve a stabilised state as illustrated in **Figure 2.7**.

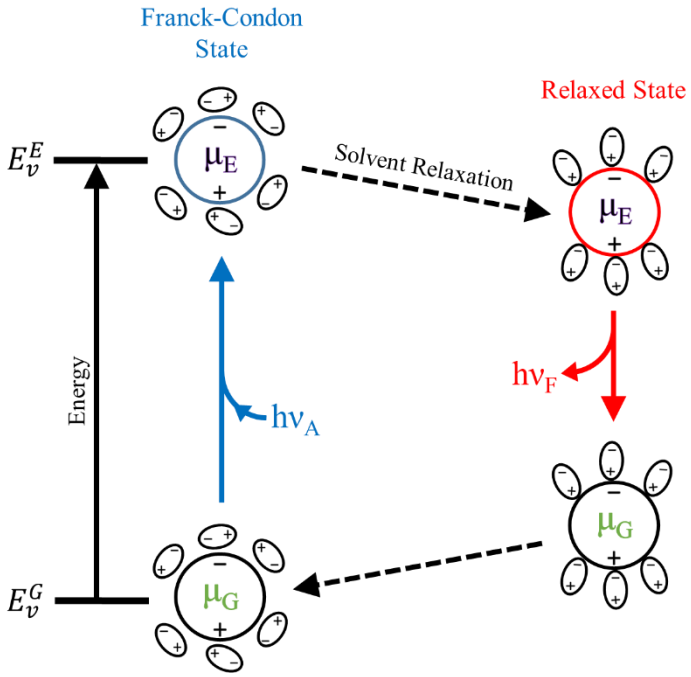

Figure 2.7. Effect of the electronic and orientation reaction fields on the energy of dipole in a dielectric medium, $\mu_E > \mu_G$. The smaller oval represents the solvent molecules and their dipole moments. Reproduced from Lakowicz.[1]

The interactions between the fluorophore and solvent affect the energy difference between the ground state and excited states. This energy difference can be described as the Lippert-Mataga equation, as shown in **Equation 2.10.**

$$\bar{\nu}_A - \bar{\nu}_F = \frac{2}{hc}\left(\frac{\varepsilon_r - 1}{2\varepsilon_r + 1} - \frac{n^2 - 1}{2n^2 + 1}\right)\frac{(\mu_E - \mu_G)^2}{a^3}$$

Equation 2.10

where n is the solvent refractive index, the ε_r is the dielectric constant of the solvent, and a is the radius of the cavity in which the fluorophore resides. The μ_E and μ_G is the molecular dipole moment of the excited and ground state, respectively. The $\bar{\nu}_A$ and $\bar{\nu}_F$ are the wavenumber of the absorption and the emission, respectively. The central term $\left(\frac{\varepsilon_r - 1}{2\varepsilon_r + 1} - \frac{n^2 - 1}{2n^2 + 1}\right)$ is referred to as the orientation polarizability, Δf. This equation only considers the effect of bulk solvation and does not considers specific solvent effects such as hydrogen bonding. The more polar the solvent, the more it can stabilise the excited state, causing the energy of the emitting state to become lower, which will make the Stokes shift larger. This solvent relaxation could also decrease the quantum yield.

For a molecule with a small Stokes shift, reabsorption of the emitted light can occur as a result of overlap of the absorption and emission spectra, as shown as the grey area in **Figure 2.6**. This reabsorption phenomenon results in a decrease in the intensity of the emission over this wavelength region and distorts the emission spectrum so that it shows an incorrect profile.

2.1.3 Quantum Yield and Fluorescence Lifetime

The most important characteristics of a fluorescent molecule are the fluorescence quantum yield, Φ, and lifetime, τ. The fluorescence quantum yield is the ratio of the number of photons emitted to the number absorbed. In other words, quantum yield defines the efficiency of radiative decay. The higher the value of quantum yield, the brighter the emission for the same value of absorbance. On the other hand, the lifetime is vital to identify whether the fluorophore has time available to interact with or diffuse in its environment. **Figure 2.8** shows the processes responsible for the emissive rate of the fluorophore, Γ, and the rate of non-radiative decay to S_0, denoted as k_{nr}.

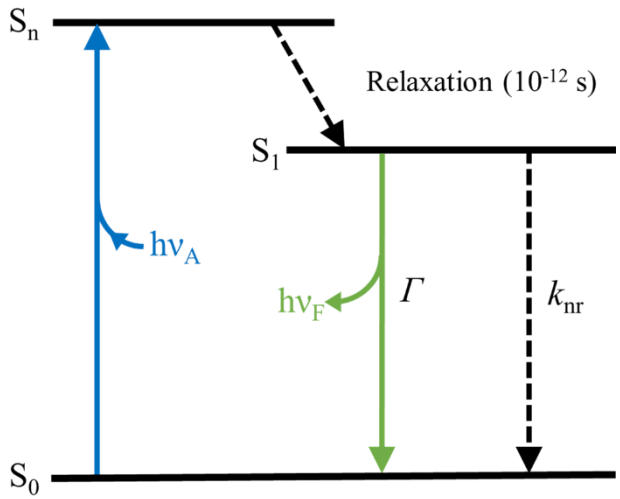

Figure 2.8. A simplified Jablonski diagram to illustrate the meaning of quantum yields and lifetimes. Adapted from Lakowicz.[1]

The fluorescence quantum yield, Φ, can be expressed in **Equation 2.11**.

$$\Phi = \frac{\Gamma}{\Gamma + k_{nr}}$$

Equation 2.11

A quantum yield can be close to unity if the Γ is much higher than k_{nr}. The energy yield of fluorescence is always less than unity because of the Stokes losses.

The lifetime of the excited state is defined by the average time molecule spends in the excited state before returning to the ground state. For the fluorophore illustrated in **Figure 2.8**, the lifetime, τ, can be written in **Equation 2.12**.

$$\tau = \frac{1}{\Gamma + k_{nr}}$$

Equation 2.12

The Jablonski diagrams in **Figure 2.5** and **Figure 2.8** only show intramolecular processes. However, in a real scenario, the excited state can have several other processes such as photo-bleaching, photon, and electron transfers with surrounding molecules.

2.1.4 Resonance Energy Transfers

The energy at the excited state can be transferred to a molecule nearby. This occurs when the emission spectrum of a fluorophore, called the donor, overlaps with the absorption spectrum of the molecule nearby, called acceptor, as shown in **Figure 2.9**. The process is actually non-radiative because it does not involve an emission from the donor and the absorption of the light by the acceptor, instead the donor and the acceptor are coupled by interaction between their transition dipole moments. This process is called Förster resonance energy transfer (FRET) after the person who first introduced the concept, Theodore Förster.

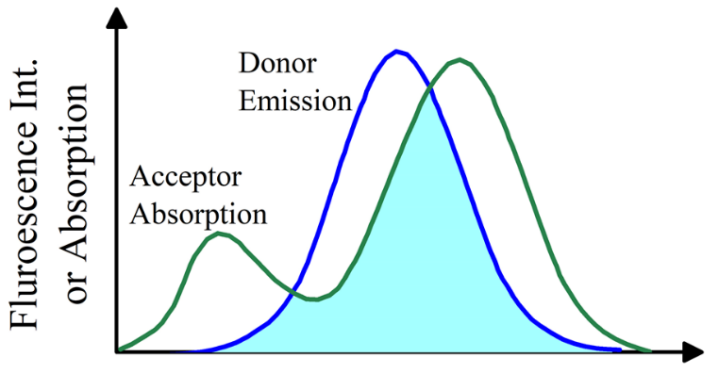

Figure 2.9. Spectral overlaps for the Förster resonance energy transfer (FRET). Reproduced from Lakowicz.[1]

The extent of the energy transfer is determined by the distance between donor and acceptor and the extent of spectral overlap. The rate of energy transfer $k_T(r)$ is given in **Equation 2.13**.

$$k_T(r) = \frac{1}{\tau_D}\left(\frac{R_0}{r}\right)^6$$

Equation 2.13

where *r* is the distance between donor and acceptor, the τ_D is the lifetime of the donor in the absence of the energy transfer. The R_0 is the Förster distance, ranges from 30 to 60 Å, comparable to the diameter of proteins or the thickness of membranes. By using this relationship in **Equation 2.13**, the distance between sites in protein can be determined. The efficiency of the FRET, η_T, for single donor-acceptor pair at a fixed distance is described in **Equation 2.14**.

$$\eta_T = \frac{R_0^6}{R_0^6 + r^6}$$

Equation 2.14

At high concentration, when the distance between donor and acceptor is very close, the electron exchange process can occur. This electron exchange is often called Dexter energy transfer, in which the electron from the excited state of the donor is exchanged with the ground-state electron of the acceptor, resulting in the excited acceptor. This process can only occur at a short distance, but it competes with the FRET, and the process is less likely to happen when there is a significant spectral overlap between the donor and acceptor.

2.1.5 Steady-State and Time-Resolved Fluorescence Spectroscopy

Fluorescence measurement can be broadly classified into two large groups: steady-state and time-resolved measurement. Steady-state is the most common measurement and is performed with continuous illumination and observation. When the sample is first irradiated with light, the steady-state is reached almost immediately.

The second type is the time-resolved measurement in which pulsed light is used to excite the molecule, and the emission intensity decay is observed. The pulse width is required to be shorter than the decay time of the sample. This intensity decay is recorded using a high-speed detection system that capable of measuring the intensity on the timescale of the fluorescence decay (typically nanoseconds). The steady-state

observation is an average of the time-resolved phenomena over the intensity decay of the sample.

The process of the formation of the excited state, ^{1}M*, from the ground state, ^{1}M, can be expressed in **Equation 2.15**.

$$^1\text{M} + h\nu_A \rightarrow {}^1\text{M}^*$$

Equation 2.15

where the $h\nu_A$ is the energy of the absorbed light.

Furthermore, its subsequent decay to the ground state can be written as in **Equation 2.16**.

$$^1\text{M}^* \rightarrow {}^1\text{M} + h\nu_F$$

Equation 2.16

where the $h\nu_F$ is the energy of emitted light, and $\nu_F < \nu_A$.

The fluorescence decay is a first-order kinetic process with a rate constant that is the sum of the rate constants for the radiative, Γ, and all non-radiative, k_{nr}, decay process. The excited state decay rate can be expressed by **Equation 2.17**.

$$-\frac{d[^1\text{M}^*]}{dt} = (\Gamma + k_{nr})[\,^1\text{M}^*]$$

Equation 2.17

By integrating **Equation 2.17**, the population of excited state as a function of time can be written as **Equation 2.18**.

$$[^1\text{M}^*]_t = [^1\text{M}^*]_0 e^{-(k_f t)}$$

Equation 2.18

Where $[^1\text{M}^*]_0$ represents the population at t=0 or the time at which the pulse excites the sample, and $k_f = \Gamma + k_{nr}$.

During the fluorescence measurement, the quantity measured is the fluorescence intensity. Fluorescence intensity is proportional to the concentration of molecules in the excited state. The relation of these two parameters is expressed in **Equation 2.19**.

$$I_t = \Gamma[\,^1\mathrm{M}^*]_t$$

Equation 2.19

The substitution of **Equation 2.19** into **Equation 2.18** gives **Equation 2.20**.

$$I_t = I_0\, e^{-\frac{t}{\tau_f}}$$

Equation 2.20

where I_0 is the intensity at t=0, τ_f, is the fluorescence lifetime, equal to $\frac{1}{k_f}$.

The fluorescence lifetime is the time when the measured intensity is e^{-1} times or 36.79% of I_0.

If several emitting species are present, the fluorescence decay will be multi-exponential, as expressed in **Equation 2.21**.

$$I_t = I_0 \sum_{i=1}^{n} A_i\; e^{-\frac{t}{\tau_i}}$$

Equation 2.21

where A_i is the pre-exponential factor which represents the fractional contribution of each emitting species to the total excited state population at the t=0. Both A_i and τ_i can be used to calculate two other parameters; the fractional contribution of each lifetime to the steady-state intensity, SS_i, and average lifetime, $\bar{\tau}_i$, as expressed in **Equation 2.22** and **Equation 2.23**, respectively.

$$SS_i = \frac{A_i\,\tau_i}{\sum A_i\,\tau_i}$$

Equation 2.22

$$\bar{\tau}_i = \frac{\sum A_i\,\tau_i}{\sum A_i}$$

Equation 2.23

2.1.6 Excimers

The quantum yield of an aromatic molecule can be quenched as the molar concentration [^{1}M] increased. This type of quenching is often accompanied by the appearance of a broad structureless fluorescence peak. This broad structureless

emission spectrum is associated with the fluorescence of excited dimers, $^1D^*$, produced by collisional interaction of an excited molecule, $^1M^*$, and an unexcited molecule, ^1M. This excited dimer is known as excimer, as coined by Stevens to make it distinct from the excited state of a dimer that is bound in the ground state.[7]

Excimer formation is not followed by the change of the absorption, which indicates the excimer is dissociated in the ground state. The excimer formation typically occurs in a timescale less than nanoseconds, and the energy diagram is illustrated in **Figure 2.10.**

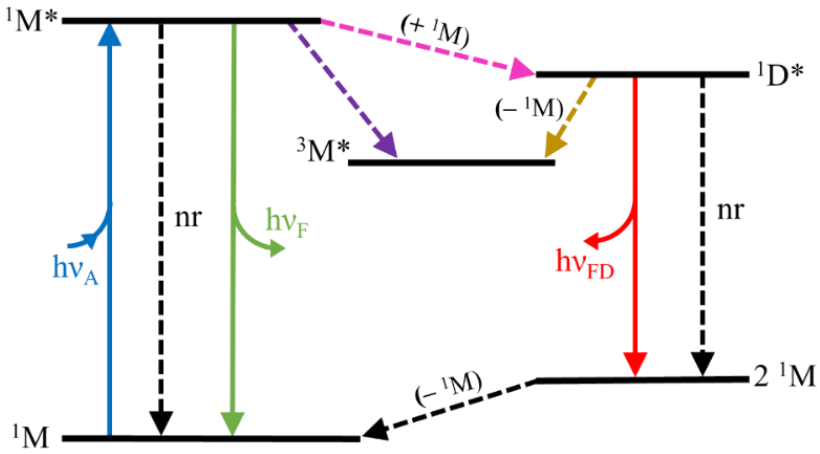

Figure 2.10. Simplified Jablonski diagram of excimer formation. The solid lines represent absorption (blue), the fluorescence emission of a molecule (green) and excimer emission (red). The pink dashed line shows the excimer formation involving the addition of a ground state molecule nearby. Reproduced from Birks.[4]

Many aromatic molecule and derivatives show excimer fluorescence in solution phase. It sometimes cannot be observed in the room temperature due to the low fluorescence quantum yield of the excimer, Φ_D, or if the solubility is too low. However, it can be observed at a lower temperature where the Φ_D is the higher or at a higher temperature where the solubility of the compound is greater.

Apart from the influence of the Φ_D and solubility, the propensity for the excimer formation is related to the interaction potential, ***V'***, and the repulsive potential, ***R'*** of the molecules in the excited state, as illustrated in **Figure 2.11** The difference between the ***V'*** and ***R'*** is denoted as ***D'***, the excimer potential. The excimer can only form only when the ***D'*** is smaller than the monomers potential, M_0. In some compounds, in which the ***V'*** is much stronger than the ***R'***, a photodimer is formed, and the photodimerisation is observed rather than excimer fluorescence. This photodimerisation is a

photochemical reaction where a chemical bond is formed. This photodimer will not return to its monomer form at the ground state and new peaks may appear in the absorption spectrum.

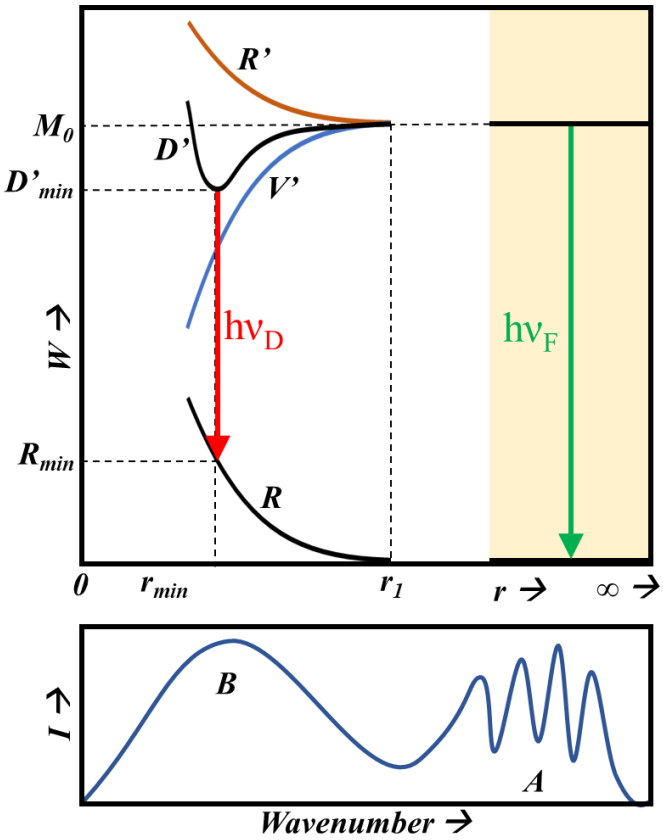

Figure 2.11. Schematic potential energy (*W*) diagram of pair of parallel molecules ^{1}M* and ^{1}M as a function of intermolecular separation (*r*). Reproduced from Birks.[4]

Figure 2.11 illustrates the ***D'***, ***V'*** and ***R'*** as a function of intermolecular distance, *r*, between molecules in the excited state and ground-state The vertical transition from the excimer state occurs from the lowest state, $\boldsymbol{D'_{min}}$, to the unstable dimer ground state, $\boldsymbol{R_{min}}$, with the emission energy, $h\nu_D$, lower than of the monomer emission, $h\nu_F$. In other words, the light emitted by the excimer is of a longer wavelength than the light emitted by the monomer.

Excimer formation also occurs in certain aromatic molecule crystals, when there are displaced-stacked or sandwich-like arrangements of the aromatic molecules, with short lateral displacement and interplanar distance, such as in pyrene crystal.[8] Aromatic molecule crystal is classified into two groups according to how aromatic molecule arrange themselves: type A, and B.[4] Type A is the most common one in large

lateral displacement and interplanar distance. Type B is the opposite of A where the lateral displacement and interplanar distance are small, as in pyrene. The fluorescence of type A is structured, and approximately a mirror image of the absorption spectrum, and it represents molecular emission. The type B, on the other hand, has structured absorption but structureless fluorescence spectrum. Often, a crystal is a mixture of type A and B, especially when a defect occurs within the crystal. This mixture of type A and B with its corresponding distances is shown at the bottom part of **Figure 2.11.** More detailed mechanism of excimer formation in benzene and in pyrene will be discussed further in **Chapter 6**.

2.1.7 Optical Spectroscopy of Molecular Crystals

While forces between molecules in a crystal are weak and short-range, and the overlap between the orbitals of adjacent molecule in the lattice is small, there is a significant difference between the electronic spectra of a molecular crystal and free molecules.[5] Some of these differences arise from the interactions between the electronic state of the molecule with the molecule(s) in proximity. The sensitivity of optical properties to the structure of and interactions within molecular crystals implies that the studies of the spectra of a molecular crystal can result in a large amount of information on the structures and interactions.

Electronic spectral measurement of solids presents a number of practical difficulties, especially for the UV-vis absorption spectra. This is due to the high concentration of the chromophore in the solid, which leads to very strong optical absorbance for all but very thin samples. A molecular crystal which could result in absorbance of ~1 would require a crystal thickness in the order of micrometres, and this reason only would make it challenging for the measurement.

Diffuse-reflectance spectroscopy (DRS) is a technique used to measure the absorption of solid samples, such as molecular crystals. This can be achieved by collecting the diffused-reflectance of the sample, usually using an integrating sphere to diffuse the reflected light, and comparing the diffused-reflected light from the sample with a reference, that is considered to have total reflection. The light absorption of a solid material can be described using the Kubelka-Munk relationship, as shown in **Equation 2.24**.

$$\frac{K}{S} = \frac{(1 - R_\infty)^2}{2\,R_\infty}$$

Equation 2.24

Where the R_∞ is the reflectivity, analogue to transmittance, K is the absorption coefficient, and the S is the scattering coefficient. The problem with this method is the difficulty in finding a standard with a 100% reflectivity and the unknown value of the scattering coefficient. While finding a standard with a known reflectance could solve the problem, such as MgO with a known 98% reflectivity across visible wavelength, getting the value of S which is independent of wavelength can be achieved by grinding the sample, so K/S is proportional to K only. The sample may be diluted using an inert substance which has no optical absorbance, such as $BaSO_4$. This method was used in this work for the validation of the high-pressure UV-vis absorption measurement setup.

2.2 Single-Crystal X-ray Diffraction

Unlike the UV-vis absorption and fluorescence spectroscopy methods, X-ray diffraction methods are based on the non-absorptive scattering of radiation by a sample.[9] These methods typically use single wavelength X-ray radiation, with wavelength comparable to the size of the scattering object, in the ~1Å range, which is close to the scale of interatomic distance. The principle of the method can be seen as analogous to an optical microscope for observing a small object, where the light is scattered by the object, and some of the scattered light enters the eye. In the eye, the scattered light is then bent (refracted) by the lenses to combine by adding up the scattered waves on the retina, forming an image interpreted by the brain. Unfortunately, in the case of X-ray radiation, upon scattering by an object as small as a molecule, the scattered light cannot be focussed by regular lenses, as the refractive index of virtually all materials for X-rays is close to 1. Therefore, mathematical methods are utilised to solve the diffracted X-ray radiation to obtain the structure of the sample. Nowadays, all the processes from collecting the diffraction pattern to solving the structure and the refinement of the structure are done with the help of a computer.

The scattering of X-rays by electrons is a weak and inefficient process, where the vast majority of the incident beam is transmitted without any deflection. A single-molecule or a small collection of molecules does not give sufficient scattering of the beam to be measured experimentally. On the other hand, a single crystal, a regular array of unit cells, constructed by many millions of molecules can give a measurable diffraction pattern. The diffraction pattern from a single crystal has three obvious properties: (a) it consists of discrete sharp points, seen as individual dots with distinct intensities; (b) it often displays rotation, reflection symmetry and almost always inversion symmetry, with respect to not only to the diffracted beam direction but also in terms of equal intensities for related diffraction beams; (c) apart from the symmetry, the intensity distribution essentially shows no obvious relation to the diffracted beam intensities. For instance, **Figure 2.12 a** shows a computer-generated diffraction pattern in *h* and *k* axes, with a symmetry relationship that can be observed between quadrants. However, there is no regular intensity pattern that can be observed in the first quadrant ($h > 0$ and $k > 0$).

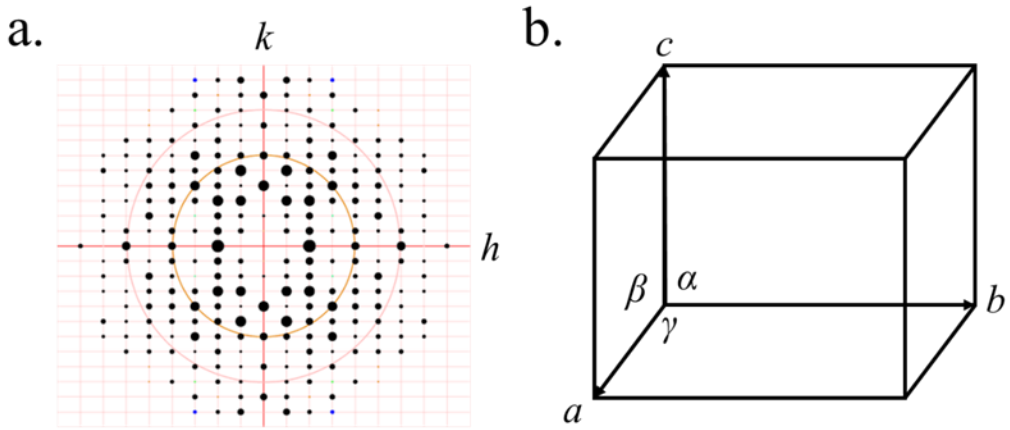

Figure 2.12. (a) A computer-generated reproduction of an X-ray diffraction pattern and (b) the unit cell parameters.[11]

Each of these properties is related to a corresponding feature of the crystal structure: (a) the diffraction geometry is a direct consequence of the crystal lattice and unit cell geometry; (b) the symmetry of the diffraction pattern is related to the symmetry of the crystal structure as expressed in its crystal system, and space group; (c) the intensities of the diffracted beams represent the content of the unit cell at these particular points, so they are dictated by the positions of atoms in the unit cell. In order to solve the crystal structure, it is vital to collect as many as possible diffraction spots in three

dimensions, by slowly rotating the sample whilst fully irradiating with the X-ray beam. An area detector synchronised with a goniometer is typically used to record diffraction spots and to record the sampling angle from the sample. Unfortunately, when the X-ray scattering pattern is recorded, the individual wave amplitudes are retained as relative intensities, but the relative phases are lost. This makes the mathematical reconstruction stage much less straightforward, which is one of the fundamental challenges of using crystallography to solve the crystal structure.[10]

As can be seen from **Figure 2.12 a**, part of the diffraction pattern shows discrete spots with a range of intensities. This pattern has a definite geometry and a degree of symmetry in the positions and intensities of individual spots. In this case, there are two mirror symmetry relationships along the *h* and *k* axes, and also inversion symmetry through the origin. The geometry of the pattern can be described by measuring the distance and angle between rows of spots. The measurement of the geometry of the diffraction pattern gives information about the regular arrangement of molecules in the crystal structure, where the symmetry of the diffraction pattern is directly related to the symmetry of the real crystal structure. The biggest task in determining a crystal structure is to measure the intensities of the diffraction spots intensities, which aided by computational methods.

The diffraction pattern, which represents the reciprocal lattice, then can be indexed using Miller indices, analogue to cartesian coordinates, with *h, k* and *l* vectors which lie along the *a**, *b** and *c** axes, respectively. The direct unit cell parameters can be determined directly using the diffraction pattern. The unit cell is the simplest building block that is repeated in three dimensions to produce the bulk crystal. A unit cell is characterised by three vectors *a*, *b* and *c*, which lie along the *x*, *y* and *z*-directions respectively, as shown in **Figure 2.12 b**. Apart from the unit cell axes, there are the angles, α, β and γ, between the vectors. Based on the symmetry and the measurement of the unit cell parameters, the crystal system is divided into seven types, as shown in **Table 2.1**. These seven crystal systems then can be divided into 14 Bravais lattices, which later can be divided into 230 possible space groups. The space groups describe the symmetry operations present in the infinitely repeating three-dimensional pattern.

Table 2.1. The essential crystal symmetry and unit cell restrictions of the seven crystal systems.

Crystal System	**Essential Symmetry**	**Unit Cell restrictions**	**Cell Types**
Triclinic	None	None	P (Primitive)
Monoclinic	2 and/or *m* for one axis	$\alpha=\gamma=90°$	P (Primitive) C (Base-Centered)
Orthorhombic	2 and/or *m* for three axes	$\alpha=\beta=\gamma=90°$	P (Primitive) C (Base-Centered) I (Body-Centred) F (Face-Centered)
Tetragonal	4 for one axis	$a = b$; $\alpha=\beta=\gamma=90°$	P (Primitive) I (Body-Centered)
Trigonal	3 for one axis	$a = b$; $\gamma=90°$, $\alpha=\beta=90°$	P (Primitive)
Hexagonal	6 for one axis	$a = b$; $\gamma=90°$, $\alpha=\beta=90°$	P (Primitive)
Cubic	3 for four directions	$a=b=c$; $\alpha=\beta=\gamma=90°$	P (Primitive) I (Body-Centered) F (Face-Centered)
The number in the second column represents the degree of rotational symmetry, and the *m* represents the mirror symmetry operation.			

The diffraction spots and positions contain information about the size of the unit cell and atomic positions in the crystal, according to Bragg's law, as illustrated in **Figure 2.13**. The law treats crystals as a series of parallel planes of atoms separated by a small distance, *d*. The planes are assumed to be reflecting the X-rays in a manner which results in the angle incidence equal to the angle of diffraction. The contributions from successive planes will be in-phase only for certain angles, which results in constructive interference, and the production of diffraction spot maxima when the Bragg equation, **Equation 2.25,** is satisfied. If an atom is found in between the planes, the diffracted X-rays will be out of phase, which results in destructive interference. The destructive

interference will result in the absence or less intense diffraction spots. This constructive and destructive interference of the X-rays is a reason why the diffraction spots appear with different intensities.

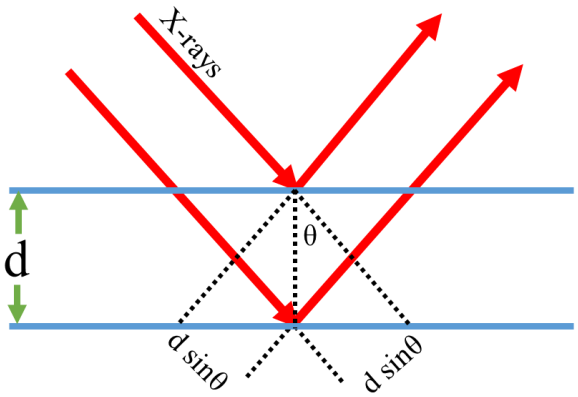

Figure 2.13. Schematic of the relationships that constitute the Bragg equation.

$$2d \sin \theta = n\lambda$$

Equation 2.25

Once the unit cell parameters and space groups are known, and the diffraction spot intensities are calculated, the data reduction process can be done. Data reduction mainly deals with absorption correction, geometrical corrections, and X-ray beam intensity correction. The absorption has to be corrected due to the different path length of the X-rays, caused by the non-spherical shape of the crystal. This causes the intensity of diffraction spots to be dependent on the orientation of the crystal, relative to the direction of the X-rays beam. The symmetrically related diffraction spots can also be merged, and scale factors can be applied. This process is also normally performed by computers.

The crystal structure can be solved from the reduced and scaled data. The structure factor, *F*, which has a square relationship to the diffraction spot intensity, is used to describe how the incident X-rays are diffracted by the constituent atoms of a crystal, as described in **Equation 2.26**.

$$F(hkl) = \sum_{j=1}^{N} f_j e^{2\pi i(hx_j + ky_j + lz_j)}$$

Equation 2.26

where N is the number of atoms within the structure, and f_j is the atomic scattering factor for the j^{th} atom. The x_j, y_j and z_j define the atomic position of the j atom in fractional coordinate. The diffraction pattern is the Fourier transform of the electron density, as shown in **Equation 2.27**.

$$F(hkl) = \int_{cell} \rho(xyz).\, e^{2\pi i(hx+ky+lz)} dV$$

Equation 2.27

where $\rho(xyz)$ is the electron density at fractional coordinate x, y and z. The equation in this form, however, is not convenient for calculation because it contains integration and continuous function $\rho(xyz)$. The electron density is the inverse Fourier transform of the diffraction pattern as described in **Equation 2.28**.

$$\rho(xyz) = \frac{1}{V} \sum_{h,k,l} |F(hkl)|.\, e^{(i\phi\,(hkl))}.\, e^{(-2\pi i\,(hx+ky+lz))}$$

Equation 2.28

where the V is the unit cell volume. This method is used to find the electron density within the unit cell. The constituent atoms in the crystal structure are determined based on the electron density map.

Once the initial structure is obtained, structure refinement can be carried out to obtain the optimum agreement between the observed structure factor, F_O, and the calculated structure factor, F_C, often measured by crystallographic R factor, as defined in **Equation 2.29**. For a correct and a complete crystal structure determined from well-measured data, the R factor is typically around 0.02-0.07.[10] The lower the R factor value, better the refinement.

$$R = \frac{\sum |F_O - F_C|}{\sum |F_O|}$$

Equation 2.29

The weighted *R* uses F^2 values instead of $|F|$ values, squaring the differences, and/or incorporating different weighting factors multiplying different reflections, as shown in **Equation 2.30**.

$$wR2 = \sqrt{\frac{\sum w(F_O^2 - F_C^2)^2}{\sum wF_O^2}}$$

Equation 2.30

The values of *wR*2 and other residual factors based on F^2 are generally higher than those based on *F* values, by a factor of two or more.

Some parameters, such as atomic displacement parameters, which represent the vibrational movement of atoms in the crystal, and some restraints such as atomic distance and angle, can also be applied during the refinement.

Additional measurement features, such as the use of low temperature to reduce the vibrational motion, can also be used during data collection to acquire better quality data. High-pressure devices can also be utilised to study the crystal structure under the influence of hydrostatic pressure and gas uptake of porous materials.[12-14]

2.3 High-Pressure Techniques

2.3.1 The Diamond Anvil Cell

A high-pressure environment at gigapascal (GPa) scale can be achieved using a diamond anvil cell (DAC). The DAC was first developed in 1958 by Weir and used the strength of diamond under compression and the shape of the opposing anvils to reduce the area to generate extreme pressure.[15] Its miniaturised version, developed by Merrill and Bassett in 1974, makes it possible to be utilised in various measurements such as spectroscopy measurements[15,16], magnetic measurements[17] and X-ray diffraction.[18,19] The pressure inside the cell depends on the size of the diamonds, as the inverse relationship between the pressure and the area, a smaller diamond with small culet size can generate more pressure. For example, a diamond culet size of 600 μm is capable of reaching 10 GPa of pressure, with an appropriate pressure transmitting medium (PTM). [20]

The Merrill-Bassett DAC is depicted schematically in **Figure 2.14**. A solid sample, typically a single-crystal or polycrystalline powder, is loaded into a premade gasket,

usually made of tungsten, alongside a ruby crystal (Al_2O_3: Cr^{3+}), as a pressure indicator, and the PTM. In this work, the gasket, made of tungsten, has a cylindrical shape with ~200 μm in diameter and ~100 μm in height. Pressure in the cell was increased by tightening three Allen screws equally; this pulls the diamonds together and squeezes the cell.[21] A pair of tungsten carbide backing discs were used in between the diamonds, and the steel body to increase the robustness of the DAC, as the direct contact between diamond and steel body could damage the steel in the long term.[22]

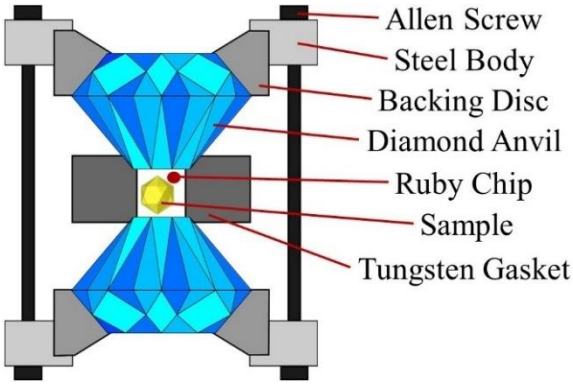

Figure 2.14. Schematic of Merrill-Bassett diamond anvil cell (DAC). The figure is not to scale.

It is essential to choose the PTM correctly, depending on the type of sample, whether it is porous, its reactivity, and the pressure to be achieved.[20] Porous materials, such as metal-organic frameworks (MOFs), behave differently under pressure in a penetrating or non-penetrating PTM, as will be discussed in **2.3.3**. Some PTMs will lose their hydrostatic properties at relatively low pressure, such as Fluorinert FC-70 (Sigma-Aldrich), which loses its hydrostatic properties at ~0.6 GPa.[23] Fluorinert FC-70 consists of a tertiary amine with fluorinated pentane, which ensures its non-reactive property. While Fluorinert FC-70 is commercially available, other PTMs can be made by mixing widely available solvents, such as MeOH: EtOH (4:1) or iso: n-pentane (5:1). In this work, Fluorinert FC-70, Daphne 7373 (Idemitsu), pentene and methanol were used in various studies of molecular crystals and MOFs.

2.3.2 In-situ High-Pressure Measurement

One of the most common materials used as an *in situ* pressure calibrant is a ruby crystal (Al_2O_3: Cr^{3+}) which is inserted in the DAC alongside the sample. Ruby has a known fluorescence spectrum under atmospheric pressure (~10^{-4} GPa) at around 694 nm, and this varies depending on the Cr^{3+} content. The fluorescence spectrum of Ruby, as

illustrated in **Figure 2.15**, shows two distinct peaks, R_1 and R_2. Both peaks merge into one at higher pressure. However, the pressures generated in this work are not high enough to see the merger between R_1 and R_2. Only the stronger peak, R_1 is used for the pressure calculation.

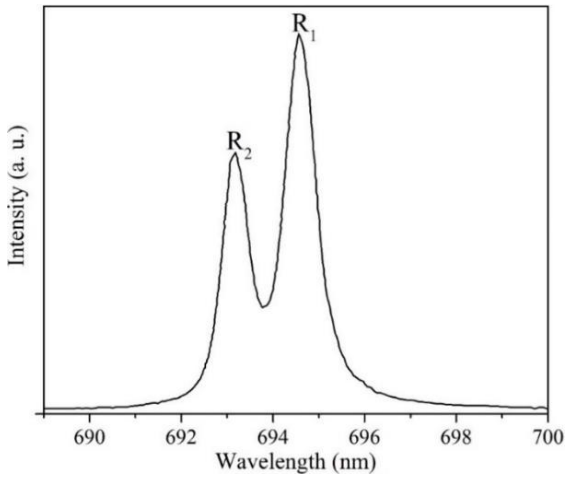

Figure 2.15. Fluorescence spectra of Ruby crystal with R_1 and R_2 peaks in hydrostatic compression.

In order to calibrate shift of the ruby R_1 fluorescence peak as a function of pressure, Piermarini *et al.* used a known NaCl crystal as a reference up to 19.5 GPa.[24] The R_1 peak wavelength shift is then plotted against pressure, as displayed in **Figure 2.16**. The effect of pressure on the R_1 peak shift as a function of pressure is found to be linear, as expressed in **Equation 2.31**.

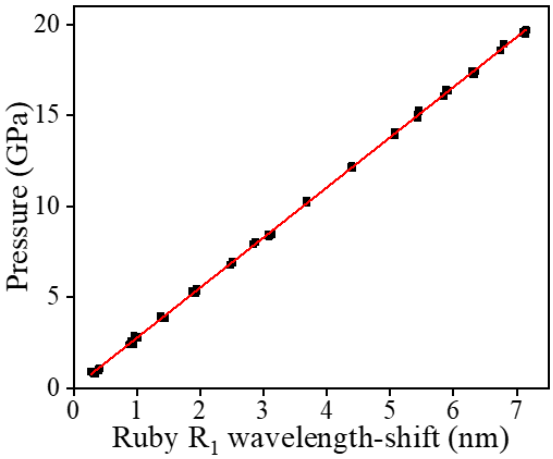

Figure 2.16. Plot of applied pressure versus Ruby R_1 fluorescence wavelength shift ($\Delta\lambda$). Adapted from Piermarini et al.[24]

$$P = 2.746(\Delta\lambda)$$

Equation 2.31

where P is the calculated pressure in gigapascal (GPa), and the $\Delta\lambda$ is the ruby R_1 fluorescence shift at a given pressure, relative to the ambient pressure. Mao *et al.* also carried out a similar experiment using a Cu crystal as a standard up to 80 GPa, with a very similar relationship between the pressure and the shift of the R_1 peak.[25]

Vos *et al.* reported that the ruby R_1 peak shift is also dependent on the temperature within the range of 150-400K, with only 0.03nm difference in the shift, this contributes to about 0.1 GPa across the temperature range.[26] The trend of the wavelength shift is given in **Equation 2.32**.

$$\Delta\lambda\ (\text{Å}) = (6.591\times10^{-2} \times T_x) + (7.624\times10^{-5} \times T_x^2) - (1.733\times10^{-7} \times T_x^3)$$

Equation 2.32

where $T_x = T(\text{K}) - 300$. The experiments reported in this thesis were carried out at room temperature with small temperature fluctuations. Therefore, the temperature-dependence of the ruby R_1 peak shift was not considered on calculating the pressure.

2.3.3 Metal-Organic Frameworks and their Response to Pressure

Since their discovery in 1965, metal-organic frameworks (MOFs) have become attractive materials for several applications, mainly in gas storage, catalysis and sensing.[27-30] The study of MOFs is a multidisciplinary area of research, including supramolecular chemistry, crystallography, materials science, surface chemistry and many more. As a consequence, there were ~20000 MOF entities registered in the Cambridge Structural Database (CSD) in 2013 and this increased to more than 88000 in 2019, which amounts to ~30 novel MOF structures per day.[31,32]

The vast number of MOFs structures constitutes ~8.8% of the overall structures deposited in the CSD. This extraordinary number of structures deposited in CSD reflects the simple and straightforward synthesis methods and a wide variety of available precursors. The MOFs typically can be synthesised with hydro- or solvothermal, microwave-induced synthesis, electrochemical or mechanochemical methods, all of which are accessible at low temperature and are available widely in even simple laboratories.[33,34]

The structure of MOFs consists of organic ligands, also known as linkers, and metal ion nodes or clusters, known as the secondary building units (SBUs), as illustrated in **Figure 2.17**. The SBU is a large cluster consisting of metal ions and, most commonly, oxygens which can increase the coordination number of the nodes, compared to conventional metal ions.[35] For instance, the typical $[Zr_6O_4(OH)_4]^{12+}$ SBU has 24-fold coordination, while Zr^{4+} typically has only 8-fold. By knowing the ligand and the coordination number of the metal ion nodes or SBUs, the structure can be predicted with ease. Several structures also emerge due to the design of the ligands and/or the SBUs.[36,37] The availability of ligand modifications make the options for novel MOFs discovery virtually unlimited. This results in the technique of tuning the MOFs to design the desired structure. [36,38-40]

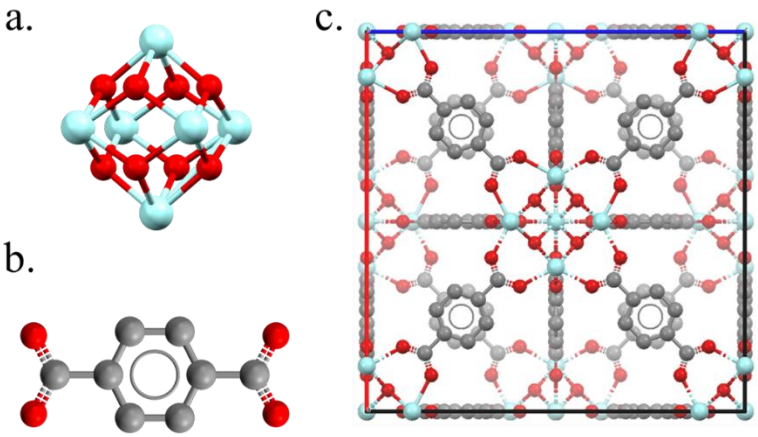

Figure 2.17. The UiO-66 MOF consisted of (a) $[Zr_6O_4(OH)_4]^{12+}$ SBU, (b) phenylbicarboxylate ligand, which constructs (c) a robust 3D structure. Colour scheme: Hf – blue, O – red, C – grey. Hydrogen atoms were omitted for clarity.

The concurrent effort by researchers in the field not only gave birth to numerous novel MOFs but also to several naming systems. This class of compound is also referred to as *hybrid inorganic-inorganic frameworks*, *coordination networks* or *nanoporous hybrid frameworks*.[41] To unify the terms and naming systems, in 2013, the International Union of Pure and Applied Chemistry (IUPAC) recommended a unified definition for MOFs.[42] IUPAC recommends that the term MOF is used for the compound with "coordination network containing ligands containing potential voids". This nomenclature is different to *coordination network* as "compound extending, through repeating coordination entities, in 1 dimension, but with cross-links between two or more individual chains, loops, or spiro links, or a coordination compound

extending through repeating coordination entities in 2 or 3 dimensions".[42] If this system works, the confusion on tracking the record of MOFs in the crystallography database could be avoided.

One of the most renowned examples of MOFs is the UiO-family, which, at the time of the writing this thesis, has over 2500 citations.[43] This type of MOF is constructed by extensible dicarboxylic ligands, where a ligand of conjugated phenyl rings is coordinated to $[M_6O_4(OH)_4]^{12+}$ (M =Zr or Hf) SBUs. The three most common and most straightforward examples are the UiO-66, UiO-67 and UiO-68, which have 1,4-benzendicarboxylate (BDC), 4,4'-biphenyldicarboxylate (BPDC) and [1,1':4',1"-terphenyl]-4,4"-dicarboxylate (TPDC) ligands, respectively (**Figure 2.18**). The UiO-66 MOF, considered the most important in the family, acts as a prototype from which the other members are developed isoreticularly.[44] UiO-68 even has a ligand that is long enough to give a large pore that accommodates the twisting of the central phenyl ring, as seen in **Figure 2.18 c**. This long and electronically conjugated ligand gives rise to fluorescent MOFs for light-emitting diode (LED) or sensing applications.[39,45,46]

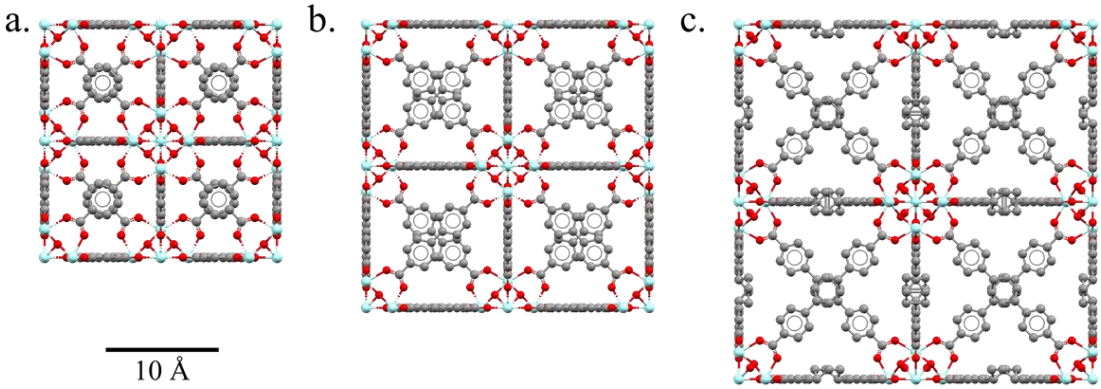

Figure 2.18. The UiO-family MOF showing (a) UiO-66, (b) UiO-67 and (c) UiO-68. It can be seen that the central phenyl ring for the UiO-68 is disordered due to its ability to twist. Hydrogen atoms are not shown for clarity.

Such a wide range of applications and ease of synthesis do not come without challenges. One of the challenges is relatively low stability; because of their organic molecule building blocks, MOFs have limited thermal stability. For example, the Li_2(2,6-NDC) (NDC = napthalenedicarboxylate) MOF is stable to 610°C and the UiO-66 MOF, can only withstand temperatures up to 500°C.[43,47] This thermal stability is poor in comparison with competing porous materials, such as zeolites which can withstand temperatures up to 800°C.[48] This high thermal stability itself is one of the

reasons why zeolites are used in industry for molecular separation and catalyst.[49] The reason for the stability of zeolite is that they mainly consists of aluminium silicate, which, by nature, is resistant to oxidation at high temperature. Nevertheless, zeolites lack potential in comparison to MOFs, in terms of the wide variety of structure, pore size, and optical properties.

One of the most recent industrial applications of a MOF is the use ION-X® (NuMat Technologies) for the storage of toxic gases, such as arsine, phosphine and BF_3, allowing the gases to be stored at sub-atmospheric pressure, preventing the accidental gas leakage that can occur when the gas is stored in pressurised storage.[50] Another example is the use of MOFs to store 1-methylcyclopropane (1-MCP), widely used as an anti-ripening agent for fruits; this development by TruPick, enables the release the 1-MCP slowly so the fruits can be stored for a more extended time.[51]

High-pressure experiments on MOFs, using the diamond anvil cell (DAC), have become the method-of-choice for exploring mechanical stability, inducing ligand exchange reactions, locating gas molecules in pores, causing changes in pore size and guest content, and inducing low-temperature melting of amorphous frameworks.[52-57]

On increasing the pressure applied to the Zirconium Imidazolate Framework-8 MOF, the pressure transmitting medium (PTM) could be observed to enter the pores, causing the crystal structure to expand, while at 1.47 GPa, the crystal underwent a phase transition which resulted in a significant increase in pore volume and content.[58] The phase transition was induced by the rotation of the imidazolate ligand upon uptake of the hydrostatic medium, indicating the flexibility of the ligand. Ligand flexibility is a common phenomenon in MOFs that can be utilised to induce a breathing mechanism for gas adsorption.[59]

A high-pressure study on the UiO-family MOFs demonstrated them to have intriguing stability towards extreme pressure.[60] For instance, the behaviour of UiO-67 and UiO-abdc (abdc = 4,4'-azobenzenedicarboxylate) was heavily dependent on the ligand, and the PTM used during the pressure experiment, as depicted in **Figure 2.19**. Both UiO-67 and UiO-abdc showed minimal compression when methanol was used as the PTM but showed a direct compression in perfluorinated oils (FC-70). The reason for the insignificant compression in methanol is that methanol can enter the pore of the MOFs,

while the FC-70 molecule is too large to penetrate. It was also found that the longer the ligand, the more bowed it became. However, the increase of the bending of the ligand structure increases mechanical robustness.[60] This phenomenon will be explored further in **Chapter 5**, from the spectroscopic and computational point of view.

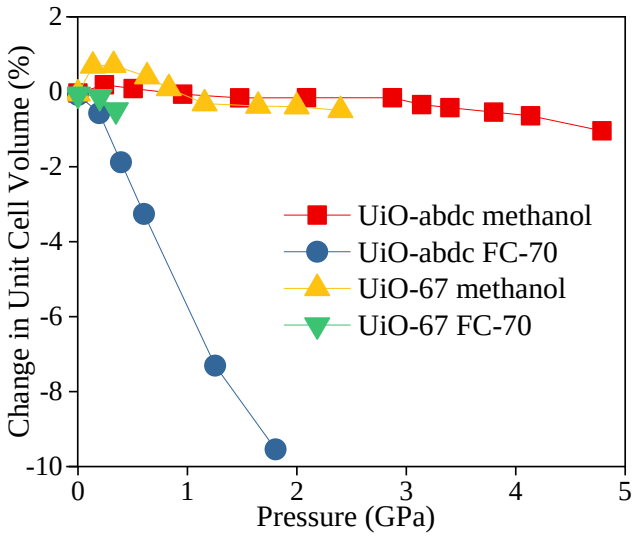

Figure 2.19. The percentage change in unit cell volume as a function of pressure for UiO-abdc in methanol and FC-70 (red squares and blue circles) and UiO-67 in methanol and FC-70 (yellow triangles and green triangle). Redrawn from Hobday *et al.*[60]

2.3.4 Effect of Pressure on Molecular Crystals

Weak intermolecular interactions play a significant role in the packing of organic molecules in a crystal.[7,61] In a molecular crystal containing non-polar molecules, the London dispersion forces govern the attraction of the molecules. Due to these forces, aromatic molecules are mainly found in face-to-face (π-π) and edge-to-face (T-shaped) configurations. The face-to-face (π-π) configurations can be found in the crystals of disc-like aromatic molecules such as pyrene and phthalocyanine.[62] On the other hand, the T-shaped interaction relies on the CH···π hydrogen bonding, forming a herringbone molecular arrangement, and can be found in small polycyclic aromatic hydrocarbons, such as benzene, and aromatic molecules with more linear structures, such as terphenyl, tetracene and picene.[61]

With increasing pressure, the intermolecular interactions are expected to strengthen. As a consequence, intramolecular bonds may be elongated.[63] This is the case for the paracetamol crystal, where the hydrogen bond length is decreased, followed by a small elongation in the carbonyl bond of only 0.023 Å at 4 GPa. However, the change of this

intramolecular covalent bond is minuscule and often ignored during the refinement of the high-pressure crystal structure, by restraining the bond length and the temperature values. Often, this restraining of bond length is due to the low data completeness and low data-to-parameter ratios, caused by the shading of the DAC. The organic compounds with low point-group symmetry are also usually crystallised in low-symmetry crystal systems, typically triclinic, and the pressure compresses the crystal in an anisotropic manner. This anisotropic effect of pressure is mainly due to the compression of the weakest intermolecular interactions, such as hydrogen bonds, which is not uniform along all axes. Anisotropic compression is a phenomenon that has been found in most of the organic molecular crystals studied in the present work.

2.3.5 Electronic Spectroscopy at High-Pressure

The study of optical spectroscopy of materials at high pressure started not long after the development of the miniaturised DAC, with Harry Drickamer as a pioneer in the field.[64] A wide variety of materials has been studied, from the liquid phase and solid-state studies, such as inorganic and organic phosphors in the 1990s. However, in the 2000s, the study of high-pressure electronic spectroscopy became less frequent.

Under high-pressure environment, bulk and microscopic changes are often investigated.[64] The bulk changes consist of the change in volume, viscosity, dielectric constant, refractive index, *etc*. On the other hand, the microscopic change consists of structural change of the molecules, including the intra- and intermolecular interactions. Both bulk and microscopic change as a function of pressure can affect the electronic spectrum of a system. In this thesis, the microscopic change is investigated with the help of single-crystal X-ray diffraction and linked to the electronic spectra.

In liquid-solution phase, Lang *et al.* reported the effect of pressure on the twisted intramolecular charge transfer (TICT) of the 4,N,N'-dimethylaminobenzonitrile (DMABN) in a series of linear alcohols; ethanol, *n*-butanol and *n*-pentanol.[65] The change of solvent viscosity as a function of pressure was estimated from the experiment conducted by Bridgman.[66] It was revealed that the ratio of emission intensity between the TICT state and locally excited (LE) state was decreasing as pressure increase. This indicates that the TICT process was suppressed with increasing pressure. This report only concerned about the pressure-induced bulk changes of the

solvent in relation to the optical properties change of DMABN and not really touch the microscopic change.

In solid-solution phase, Zhu *et al.* reported that the pressure affects the excited-state intramolecular proton transfer (ESIPT) and intramolecular charge transfer (ICT) of 4'-N-(dimethylamino)-3-hydroxyflavone in various polymeric solvents.[67] The fluorescence spectra were redshifted with increasing pressure, which was speculated due to an increase in interaction between the molecule and the solvent. The pressure suppressed the ESIPT emission and causes change in fluorescence profile. It also reported that the quantum yield is increased with increasing pressure up to ~6 GPa when excited with 325 nm light.

A more recent study of the fluorescence, UV-vis absorption and powder X-ray diffraction (PXRD) method of the DMABN crystal have been carried out by Dai *et al.*, and it is reported that the emission from the LE state decreased followed by an increase in emission from the intramolecular charge transfer (ICT) state with increasing pressure.[68] This phenomenon is followed by a redshift in the absorption spectrum and a decrease in the fluorescence intensity as a function of pressure. It is speculated that the pressure caused a more planar molecule which increases the stacking of the molecular plane, which is responsible for the quenching. Liu *et al.* also reported a redshift of the fluorescence emission spectrum and decrease in intensity as a function of the pressure for crystals of anthracene derivates.[69] The anthracene excited state π-π interplanar stacking distance was estimated from the change of unit cell dimensions using PXRD method. It is predicted that with increasing pressure, the anthracenes stacking distance becomes smaller, causing both a redshift and quenching. However, these studies were using PXRD method to determine intermolecular distance, which is less reliable as the distance can only be estimated, and not directly measured as in the single-crystal X-ray diffraction method, used in this thesis.

This thesis reports development of custom-built *in situ* high-pressure fluorescence emission and UV-vis absorption spectra measurement setup to investigate the change in optical properties of materials as a function of pressure. The spectroscopy method also combined with *in situ* high-pressure single-crystal X-ray diffraction method, to directly link the change in the optical properties with the evolution of the molecular

structure as well as intra- and intermolecular interactions measured directly from the crystal structures as a function of pressure, which is much more reliable technique than the PXRD.

2.4 References

1. Lakowicz, J. R., *Principles of fluorescence spectroscopy*. 3rd ed.; Springer: New York, **2006**.
2. Atkins, P. W.; De Paula, J., *Atkins' Physical Chemistry*. Tenth edition. ed.; Oxford University Press: Oxford ; New York, **2014**.
3. Hollas, J. M., *Modern spectroscopy*. 4th ed.; J. Wiley: Chichester ; Hoboken, NJ, **2004**.
4. Birks, J. B., *Photophysics of Aromatic Molecules*. Wiley-Interscience: London, New York, **1970**.
5. Wright, J. D., *Molecular Crystals*. Second Ed.; Cambridge University Press: Cambridge, **1995**.
6. Braslavsky, S. E., *Pure Appl. Chem.* **2007,** *79* (3), 293-465.
7. Stevens, B., *Spectrochim. Acta* **1962,** *18* (4), 439-448.
8. Pensack, R. D.; Ashmore, R. J.; Paoletta, A. L.; Scholes, G. D., *J. Phys. Chem. C* **2018,** *122* (36), 21004-21017.
9. The 14th BCA/CCG Intensive Teaching School in X-ray Structure Analysis Lecture Note **2013**.
10. Clegg, W., *Crystal structure determination*. Oxford University Press: Oxford ; New York, **1998**.
11. Parsons, S. Chemistry 3 Lecture Notes **2019**.
12. Yufit, D. S.; Howard, J. A. K., *Acta Crystallogr. A* **2005,** *61*, C468-C468.
13. McKellar, S. C.; Moggach, S. A., *Acta Cryst. B* **2015,** *71* (Pt 6), 587-607.
14. McMonagle, C. J.; McKellar, S. C.; Sotelo, J.; Warren, M. R.; Allan, D. R.; Moggach, S. A., *Acta Crystallogr. A* **2015,** *71*, S84-S84.
15. Weir, C. E.; Lippincott, E. R.; Vanvalkenburg, A.; Bunting, E. N., *J. Res. Nat. Bur. Stand. A Phys. Chem.* **1959,** *63* (1), 55-62.
16. Drickamer, H. G., *Abstr. Pap. Am. Chem. Soc.* **1987,** *193*, 6-Phys.
17. Graf, D. E.; Stillwell, R. L.; Purcell, K. M.; Tozer, S. W., *High Pressure Res.* **2011,** *31* (4), 533-543.

18. Merrill, L.; Bassett, W. A., *Rev. Sci. Instrum.* **1974,** *45* (2), 290-294.
19. Ridley, C. J.; Kamenev, K. V., *Z. Kristallogr. Cryst. Mater.* **2014,** *229* (3), 171-199.
20. Millar, D. I. A., *Energetic Materials at Extreme Conditions*. PhD Thesis, The University of Edinburgh **2012**, 1-222.
21. McKellar, S. C.; Moggach, S. A., *Acta. Crystallogr. B Struct. Sci. Cryst. Eng. Mater.* **2015,** *71* (Pt 6), 587-607.
22. Moggach, S. A.; Allan, D. R.; Parsons, S.; Warren, J. E., *J. Appl. Crystallogr.* **2008,** *41*, 249-251.
23. Varga, T.; Wilkinson, A. P.; Angel, R. J., *Rev. Sci. Instrum.* **2003,** *74* (10), 4564-4566.
24. Piermarini, G. J.; Block, S.; Barnett, J. D.; Forman, R. A., *J. Appl. Phys.* **1975,** *46* (6), 2774-2780.
25. Mao, H. K.; Xu, J.; Bell, P. M., *J. Geophys. Res. Solid Earth and Planets* **1986,** *91* (B5), 4673-4676.
26. Vos, W. L.; Schouten, J. A., *J. Appl.Phys.* **1991,** *69* (9), 6744-6746.
27. Ahmed, A.; Seth, S.; Purewal, J.; Wong-Foy, A. G.; Veenstra, M.; Matzger, A. J.; Siegel, D. J., *Nat. Commun.* **2019,** *10*.
28. Lee, J.; Farha, O. K.; Roberts, J.; Scheidt, K. A.; Nguyen, S. T.; Hupp, J. T., *Chem. Soc. Rev.* **2009,** *38* (5), 1450-9.
29. Lin, R. B.; Liu, S. Y.; Ye, J. W.; Li, X. Y.; Zhang, J. P., *Adv. Sci.* **2016,** *3* (7).
30. Gangu, K. K.; Maddila, S.; Mukkamala, S. B.; Jonnalagadda, S. B., *Inorg. Chim. Acta.* **2016,** *446*, 61-74.
31. Moghadam, P. Z.; Li, A.; Wiggin, S. B.; Tao, A.; Maloney, A. G. P.; Wood, P. A.; Ward, S. C.; Fairen-Jimenez, D., *Chem. Mater.* **2017,** *29* (7), 2618-2625.
32. Moghadam, P. Z.; Rogge, S. M. J.; Li, A.; Chow, C.; Wieme, J.; Moharrami, N.; Aragones-Anglada, M.; Conduit, G.; Gomez-Gualdron, D. A.; Van Speybroeck, V.; Fairen-Jimenez, D., *Matter* **2019,** *1*, 219-234.
33. Safaei, M.; Foroughi, M. M.; Ebrahimpoor, N.; Jahani, S.; Omidi, A.; Khatami, M., *Trac-Trend Anal. Chem.* **2019,** *118*, 401-425.
34. Lee, Y. R.; Kim, J.; Ahn, W. S., *Korean. J. Chem. Eng.* **2013,** *30* (9), 1667-1680.

35. Eddaoudi, M.; Moler, D. B.; Li, H. L.; Chen, B. L.; Reineke, T. M.; O'Keeffe, M.; Yaghi, O. M., *Acc. Chem. Res.* **2001,** *34* (4), 319-330.
36. Lu, W. G.; Wei, Z. W.; Gu, Z. Y.; Liu, T. F.; Park, J.; Park, J.; Tian, J.; Zhang, M. W.; Zhang, Q.; Gentle, T.; Bosch, M.; Zhou, H. C., *Chem. Soc. Rev.* **2014,** *43* (16), 5561-5593.
37. Deria, P.; Mondloch, J. E.; Karagiaridi, O.; Bury, W.; Hupp, J. T.; Farha, O. K., *Chem. Soc. Rev.* **2014,** *43* (16), 5896-5912.
38. Kosaka, W.; Yamagishi, K.; Matsuda, R.; Kitagawa, S.; Takata, M.; Miyasaka, H., *Chem. Lett.* **2014,** *43* (6), 890-892.
39. Muller-Buschbaum, K.; Beuerle, F.; Feldmann, C., *Micropor. Mesopor. Mat.* **2015,** *216*, 171-199.
40. Fernandez, B.; Beobide, G.; Sanchez, I.; Carrasco-Marin, F.; Seco, J. M.; Calahorro, A. J.; Cepeda, J.; Rodriguez-Dieguez, A., *Crystengcomm* **2016,** *18* (8), 1282-1294.
41. Cheetham, A. K.; Rao, C. N. R.; Feller, R. K., *Chem. Commun.* **2006,** (46), 4780-4795.
42. Batten, S. R.; Champness, N. R.; Chen, X.; Garcia-Martinez, J.; Kitagawa, S.; Ohrstrom, L.; O'Keeffe, M.; Suh, M. P.; Reedijk, J., *Pure Appl. Chem.* **2013,** *85* (8), 1715-1724.
43. Cavka, J. H.; Jakobsen, S.; Olsbye, U.; Guillou, N.; Lamberti, C.; Bordiga, S.; Lillerud, K. P., *J. Am. Chem. Soc.* **2008,** *130* (42), 13850-13851.
44. Eddaoudi, M.; Kim, J.; Rosi, N.; Vodak, D.; Wachter, J.; O'Keeffe, M.; Yaghi, O. M., *Science* **2002,** *295* (5554), 469-472.
45. Angioni, E.; Marshall, R. J.; Findlay, N. J.; Bruckbauer, J.; Breig, B.; Wallis, D. J.; Martin, R. W.; Forgan, R. S.; Skabara, P. J., *J. Mater. Chem. C* **2019,** *7* (8), 2394-2400.
46. Lustig, W. P.; Mukherjee, S.; Rudd, N. D.; Desai, A. V.; Li, J.; Ghosh, S. K., *Chem. Soc. Rev.* **2017,** *46* (11), 3242-3285.
47. Banerjee, D.; Kim, S. J.; Parise, J. B., *Cryst. Growth. Des.* **2009,** *9* (5), 2500-2503.
48. Cruciani, G., *J. Phys. Chem. Solids.* **2006,** *67* (9-10), 1973-1994.
49. Weckhuysen, B. M.; Yu, J. H., *Chem. Soc. Rev.* **2015,** *44* (20), 7022-7024.

50. Notman, N. MOFs find a use. (accessed March 3) https://www.chemistryworld.com/features/mofs-find-a-use/2500508.article.
51. Urquhart, J. World's first commercial MOF keeps fruit fresh. (accessed March 3) https://www.chemistryworld.com/news/worlds-first-commercial-mof-keeps-fruit-fresh/1017469.article.
52. Yang, K.; Zhou, G.; Xu, Q., *RSC Adv.* **2016,** *6* (44), 37506-37514.
53. McKellar, S. C.; Graham, A. J.; Allan, D. R.; Mohideen, M. I. H.; Morris, R. E.; Moggach, S. A., *Nanoscale* **2014,** *6* (8), 4163-4173.
54. Sotelo, J.; Woodall, C. H.; Allan, D. R.; Gregoryanz, E.; Howie, R. T.; Kamenev, K. V.; Probert, M. R.; Wright, P. A.; Moggach, S. A., *Angew. Chem. Int. Ed.* **2015,** *54* (45), 13332-13336.
55. McKellar, S. C.; Sotelo, J.; Greenaway, A.; Mowat, J. P. S.; Kvam, O.; Morrison, C. A.; Wright, P. A.; Moggach, S. A., *Chem. Mater.* **2016,** *28* (2), 466-473.
56. Chapman, K. W.; Halder, G. J.; Chupas, P. J., *J. Am. Chem. Soc.* **2008,** *130* (32), 10524-10526.
57. Widmer, R. N.; Lampronti, G. I.; Anzellini, S.; Gaillac, R.; Farsang, S.; Zhou, C.; Belenguer, A. M.; Wilson, C. W.; Palmer, H.; Kleppe, A. K.; Wharmby, M. T.; Yu, X.; Cohen, S. M.; Telfer, S. G.; Redfern, S. A. T.; Coudert, F.-X.; MacLeod, S. G.; Bennett, T. D., *Nat. Mater.* **2019,** *18* (4), 370-376.
58. Moggach, S. A.; Bennett, T. D.; Cheetham, A. K., *Angew. Chem. Int. Ed.* **2009,** *48* (38), 7087-7089.
59. Schneemann, A.; Bon, V.; Schwedler, I.; Senkovska, I.; Kaskel, S.; Fischer, R. A., *Chem. Soc. Rev.* **2014,** *43* (16), 6062-6096.
60. Hobday, C. L.; Marshall, R. J.; Murphie, C. F.; Sotelo, J.; Richards, T.; Allan, D. R.; Düren, T.; Coudert, F.-X.; Forgan, R. S.; Morrison, C. A.; Moggach, S. A.; Bennett, T. D., *Angew. Chem. Int. Ed.* **2016,** *128* (7), 2447-2451.
61. Guijarro, A.; Verges, J. A.; San-Fabian, E.; Chiappe, G.; Louis, E., *Chemphyschem* **2016,** *17* (21), 3548-3557.
62. Jiang, H.; Hu, P.; Ye, J.; Ganguly, R.; Li, Y. X.; Long, Y.; Fichou, D.; Hu, W. P.; Kloc, C., *Angew. Chem. Int. Ed.* **2018,** *57* (32), 10112-10117.
63. Boldyreva, E. V., *J. Mol. Struct.* **2003,** *647* (1-3), 159-179.

64. Drickamer, H. G., *Ann Rev. Mater. Sci.* **1990,** *20*, 1-17.
65. Lang, J. M.; Dreger, Z. A.; Drickamer, H. G., *Chem. Phys. Lett.* **1995,** *243* (1-2), 78-84.
66. Bridgman, P. W., *Proc. Am. Acad. Arts Sci.* **1926,** *61* (3/12), 57-99.
67. Zhu, A.; Wang, B.; White, J. O.; Drickamer, H. G., *J. Phys. Chem. B* **2004,** *108* (3), 891-894.
68. Dai, Y. X.; Zhang, S. T.; Liu, H. C.; Wang, K.; Li, F. F.; Han, B.; Yang, B.; Zou, B., *J. Phys. Chem. C* **2017,** *121* (9), 4909-4916.
69. Liu, H. C.; Dai, Y. X.; Gao, Y.; Gao, H. C.; Yao, L.; Zhang, S. T.; Xie, Z. Q.; Wang, K.; Zou, B.; Yang, B.; Ma, Y. G., *Adv. Opt. Mater.* **2018,** *6* (15).

Chapter 3
Experimental

This chapter provides an overview of the techniques which are relevant to all of the studies presented in the thesis. This chapter will cover the methodologies of high-pressure X-ray diffraction and high-pressure steady-state UV-vis absorption and fluorescence emission spectroscopy. Further specialised techniques, such as computational methods and time-resolved fluorescence spectroscopy, will be explained in the specific chapters where they are relevant.

The experimental methodology for structure determination has been established prior to the research conducted in this thesis. On the other hand, the experimental setup and methodology for high-pressure spectroscopy, which will be discussed more in-depth, have been developed as part of the work for this thesis.

3.1 Sample Loading and Measurement of Pressure in DAC

The design of the Merrill-Bassett diamond anvil cell (DAC) has been explained in **Chapter 2**. The DAC used for X-ray crystallography consisted of a pair of identical 600-μm culet size diamonds with 80° opening angle, whereas, for the spectroscopy, a 60° opening angle is used. For each measurement, a tungsten gasket with 300-μm thickness was used, with a two-sided notch with a thickness of ~100 μm created by pressing the diamonds. A 200-μm hole was drilled in the middle of the notch, through the gasket, using a Motorised Electric Discharge Machine by Betsa®. During the drilling process, the gasket was submerged in kerosene to prevent oxidation by the oxygen in the atmosphere triggered by the generation of high temperature, and to prevent the tungsten dust escaping to the atmosphere. A ruby (Cr: Al_2O_3) chip with an approximate diameter of 20 μm was loaded into the cell next to the sample to act as a pressure indicator.

The pressure-dependence of the ruby fluorescence spectrum was used to determine the pressure in the DAC, as explained in **Chapter 2**. The ruby wavelength shift ($\Delta\lambda$), relative to the wavelength at ambient pressure, attributed to the pressure change, was

measured using an established setup, as shown in **Figure 3.1**. An objective lens (Mitutoyo 20X/0.21) was used to focus the output (532 nm) from a Nd:YAG laser pointer into the DAC. The fluorescence of the ruby was then collected with the same objective lens, and the light was guided into an Ocean Optics HR2000+ spectrometer, using mirrors. A dichroic mirror was used to prevent the excitation light from the laser reaching the detector. Spectra were collected using SpectraSuite software (Ocean Optics).

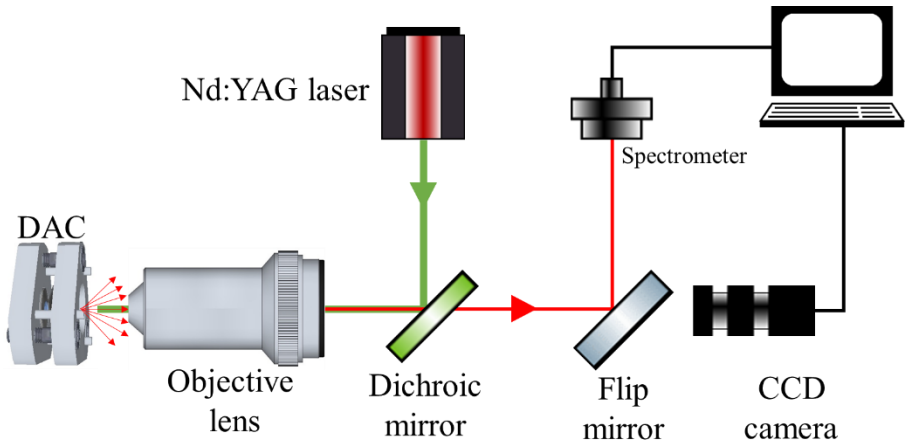

Figure 3.1. Schematic of Ruby fluorescence measurement setup.

During high-pressure X-ray diffraction measurement using synchrotron radiation, ruby spheres were used as pressure markers instead of ruby chips, to minimise the strong diffraction of the ruby. These pressure measurements were carried out using a similar system available at station I-19 at the Diamond Light Source, Rutherford Appleton Laboratory.

3.2 Ambient Pressure Single-Crystal X-ray Diffraction

Single-crystal X-ray diffraction data for the Hf-peb MOF (**Chapter 4**) at ambient pressure and room temperature were collected on a laboratory diffractometer. A single crystal was mounted on a MiTiGen Micro-loop and data were collected in all directions forming a sphere with a resolution of 0.3º ω, using a Bruker APEX2 diffractometer with graphite monochromated Mo Kα radiation (λ = 0.71073 Å) and a CCD detector. The data were integrated with the SAINT[1] program, and the absorption correction was carried out using SADABS[2] within the APEX2[3] software bundle. A run-list of the single-crystal diffraction at ambient pressure is given in **Table 3.1**.

Table 3.1. Run list of single-crystal diffraction at ambient pressure.

Run	2θ / °	κ / °	ϕ / °	ω / °	
				Initial	Final
1	28	73.85	-25.78	2.22	182.22
2	28	73.85	94.22	2.22	182.22
3	28	73.85	-145.79	2.22	182.22
4	-28	73.85	34.21	-53.78	126.22

3.3 Laboratory High-Pressure Single-Crystal X-ray Diffraction

The laboratory high-pressure single-crystal X-ray data of the Hf-peb MOF (**Chapter 4**) were collected using the same diffractometer and detector, as described in **3.2**. The sample, however, was put into a diamond anvil cell (DAC), and the DAC was glued onto a goniometer. A modified data collection strategy was used, taking into account the shading from the DAC to shorten data collection time, as shown in **Table 3.2**.[4] Data were also collected using Bruker APEX2 diffractometer with graphite monochromated Mo Kα radiation ((λ = 0.71073 Å) and CCD diffractometer with a resolution of 0.3ºω.

Table 3.2. Typical run list of high-pressure diffraction experiment.[4]

Run	2θ / °	ϕ / °	ω / °	
			Initial	Final
1	-28	90	-10	-40
2	28	90	40	-25
3	-28	90	-155	-220
4	28	90	-140	-170
5	-28	270	-155	-220
6	28	270	-140	-170
7	-28	270	-10	-40
8	28	270	40	-25

The reflection data were then selected using the SAINT[1] program, within the APEX2[3] software bundle, to remove the unwanted reflections, typically the reflections from the

diamond, ruby chip and the powder diffraction rings of the tungsten gasket. These unwanted reflections and rings prevent the sample data that coincide with them being used and reduce the number of reflections for the refinement. The reflections were then indexed and integrated with dynamic masks, which remove the areas of the images shaded by the DAC. Samples with a high symmetry crystal system, such as cubic, will have comparable data completeness with samples measured at ambient pressure. However, samples with a low-symmetry crystal system, such as triclinic, will have significantly low completeness which may result in a poor refinement of the structure. The refinement process is explained in the relevant Results chapter.

3.4 Synchrotron High-Pressure Single-Crystal X-ray Diffraction

The High-Pressure data for the Ph_7C_7H (**Chapter 6**), BCPEB (**Chapter 7**), 4CzIPN and 4CzIPN-$^tBu_8$ crystals (**Chapter 8**) were collected in station I-19 at the Diamond Light Source, Rutherford Appleton Laboratory. The measurements were carried out with a Huber 4-circle goniometer and DECTRIS Pilatus 300K detector, using synchrotron radiation (λ = 0.4859 Å). Eight runs scans were performed at different values of ϕ and θ with the resolution of 0.2° ω to ensure the angle between the incident beam and the cell axis is less than 40°, and less than 80% of the detector is shaded, as listed in **Table 3.3**.[4]

Table 3.3. Run list used for the high-pressure measurement at I-19 Diamond. Run 1 – 8 using ω scans and run 9 using *Φ* scan.

Run	2θ / °	κ / °	ϕ / °		ω / °	
			Initial	Final	Initial	Final
1	-11	70	-24.232	-	-141	-85
2	-11	70	155.768	-	-141	-85
3	12	70	155.770	-	-113	-82
4	12	70	-24.230	-	-113	-82
5	12	-70	24.230	-	-104	-41
6	12	-70	-155.770	-	-104	-41
7	-11	-70	-155.770	-	-97	-64
8	-11	-70	24.230	-	-97	-64
9	-11	0	-35	35	-90	-

Data were also selected to remove the unwanted reflections from diamonds, ruby, tungsten powder rings, and additional tungsten carbide (WC) powder rings due to the intense synchrotron radiation. The selected data were then indexed and integrated using an opening angle rejection of 38° to a resolution limit of 0.9 Å. All of these processes were carried out within CrysAlis PRO program.[5] The absorption corrections were also carried out automatically within the CrysAlis PRO. The reflections were then merged and transformed using XPREP.[6] All of the crystal structures at various pressures were solved using SHELXT[7] algorithm within OLEX2[8] program. The refinement processes are explained in the appropriate Results chapter.

3.5 Solid-State Ambient Pressure Fluorescence Emission Spectroscopy

Fluorescence excitation and emission spectra were collected using FluoroMax®-P Spectrofluorimeter (Jobin-Yvon Horiba) with FluorEssence™ v.3.5 software. A schematic of the spectrofluorimeter is displayed in **Figure 3.2**. The spectrofluorimeter uses a broadband xenon arc lamp with a spectral range from 240 to 700 nm. The light is then directed through a monochromator (1200 groves/mm Czerny-Turner) to select the wavelength for excitation. The selected light is then guided to the cuvette, or measurement accessories to measure the sample. The emitted fluorescence from the

sample is collected perpendicular to the excitation beam in the case of measurement using a cuvette. The emitted light then passes through a monochromator, and the dispersed emission is detected by a photon-counting photomultiplier tube. The spectra are corrected for the wavelength-dependence of the lamp intensity by detecting a small portion of the excitation light using a reference photodiode (**5c** of **Figure 3.2**).

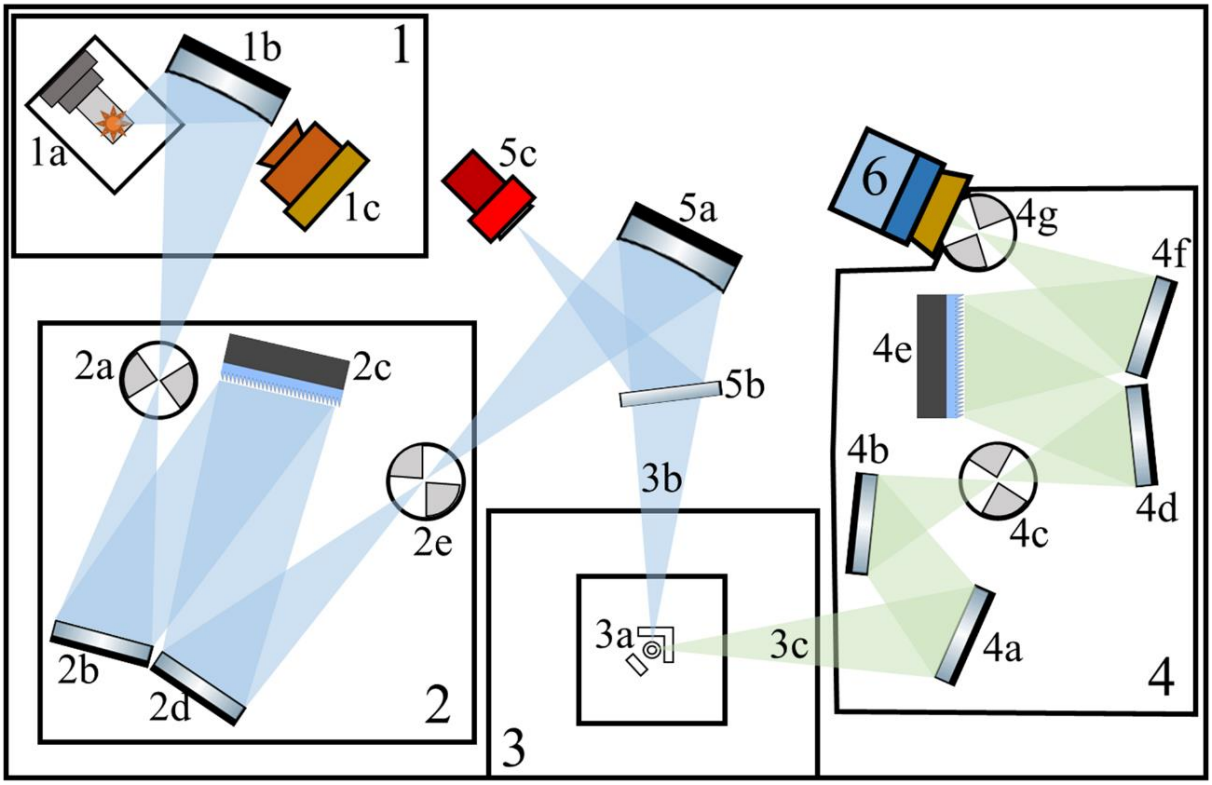

1: Light source
- **1a** : Xenon-arc lamp
- **1b** : Collection mirror
- **1c** : Xenon flash lamp

2: Excitation monochromator
- **2a** : Entrance slit
- **2b** : Collecting mirror
- **2c** : Grating
- **2d** : Focussing mirror
- **2e** : Excitation slit/shutter

3: Sample chamber
- **3a** : Cuvette holder
- 3b : Excitation gate
- 3c : Emission gate

4: Emission monochromator
- **4a** : Sample collection mirror
- **4b** : Collection mirror
- **4c** : Emission shutter/slit
- **4d** : Collection mirror
- **4e** : Grating
- **4f** : Focussing mirror
- **4g** : Exit slit

5: Reference detection
- **5a** : Collecting mirror
- **5b** : Beam Splitter
- **5c** : Reference detector (Photodiode and current-acquisition module)

6: Signal detector (photomultiplier tube)

Figure 3.2. Schematic of Jobin-Yvon Fluoromax-P.

In order to measure a solid-state sample, the cuvette holder (**3a** of **Figure 3.2**) was replaced with an F-3000 Fibre Optic Mount (Jobin-Yvon), which guide the excitation light and emission light to and from the sample via optical fibre bundles, as illustrated in **Figure 3.3**. The solid sample was deposited on the surface of the non-fluorescent carbon-black tape. The excitation optical fibre was mounted normal to the sample

surface, and the collection optical fibre was mounted at ~45° angle to avoid a strong specular reflection of the excitation light. The excitation and emission spectra were collected typically with a slit bandwidth of 3 nm.

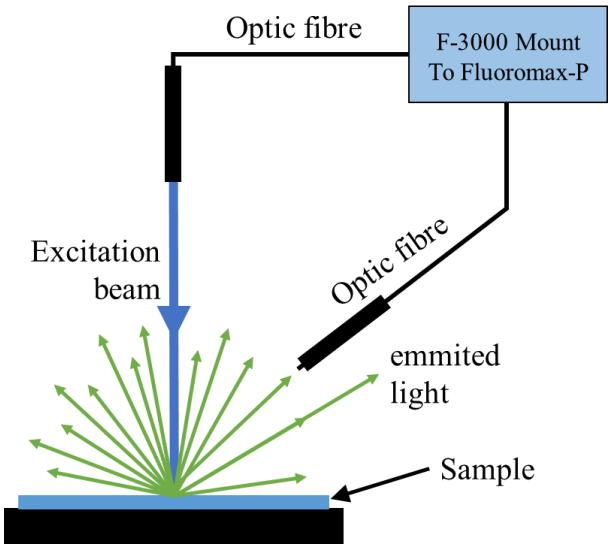

Figure 3.3. Schematic of ambient pressure measurement of powder fluorescence using optical fibres connected to the Fluoromax-P spectrometer.

3.6 High-Pressure Solid-State UV-Vis Absorption Spectroscopy

High-pressure spectroscopic measurements of the crystal were carried out by using a custom-built setup. The schematic layout of the setup is illustrated in **Figure 3.4**. A broadband Ocean Optics Balanced Deuterium-Halogen lamp (DH-2000-BAL) was used as a light source. The DAC is mounted onto a 3D-printed mount to keep it in place before and after a pressure change. The light was then focussed into the DAC using an infinity-corrected 15x reflective-objective lens (Edmund Optics). The transmitted light from the DAC was collected by a second reflective-objective lens, and an image of the cell was projected onto a plane coincident with the optical fibre input of the Ocean Optics USB-2000+ spectrometer. The reference spectrum, I_0, and the transmitted spectrum of the sample, I_S, were recorded by carefully translating the DAC on a 3-axis MicroBlock compact flexure stage (THORLABS). In this way, an image of either an empty part of the cell or the sample crystal was directed onto the spectrometer input. The spectra were processed using SpectraSuite software (Ocean Optics).

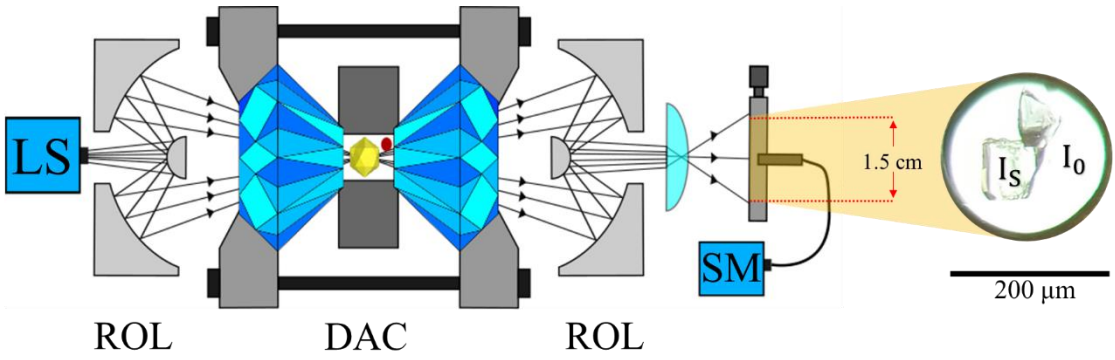

Figure 3.4. Schematic layout of the UV-vis absorption measurement setup. Ocean Optics LS stands for Light Source, ROL stands for the reflective objective lens.

The DAC must have been optically uniform to enable the absorption spectrum of a sample to be collected anywhere within the DAC. To establish this, an empty DAC with a ruby chip was placed in the cell, with pentane as a pressure transmitting medium, as shown in **Figure 3.5**. Five spots were labelled, and the central spot was used as a reference. It was found that all spots had the same transmittance spectra, as shown in **Figure 3.6 a**. The absorbance was calculated for each spot using the Beer-Lambert equation, and all showed the same zero absorbance, as displayed in **Figure 3.6 b**. From the absorption spectra, it is shown that the sample volume of the DAC is optically uniform.

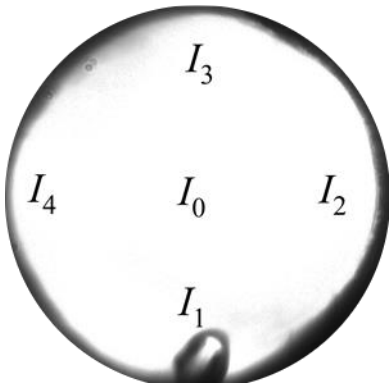

Figure 3.5. Snapshot of a cell (Ø = 200 µm) with ruby chip near I_1 spot.

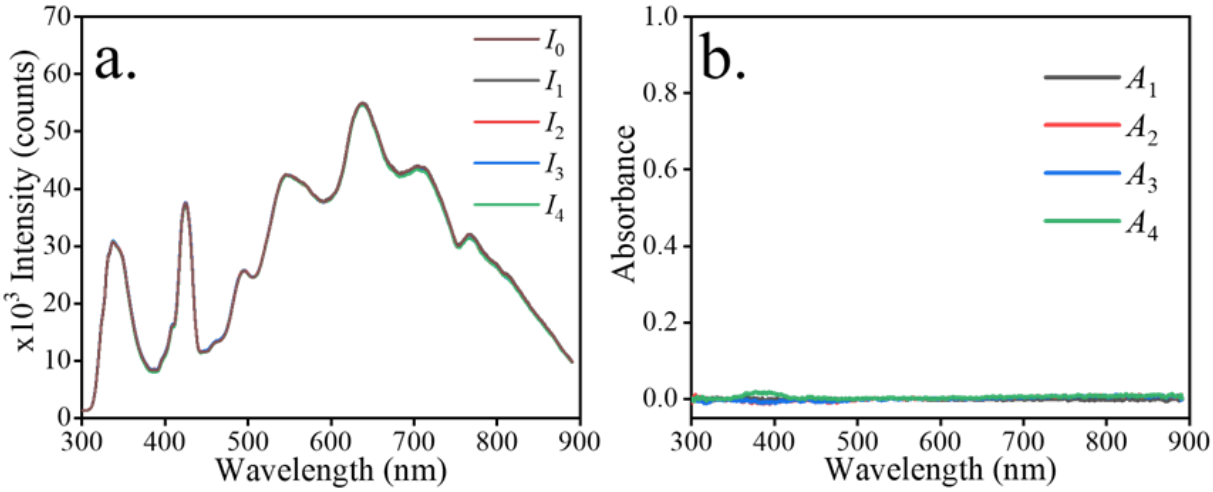

Figure 3.6. (a) Transmission spectrum from each spot measured within the DAC and (b) the absorption spectrum determined at spots 1–4 (with spot 0 as reference)

To validate the measurement of absorption spectra using this setup, spectra were determined for solution samples of Coumarin 102, Coumarin 153, Disperse Orange 1, and Rose Bengal in methanol. Samples were contained in 750 µL fused silica cuvette, placed at the same location as the DAC in the custom-built setup, and compared to the spectra measured using a double-beam CARY UV-vis spectrophotometer. The absorption spectra that were measured with two different measurement systems are shown in **Figure 3.7**. The spectral profiles are in excellent agreement, but the absorbance measured in the custom-built setup has a lower value (about 80%) compared with that measured in the conventional UV-vis spectrometer. This could be due to the focused nature of the light beam in the custom-built setup, compared with the collimated beam in the conventional UV-vis spectrometer, as illustrated in **Figure 3.8**. This makes the custom-built setup sensitive to the changes of the refractive index or a slight change in the translational movement of the sample between the measurement of sample and reference spectra. However, the shape and peak positions of the spectra are the same, which is the main requirement of this thesis.

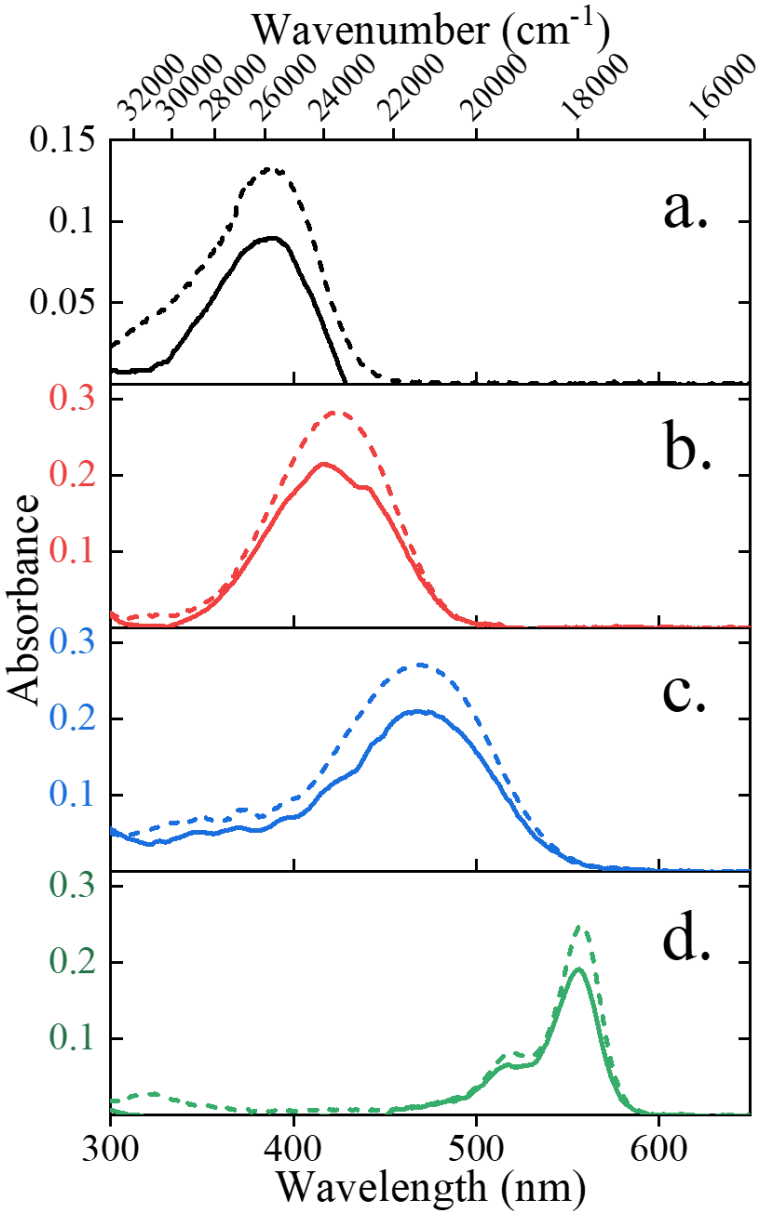

Figure 3.7. Absorption spectra of (a) Coumarin 102, (b) Coumarin 153, (c) Disperse Orange 1 and (d) Rose Bengal in methanol measured with custom-made setup (solid line) and with CARY UV-vis Spectrophotometer (dashed line).

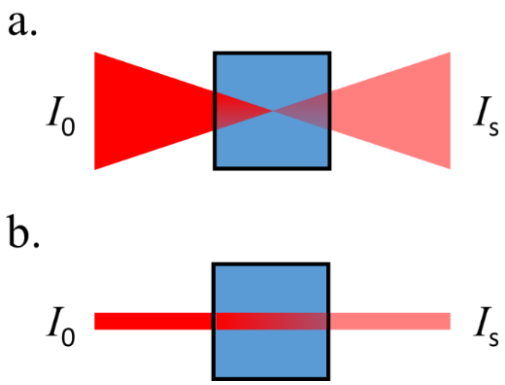

Figure 3.8. Comparison of beam profiles in (a) the custom-made setup and (b) the conventional UV-vis spectrophotometer.

Absorption spectra were also measured for single crystals of Disperse Red 1 and Coumarin 153, in a DAC at 0 GPa, in Daphne 7373 pressure transmitting medium, using the custom-built setup. These were compared to spectra measured using a JASCO V-670 UV-Vis spectrophotometer with Diffuse Reflectance Spectroscopy (DRS) accessory. These two dyes were chosen as transparent crystals were readily formed. For the measurement in the custom-built setup, the crystals were placed in the same manner as for X-ray measurements, loading the sample crystal and ruby chip carefully to leave a blank spot for the reference measurement. The DRS measurements were carried out on the solid dyes diluted in $BaSO_4$, with $BaSO_4$ powder as the standard. The spectra from both measurements show good agreement, as displayed in **Figure 3.9**.

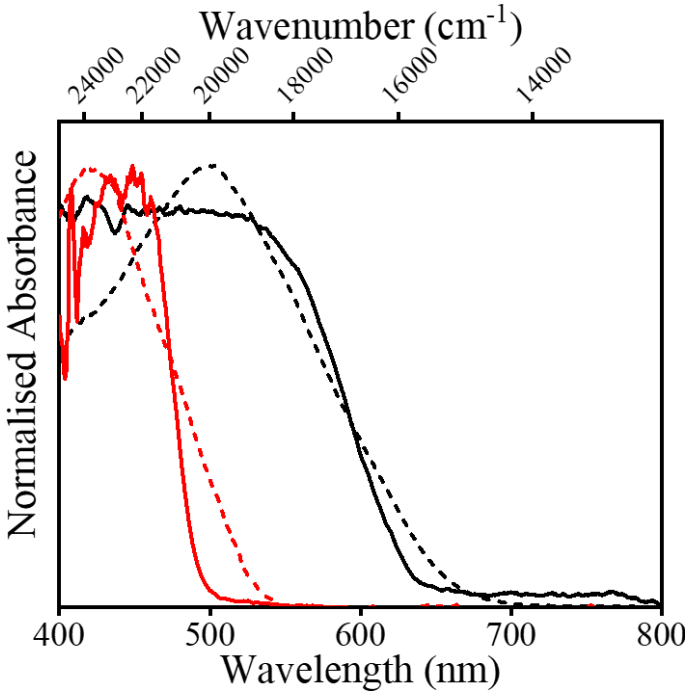

Figure 3.9. UV-vis absorption spectra of Disperse Red 1 (black) and Coumarin 153 (red) measured with JASCO V-670 (dashed line) and custom-made setup (solid line).

Figure 3.9 shows that the absorption spectra obtained from the custom-built setup appeared to be saturated. This saturation is due to the high concentration of the dye molecules in the crystal. To put this into perspective, the coumarin 153 contains four molecules in a unit cell (Cambridge Crystallographic Database reference code: VUTGOG[9]) with the unit cell volume of 1390.51 $Å^3$, which corresponds to a chromophore concentration of 4.78 M. Given the maximum extinction coefficient of ~20000 M^{-1} cm^{-1}, to give an absorbance value of 1, the crystal would need to be as thin as 0.1 μm.[10] The thickness of the crystals that were measured in this thesis were ~20 μm, which made the absorption spectra appear to be saturated.

3.7 High-Pressure Solid-State Fluorescence Emission Spectroscopy

A high-pressure fluorescence emission spectroscopy setup was built, based on the UV-vis absorption setup, with an additional lens employed to focus the emission into the fibre optic input of the detector, rather than projecting an image onto the detector. The schematic of the fluorescence measurement setup is displayed in **Figure 3.10**. The light sources that have been used could vary, for instance; 365 nm and 380nm LS-LED (Ocean Optics) or 470 nm diode laser (PicoQuant). A bandpass filter can be inserted

to spectrally narrow the excitation light before reaching the sample, and a long-pass filter can be used after the sample to prevent the excitation light from reaching the detector. In all cases in this thesis, multiple crystals were loaded into the DAC, to increase the emission intensity. However, it was important not to load the crystals not too tightly, so that they were not crushed during the application of pressure.

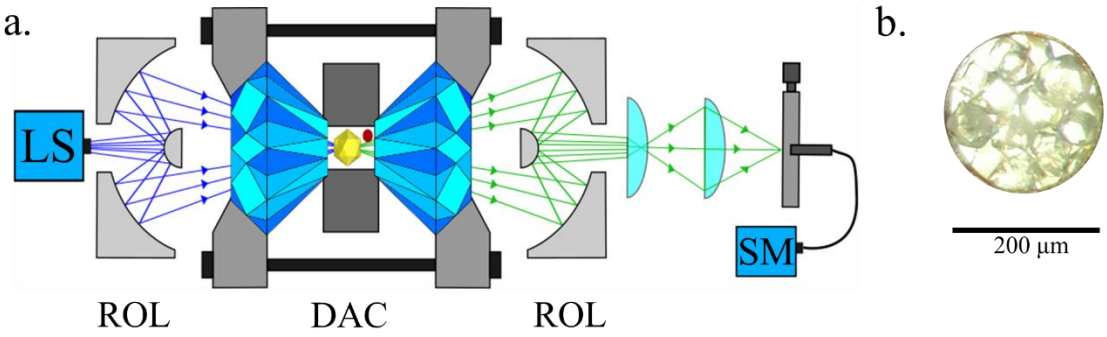

Figure 3.10. (a) Schematic layout of setup for measurement of fluorescence emission spectra. (b) Crystal loaded inside the cell; the darkest crystal apparent on the left is the ruby chip.

The sensitivity of the solid-state detector in the Ocean Optics USB-2000+ spectrometer is wavelength-dependent. For example, at a wavelength shorter than 500 nm, the intensity is underestimated compared to the longer wavelength region. Thus, a correction factor was determined to account for this. The output of an Ocean Optics HL-2000-FHSA halogen lamp was passed through an empty DAC, and the spectra were collected using both the USB-2000+ spectrometer and Fluoromax-P, as shown in **Figure 3.11 a**.

The correction factor was then calculated from the ratio of the two spectra, as expressed in **Equation 3.1**.

$$\boldsymbol{F_C} = \frac{I_{FM}}{I_{OO}}$$

Equation 3.1

where I_{FM} and I_{OO} represent the spectrum of halogen lamp obtained with Fluoromax-P and Ocean Optics USB2000+ spectrometer, respectively. Both spectra were baseline corrected and normalised before the correction factor ($\boldsymbol{F_C}$) was computed. The correction factor is illustrated in **Figure 3.11 b**. This correction factor was used to correct all fluorescence spectrum obtained from the USB2000+ spectrometer. The correction of the fluorescence spectra was carried out using Spectragryph software.[11]

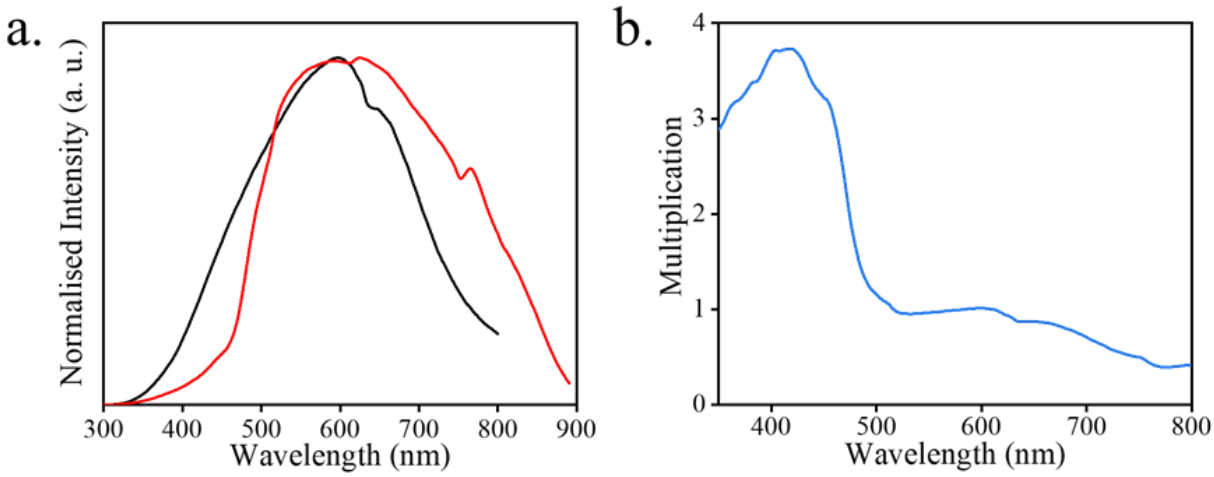

Figure 3.11. (a) Spectra of Ocean Optics HL-2000-FHSA broadband light source measured with Fluoromax-P (black) and Ocean Optics USB-2000+ spectrometer (red). (b) The correction factor for the USB-2000+.

The comparison between the corrected fluorescence spectra of BCPEB, Hf-peb MOF, 4CzIPN and 4CzIPN-$^{t}Bu_8$ measured using custom-built measurement setup in the DAC, and the spectra of the solid-state samples at ambient pressure measured by the Fluoromax-P is shown in **Figure 3.12**. The latter spectra were measured using front-surface excitation. There is a difference in the spectra for both BCPEB and Hf-peb MOF (**Figure 3.12 a** and **b**) which can be observed at wavelengths shorter than 415 nm, due to absorption by the diamond of the DAC. For 4CzIPN and 4CzIPN-$^{t}Bu_8$ (**Figure 3.12 c** and **d**) the difference seen on the blue edge of the spectra is caused by reabsorption of fluorescence by the crystal. The reabsorption of the crystal is unavoidable due to the collinear excitation/detection geometry in the DAC. This can be troublesome for a sample with a large spectral overlap between absorption and emission spectra. However, the main interest in this thesis is to observe the shift in the spectra as a function of pressure; therefore, it will not affect the importance of the results.

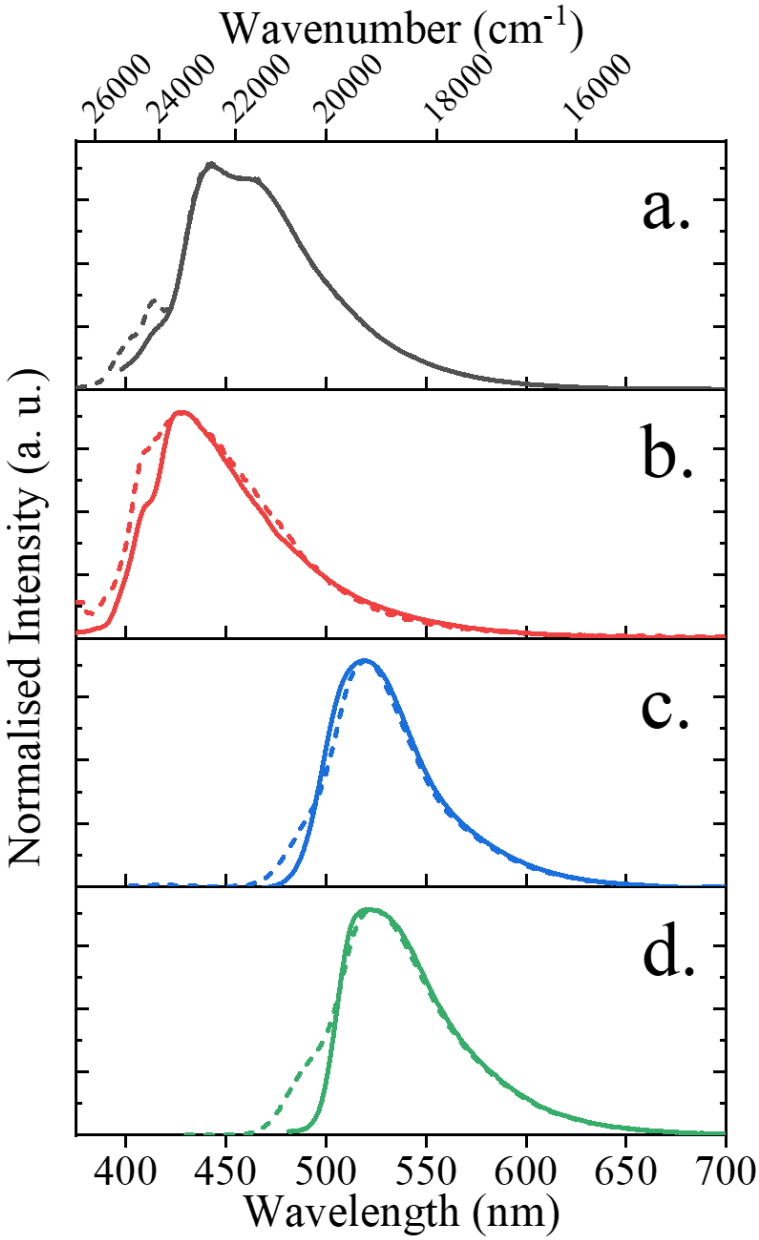

Figure 3.12. Fluorescence emission spectra of (a) BCPEB (λ_{ex} = 365 nm), (b) Hf-peb MOF (λ_{ex} = 376 nm), (c) 4CzIPN (λ_{ex} = 365 nm) and (d) 4CzIPN-^{t}Bu$_8$ (λ_{ex} = 365 nm) measured with custom setup (solid line) and with Fluoromax-P (dashed line).

In the process of application of pressure, the pressure cell is squeezed, resulting in an increase in the distance between the sample in the DAC and the focal point of the excitation light, generated by the reflective objective lens, causing a decrease in the detected intensity. Ideally, the focal point of the excitation light (ø ~20 µm) should be precisely on the spot of the cell opening (ø ~200 µm), therefore, an adjustment of the position the DAC has to be carried out to realign the opening of the pressure cell with

the focal point of the excitation light to achieve the highest intensity possible. This constant adjustment makes it difficult to get a consistent fluorescence intensity and makes it troublesome to compare the change in intensity as a function of pressure quantitatively. Therefore, the measured fluorescence spectra were normalised.

In conclusion, the custom-built measurement setups for UV-vis absorption and fluorescence emission spectroscopy at high-pressure were demonstrated to deliver reliable results, with some limitations due to the diamond absorption at wavelengths shorter than 415 nm, and the presence of reabsorption of fluorescence by the sample.

3.8 References

1. Bruker *SAINT*, Bruker AXS Inc: Madison, Wisconsin, USA, **2004**.
2. Haming, L.; Sheldrick, G. M., *Acta Crystallogr. A.* **1999,** *55*, 206-206.
3. Bruker *APEX2*, Bruker AXS Inc: Madison, Wisconsin, USA, **2012**.
4. Dawson, A.; Allan, D. R.; Parsons, S.; Ruf, M., *J. Appl. Crystallogr.* **2004,** *37*, 410-416.
5. Agilent *CrysaAlis PRO*, Agilent Technologies Ltd: Yarnton, Oxfordshire, England, **2014**.
6. Bruker-Nonius, B.-A. X. S. *XPREP*, Madison, Wisconsin, USA, **2004**.
7. Sheldrick, G. M., *Acta Crystallogr. A.* **2015,** *71*, 3-8.
8. Dolomanov, O. V.; Bourhis, L. J.; Gildea, R. J.; Howard, J. A. K.; Puschmann, H., *Crystallogr.* **2009,** *42*, 339-341.
9. Gridunova, G. V.; Yufit, D. S.; Struchkov, Y. T.; Khrolova, O. R.; Reznichenko, A. I.; Tavrizova, M. A., *Kristallografiya.* **1992,** *37* (2), 366-372.
10. Kitamura, N.; Fukagawa, T.; Kohtani, S.; Kitoh, S.; Kunimoto, K. K.; Nakagaki, R., *J. Photoch. Photobio. A.* **2007,** *188* (2-3), 378-386.
11. Menges, F. *Spectragryph - optical spectroscopy software*, 1.2.14; **2020**. http://www.effemm2.de/spectragryph/

Chapter 4
The Effect of Pressure on the Structural and Spectroscopic Properties of a Luminescent Hf-peb MOF

4.1 Introduction

A combination of high-pressure single-crystal diffraction and electronic spectroscopy have been used to study a two-fold interpenetrated Hf MOF with 1,4-phenylenebis(4-ethynylbenzoate) ligands. The results reported in this chapter reveal that the ligand exists in two conformational forms and their fractional populations are pressure dependent. The change in conformational population as a function of pressure can be directly linked to the pressure-dependence of the UV-vis absorption and fluorescence spectra, from ambient pressure to 2.1 GPa.

4.1.1 Fluorescence in MOFs

MOFs containing ligands with extended and conjugated aromatic groups are known to exhibit fluorescence.[1-3] In the MOFs, ligands are anchored into metal nodes or secondary building units (SBUs), and as a consequence, aggregation-caused quenching (ACQ) is prevented. ACQ occurs in the vast majority of conventional aromatic crystals, causing problems in scaling up the fluorescent compounds for applications in solid-state form.[4,5] The prevention of ACQ, making the fluorescence intensity stay high, is particularly attractive for light-emitting diode (LED) applications, which require a robust yet bright material.[6]

One example of ACQ prevention in a MOF is the benzothiadiazole derivative (BTBMBA) MOF, which has a structure isoreticular to the UiO-family MOFs.[2] The BTBMBA ligand alone experiences a π-π stacked arrangement in its aggregate form, resulting in low quantum yield (2.3%), but shows a significant increase in quantum yield (42.5%) when the ligand molecule is incorporated in the $[Zr_6O_4(OH)_4]^{12+}$ SBU to form a MOF. This is a significant new application of MOFs, which have been developed mainly as gas storage materials.

In terms of sensing applications, incorporation of a guest molecule inside the pore of a MOF can cause changes in the fluorescence emission spectra. For instance, the intrinsic fluorescence of UiO-66 and its amine derivative, UiO-66-NH_2, also the porphyrin-based Zr-MOF, PCN-225, both show pH-dependent shifts in fluorescence wavelength and modulated intensity, and are excellent candidates for pH sensing.[7,8]

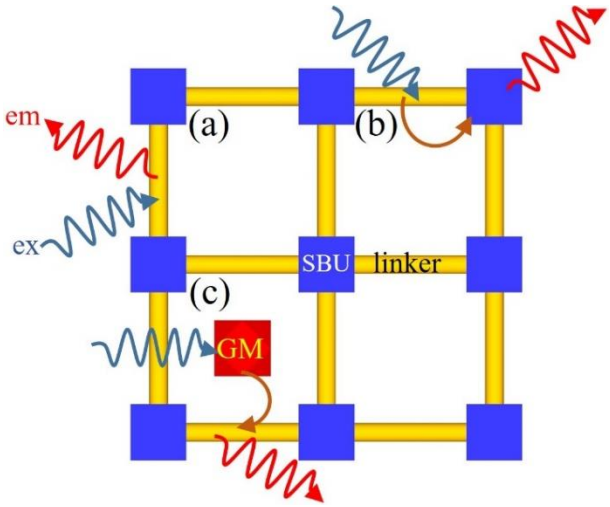

Figure 4.1. Excitation and emission processes that can occur in MOFs. (a) direct excitation of a fluorescent ligand; (b) excitation of the ligand followed by energy transfer to the SBU and the emission from the SBU; (c) excitation of a guest molecule (GM) followed by energy transfer to a fluorescent ligand.

Several excitation and emission processes can occur in MOFs**,** as exemplified in **Figure 4.1**. Most commonly, fluorescence arises from direct excitation of the ligand (**Figure 4.1 a**); especially when no guest molecules are present within the pores. Excitation via MOF ligand and emission from the SBU can also occur especially for SBUs containing lanthanides, such as Eu and Tb, which are known to exhibit an antenna effect (**Figure 4.1 b**).[9] Moreover, there may be excitation via a guest molecule and emission from the ligand, or vice versa, which is particularly useful for sensing applications (**Figure 4.1 c**). Multiple factors may affect the fluorescence of a MOF, such as the presence of a guest molecule, incorporation of nanoparticles in the pore, pH and also the influence of temperature and pressure. The work presented in this chapter is concerned with the direct excitation of an emissive ligand, and the effect of pressure on this emission.

4.1.2 Hf-peb MOF

Hf-peb MOF consists of the $[Hf_6O_4(OH)_4]^{12+}$ SBU and 1,4-phenylene-bis(4-ethynylbenzoate) (peb^{2-}) ligands, arranged isoreticular to the UiO MOF family, with 2-fold interpenetrated in ¼, ¼, ¼ position, as shown in **Figure 4.2**. The peb^{2-} ligand, in its methyl ester form, is known to exhibit fluorescence in both solution and solid phase as reported in **Chapter 7**. The Zr-peb MOF, also known as a Porous Interpenetrated Zirconium-Organic Framework (PIZOF), and its derivatives have been studied extensively since its first synthesis in 2011 by Schaate *et al.*[10] However, the Hf- equivalent was not reported until 2015 by Doan *et al.*[10,11] The synthesis of both MOFs is straightforward, using a hydrothermal method, by mixing the solution of the ligand and its metal ions in DMF; the mixture is then stored in the oven overnight. Doan *et al.* conducted a thermal stability test for both Zr- and Hf-peb MOFs and both are reported to have excellent thermal stability. Doan *et al.* named the Zr- and Hf-peb MOF as VNU-1 and VNU-2, respectively (VNU stands for Vietnam National University). Photocatalytic degradation of both MOFs was investigated by dispersing them in methyl blue (MB) and methyl orange, under irradiation of UV-visible light. Upon 3 hours of irradiation in Zr-peb, the MB and MO were degraded by 100% and 83%, respectively. However, in Hf-peb, both MB and MO were less degraded, by only 53% and 72%, respectively.

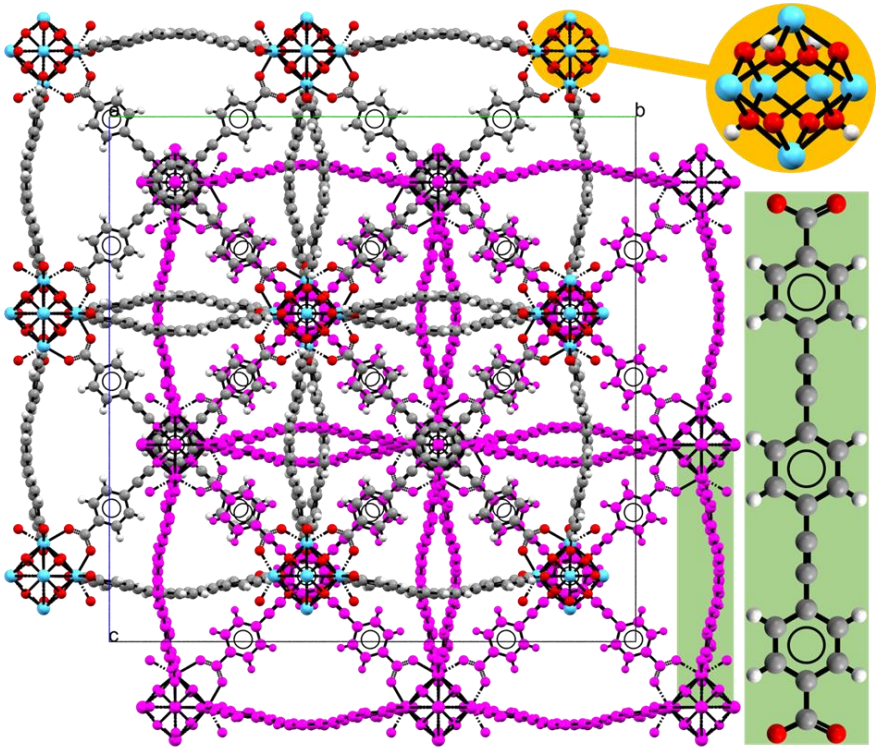

Figure 4.2. The structure of the Hf-peb MOF.[11] The $Hf_6O_4(OH)_4$ SBU, highlighted in yellow, and the 1,4-phenylene-bis(4-ethynylbenzoate) (peb) ligand, highlighted in green. Colour scheme: Hf – blue, O – oxygen, C – grey, H – white.

Hf-peb has also been synthesised and studied independently by Marshall *et al.* in 2016, for its post-synthetic bromination behaviour.[12] It is reported that Hf-peb MOF can be brominated using N-bromosuccinimide (NBS) or neat bromine. The bromination caused the triple-bond in both ethynyl bridges to be broken down to a single-bond, and 2 bromine atoms were added to each bridge. This bromination broke the planarity and backbone linearity of the ligand. This technique could be beneficial for synthesis of UiO-MOF containing a non-planar ligand.

A subsequent study by Marshall *et al.* reported that Zr-peb and its derivatives have consistent topology throughout incorporation of functional groups, such as methyl, fluoro, naphthyl and benzothiadiazolyl units, at the central phenyl ring.[13] This is interesting, as a quite dramatic structural modification of the ligand would not alter the overall structure, in spite of the modification of the chemical environment in the pores, such as its hydrophobicity and polarity. Therefore, Zr-peb could have a vast range of potential in applications, based on the functionalisation of its ligand without changing its topology. The solid-state UV-visible absorption of the dried crystal, measured with

diffuse-reflectance technique, and fluorescence emission spectra of the dried and wet crystals are illustrated in **Figure 4.3 a.** It is shown that, upon wetting, the emission spectrum of the crystal is red-shifted, and the profile is changed. However, the cause of such a change in the emission spectrum was not explained clearly whether the cause is the solvation of the ligand or a change in the structure.

In the same paper, it is reported that the closely related MOF with dimethyl substituted peb^{2-} as a ligand, listed as Zr-L2 MOF, also showed different fluorescence emission spectra in wet and dry forms, as shown in **Figure 4.3 b**. This MOF, aside from the majority of the crystal with $Fd\bar{3}m$ space group, contains few crystals with lower symmetry (*Imma*) upon investigation with powder X-ray diffraction (PXRD), attributed to the different ligand orientation. The redshift of the emission spectrum upon wetting is hypothesized due to the change in orientation of the ligand. However, the change of the ligand orientation is only a speculation based on PXRD data and not directly observed through more rigorous single-crystal X-ray diffraction.

Marshall *et al.* also report that both Zr-peb MOF and its Hf- counterpart have a very comparable thermal stability upon thermal gravimetric analysis (TGA) at ~475ºC, with Hf-peb having ~20% lower BET surface area. However, the optical studies that have been conducted have been concerned mainly with Zr-peb and its substituted ligand, with little attention paid to the Hf- counterparts.

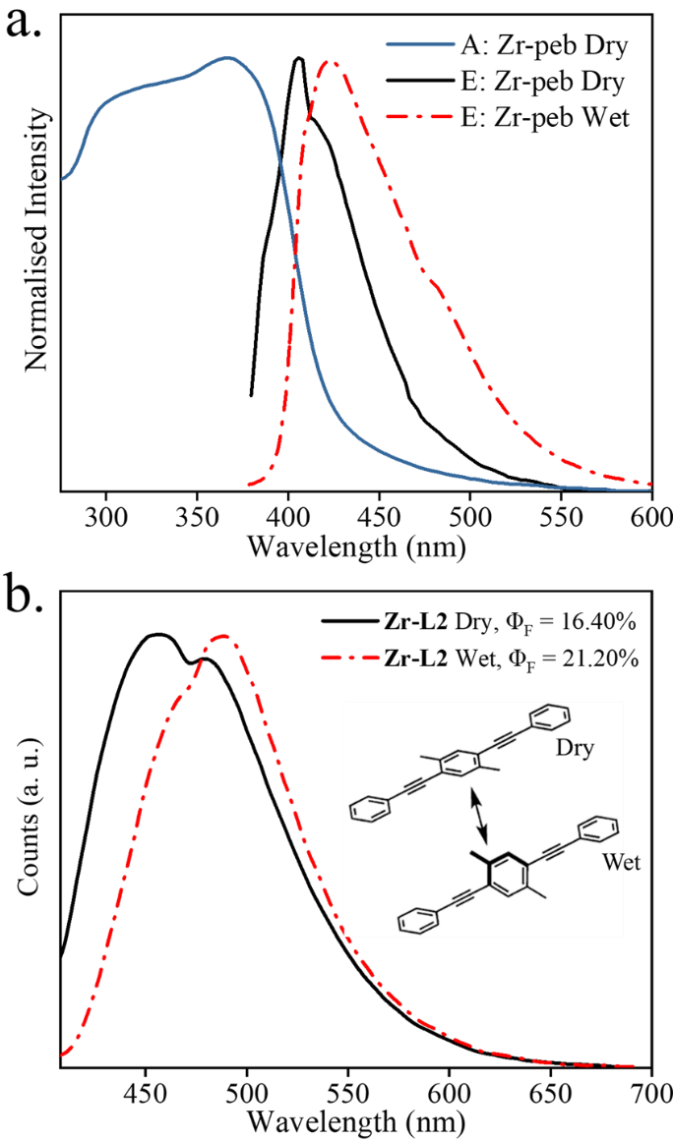

Figure 4.3. (a) Solid-state UV-vis absorption of dry crystal (blue line) and fluorescence emission of the Zr-peb MOF in a dry (black line) and wet crystal (red dashed line) (λ_{ex} = 397 nm). (b) Solid-state fluorescence emission spectra of Zr-L2 under dry (black line) and wet conditions (red dashed line) (λ_{ex} = 396 nm). Redrawn from Marshall *et al.*[13]

The work presented in this chapter is concerned with an investigation of the effect of high-pressure on the crystal structure of the Hf-peb MOF in parallel with UV-vis absorption and fluorescence emission spectroscopy, conducted under the same conditions, on a crystalline sample in a diamond anvil cell. This enables the effect of pressure on the structure of the peb^{2-} ligand to be directly related to the effect on its optical properties.

4.2 Experimental

It should be noted that the synthesis of the Hf-peb MOF was carried out by Dr Ross Marshall and Prof Ross Forgan of the University of Glasgow and the X-ray diffraction data were collected by Dr Claire Hobday (University of Edinburgh). However, the crystal structures were solved and refined by the author.

4.2.1 Synthesis

Hf-peb MOF: Methyl 4-ethynylbenzoate (2.5eq) was dissolved in TEA (160 ml) and degassed for 10 minutes before 1,4-diethynyl benzene (1eq), bis(triphenylphosphine)-palladium(II) dichloride (0.42mmol) and Copper(I) iodide (0.38mmol) were added and stirred overnight in an N_2 environment. The mixture was then cooled down to room temperature and the colourless product of dimethyl-4,4'-[1,4-phenylene-bis(ethyne-2,1-diyl)]-dibenzoate (peb-Me_2) obtained by vacuum filtering. The product was then washed in hexane and then stirred in H_2O overnight before collected by vacuum filtration. The peb-Me_2 compound was then dissolved in 1:1 MeOH/THF with the addition of Potassium Hydroxide (10eq) at 85°C to obtain the peb-H_2 ligand. The peb-H_2 ligand (1eq) and HCl (0.02 ml) were added into a mixture of Benzoic acid (30 eq) and Hafnium chloride (1eq) in 13 ml of DMF. The mixture was sonicated for 10 minutes before placed in an oven at 120°C for 24 hours. The post-heated mixture was cooled to room temperature where crystals of Hf-peb MOF were obtained.

4.2.2 High-Pressure Single-Crystal Structure Determination

A single crystal of Hf-peb MOF was loaded into a Merrill-Bassett diamond anvil cell (DAC) with a half-opening angle of 40º, composed of Boehlar Almax diamonds with 600-μm culet diamond anvils, a tungsten gasket and tungsten carbide backing plates.[14] A small ruby chip was also loaded into the cell to act as an internal pressure calibrant, using the pressure-dependent fluorescence of the ruby to measure the pressure,[15] while pentane was added as a pressure transmitting medium (PTM). Three Allen screws were tightened equally and carefully to increase the pressure in the cell, so the pressure increased slowly in a controllable manner, to avoid the sample being crushed. After increasing the pressure, the DAC was allowed to sit for at least 30 minutes before the measurement in order for the pressure to stabilise.

Diffraction data were collected on a Bruker Apex II diffractometer and CCD detector using Mo-Kα radiation (λ = 0.71073 Å). Data collections were carried out using an exposure time and a step size of 1 second and 0.5 degrees, respectively. The reflection data were integrated with the programme SAINT using dynamic masks; these mask the regions of the detector, which are shaded due to the pressure cell. The omission of shaded reflections, absorption correction and merging of data were carried out in a three-step process, firstly with the programme SHADE, then SADABS and finally XPREP.[16-18] For ambient pressure measurement, the crystal was placed on fibre, and dynamic masks were not used.

The structure was solved using OLEX2 program with SHELXT algorithm.[19] The structure then was refined using CRYSTALS.[20] All structures were refined against F^2 with I/σ cut-off of -3 to reject noise of weak reflections. The amplitude of atomic displacement parameters of the ligand was restrained along the bonding directions of two bonded atoms (1,2 distances) and two atoms bonded to the same atom (1,3 distances), while all torsion angles and metal-ligand bond distances were allowed to refine freely. Hydrogen atoms on the ligand were placed geometrically and constrained to ride their adjacent atoms. On the other hand, the hydrogen atoms on the metal cluster were added manually for all oxygen atoms that are not bonded to the carbonyl group, with half occupancy due to the randomly occupied nature of the hydrogen. The process of hydrogen assignment to the SBU does not reduce the symmetry of the crystal structure, and the space group is conserved. The electron count per unit cell was calculated using SQUEEZE algorithm within PLATON.[21,22] The solvent-accessible volume was calculated with a 1.2 Å probe radius and 0.2 Å grid using the *Voids* routine within Mercury.[23]

4.2.3 High-Pressure Fluorescence Emission Spectroscopy

Crystals of Hf-peb MOF were loaded into a DAC with half opening angle of 30° with 600 μm culet diamond anvils manufactured by Almax-easyLab. Pentane was used as a hydrostatic pressure medium, and a small ruby chip was added as a pressure marker next to the crystals. A number of crystals were loaded into the DAC to increase the fluorescence intensity. The DAC was then placed in the spectrometer setup described in **Chapter 3**. A 380-nm LED (Ocean Optics LS-LED 380) was used as the excitation light source. A band-pass filter (Semrock Brightline 370/36) was inserted in the

excitation path to narrow the excitation bandwidth. A long-pass filter was inserted in the detection path to prevent the transmitted excitation light from reaching the detector. The fluorescence emission spectra were collected at a series of pressures closely matched to those used for X-ray diffraction measurement, up to a maximum of 2.1 GPa.

4.2.4 High-Pressure UV-Vis Absorption Spectroscopy

A crystal of Hf-peb MOF was loaded into the same DAC as described in **4.2.3** Pentane was used as a hydrostatic pressure medium, and a small ruby chip was added as a pressure marker next to the crystal. The absorption spectra were also collected at a pressure series closely match those used for X-ray diffraction measurements for up to 2.1 GPa.

4.3 Results and Discussions

4.3.1 Structural Response of Hf-peb MOF to High Pressure

From the structural study conducted independently by Doan *et al.* and Marshall *et al.*, it is known that Hf-peb crystallises in the cubic system, with $Fd\bar{3}m$ space group and with a lattice constant of 39.7901(8) Å.[11,12] Both MOF structures were reported at ambient pressure, and low temperature showed a bowing of the peb^{2-} ligand with a quite noticeable amplitude of anisotropic atomic displacement ellipsoid at a perpendicular direction to the ligand plane, especially for the central phenyl ring. The bowing of the ligand is not unique to this MOF, and can also be seen in other MOFs with long ligands, such as UiO-67 and Zr-abdc.[24] In these previously reported low-temperature structures of Hf-peb, the three phenyl rings of the ligand were found to be in a coplanar arrangement with no evidence of conformational disorder.

In contrast to previous studies[11,12], in the present work, the crystal structures were measured at room temperature. The analysis confirmed that the crystal structure follows the cubic system with $Fd\bar{3}m$ space group, with the lattice constant of 39.8212(18) Å. A slight expansion of ~0.03 Å (2σ) in the lattice constant, compared to that reported by Doan *et al.* is very small and could be due to thermal expansion. The asymmetric unit of the MOF structure was solved, and the atoms were labelled and numbered, as shown in **Figure 4.4**. Significant electron density spots were identified at a perpendicular position from the central phenyl ring of the ligand, with

~7 and ~5.5 electrons/Å^3, and are assigned to C(9) and C(10). The C(9) and C(10), following the symmetry operations, construct a central phenyl ring perpendicular to the terminal phenyl rings, referred to as twisted (**Figure 4.5 b**). The twisted conformer that is described in this thesis is newly discovered and has not been reported prior to this research. On the other hand, the C(11) constructs a central phenyl ring in which coplanar relative to the terminal phenyl rings, referred to as coplanar (**Figure 4.5 a**). The peb^{2-} ligand shows bowing of its backbone geometry, with significant thermal disorder occurring within the ligand, especially on the central phenyl ring as displayed in **Figure 4.5 a** and **b**. A weighted fractional occupancy refinement was used to determine the relative population of each conformer, as discussed below.

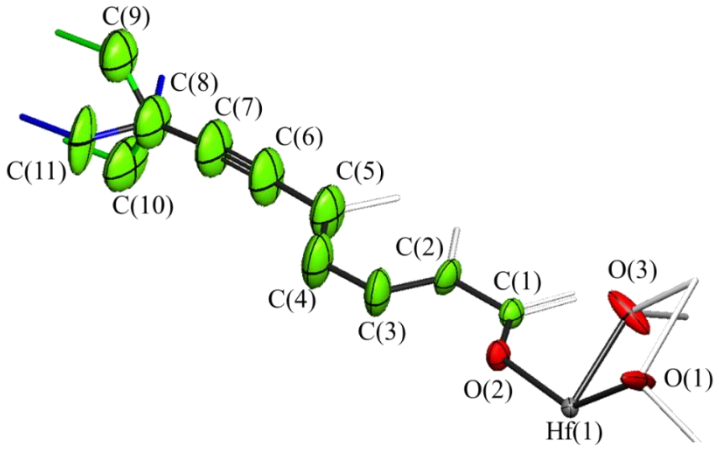

Figure 4.4. The numbering of the asymmetric unit of the Hf-peb MOF. Colour scheme: C – green, O – red and Hf – grey. The hydrogen atoms have been omitted for clarity.

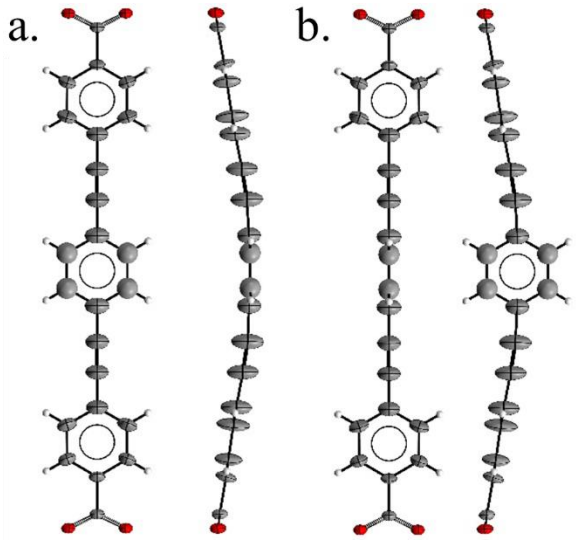

Figure 4.5. The coplanar (a) and twisted (b) conformers of the peb^{2-} ligand viewed perpendicular and parallel to the ligand plane. Anisotropic displacement parameters are drawn at 30% probability for all but the central phenyl ring. Note that four carbons at the centre of the ligand structure were refined isotropically. Colour scheme: O – oxygen, C – grey, H – white.

The weighted fractional occupancy refinement was carried out for the C(10) and C(9) as coplanar, against C(11) as twisted within the CRYSTALS software, by initially setting the occupancy of each conformer to 0.5, and then refining the occupancy the sum of fractional populations constrained to 1. The result this refinement at ambient pressure revealed that the occupancy of the coplanar conformer constituting 73% of the total population, with the remaining 27% occupied by the twisted conformer. The energy difference between the coplanar and twisted conformers at ambient pressure can be calculated using the Boltzmann distribution equation, as expressed in **Equation 4.1**.

$$\frac{\chi_C}{\chi_T} = e^{\left(\frac{E_T - E_C}{k_B T}\right)}$$

Equation 4.1

where χ_C and χ_T are the fraction of coplanar and twisted conformers, the E_C and E_T are the energy of the coplanar and twisted conformers, and the k_B is the Boltzmann's constant and the T is the temperature. From this calculation, the energy difference at ambient pressure and room temperature is ~2.5 kJ mol^{-1}, which is very close to the value of 2.7 kJ mol^{-1} reported for the barrier to torsion of the central ring in the

analogous free molecule,1,4-bis(phenylenethynyl)benzene (BPEB), where the twisted structure is the transition state on the torsional potential (see **Chapter 7**).[25,26]

The crystal structure was then studied as a function of pressure at 0.1 GPa, 0.23 GPa, 0.55 GPa, 1.1 GPa, 1.40 GPa, 1.64 GPa and 2.1 GPa. As shown in **Figure 4.7 a**, upon the loading of the crystal in the DAC, the unit cell appeared to be slightly increased, equivalent to a pressure of 0.1 GPa (39 $Å^3$, 0.06%). This slight expansion is normal in the case of MOFs with an interpenetrating hydrostatic medium and is caused by the entry of the medium into the pore at the initial pressure. Upon further increasing pressure, the unit cell volume decreased as the pressure increased, with a total reduction of ~2.6% at 2.1 GPa, resulting in the shrinking of *a*-axis by 0.349(2) Å, but the space group remains the same throughout the pressure range.

The occupancy of coplanar and twisted conformers was refined with isotropic (spherical) and anisotropic (ellipsoid) atomic displacement models, as shown in **Figure 4.6 a** and **b**. The occupancy obtained from both models were plotted against each other and shows that both are the essentially same, and there is no statistically significant difference, as shown in **Figure 4.6 c**. However, the model with only isotropic thermal parameters is preferred, as refinement with anisotropic atomic displacement parameters, resulted in significant disorder around the C(11) atomic displacement ellipsoid, especially at higher pressure when the fractional population of the coplanar conformer is low. Moreover, the model with anisotropic atomic displacement parameters has significantly more parameters to refine.

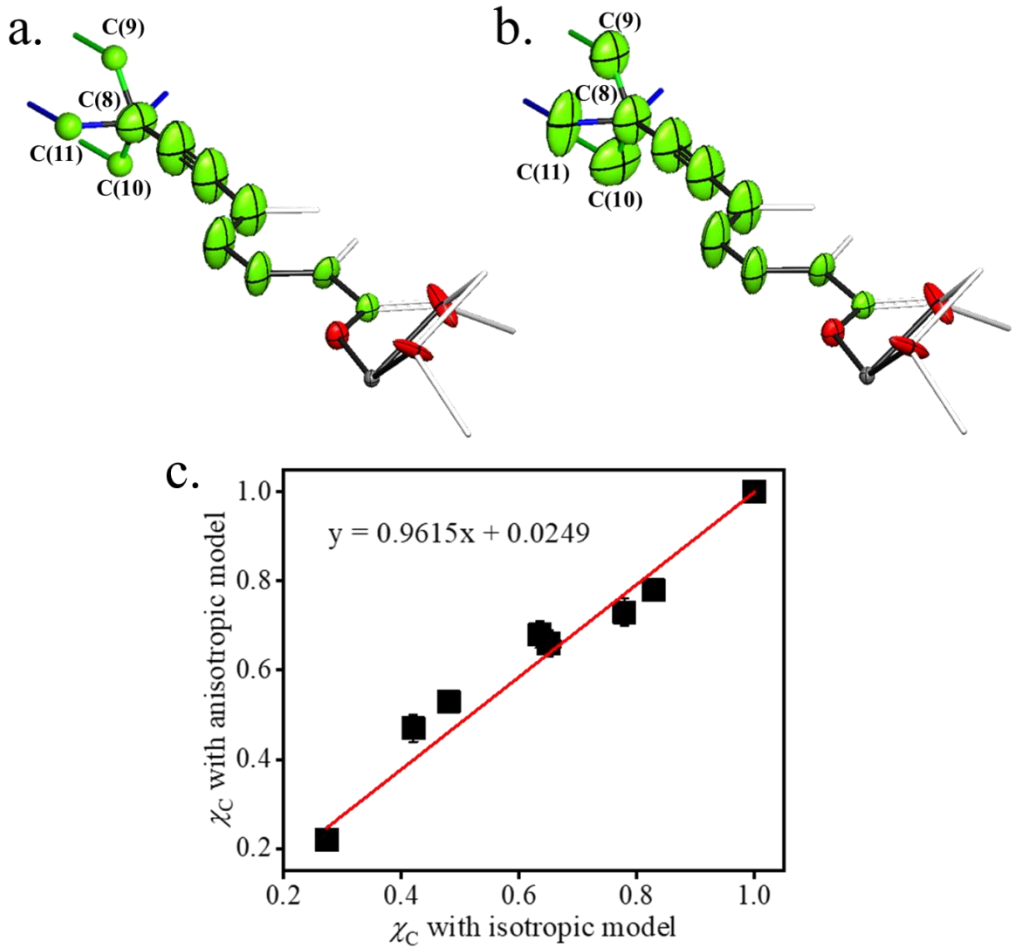

Figure 4.6. The disorder coplanar and twisted conformer of the peb^{2-} ligand at ambient pressure, with disorder modelled with (a) isotropic and (b) anisotropic displacement parameters and (c) the coplanar occupancies, χ_C, refined with isotropic and anisotropic displacement parameters. Colour scheme: C – green, O – red and Hf – green. The hydrogen atoms have been omitted for clarity.

As shown in **Figure 4.7 a** and **Table 4.1**, the fractional population of the coplanar conformer decreases with increasing pressure. This appears to occur in two stages. Following the initial decrease in population up to 0.5 GPa, there is a plateau, followed by a further decreasing trend above 1.1 GPa until its complete disappearance at 2.1 GPa. Interestingly, the decrease of the coplanar population as a function of pressure follows a similar two-step trend to the shrinkage in the unit cell volume (**Figure 4.7 b**).

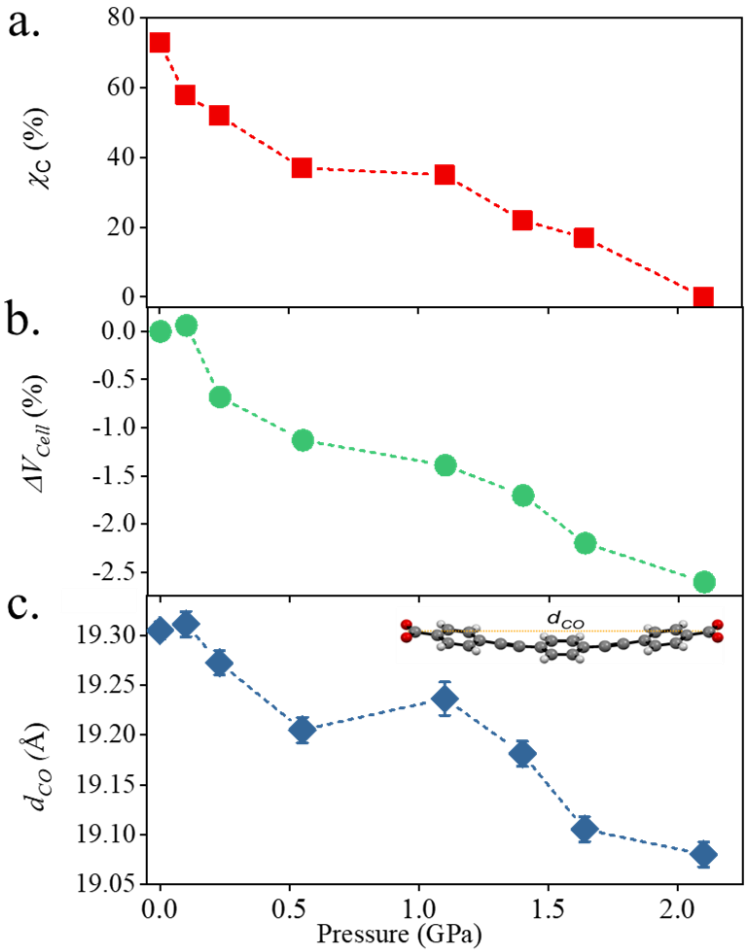

Figure 4.7. The responses of (a) the fractional population of the coplanar structure, χ_C, obtained from occupancy refinement of the X-ray data, (b) the unit cell volume, ΔV_{cell}, and (c) the peb^{2-} length, d_{CO}, to increasing pressure.

Table 4.1. The fractional populations of the coplanar conformer (χ_C) and the twisted conformer (χ_T), together with the inter-carbonyl distance (d_{CO}) of the ligand, as a function of pressure.

Pressure (GPa)	χ_C	χ_T	d_{CO} length (Å)
ambient	0.727(10)	0.273(10)	19.305(9)
0.10	0.580(15)	0.420(15)	19.311(13)
0.23	0.520(14)	0.480(14)	19.272(12)
0.55	0.365(18)	0.635(18)	19.205(13)
1.10	0.350(20)	0.650(20)	19.236(17)
1.40	0.221(16)	0.779(16)	19.181(13)
1.64	0.172(12)	0.828(12)	19.106(13)
2.10	0.000	1.000	19.080(13)

The bending of the ligand also appears to increase with increasing pressure, as indicated by the decrease in distance between the terminal carbonyl groups, d_{CO}, as shown in **Figure 4.7 c**. The inter-carbonyl distance shows a very similar trend with increasing pressure to that observed for the pressure-dependent coplanar population and unit cell volume. It is suggested that the sudden decrease in the coplanar conformer population and the unit cell volume at 1.1 GPa is caused by a subtle increase in the degree of bending in the peb^{2-} ligand, which distorts to allow the SBU to become closer together. It would appear that a decrease in population of the coplanar conformer (and the consequent increase of the twisted conformer) gives rise to a less rigid and more flexible framework, as indicated by the reduction in d_{CO}, and the consequence of these effects is the decrease in the unit cell volume. A similar increase in the degree of bending of a linker with increasing pressure has also been observed in Zr-abdc (see **Chapter 5**).[24]

The solvent-accessible volume of the crystal was calculated independently for coplanar and twisted conformers, and then the average was computed according to **Equation 4.2**.

$$\bar{V}_{SA} = \chi_C V_{PC} + \chi_T V_{PT}$$

Equation 4.2

where $\bar{V}_{SA}$, V_{PC} and V_{PT} are the average solvent-accessible volume, the solvent-accessible volume of crystal with coplanar and twisted conformers, respectively, and χ_C and χ_T are the fractional population of coplanar and twisted conformers, respectively. The change in the $\bar{V}_{\mathrm{SA}}$ and the pore content as a function of pressure is listed in **Table 4.2**. The difference in the solvent-accessible volume between the coplanar, majority population, at ambient pressure, and the twisted, exclusive population at 2.1 GPa is illustrated in **Figure 4.8 a** and **b**. The solvent-accessible volume and its fraction of unit cell volume appear to increase with increasing pressure, as displayed in **Figure 4.8 c**. The solvent-accessible volume appears to increase rapidly at pressures up to 1.1 GPa and more slowly at pressures higher than 1.1 GPa. This can be related to the increase in the degree of bending of the ligand and the increase in population of the twisted conformer (**Figure 4.7**), which facilitate the accommodation of the solvent.

Table 4.2. The summary of average solvent-accessible volume, $\bar{V}_{SA}$, and pore content as a function of pressure.

Pressure / GPa	$\bar{V}_{SA}$ / Å^3	$\bar{V}_{SA} : V_{cell}$ / %	**Pore content / e$^-$**
ambient	31695	50.19	21293
0.10	31670	50.12	9180
0.23	31849	50.78	6570
0.55	32121	51.45	7199
1.10	32186	51.69	8088
1.40	32227	51.92	7347
1.64	32144	52.05	8296
2.10	32214	52.38	8449

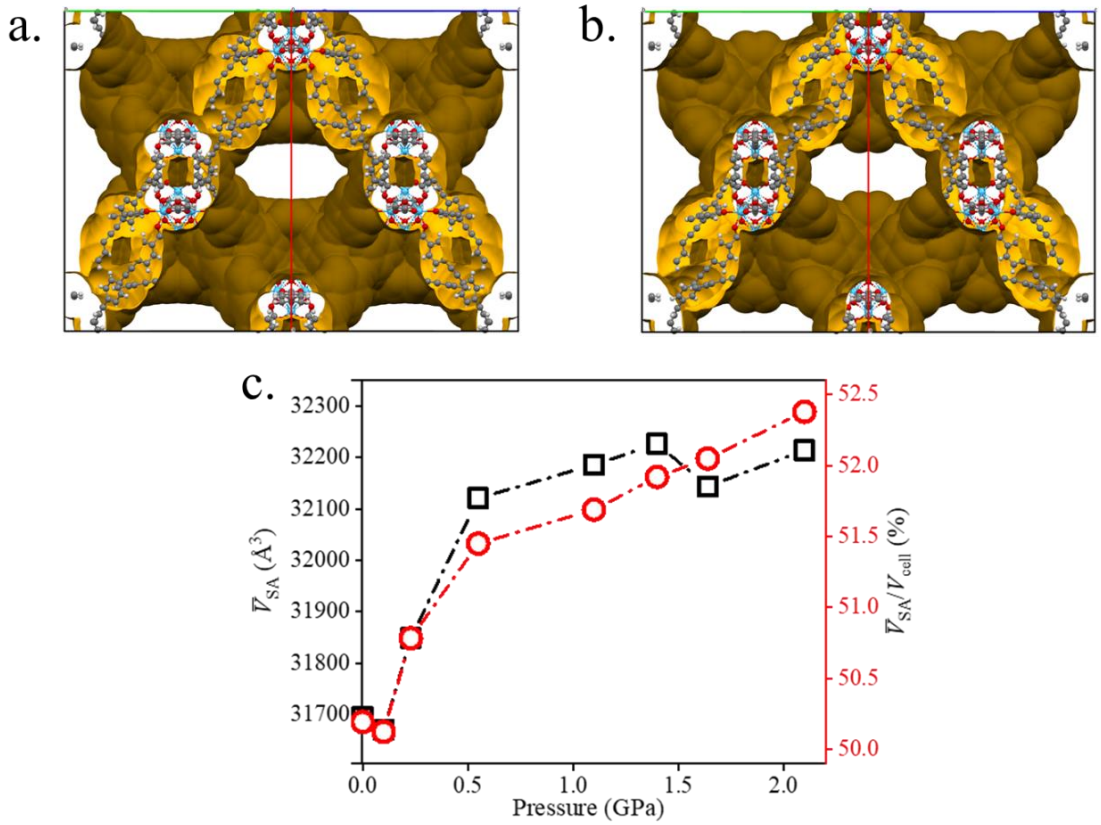

Figure 4.8. The solvent-accessible pore channel image of the structure of Hf-peb MOF at (a) ambient pressure and (b) at 2.1 GPa showing a slight increase and (c) the plot of pore volume and its percentage in the unit cell as a function of pressure.

With the decrease of unit cell volume and the increase in solvent-accessible volume, the intermolecular distance between ligands decreases, making a more packed ligand framework. For the coplanar conformer, the inter-ligand distance can be quantified as the distance between the centroids of the central phenyl ring and the terminal ring of adjacent ligands, as shown in **Figure 4.9 a**. For the twisted conformer, the inter-ligand distance can be measured as the distance between a hydrogen atom on the central phenyl ring (CH) of and an oxygen atom on the adjacent ligand, noted as CH-O distance, as shown in **Figure 4.9 b**. As shown in **Figure 4.9 c,** the inter-centroids distance decreases with increasing pressure, to accommodate a larger pore. The CH-O distance also decreases with increasing pressure, as shown in **Figure 4.9 d**. It is likely that, as pressure increases, and the inter-carbonyl distance shortens (i.e. the ligand become more bent), the intermolecular distance decreases. However, the coplanar conformer could not accommodate a higher degree of bending, due to the inter-ligand steric interaction the central and terminal phenyl rings. The twisted conformer, on the

other hand, could go further and facilitate more bending by decreasing the CH-O distance. This could explain why the twisted conformer is more preferred at higher pressure. This also shows that the peb^{2-} ligand experiences intermolecular interactions that are not present for the free molecule in solution, but still exists in a more isolated environment than the molecule in the crystal.

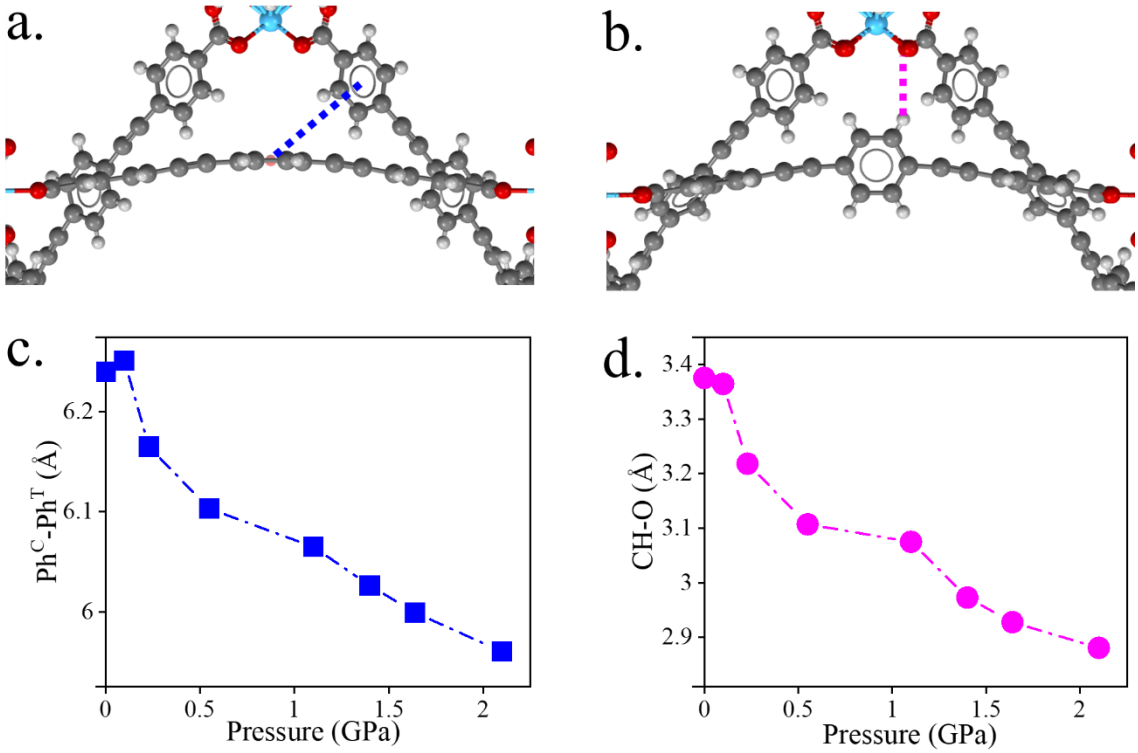

Figure 4.9. (a) The structure of coplanar conformer identifying an inter-centroid distance between central and terminal phenyl rings of adjacent ligands, (b) the structure of twisted conformer, identifying an inter-ligand CH-O distance. (c) and (d) Plots of the pressure-dependence of the inter-centroid distance CH-O distance, respectively. Colour scheme: Hf – blue, O – oxygen, C – grey, H – white.

The role of ligand flexibility in facilitating the increase of pore volume with increasing pressure is not unique for the Hf-peb MOF but has also been observed in other MOFs with long and flexible ligands, such as ZIF-8[27,28], HKUST-1[29,30], Sc_2BDC_3[31] and ZAG-based MOFs[32]. However, the pressure-induced transformation of linker conformation has not been observed previously.

4.3.2 High-Pressure Fluorescence Emission Spectroscopy

In order to study the effect of pressure on the electronic transition of Hf-peb MOF, fluorescence emission spectra were measured as a function of pressure from 0 GPa to 2.12 GPa at intervals that closely matched the pressures used in the X-ray diffraction measurements.

The intensity-normalised fluorescence spectra at the various pressures are depicted in **Figure 4.10** It can be seen that there is a bathochromic shift in the spectrum with increasing pressure. As shown in **Table 4.3,** the maximum is shifted from 428 nm (23360 cm^{-1}) at 0 GPa to 450 nm (22220 cm^{-1}) at 2.1 GPa, a total shift of 1140 cm^{-1}.

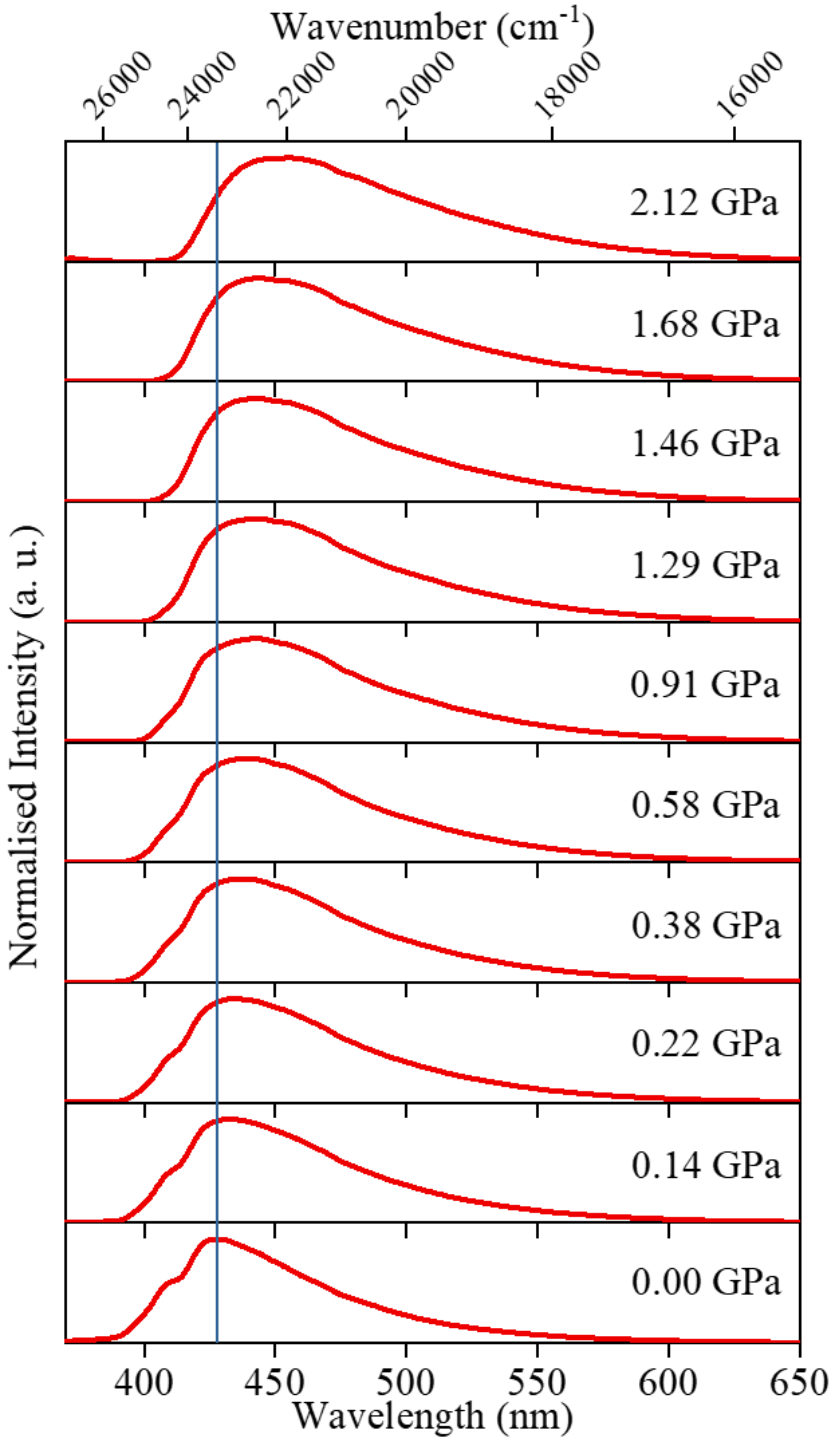

Figure 4.10. Fluorescence emission spectra of Hf-peb MOF as a function of pressure. The blue vertical line marks the maximum of the spectrum at 0.00 GPa.

Table 4.3. The wavelength and wavenumber of the fluorescence emission maximum as a function of pressure.

Pressure / GPa	Emission Peak / nm	Emission Peak / cm^{-1}
0.00	428	23360
0.14	433	23090
0.22	434	23040
0.38	438	22830
0.58	440	22730
0.91	443	22570
1.29	443	22570
1.46	443	22570
1.68	444	22520
2.12	450.0	22220

It was hypothesised that if both conformers contribute to the emission spectrum, then it should be possible to describe the total emission spectrum as a linear combination of the two individual spectra. The redshift could then be attributed to the change in conformational populations. To investigate this theory, the measured spectra were fitted to a linear combination of the 0 GPa and 2.1 GPa spectra, where the latter is known to correspond to the spectrum of the twisted conformer, as expressed by **Figure 4.3**. Using the Solver facility in Excel, it was found that the spectra could be well-fitted in this way, as illustrated in **Figure 4.11**. The fitted parameters are given in.

$$S_P = A_P S_0 + B_P S_T$$

Equation 4.3

Where S_P is the emission spectrum at given pressure, Where the S_0 is the emission spectrum at 0 GPa, S_T is the emission spectrum of the twisted conformer, A_P and B_P are the fractional amplitudes which represent the contribution of the ambient pressure and twisted structure (2.1 GPa) spectra, respectively.

From the crystallographic results, the fluorescence spectrum at ambient pressure can be assigned to the fluorescence contribution from both coplanar and twisted

conformers with the fractional population of 0.727 and 0.273, respectively. This can be expressed by **Equation 4.4**.

$$S_0 = 0.727\ S_C + 0.273\ S_T$$

Equation 4.4

where S_C and S_T are the spectra of the coplanar and twisted conformers, respectively.

Substitution of **Equation 4.4** into **Equation 4.3** results in **Equation 4.5**.

$$S_P = 0.727A_P\ S_C + (0.273A_P + B_P)\ S_T$$

Equation 4.5

Hence the fractional contribution of the coplanar and twisted conformers to each spectrum is given by **Equation 4.6** and **Equation 4.7**, respectively.

$$\chi_{PC} = 0.727A_P$$

Equation 4.6

$$\chi_{PT} = 0.273A_P + B_P$$

Equation 4.7

where the χ_{PC} and χ_{PT} are the fractional contribution of coplanar and twisted conformers, respectively. The values of χ_{PC} and χ_{PT} obtained from the fitting are given in **Table 4.4.**

Table 4.4. The fractional spectral contributions, A_P and B_P, determined by fitting the measured spectra with Equation 4.7. The fractional populations of the coplanar (χ_{PC}) and twisted conformers (χ_{PT}) as a function of pressure, determined from the fitted parameters. The boldened χ_{PC} and χ_{PT} were obtained from the X-ray structure data.

Pressure / GPa	**A_P**	**B_P**	**χ_{PC}**	**χ_{PT}**
0.00	1	0	**0.727**	**0.273**
0.14	0.785	0.215	0.571	0.429
0.22	0.713	0.287	0.518	0.482
0.38	0.667	0.333	0.485	0.515
0.58	0.611	0.389	0.444	0.556
0.91	0.509	0.491	0.370	0.630
1.29	0.425	0.575	0.309	0.691
1.46	0.346	0.654	0.252	0.748
1.68	0.262	0.738	0.191	0.809
2.12	0	1	**0**	**1**

An example of the spectral fitting is shown in **Figure 4.11** where the fluorescence spectrum at 0.58 GPa was constructed by fluorescence spectrum of 0 GPa spectral component and the 2.1 GPa spectral component with a fractional amplitude of 0.61 and 0.39, respectively, which translated to 0.44 and 0.56 fractional contribution of coplanar and twisted conformers, respectively. From the inset panel in **Figure 4.11 b**, a structured residual around ~410 nm can be observed, which may arise from the reabsorption of the sample and the absorption of the diamond.

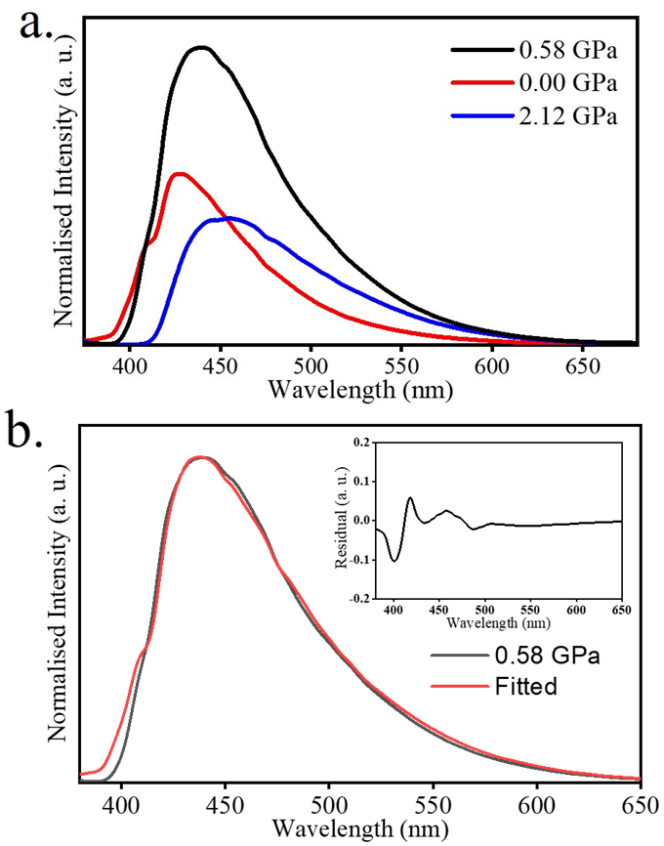

Figure 4.11. (a) The fluorescence spectrum at 0.58 GPa can be constructed by 61% spectrum of 0 GPa and 39% spectrum of 2.1 GPa. (b) The comparison between the fluorescence spectrum at 0.58 GPa and its fitted spectrum.

It was found that the fractional population of the conformers predicted from the fluorescence emission fitting was in good agreement with the values determined from the X-ray diffraction data, as depicted in **Figure 4.12**. A global confidence interval of 5% is used for the fractional conformation obtained from the fluorescence emission linear fit. This close relation comes from measurement on two separate crystals, indicating these effects are not crystal dependent. The close correlation suggests that the ground-state population determines the contribution of each conformer to the observed emission spectrum; hence the two conformers must have very similar fluorescence brightness (the product of the molar absorption coefficient, ε, at the excitation wavelength of 380 nm and the fluorescence quantum yield, Φ). The brightness and the emission spectral profile of each conformer must also be substantially independent of pressure. Ideally, the correlation could be confirmed by fitting the absorption spectra, which directly reflects the ground state population. However, this was not possible as only the red edge of the absorption spectrum can be measured for the solid sample (as shown in **4.3.3**).

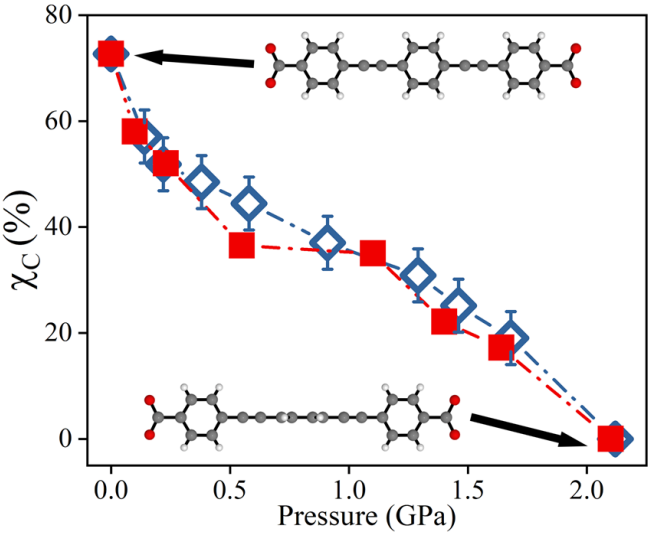

Figure 4.12. The fractional population of the coplanar structure, χ_C, obtained from occupancy refinement of the X-ray data (red rectangle) and from fitting the fluorescence spectra (blue diamond). Lines are for guidance only.

The fluorescence spectrum of the coplanar conformer alone can be obtained by rearranging **Equation 4.5** to **Equation 4.8** so that the spectrum can be obtained using the 0 GPa and 2.12 GPa spectra.

$$S_C = \frac{S_0 - 0.273\ S_T}{0.727}$$

Equation 4.8

The fluorescence spectrum of the coplanar conformer is plotted in **Figure 4.13**. The spectrum has its fluorescence maximum at 424 nm, compared with 450 nm for the twisted form. The coplanar conformer also appears to have a narrower spectrum than the twisted form. This result is essential as the individual spectra of the two conformers of BPEB, coplanar and twisted, have not been extracted previously.

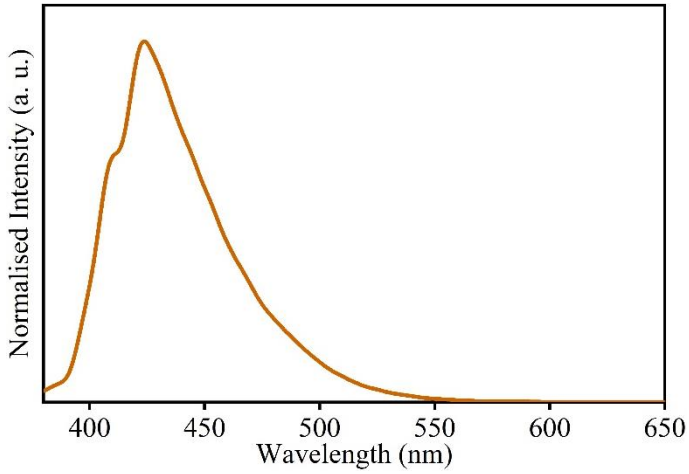

Figure 4.13. The fluorescence spectrum of the coplanar conformer, extracted from the 0 GPa spectrum based on the fractional distribution shown in Table 4.4.

4.3.3 High-Pressure UV-Vis Absorption Spectroscopy

The UV-vis absorption spectra were collected at pressures chosen to closely match the pressures in the X-ray diffraction measurement and the fluorescence spectra, as depicted in **Figure 4.14**. The absorption spectra show a bathochromic shift with increasing pressure which could be attributed to the shift in the ligand conformal population towards the twisted conformer. However, it is not possible to quantify the fractional population of conformers from the absorption spectrum since the peak of the spectrum cannot be observed. The absence of peak is not surprising for a solid sample due to the high concentration of the chromophore in a very small volume.[33] Therefore, to quantify the shift of the absorption spectrum with increasing pressure, the red-edge of the spectrum is used.

The red edge was defined as point of the steepest rise of the absorption spectrum, which could be obtained by selecting the peak of the first derivative of the spectrum. The absorption red-edge as a function of pressure summarised in **Table 4.5**. At 0 GPa, the red-edge is found to be 391 nm (25608 cm^{-1}) and is shifted by ~550 cm^{-1} to 399 nm (25062 cm^{-1}) at 2.1 GPa.

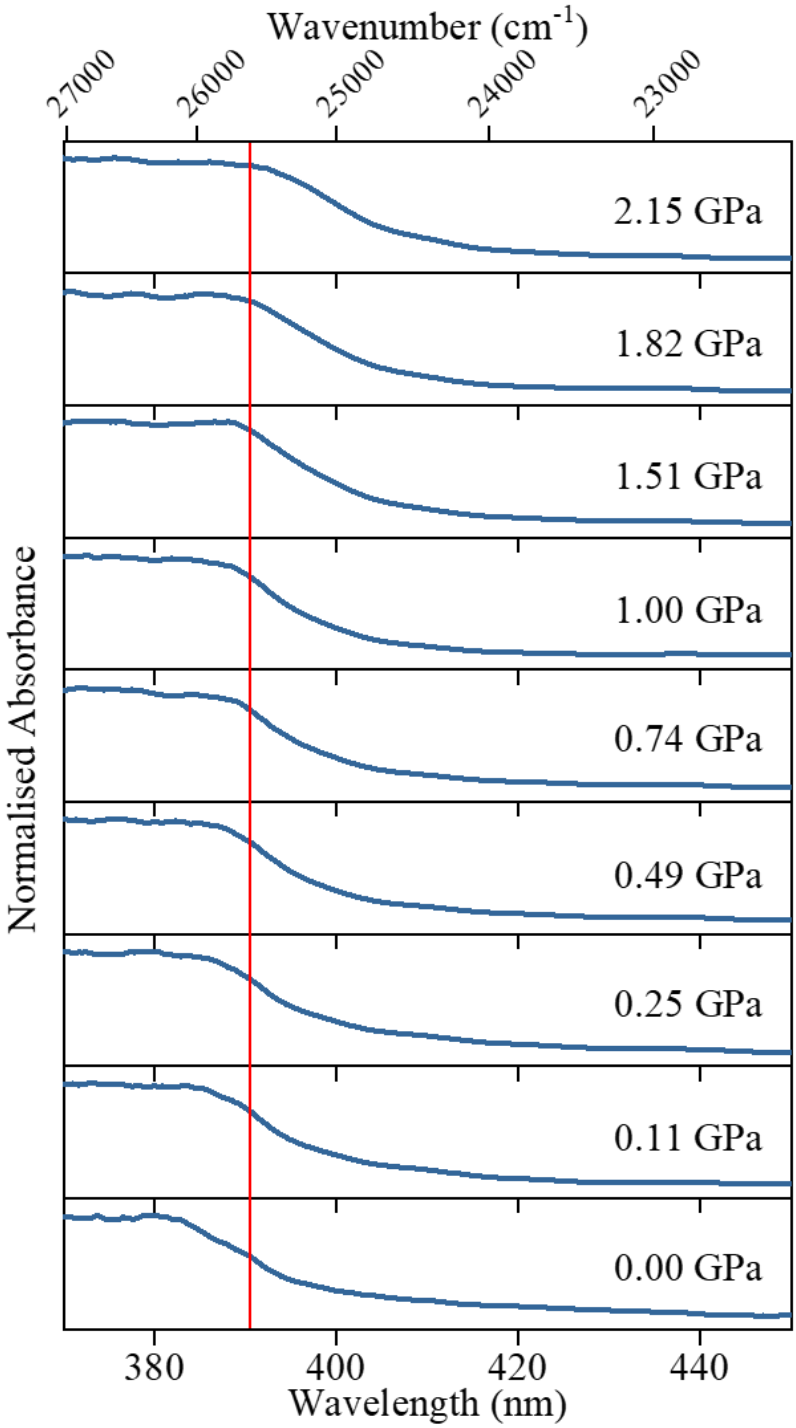

Figure 4.14. UV-vis absorption spectra of Hf-peb MOF as a function of pressure. The red vertical line marks the absorption edge of the spectrum at 0.00 GPa.

Table 4.5. Wavelength and wavenumber of the UV-Vis absorption edge as a function of pressure

Pressure / GPa	Absorption Edge / nm	Absorption Edge / cm^{-1}
0.00	391	25608
0.11	392	25542
0.25	392	25510
0.49	393	25477
0.74	393	25464
1.00	393	25458
1.51	396	25271
1.82	396	25278
2.15	399	25062

4.3.4 Comparison Between UV-Vis Absorption and Fluorescence Spectra

Both UV-vis absorption and fluorescence spectra show a bathochromic shift with increasing pressure. However, the shift of the fluorescence (1140 cm^{-1}) is much more significant than that of the UV-vis absorption (550 cm^{-1}) at ~2.1 GPa, indicating that the twisted conformer structure experiences a more significant structural relaxation in the excited state. The Stokes shift for coplanar conformer is found to be ~2250 cm^{-1} while the twisted conformer is ~2840 cm^{-1}. This indicates that following excitation of the twisted conformer to the Franck-Condon geometry, structural relaxation occur prior to emission with the magnitude of this relaxation is greater than the relaxation of the coplanar conformer. This also consistent with molecular orbital calculations of the free BPEB molecule, which show that the excited-states electronic structure of the twisted form differs substantially from the ground state, showing more localised quinoid structure, while the coplanar electronic structure retains the delocalised benzenoid structure of the ground state.[34,35] In the Hf-peb MOF, upon excitation of the twisted conformer, the local MOF structure responds to the change in electronic structure of the ligand which further illustration of the flexibility of the MOF framework, and how this can affect the photoluminescence properties.[36] This

behaviour is different to the tetraphenylethylene-based Zr MOF which show change in luminescence due to the breathing behaviour up to 20 MPa, where the two interpenetrating frameworks were compressed towards one another, without changing ligand conformation, and the unit cell contracted dramatically.[37]

The electronic spectra, especially the fluorescence emission spectrum of the peb^{2-} ligand (referred to as BCPEB) in the MOF, differ from those of the free BPEB fluorophore in solution, as discussed in **Chapter 7**.[36] For the free molecule in solution, the excitation energy of the twisted conformer is higher than that of the coplanar conformer. This difference could be due to the bent nature of the ligand backbone in the MOF, which will affect the electronic structure of the molecule. Moreover, intermolecular interactions in the MOF (**Figure 4.9**) may affect the relative excitation energies of the two conformers.

4.4 Conclusions and Further Work

A high-pressure single-crystal X-ray diffraction experiment to determine the structure of the Hf-peb MOF has been successfully carried out for pressures up to 2.1 GPa, in a DAC with pentane as a hydrostatic medium. Upon increasing pressure to 2.1 GPa, the unit cell volume of the MOF is decreased by ~2.6%. For the first time, a twisted conformer of the ligand, in which the central phenyl ring is twisted by 90º, was observed in the crystal structure. At ambient pressure and room temperature, the ligand exists in two conformational states, the major, coplanar conformer, where the central phenyl ring coplanar to the terminal rings, which comprises 73% of the population, and the twisted conformer, which comprises 27% of the population. With increasing pressure, the fractional population of the twisted conformer increases until it becomes exclusive at 2.1 GPa. The conformational changes, however, neither transform the crystal system nor the space group.

High-pressure fluorescence emission and UV-vis absorption spectral measurements were also successfully carried out with a bespoke measurement setup and show that the pressure-induced red-shift in UV-vis absorption and fluorescence spectra are due to the change of the ligand conformal populations. Fitting of the fluorescence spectra showed that the bathochromic shift is not caused by the pressure-induced shift in excitation energy of single emitting species, but by the interconversion of two ground-

state species whose emission spectra are independent of pressure. The fractional populations of the two conformations derived from the spectral fitting were in very good agreement with those derived from the crystallographic analysis. The twisted conformer showed a greater Stokes shift than the coplanar species, implying a greater relaxation of the local MOF environment about the twisted ligand excited state. By combining high-pressure crystallography and spectroscopy, it has been possible to directly correlate pressure-induced changes in the linker conformation with changes in its optical properties.

Further experiments, such as time-resolved fluorescence spectroscopy or transient absorption spectroscopy, as a function of pressure could be carried out to study further the processes that occur in between the absorption and emission of light. Moreover, a thinner crystal (with ~7 μm thickness) could be grown to enable the absorption spectral profile to be measured. This would be beneficial to corroborate the pressure-induced change in conformation, as the vertical excitation energy can be related directly to the ground state species observed in the crystal structure.

4.5 References

1. Cui, Y. J.; Yue, Y. F.; Qian, G. D.; Chen, B. L., *Chem. Rev.* **2012,** *112* (2), 1126-1162.
2. Angioni, E.; Marshall, R. J.; Findlay, N. J.; Bruckbauer, J.; Breig, B.; Wallis, D. J.; Martin, R. W.; Forgan, R. S.; Skabara, P. J., *J. Mater. Chem. C* **2019,** *7* (8), 2394-2400.
3. Cui, Y. J.; Zhu, F. L.; Chen, B. L.; Qian, G. D., *Chem. Commun.* **2015,** *51* (35), 7420-7431.
4. Li, Z.; Qin, A. J., *Natl Sci Rev* **2014,** *1* (1), 22-24.
5. Birks, J. B., *Photophysics of Aromatic Molecules*. Wiley-Interscience: London, New York, **1970**.
6. Sun, C. Y.; Wang, X. L.; Zhang, X.; Qin, C.; Li, P.; Su, Z. M.; Zhu, D. X.; Shan, G. G.; Shao, K. Z.; Wu, H.; Li, J., *Nat. Commun.* **2013,** *4*.
7. Aguilera-Sigalat, J.; Bradshaw, D., *Chem. Commun.* **2014,** *50* (36), 4711-4713.
8. Jiang, H.-L.; Feng, D.; Wang, K.; Gu, Z.-Y.; Wei, Z.; Chen, Y.-P.; Zhou, H.-C., *J. Am. Chem. Soc.* **2013,** *135* (37), 13934-13938.

9. Su, Y.; Yu, J. H.; Li, Y. B.; Phua, S. F. Z.; Liu, G. F.; Lim, W. Q.; Yang, X. Z.; Ganguly, R.; Dang, C.; Yang, C. L.; Zhao, Y. L., *Commun. Chem.* **2018,** *1*.
10. Schaate, A.; Roy, P.; Preusse, T.; Lohmeier, S. J.; Godt, A.; Behrens, P., *Chem-Eur J* **2011,** *17* (34), 9320-9325.
11. Doan, T. L.; Nguyen, H. L.; Pham, H. Q.; Pham-Tran, N. N.; Le, T. N.; Cordova, K. E., *Chem. Asian. J* **2015,** *10* (12), 2660-8.
12. Marshall, R. J.; Griffin, S. L.; Wilson, C.; Forgan, R. S., *Chem-Eur J* **2016,** *22* (14), 4870-4877.
13. Marshall, R. J.; Kalinovskyy, Y.; Griffin, S. L.; Wilson, C.; Blight, B. A.; Forgan, R. S., *J. Am. Chem. Soc.* **2017,** *139* (17), 6253-6260.
14. Moggach, S. A.; Allan, D. R.; Parsons, S.; Warren, J. E., *J. Appl. Crystallogr.* **2008,** *41*, 249-251.
15. Barnett, J. D.; Block, S.; Piermarini, G. J., *Rev. Sci. Instrum.* **1973,** *44* (1), 1-9.
16. Bruker-Nonius, B.-A. X. S. *XPREP*, Madison, Wisconsin, USA, 2004.
17. Parsons, S. *SHADE*, 2004.
18. Sheldrick, G. M. *SADABS Version 2016/2*, 2008.
19. Sheldrick, G. M., *Acta. Crystallogr. A* **2015,** *71*, 3-8.
20. Betteridge, P. W.; Carruthers, J. R.; Cooper, R. I.; Prout, K.; Watkin, D. J., *J. Appl. Crystallogr.* **2003,** *36*, 1487-1487.
21. Spek, A. L., *J. Appl. Crystallogr.* **2003,** *36*, 7-13.
22. Spek, A. L., *Acta. Crystallogr. C* **2015,** *71*, 9-18.
23. Macrae, C. F.; Sovago, L.; Cottrell, S. J.; Galek, P. T. A.; McCabe, P.; Pidcock, E.; Platings, M.; Shields, G. P.; Stevens, J. S.; Towler, M.; Wood, P. A., *J. Appl. Crystallogr.* **2020,** *53*, 226-235.
24. Hobday, C. L.; Marshall, R. J.; Murphie, C. F.; Sotelo, J.; Richards, T.; Allan, D. R.; Düren, T.; Coudert, F.-X.; Forgan, R. S.; Morrison, C. A.; Moggach, S. A.; Bennett, T. D., *Angew. Chem. Int. Ed.* **2016,** *128* (7), 2447-2451.
25. Greaves, S. J.; Flynn, E. L.; Futcher, E. L.; Wrede, E.; Lydon, D. P.; Low, P. J.; Rutter, S. R.; Beeby, A., *J. Phys. Chem. A* **2006,** *110* (6), 2114-2121.
26. Fujiwara, T.; Zgierski, M. Z.; Lim, E. C., *J. Phys. Chem. A* **2008,** *112* (21), 4736-4741.

27. Fairen-Jimenez, D.; Moggach, S. A.; Wharmby, M. T.; Wright, P. A.; Parsons, S.; Duren, T., *J. Am. Chem. Soc.* **2011,** *133* (23), 8900-8902.
28. Hobday, C. L.; Woodall, C. H.; Lennox, M. J.; Frost, M.; Kamenev, K.; Duren, T.; Morrison, C. A.; Moggach, S. A., *Nat. Commun.* **2018,** *9* (1), 1429.
29. Chapman, K. W.; Halder, G. J.; Chupas, P. J., *J. Am. Chem. Soc.* **2008,** *130* (32), 10524-10526.
30. Graham, A. J.; Tan, J.-C.; Allan, D. R.; Moggach, S. A., *Chem. Commun.* **2012,** *48* (10), 1535-1537.
31. McKellar, S. C.; Sotelo, J.; Greenaway, A.; Mowat, J. P. S.; Kvam, O.; Morrison, C. A.; Wright, P. A.; Moggach, S. A., *Chem. Mater.* **2016,** *28* (2), 466-473.
32. Gagnon, K. J.; Beavers, C. M.; Clearfield, A., *J. Am. Chem. Soc.* **2013,** *135* (4), 1252-1255.
33. Wright, J. D., *Molecular Crystals*. Second ed.; Cambridge University Press: Cambridge, **1995**.
34. Levitus, M.; Schmieder, K.; Ricks, H.; Shimizu, K. D.; Bunz, U. H.; Garcia-Garibay, M. A., *J. Am. Chem. Soc.* **2001,** *123* (18), 4259-65.
35. Seminario, J. M.; Zacarias, A. G.; Tour, J. M., *J. Am. Chem. Soc.* **2000,** *122* (13), 3015-3020.
36. Roy, K.; Kayal, S.; Ariese, F.; Beeby, A., *J. Chem. Phys.* **2017,** *146* (6).
37. Chen, C. X.; Wei, Z. W.; Cao, C. C.; Yin, S. Y.; Qiu, Q. F.; Zhu, N. X.; Xiong, Y. Y.; Jiang, J. J.; Pan, M.; Su, C. Y., *Chem. Mater.* **2019,** *31* (15), 5550-5557.

Chapter 5
The Effect of Pressure on the Spectroscopic Properties of the Azobenzene Ligand in a UiO-type MOF

5.1 Introduction

A combination of UV-vis absorption spectroscopy and time-dependent density functional theory (TDDFT) computation have been used to study the effect of pressure on a UiO-type MOF containing the azobenzene dicarboxylate ($abdc^{2-}$) ligand, Zr-abdc MOF. The results reported in this chapter give insight into the effect of pressure-induced bending of the $abdc^{2-}$ ligand on the electronic spectrum. The effect of pressure-induced polar solvation of the azobenzene chromophore is also reported.

5.1.1 Electronic Spectroscopy of Azobenzenes

Azobenzenes (**AB**) is a well-known chromophore which consists of two phenyl rings linked by an N=N (azo) bridge. In the solution phase, **AB** undergoes photo-induced *cis*-*trans* isomerisation. Due to this photoisomerisation feature, azobenzene-based molecules have been extensively studied for applications as photo-induced molecular switches, molecular machines, and materials for liquid crystals.[1-3]

The **AB** *trans*-isomer is the more energetically favoured species in the ground state due to its planar structure. In order to exhibit *trans*→*cis* isomerisation, the N=N double bond should be broken to N-N single bond and rotated by 180º to form the higher-energy *cis*-isomer. The breaking of the N=N bond can be achieved by optical excitation, which causes the symmetry allowed $\pi \rightarrow \pi^*$ ($S_0 \rightarrow S_2$) and symmetry forbidden $n \rightarrow \pi^*$ ($S_0 \rightarrow S_1$) transitions, as shown in **Figure 5.1**. The former transition gives rise to an intense absorption band at ~320 nm and the latter to a much weaker band at ~440 nm. The freely rotating N-N bond in the excited state (S_1) then permits relaxation to the *cis* or *trans* isomer at the ground state (S_0). Internal conversion occurs very rapidly through a conical intersection that connects the excited (S_1) and ground (S_0) states potential energy surfaces, resulting in an extremely low fluorescence

quantum yield (~10^{-6}). The mechanism isomerisation in the excited state remains controversial and could happen in several ways, such as torsional rotation about the N-N bond, inversion of one phenyl ring, concerted inversion of both phenyl rings and inversion-assisted rotation.[4]

A reverse thermal *cis*→*trans* isomerisation can happen in the ground state, in the dark, due to a relatively low activation energy. The rate of this *cis*→*trans* isomerisation depends on the polarity and viscosity of the solvent, pH and temperature.

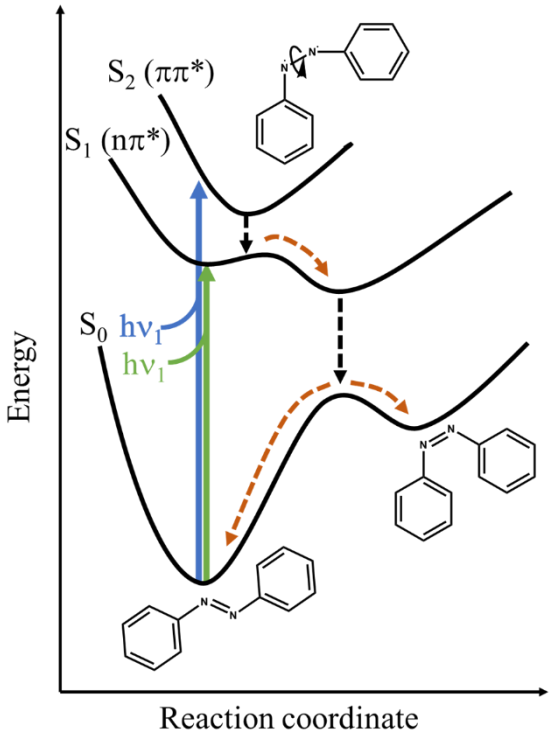

Figure 5.1. Schematic of potential energy surface of azobenzene during photo-induced isomerisation.

Many researchers have tried to investigate the photophysical effect of restricting the isomerisation, either by creating a small enclosed space or anchoring both ends of the **AB** molecules. Bahrenberg *et al.* investigated the effect of cross-linking of acetamide-substituted azobenzene into a polymer (named as **P-BAAB-P**), restricting the *cis-trans* isomerisation.[5] They reported that the excited state lifetime is prolonged from 3 ps in solution to 65 ps in the polymer, with a consequent 20-fold increase in fluorescence quantum yield.

A study by Lee *et al.* suggested that growing an azobenzene in a highly single-crystalline molecular wire could increase the lifetime of the S_1 (nπ*) state to 1.17 ns,

which is remarkably longer than in solution phase (~3 ps). This was suggested to be caused by the tight molecular packing in the crystal that hindered isomerisation pathways.[6]

Another way to restrict isomerisation is by the encapsulation of the **AB** molecule inside a molecular cage. Raj *et al.* reported that encapsulation of **AB** molecules in bimolecular cavitand octa acid molecular cage could increase the *trans*-isomer population, although the *cis*-isomer formation was not completely inhibited.[7] A recent follow-up paper by Otolski *et al.* using ultrafast spectroscopy revealed a prolonged excited-state lifetime, due to stabilisation of non-planar excited-state structures.[8] This excited-state structure is stabilised or forced to stabilise due to the confined space in the cage, which facilitates rapid deactivation of the excited-state from *cis*-like structure.

Wang *et al.* reported attachment of **AB** molecule onto bipyridine (**bipy**), and longer biphenyl dicarboxylates (**bpdc**) linkers in a Cu-based MOF.[9] The **AB** molecules have one of the phenyl rings bonded to the linkers so that the tethered molecule sits freely in the pore of the MOF. The *trans*→*cis* and the reverse *cis*→ *trans* isomerisation could be induced by irradiation with ultraviolet and visible light, respectively. The *trans*→*cis* and *cis*→*trans* isomerisation is reversible and often referred to as an on-off mechanism. In the MOF with more extended ligand (**bpdc**), the *trans*→*cis* isomerisation and reverse isomerisation could occur freely. However, in the MOF with a shorter ligand (**bipy**), the isomerisation did not occur due to steric hindrance from the neighbouring ligand.

5.1.2 Zr-abdc MOF

A MOF with the 4,4-azobenzene dicarboxylate ($abdc^{2-}$) ligand and $[Zr_6O_4(OH)_4]^{12+}$ as the secondary building unit (SBU), isoreticular to the UiO-family MOF was first synthesised by Schaate *et al.* in 2012.[10] The MOF crystalised in a cubic system with $Fm\bar{3}m$ space group [a = 29.4433(4) Å]. The particle size of the crystal could be controlled, from 1 μm to 100 μm, by increasing the amount of benzoic acid during synthesis. Thermogravimetric analysis revealed that, at a temperature of 300 ºC, the guest molecules within the pore were getting purged. A further increase in the temperature to 400ºC caused the linker to combust. Hobday *et al.* reported that the structure of the MOF has significant disorder on the $abdc^{2-}$ ligand, caused by the

vibrational motion, as can be seen in **Figure 5.2 a** as large amplitude of atomic displacement ellipsoid.[11] It was also reported that the unit cell volume of the MOF shrunk radically with increasing pressure in a non-penetrating hydrostatic medium, Fluorinert FC-70, by ~8% at 1.8 GPa, as shown in **Figure 5.3**. However, as also shown in **Figure 5.3**, when compressed in a penetrating hydrostatic medium, methanol, the unit cell slightly expanded at initial pressure (~0.2% at 0.2 GPa) but showed minimal decrease at higher pressure, ~1% at 5.4 GPa, compared to the decrease in FC-70. Due to the difficulty in solving the crystal structure, computational modelling on the dynamics of the ligand was carried out to see the effect of decreasing volume on the $abdc^{2-}$ ligand. It was predicted that the ligand experiences a higher degree of bending with increasing pressure.

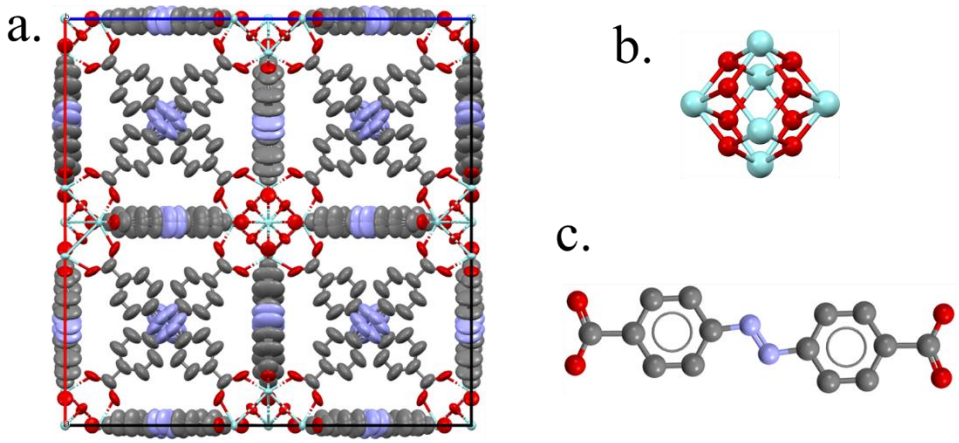

Figure 5.2. The Zr-abdc MOF (a) with unit cell parameters of 29.3248 Å, (b) the $Zr_6O_4(OH)_4$ SBU and (c) the $abdc^{2-}$ ligand. Hydrogen atoms are omitted for clarity. Colour scheme: Zr – blue, O – oxygen, N – purple, C – grey. The figure is redrawn from the structure deposited by Hobday *et al*.[11]

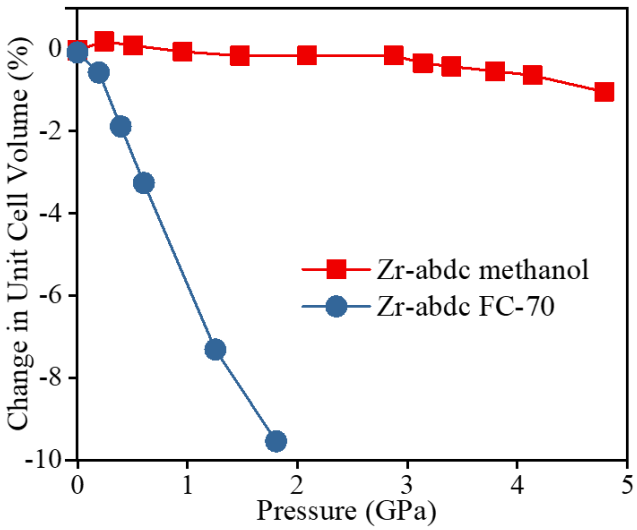

Figure 5.3. The percentage change in unit cell volume as a function of pressure for Zr-abdc in methanol and FC-70 (red squares and blue circles, respectively). Redrawn from Hobday *et al.*[11]

Epley *et al.* reported that particle-size control, from 100 nm to 600 nm, could be achieved by varying acetic acid concentration during synthesis. This is particularly important for the use of the MOF as a photo-degradative drug delivery system.[12] It was reported that the MOF experienced a photo-degradation up to ~8.5% per-hour by irradiation with 1000W of white light. The photo-degradation of dye is not uncommon upon intense irradiation. The pore environment is found to be hydrophobic, indicated by the release of preloaded caffeine (hydrophilic) to the environment within 3h, while ibuprofen (hydrophobic) was kept within the pore without irradiation of light. On the other hand, irradiation upon the MOF with preloaded Nile Red showed that ~0.36% of the preloaded dye was released upon 1h irradiation with 1000W of white light. This opens a potential application of the Zr-abdc MOF as a material for drug delivery applications.

This chapter reports the effect of the bending of the $abdc^{2-}$ ligand in Zr-abdc MOF as a function of pressure on the UV-vis absorption spectrum in non-penetrating FC-70 and penetrating methanol hydrostatic media. In this chapter Zr-abdc MOF with a particle size of ~20 μm was used in the UV-vis absorption measurement using ~1μW broadband light source, therefore no photo-degradation is expected to occur.

5.2 Experimental

It should be noted that the synthesis of the Zr-abdc MOF was carried out by Dr Ross Marshall, Dr Colin Murphie and Prof Ross Forgan of the University of Glasgow.

5.2.1 Synthesis

$ZrCl_4$ (0.052g, 0.225 mmol, 1 eq.), 4,4-azobenzenedicarboxylic acid (0.061 g, 0.225 mmol, 1 eq.) and L-proline (0.104 g, 0.900 mmol, 4 eq.) were added to a 50 ml Pyrex jar. 10 ml of DMF was added, and the jar was placed in a sonicator for 5 minutes. HCl (0.02 ml) was added to the resulting suspension, and the jar was placed in a sonicator for a further 5 minutes. The Pyrex jar then was stored in the oven at 100 °C for 48 hours. The jar was then removed from the oven and allowed to cool to room temperature. The reaction DMF was exchanged for fresh DMF several times.

5.2.2 High-pressure UV-Vis Absorption Spectroscopy

Before the UV-vis absorption measurement, the Zr-abdc MOF crystals were washed with acetone and left to dry at room and atmospheric pressure. Spectra were measured with either Fluorinert FC-70 or methanol as the PTM. In the case of FC-70, a crystal was loaded into the DAC alongside ruby, with clear Corning high-vacuum grease used as an adhesive for the crystal and the diamond culet. In the case of methanol, a clear Part A of Araldite® rapid resin was used as an adhesive for the crystal, instead of vacuum grease, due to solubility of the high-vacuum grease in methanol. The rapid resin was significantly more viscous than the high-vacuum grease making the loading more challenging. Only one side of the crystal has to stick to adhesives, exposing the other sides to the interpenetrating methanol so that the methanol can enter the pore of the MOF. The DAC was then placed in the custom-made measurement setup, as explained in **Chapter 3.**

5.2.3 Computational Methods

All calculations were performed in Gaussian 09 package which was running on the University of Edinburgh cluster: Eddie.[13]

5.3 Results and Discussions

5.3.1 High-pressure UV-Vis Absorption Spectra

The absorption spectra were measured from 0 GPa up to 2.1 GPa in FC-70 to investigate the effect of compression of the unit cell volume (**Figure 5.3**) on the electronic structure of the $abdc^{2-}$ linker. The pressures were chosen to correspond (approximately) to those used in the previous structural study.[11] The absorption spectrum appears to be saturated due to the intense absorption of the crystal, caused by high concentration of the chromophore. This is not unique for this MOF but was also observed in the Hf-peb MOF in **Chapter 4**.

The spectra are shown in **Figure 5.4** and the wavelength and wavenumber of the red-edge at each pressure The transition being observed here is the lowest energy nπ* transition of the azobenzene chromophore, as discussed further in Section **5.3.5**, is listed in **Table 5.1**. The spectra exhibit a bathochromic shift with increasing pressure, as shown in **Figure 5.5 a**, which correlates with the decrease in unit cell volume (**Figure 5.5 b**) up to a pressure of 0.82 GPa. At pressures higher than 0.82 GPa, the bathochromic shift becomes essentially constant at a value of ~330 cm^{-1}. It seems likely that the bathochromic shift of the spectra can be related to the bending of the ligand with increasing pressure. This will be discussed further in **5.3.3**

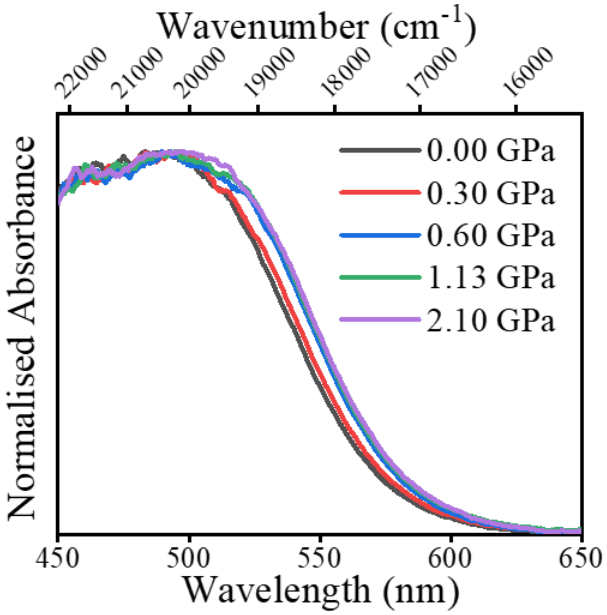

Figure 5.4. UV-vis absorption spectra of Zr-abdc MOF in Fluorinert FC-70 as a function of pressure.

Table 5.1. Wavenumber of the UV-vis absorption red-edge in Fluorinert FC-70 as a function of pressure.

Pressure / GPa	Absorption Edge / nm	Absorption Edge / cm^{-1}
0.00	543	18410
0.21	546	18320
0.30	547	18300
0.60	552	18120
0.82	553	18080
1.13	552	18120
1.84	554	18050
2.10	553	18080

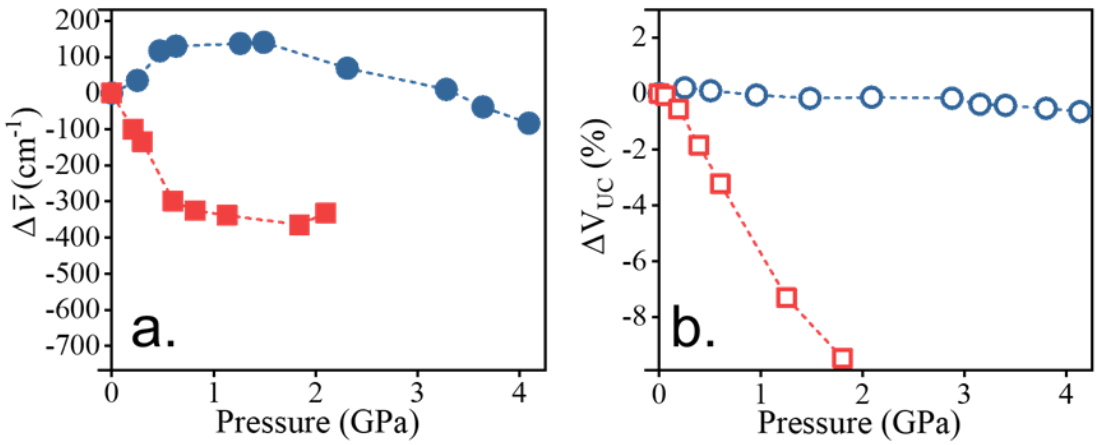

Figure 5.5. (a) The shift of the wavenumber of the absorption red-edge as a function of pressure in FC-70 (red) and methanol (blue). (b) The percentage change in unit cell volume in FC-70 (red) and methanol (blue). The change in unit cell volume is reproduced from Hobday *et al.*[11]

UV-vis absorption spectra of the MOF in methanol were also measured as a function of pressure to study the effect of an interpenetrating hydrostatic medium on the electronic transition. The spectra are shown in **Figure 5.6**, and the position of the absorption red-edge at each pressure is shown in **Table 5.2**.

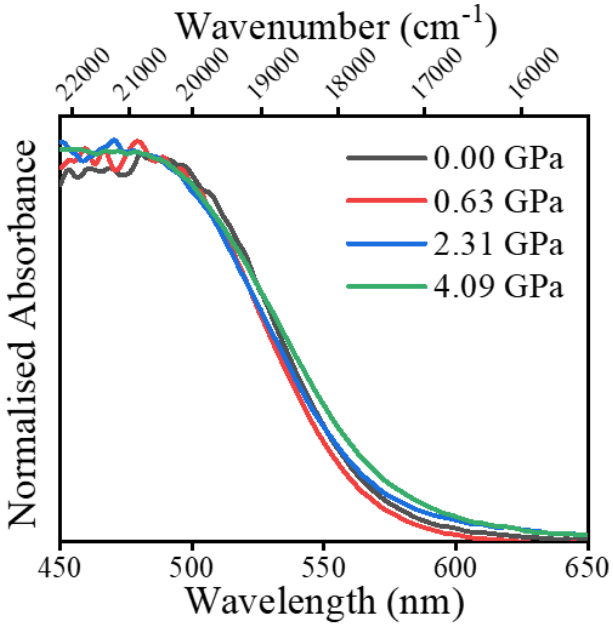

Figure 5.6. UV-vis absorption spectra of Zr-abdc MOF in methanol as a function of pressure.

Table 5.2. Wavenumber of the UV-vis absorption red-edge in methanol as a function of pressure.

Pressure / GPa	Absorption Edge / nm	Absorption Edge / cm^{-1}
0.00	535	18680
0.25	534	18720
0.47	532	18800
0.63	532	18810
1.26	531	18820
1.49	531	18820
2.31	533	18750
3.28	535	18690
3.64	536	18640
4.09	538	18600

In methanol, at 0 GPa, the absorption red-edge occurs at a shorter wavelength (535 nm) compared to the 0 GPa spectrum in FC-70 (543 nm). This can be attributed to the effect of solvation of the azobenzene chromophore by the polar methanol. It is

generally observed that nπ* transitions are subject to hypsochromic shifts in polar solvents since the ground state is more polar than the excited state. On excitation, the transfer of an electron localised in the lone pair orbital to the delocalised aromatic π system reduces the dipole moment.[14] Polar solvents, therefore, stabilise the ground state with respect to the excited state, and the energy of the transition is raised. As shown in **Figure 5.5 a**, the hypsochromic shift initially increases with increasing pressure, due to increased penetration of methanol into the framework. At pressures higher than 1.49 GPa, the spectrum then shows a small bathochromic with increasing pressure, but this is very slight compared with the shift observed in FC-70. As shown in **Figure 5.5 b**, the penetration of methanol into the pores of the MOF prevents shrinking of the unit cell volume, and hence decrease in the linker length, with increasing pressure.

5.3.2 Absence of Fluorescence Emission

Fluorescence emission spectroscopy measurements were also attempted in FC-70 and methanol at ambient pressure and high pressure using 365-nm (LS-LED Ocean Optics) excitation wavelength. However, no fluorescence could be detected. This means that even though the *trans*→*cis* isomerisation is highly restricted, especially in the exceptionally rigid methanol-penetrated framework, the non-radiative deactivation of the excited state still occurs with very high efficiency. To investigate the limit of detection, the fluorescence spectrum of a Coumarin 120 crystal (Sigma-Aldrich) with a known quantum yield of 0.01 was measured in the DAC.[15] The fluorescence spectrum is shown in **Figure 5.7**, together with the signal measured for Zr-abdc MOF under the same excitation/detection conditions. On this basis, the fluorescence quantum yield of the azobenzene linker can be estimated to be lower than 10^{-4}.

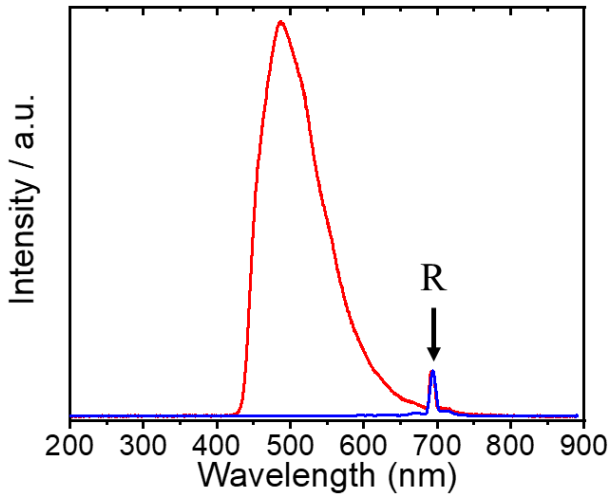

Figure 5.7. The fluorescence spectra of Coumarin 120 (red) and the signal for Zr-abdc MOF (blue) measured in DAC (λ_{ex} = 365 nm), normalised at the ruby fluorescence (R).

5.3.3 Computational Prediction of Ligand Bending with Increasing Pressure

A computational study was carried out to investigate the hypothesis that the pressure-induced bathochromic shift in the UV-vis absorption spectra, in FC-70, is due to the bending of the ligand. Initially, the length of the ligand, as a function of pressure was determined from the unit cell parameter, as described in section **5.3.4**. Then DFT and TDDFT calculations were carried out to predict the linker geometry (with fixed length) as a function of pressure and the corresponding vertical electronic transitions, as described in section **5.3.5**.

5.3.4 Determination of the $abdc^{2-}$ Linker Length

The starting structure was obtained from the crystal structure of the Zr-abdc MOF from Cambridge Crystallographic Database (Reference code: MAFWEY) with unit cell volume (V_{CU}) and unit cell parameter (a) of 25217.7(12) $Å^3$ and 29.3248(8) Å, respectively.[11] By using the relation between the unit cell volume and the pressure applied upon the crystal from the same paper, the deposited structure was found to be measured at 0.5 GPa, as shown in **Figure 5.8**. The structure around the ligand, however, is very disordered and divided between three different occupancies, due to a large libration of the ligand, which makes the direct use of the ligand structure of from the crystal structure impossible.

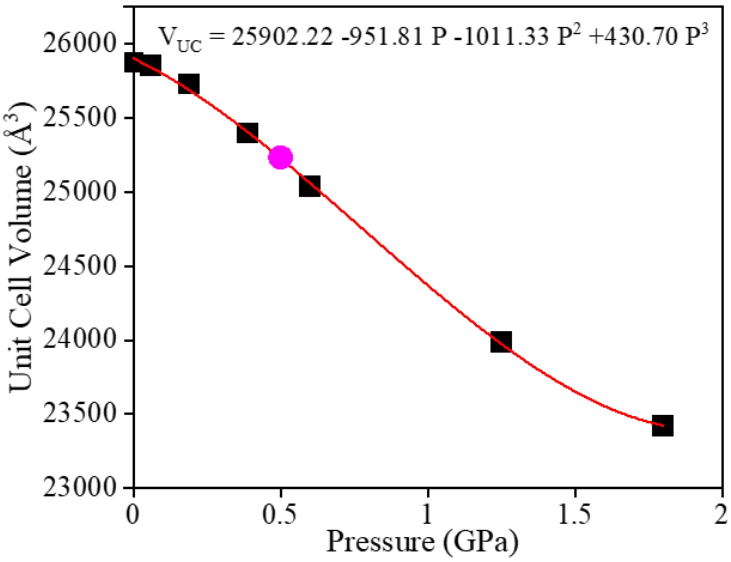

Figure 5.8. Unit Cell Volume as a cubic function of pressure. The pink circle is the Zr-abdc structure with known UCV and d_{CO}.

The structure of the Zr-abdc MOF, apart from the disorder of the ligand, is quite simple as represented in **Figure 5.9**. From **Figure 5.9**, it is possible to find the relation between the unit cell parameters (a), the radius of the secondary building units (r_{SBU}) and the length of the ligand (d_{CO}) using relation in **Equation 5.1**.

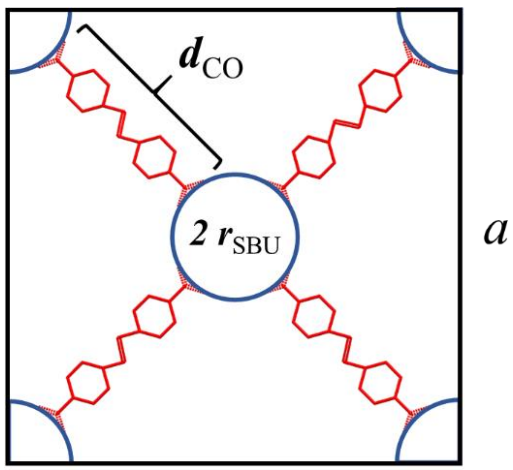

Figure 5.9. Schematic illustration of the determination of d_{CO} from the unit cell parameter (a).

$$a\sqrt{2} = 4\,r_{SBU} + 2\,d_{CO}$$

Equation 5.1

Using the unit cell parameters from the literature (0.5 GPa), the values of r_{SBU} and d_{CO} for the structure were calculated as 3.8879 Å and 12.960 Å, respectively. Assuming

that $\boldsymbol{r}_{SBU}$ is independent of pressure, the decrease in unit cell parameter results only in a decrease in the length of the linker; then $\boldsymbol{d}_{CO}$ can be calculated from the known unit cell parameters, according to **Equation 5.2**.

$$\boldsymbol{d}_{CO} = \frac{(a)\sqrt{2} - 4\ (\mathbf{3.8879})}{2}$$

Equation 5.2

A direct relationship between the $\boldsymbol{d}_{CO}$ and the pressure is illustrated in **Figure 5.10**, and the values of $\boldsymbol{d}_{CO}$ as a function of pressure are listed in **Table 5.3**. The structures of abdc^{2-} corresponding to the various $\boldsymbol{d}_{CO}$ lengths were then constructed using GaussView 5 software[16] as starting structures for geometry optimisation.

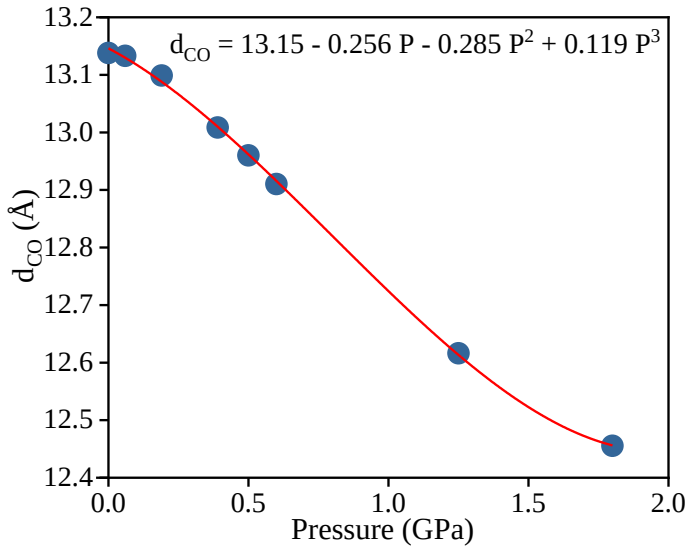

Figure 5.10. The d_{CO} as a cubic function of the pressure.

Table 5.3. The values of the linker length, d_{CO}, used in the DFT calculations and the corresponding pressures. The yellow highlight indicates the reference value of d_{CO} obtained directly from the X-ray molecular structure. The other d_{CO} values were calculated from the unit cell parameters. The pressures were calculated according to the d_{CO} length.

d_{CO} / Å	Calculated Pressure / GPa
13.144	0.00
13.110	0.12
13.019	0.37
12.960	0.50
12.921	0.59
12.820	0.80
12.772	0.90
12.627	1.22
12.500	1.58
12.466	1.74

5.3.5 Prediction of Linker Geometry and Electronic Transitions

Ground-state geometry optimisations on the abdc^{2-} ligands with varying length (see **Table 5.3**) were carried out using BH&HLYP functional and 6-311g(d,p) basis sets within Gaussian 09 program. The $\boldsymbol{d}_{CO}$ distance was fixed (the positions of the carboxylate oxygens constrained) during the geometry optimisation. The structure of the linker with constrained length was then optimised freely with respect to all other parameters. Frequency calculations on the optimised structures confirmed the energy was minimised with respect to all other coordinates. The optimised ground-state geometry of the ligand obtained for each pressure is shown in **Figure 5.11**.

The energy of the vertical electronic transitions was then calculated for each optimised ground-state geometry using time-dependent density functional theory (TDDFT) with the same functional and basis set, up to 10 excited states.

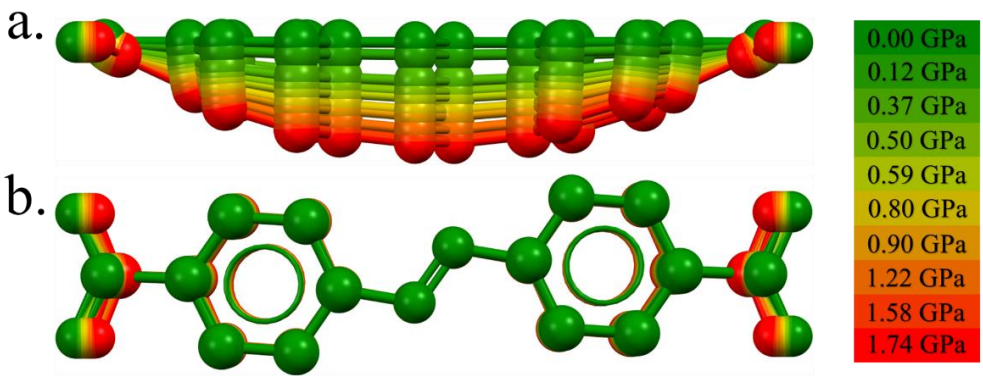

Figure 5.11. The optimised linker geometry (with fixed d_{CO}) at each pressure, (a) viewed parallel to the linker plane and (b) perpendicular to the linker plane.

From **Figure 5.11**, it is clear that with the shortening of d_{CO}, the ligand becomes more bent, this phenomenon has also been reported by Hobday *et al.* using molecular simulation methodology.[11] The optimised potential energy of the molecule also increases with the increase of the ligand bending, as shown in **Figure 5.12**. This is not surprising, as in solution phase, at ambient pressure, the azobenzene dicarboxylic acid molecule has a planar structure, which represents the lowest energy state.

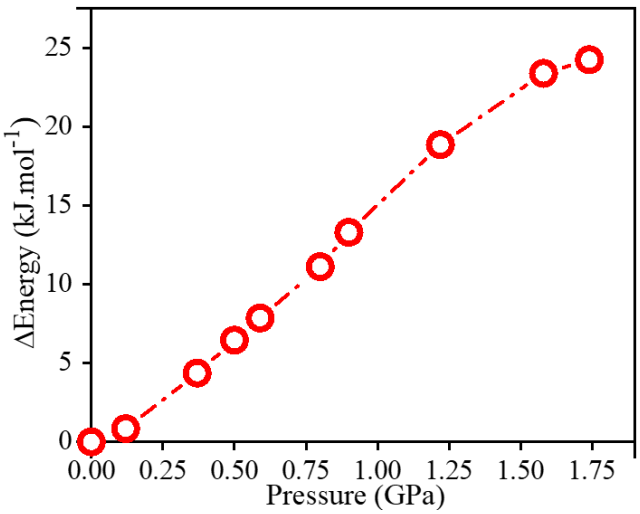

Figure 5.12. The optimised potential energy, relative to that at ambient pressure, of abdc^{2-}-linker as a function of pressure.

The wavelengths and oscillator strengths of the first two vertical electronic transitions predicted for each structure are given in **Table 5.4**, The longest wavelength (lowest energy) transition, highlighted as yellow, is the one of interest in this chapter, where the predicted wavelength is close to the value of the absorption peak (430 nm observed) for the lowest energy n→π* transition of azobenzene dicarboxylic acid in

solution.[17] The low oscillator strength is consistent with an n→π* transition, as it is symmetry forbidden transition. The second-longest wavelength transition corresponds to the more intense π→π* transition. The assignment of the n→π* transition is confirmed by the examination of the molecular orbitals involved in the transition, as shown in **Figure 5.13**.

Table 5.4. Wavelength and oscillator strength of azobenzene dicarboxylate at various pressures. The ~420 nm transition is the n→π* transition and the ~320 nm transition is π→π* transition.

0.00 GPa		**0.12 GPa**		**0.37 GPa**		**0.50 GPa**		**0.59 GPa**	
λ / nm	***f***	**λ / nm**	***f***	**λ / nm**	***f***	**λ / nm**	***f***	**λ / nm**	***f***
417.03	0	**416.24**	0.0011	**418.12**	0.0094	**419.45**	0.0142	**420.38**	0.0172
318.41	1.0242	**319.22**	1.0159	**319.43**	0.9904	**319.5**	0.9753	**319.53**	0.9662
0.80 GPa		**0.90 GPa**		**1.22 GPa**		**1.58 GPa**		**1.74 GPa**	
λ / nm	***f***	**λ / nm**	***f***	**λ / nm**	***f***	**λ / nm**	***f***	**λ / nm**	***f***
422.6	0.0244	**423.67**	0.0276	**426.85**	0.036	**429.62**	0.0427	**430.31**	0.0441
319.64	0.9425	**319.69**	0.9329	**319.84**	0.9048	**319.98**	0.8808	**320.01**	0.8741

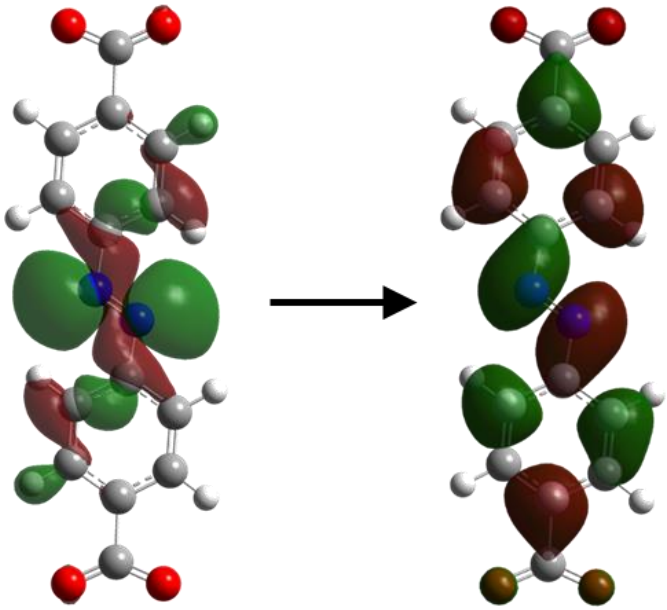

Figure 5.13. The orbitals involved in the lowest energy electronic transition.

The predicted pressure-dependence of the wavelengths and oscillator strengths of the n→π* transition and the higher energy π→π* transition is shown in **Figure 5.14**. With

increasing pressure, the n→π* transition is predicted to shift to longer wavelength, and its oscillator strength is predicted to increase. This is consistent with the bathochromic shift observed in the UV-vis absorption spectrum with increasing pressure.

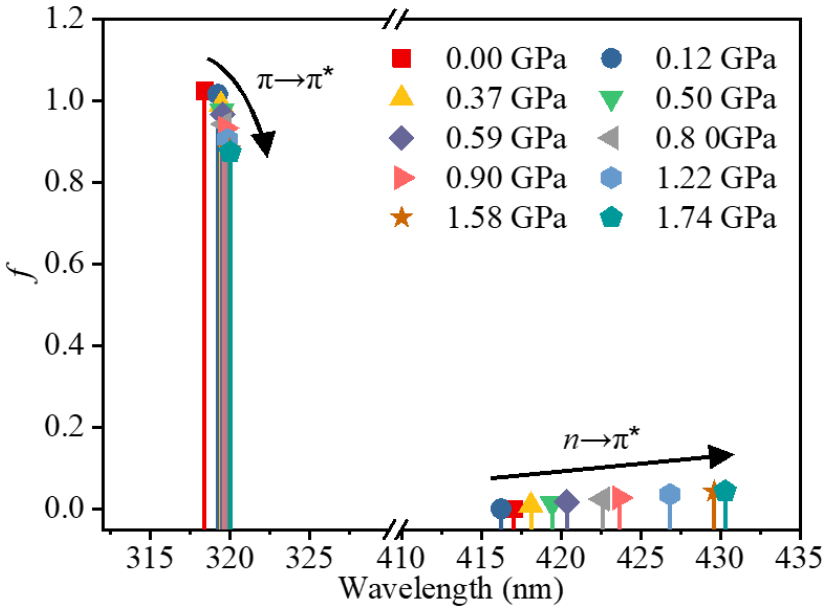

Figure 5.14. The predicted pressure-dependence of the wavelengths and oscillator strengths of the n→π* and π→π* transitions.

Figure 5.15 compares the predicted bathochromic shift in the wavenumber of the n→π* transition, due to the pressure-induced structural distortion, with the experimentally observed pressure-induced shift in red-edge of the UV-vis absorption spectrum. At pressures up to about 0.8 GPa, the magnitudes and the trends of the predicted and observed spectral shifts are similar and there is excellent agreement between them. However, at pressures above 0.8 GPa, the observed and predicted trends deviate significantly. The experimental measurements show that the absorption wavelength becomes essentially constant above 0.8 GPa, suggesting that there is no further bending of the linker structure at higher than this pressure. This suggests that the decrease in unit cell volume above 0.8 GPa cannot be correlated to a decrease in $\boldsymbol{d}_{CO}$.

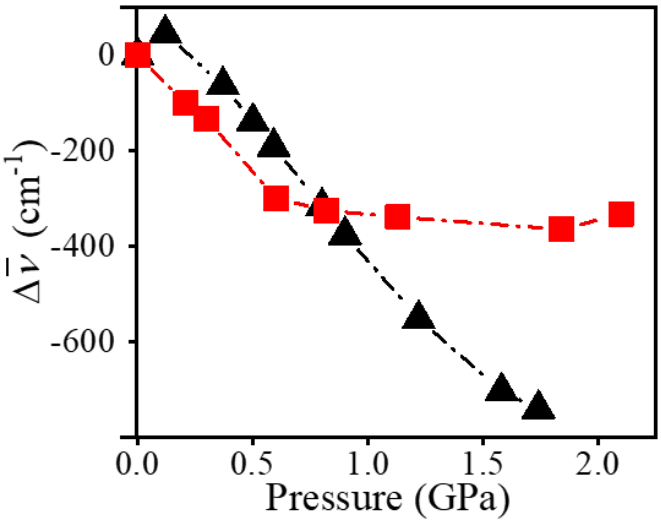

Figure 5.15. Comparison of the observed pressure-induced bathochromic shift in the absorption spectrum red-edge in FC-70 (blue) with the bathochromic shift predicted by TD-DFT for pressure-induced bending of linker geometry (red).

Two explanations can be proposed to account for what happens to the crystal at a pressure above 0.8 GPa. First, at a pressure at ~0.8 GPa, which happens to be slightly higher than the hydrostatic limit of ~0.6 GPa for the FC-70 PTM[18], some parts of the crystals might be crushed and become amorphised, which would not result in an additional bending of the ligand in a uniform manner. Various degrees of the bending of the ligands could result in the observed average UV-vis absorption red-edge remaining at about 553 nm. The second explanation could be that at ~0.8 GPa, the decrease in unit cell volume translates to the shrinkage of the radius of the SBU by ~6%. However, this is unlikely to happen due to a more rigid ionic bond between Zr^{4+} and O^{2-}, as the Zr-O bond length is relatively constant up to 3 GPa.[19]

5.4 Conclusion

High-pressure UV-vis absorption spectral measurements have been successfully carried out for the Zr-abdc MOF using Fluorinert FC-70 or methanol as the PTM. In Fluorinert FC-70, the red-edge of the absorption spectrum, corresponding to the $n\pi^*$ transition of the azobenzene chromophore, was found to be red-shifted up to ~0.8 GPa and then essentially unchanged with increasing pressure. The bathochromic shift was predicted to be caused by the bending of the azobenzene dicarboxylate ligand, as a result of compression of the unit cell volume.

A time-dependent density functional theory (TDDFT) study showed that decrease of the ligand length, $\boldsymbol{d}_{CO}$, and consequent increase in the ligand bending, causes a bathochromic shift in the nπ∗. The magnitude of the predicted pressure-dependent shift is in excellent agreement with that observed experimentally, up to a pressure of ~0.8 GPa. At pressures higher than 0.8 GPa, however, the predicted bathochromic shift deviates from the measurement indicating that shrinkage of the unit cell does not translate into increased ligand bending (on average) at higher pressures.

In methanol, the UV-vis absorption spectrum exhibits a hypsochromic shift at initial pressures (up to 1.5 GPa), as the methanol enters the pores and stabilises the ground-state of the azobenzene chromophore relative to the less polar, nπ* excited state. At pressures above 1.5 GPa, there is negligible shift in the spectrum with increasing pressure, consistent with the incompressibility of the MOF framework, and hence the linker length, in the presence of this interpenetrating PTM.

5.5 References

1. Mahimwalla, Z.; Yager, K. G.; Mamiya, J.; Shishido, A.; Priimagi, A.; Barrett, C. J., *Polym. Bull.* **2012,** *69* (8), 967-1006.
2. Choi, Y. J.; Kim, J. T.; Yoon, W. J.; Kang, D. G.; Park, M.; Kim, D. Y.; Lee, M. H.; Ahn, S. K.; Jeong, K. U., *Acs Macro Lett.* **2018,** *7* (5), 576-581.
3. Pang, X. L.; Lv, J. A.; Zhu, C. Y.; Qi, L.; Yu, Y. L., *Adv. Mater.* **2019,** *31* (52).
4. Bandara, H. M. D.; Burdette, S. C., *Chem. Soc. Rev.* **2012,** *41* (5), 1809-1825.
5. Bahrenburg, J.; Renth, F.; Temps, F.; Plamper, F.; Richtering, W., *Phys. Chem. Chem. Phys.* **2014,** *16* (23), 11549-11554.
6. Jee, A. Y.; Lee, Y.; Lee, M.; Kim, M. H., *J. Chem. Phys.* **2012,** *136* (12).
7. Raj, A. M.; Ramamurthy, V., *Org. Lett.* **2017,** *19* (22), 6116-6119.
8. Otolski, C. J.; Raj, A. M.; Ramamurthy, V.; Elles, C. G., *J. Phys. Chem. Lett.* **2019,** *10* (1), 121-127.
9. Wang, Z. B.; Heinke, L.; Jelic, J.; Cakici, M.; Dommaschk, M.; Maurer, R. J.; Oberhofer, H.; Grosjean, S.; Herges, R.; Brase, S.; Reuter, K.; Woll, C., *Phys. Chem. Chem. Phys.* **2015,** *17* (22), 14582-14587.

10. Schaate, A.; Duhnen, S.; Platz, G.; Lilienthal, S.; Schneider, A. M.; Behrens, P., *Eur. J. Inorg. Chem.* **2012,** (5), 790-796.
11. Hobday, C. L.; Marshall, R. J.; Murphie, C. F.; Sotelo, J.; Richards, T.; Allan, D. R.; Düren, T.; Coudert, F.-X.; Forgan, R. S.; Morrison, C. A.; Moggach, S. A.; Bennett, T. D., *Angew. Chemie. Int. Ed.* **2016,** *128* (7), 2447-2451.
12. Epley, C. C.; Roth, K. L.; Lin, S. Y.; Ahrenholtz, S. R.; Grove, T. Z.; Morris, A. J., *Dalton Trans.* **2017,** *46* (15), 4917-4922.
13. Frisch, M. J.; Trucks, G. W.; Schlegel, H. B.; Scuseria, G. E.; Robb, M. A.; Cheeseman, J. R.; Scalmani, G.; Barone, V.; Petersson, G. A.; Nakatsuji, H.; Li, X.; Caricato, M.; Marenich, A.; Bloino, J.; Janesko, B. G.; Gomperts, R.; Mennucci, B.; Hratchian, H. P.; Ortiz, J. V.; Izmaylov, A. F.; Sonnenberg, J. L.; Williams-Young, D.; Ding, F.; Lipparini, F.; Egidi, F.; Goings, J.; Peng, B.; Petrone, A.; Henderson, T.; Ranasinghe, D.; Zakrzewski, V. G.; Gao, J.; Rega, N.; Zheng, G.; Liang, W.; Hada, M.; Ehara, M.; Toyota, K.; Fukuda, R.; Hasegawa, J.; Ishida, M.; Nakajima, T.; Honda, Y.; Kitao, O.; Nakai, H.; Vreven, T.; Throssell, K.; Montgomery, Jr., J. A.; Peralta, J. E.; Ogliaro, F.; Bearpark, M.; Heyd, J. J.; Brothers, E.; Kudin, K. N.; Staroverov, V. N.; Keith, T.; Kobayashi, R.; Normand, J.; Raghavachari, K.; Rendell, A.; Burant, J. C.; Iyengar, S. S.; Tomasi, J.; Cossi, M.; Millam, J. M.; Klene, M.; Adamo, C.; Cammi, R.; Ochterski, J. W.; Martin, R. L.; Morokuma, K.; Farkas, O.; Foresman, J. B.; and Fox, D. J., *Gaussian 09, Revision A.02,*, Gaussian, Inc.: Wallingford CT, **2016**.
14. Karelson, M.; Zerner, M. C., *J. Am. Chem. Soc.* **1990,** *112* (25), 9405-9406.
15. Park, S. Y.; Ebihara, M.; Kubota, Y.; Funabiki, K.; Matsui, M., *Dyes Pigm.* **2009,** *82* (3), 258-267.
16. Dennington, R.; T. A. K.; Millam, J. M., *GaussView 5.0.8*, Semichem Inc. Shawnee Mission KS: **2008**.
17. Fitz, J.; Mammana, A., *Spectrochim. Acta A.* **2020,** *227*.
18. Varga, T.; Wilkinson, A. P.; Angel, R. J., *Rev. Sci. Instrum.* **2003,** *74* (10), 4564-4566.
19. Kudoh, Y.; Takeda, H.; Arashi, H., *Phys. Chem. Miner.* **1986,** *13* (4), 233-237.

Chapter 6
The Effect of Pressure on Crystal Structures and Optical Spectra of Phenyl-Ring Molecular Rotors, Ph_5C_5H and Ph_7C_7H

6.1 Introduction

A combination of high-pressure single-crystal diffraction, UV-vis absorption and fluorescence emission spectroscopy has been used to study the effect of pressure on the molecular rotor, *sym*-heptaphenylcycloheptatriene (Ph_7C_7H). High-pressure UV-vis absorption and fluorescence emission spectroscopy have also been used to study the effect of pressure on a related molecular rotor, *sym*-pentaphenylcyclopentadiene (Ph_5C_5H). The results reveal the effects of specific intermolecular interactions between the phenyl substituents of these molecular rotors on their optical spectra.

6.1.1 Molecular Rotors

Ph_7C_7H and Ph_5C_5H (**Figure 6.1**) are examples of molecular rotors. A molecular rotor is a fluorescent molecule in which the substituents, typically aromatic, undergo internal rotation that influences the photophysical properties of the molecule. Such molecules are interesting not only from a photophysical perspective but also for their applications as fluorescent probes of the viscosity or temperature of the local molecular environment.[1-3] In a non-viscous environment, the intramolecular rotation can occur freely and facilitates non-radiative deactivation of the excited state. On the other hand, a viscous environment will prevent the intramolecular rotation causing a decline in the rate of non-radiative decay. The suppression of the non-radiative deactivation causes an increase in the fluorescence intensity (quantum yield) and fluorescence lifetime of the molecule.

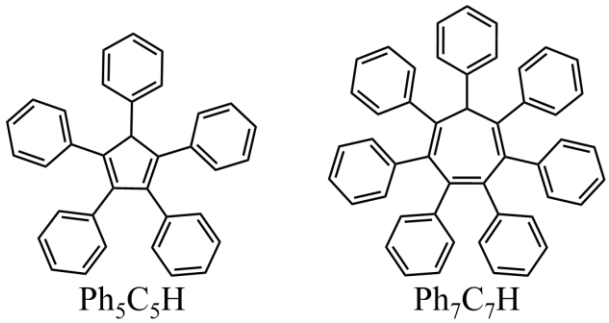

Figure 6.1. The molecular rotors, Ph_5C_5H and Ph_7C_7H.

6.1.2 Aggregated-Induced Emission

The idea of suppressing non-radiative deactivation of the excited state to improve the quantum yield has inspired scientists to design materials with weak fluorescence emission in a solution phase but which exhibit bright emission intensity in the solid phase. This phenomenon, in which the fluorescence intensity increases upon aggregation, is known as aggregation-induced emission (AIE).[4] This is in contrast to aggregation-caused quenching (ACQ) when the aggregation causes a decrease in the quantum yield. ACQ is common in planar luminophores in which the aggregation causes the deactivation of the excited state through non-radiative pathways, with formation of excimers or exciplexes, which commonly involves π-π stacking interaction.[5] The AIE phenomenon is attractive for applications in optoelectronic devices, such as organic light-emitting diodes (OLEDs)[6-8] and optical storage devices.[9]

In 2001, Tang *et al.* reported hexaphenylsilole (HPS), as shown in **Figure 6.2**, a molecule which is non-fluorescent in solution phase but emissive in the aggregated form, and coined the AIE term.[10,11] Another example is tetraphenylsilole (TPS) (**Figure 6.2**), which is a non-fluorescent compound in solution but having about 95% quantum yield in its aggregate form.[12] However, the most widely studied molecules for AIE are based on tetraphenylethene (TPE) (**Figure 6.2**), due to its simple structure and its straightforward synthesis.[13-16] The mechanism of AIE is proposed to be the restriction of intramolecular rotation (RIR), where the rotation of the substituent phenyls is restricted by intermolecular steric hindrance in the aggregated form.[4]

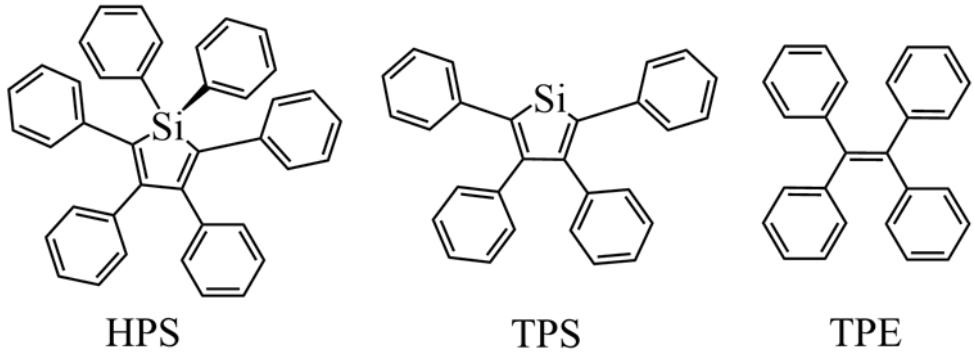

Figure 6.2.The most well-known molecules to exhibit AIE, the HPS and TPE.

The RIR mechanism has led to the design of phenyl-substituted molecules with a larger cyclical core (stator), such as Ph_7C_7H, to accommodate simple aromatic groups (rotor), such as phenyl rings positioned in close proximity which favour nonplanar conformations and hinder the single-bond rotations.[17,18] In the crystal form, the tightly packed phenyl substituents form a network of intermolecular CH-π and π-π interactions which result in fluorescence in the UV-visible region.

6.1.3 The Ph_5C_5H and Ph_7C_7H Molecules

In 2017, Sturala *et al.* reported an investigation of a series of phenyl-ring molecular rotors and the effect of aggregation on their fluorescence properties.[18] Four molecular rotors, *sym*-triphenylcyclotriene (Ph_3C_3H); *sym*-pentaphenylcyclopentadiene (Ph_5C_5H); *sym*-hexaphenylbenzene (Ph_6C_6) and *sym*-heptaphenylcycloheptatriene (Ph_7C_7H), were synthesised and their fluorescence properties were investigated as a function of temperature, concentration, solvent, and in their crystal form. The Ph_3C_3H and Ph_6C_6 molecules are illustrated in **Figure 6.3**.

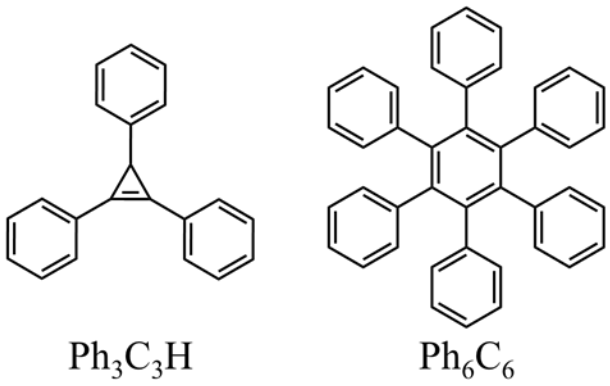

Figure 6.3. The molecular rotors, Ph_3C_3H and Ph_6C_6, that were also investigated by Sturala *et al.* alongside Ph_5C_5H and Ph_7C_7H.[18]

It was reported that upon aggregation, Ph_3C_3H forms a coplanar, stilbene-like conformation, which leads to static quenching. The molecules packed mainly with an edge-to-face arrangement of the phenyl rings, preventing excitonic interaction. In solution phase, the intensity of fluorescence increased with decreasing temperature (inset in **Figure 6.4**), as a result of attenuated internal vibration. However, the fluorescence spectral profile did not change as a function of temperature, indicative of the lack of intra- and intermolecular interactions. The formation of aggregates in solution-phase (in a mixed water/acetonitrile solvent system) did not cause an increase in fluorescence intensity, which is a sign that this molecule does not exhibit the AIE phenomenon.

Ph_6C_6 has the most structural rigidity compared to the other molecules, around both the benzene core and the phenyl substituents, as the internal rotation is prevented by steric hindrance. The temperature-dependent behaviour was similar to that of Ph_3C_3H, the intensity increased with the decreasing temperature (inset in **Figure 6.4**) with no change in the emission profile. On the other hand, the emission intensity increased on aggregation in solution, which is indicative of AIE.

Both Ph_5C_5H and Ph_7C_7H molecules appear to show moderate flexibilities around the single sp^3 centre present in their five- and seven- cyclical core, respectively. For both molecules, the fluorescence intensity increased with decreasing temperature, with the disappearance of peak at a longer wavelength and the emerge of vibronic structures at a shorter wavelength, as shown in **Figure 6.4**. The featured emission at a shorter wavelength at low temperature emerges from the lowest excited state. On the other hand, the presence of a broad emission peak at longer wavelength suggested that an inter-phenyl excimer was present at higher temperature, but ceased to exist at low temperature, especially for Ph_7C_7H. Both molecules also showed AIE in solution.

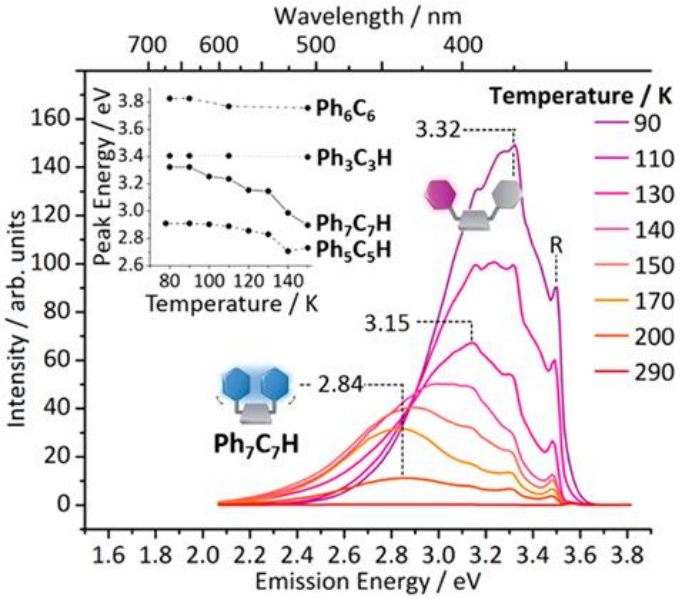

Figure 6.4. Fluorescence spectra of Ph_7C_7H (10μM in 2-MeTHF, λ_{ex}=315 nm) at a range of temperatures. Inset: The emission maxima of Ph_3C_3H, Ph_6C_6, Ph_5C_5H and Ph_7C_7H as a function of temperature. The peak labelled "R" is the Raman scattering from the solvent. This figure is taken from the paper written by Sturala *et al.*[18]

As seen in **Figure 6.5**, the fluorescence spectrum of Ph_5C_5H in the crystal appears at longer wavelength (~460 nm) compared to that in a non-polar solid solution, ZEONEX® (~442 nm) and PMMA (~436 nm), indicating that the molecule forms stronger inter-phenyl interactions in the crystal than in solution. In contrast, Ph_7C_7H shows a fluorescence spectrum at shorter wavelength in the crystal (~406 nm) compared to that in ZEONEX® (~450 nm) and PMMA (~425 nm), indicating that in crystal, the formation of the inter-phenyl interactions is restricted, causing the emission to arise from the locally excited phenyl ring. The crystal of Ph_5C_5H is rather non-crystalline, and this could be the reason why Sturala *et al.* did not measure the crystal structure for Ph_5C_5H and rather use powder diffraction for the characterisation.[18] On the other hand, the crystal of Ph_7C_7H has good crystallinity.

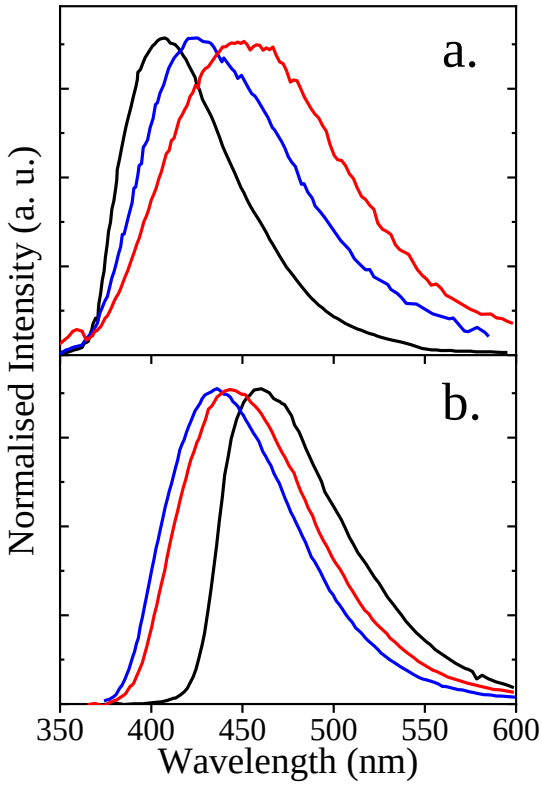

Figure 6.5. The emission spectra of (a) Ph_7C_7H and (b) Ph_5C_5H in crystal phase (black), solid solution in PMMA (blue) and ZEONEX (red). Redrawn from Sturala *et al.*[18]

A TDDFT calculation, conducted in the same study, predicted the change in geometry from the Franck-Condon excited state (ground-state geometry) to the relaxed excited state, for Ph_3C_3H, Ph_5C_5H, Ph_6H_6 and Ph_7C_7H, as depicted in **Figure 6.6**. It was shown that for Ph_7C_7H an intramolecular phenyl-dimer interaction occurs in the relaxed excited, which accounts for the emission at longer wavelength in solution phase, whereas this relaxation will be inhibited in the crystal form and at the low temperature. Sturala *et al.* proposed, therefore, that the change in emission intensity of the Ph_5C_5H and Ph_7C_7H aggregates emerges from the AIE mechanism which occurs as a result of the restriction of the vibration and rotation of the phenyl rings. Moreover, variation in the emission energy arises from the presence of inter-phenyl dimer interaction.

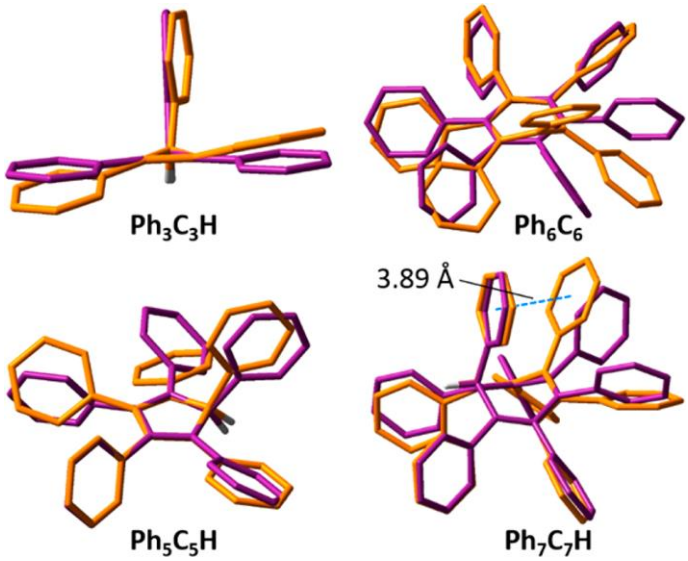

Figure 6.6. The predicted minimum energy geometry for the S_0 state (purple) and the relaxed S_1 state (orange) of molecular rotors. This figure is taken from the paper written by Sturala *et al.*[18]

6.1.4 High-Pressure Studies on Molecular Rotors

Recently, Zhang *et al.* applied pressure-tuning spectroscopy to the study of the molecular rotor sym-tetraphenylcyclopentadiene ($Ph_4C_5H_2$) combined with powder angle-dispersive X-ray Diffraction (ADXRD).[19] The $Ph_4C_5H_2$ has a very similar structure to the Ph_5C_5H, but with a phenyl at the C(sp^3) substituted with hydrogen. Under ambient pressure, the $Ph_4C_5H_2$ exhibited emission with emission maximum of 456 nm. The emission maximum was redshifted by 120 nm up to 19.1 GPa. An increase in the emission intensity could be observed between 1.0–10.3 GPa, while between 0.0–1.0 GPa and 10.3–19.1 GPa, the emission experienced a decrease in intensity. The UV-vis absorption spectra also show redshift of ~200 nm up to 19.1 GPa, larger than of the emission redshift. The increase in the emission intensity is proposed to be caused by a restriction of intramolecular rotation by newly formed C–H···C hydrogen bonds between 1.0–10.3 GPa. Beyond 10.3 GPa, however, the spectra were quenched due to the π-π stacking.

Zhang *et al.* have also done the pressure-tuning spectroscopy to triphenylethylene (TriPE), also combined with ADXRD and Infrared (IR) analysis.[20] At ambient pressure, the emission maximum of the TriPE is found at 432 nm. The emission maximum was redshifted to 440 nm up to 0.8 GPa, with an increase in intensity. Upon further increase of pressure, the emission maximum was redshifted to 485 nm up to

20.4 GPa, followed by decrease in intensity. This phenomenon is hypothesised due to the suppression of the intramolecular motion up to 0.8 GPa by the CH···π and CH···C hydrogen bonds, but quenching takes place at higher pressure. However, the increase in the fluorescence intensity may be due to increase of relative absorbance at the excitation wavelength of 355 nm.

The structural analysis reported by Zhang *et al.* were obtained from powder ADXRD data, modelled with Pawley refinement, which are less reliable than single-crystal X-ray diffraction method. Moreover, detailed method to obtain UV-vis absorption and fluorescence emission spectra were also unclear. In this chapter, however, structural analysis was carried out using crystal structures obtained with single-crystal X-ray diffraction method. Furthermore, measurement of inter-phenyl interaction could be carried out directly, which gives a more accurate result than the ADXRD method.

6.1.5 Inter-phenyl Interactions: The Benzene Dimer

The benzene dimer is an important reference system for understanding the interactions between aromatic rings. It is particularly relevant to the present investigation of phenyl-ring molecular rotors, in which pair-wise inter-phenyl interactions have a strong influence on optical properties. The intermolecular interaction in the non-covalent benzene dimer, in several inter-phenyl arrangements, has been the subject of several computational studies, as discussed by Lee *et al.*[21] The conclusion of these studies is that the benzene dimer exists in two, almost isoenergetic conformations, tilted T-shape (***Bz T***) and parallel, displaced-stacked (***Bz DS***), as shown in **Figure 6.7**. The structural parameters of the dimers, the inter-phenyl centroid distance (***C***), interplanar distance (***P***), lateral displacement distance (***d***) and interplanar angle (∠) and are given in **Table 6.1**. Experimental, spectroscopic studies[22-31] have shown that, in the gas phase, the dimer exists in both T-shaped and displaced-stacked conformations, with the former seeming to be more favoured. In the present work, the ***Bz T*** and ***Bz DS*** structures will be used as a reference for assessing the effective inter-phenyl interactions in both Ph_5C_5H and Ph_7C_7H crystals.

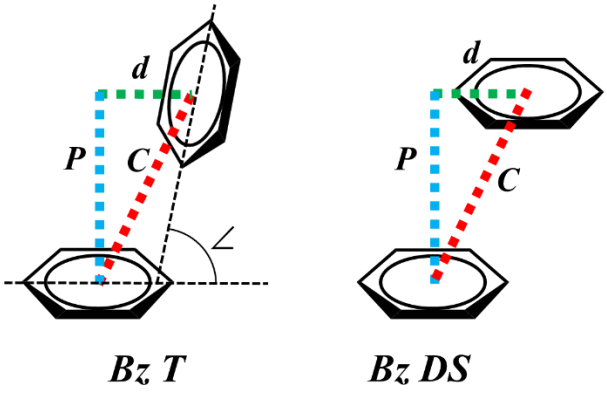

Figure 6.7. Structures of benzene dimer, the T-shaped (*Bz T*) and parallel, displaced-stacked (*Bz DS*) conformations. The structural parameters of the dimers are given as: the inter-phenyl centroid distance (*C*), interplanar distance (*P*), lateral displacement distance (*d*), and interplanar angle (∠).

Table 6.1. The summary of the computed inter-phenyl distances of the benzene dimer in the T-shaped and displaced-stacked arrangement.[21]

Interactions	*C* / Å	*P* / Å	*d* / Å	∠ / °
Bz T	**5.01**	**4.92**	**0.90**	**75.40**
Bz DS	**3.95**	**3.54**	**1.74**	**0**

Benzene exists as a volatile liquid at room temperature and ambient pressure. Both stacked and T-shaped dimers are found in liquid benzene. However, it can form a crystal with orthorhombic structure (*Pbca*) at a pressure of 0.15 GPa. This structure undergoes a phase transformation at 0.91 GPa to monoclinic ($P2_1/c$).[32] The crystallisation of benzene can also be achieved by cooling liquid benzene to 265 K.[33] In the crystalline state nearest neighbours adopt a T-shape dimer geometry, facilitating CH···π interaction, as illustrated in **Figure 6.8**. The T-shaped intermolecular packing is a result of balancing act between minimising the intermolecular repulsion and maximising the molecular packing.[34] In the case of benzene crystal, the T-shaped geometry gives the weakest intermolecular repulsion. The structural difference between benzene I (*Pbca*) and II ($P2_1/c$) crystal forms is the mutual orientation of the two rings, forming the CH···π, contact as illustrated in **Figure 6.8 a** and **b**, respectively. It can also be seen that benzene II has more efficient intermolecular packing, with a smaller void between molecules. This is unsurprising as benzene II is formed at significantly higher pressure. The inter-phenyl distances in the benzene I and benzene II crystals, as illustrated in **Figure 6.8 c** and **d**, respectively, are given in

Table 6.2. It can be seen that the inter-benzene distance of benzene I closely matches the inter-phenyl distance in the isolated ***Bz T*** dimer.[21] The benzene II structure show a considerably shorter inter-phenyl distance and a smaller interplanar angle than ***Bz T***, as a consequence of high pressure.

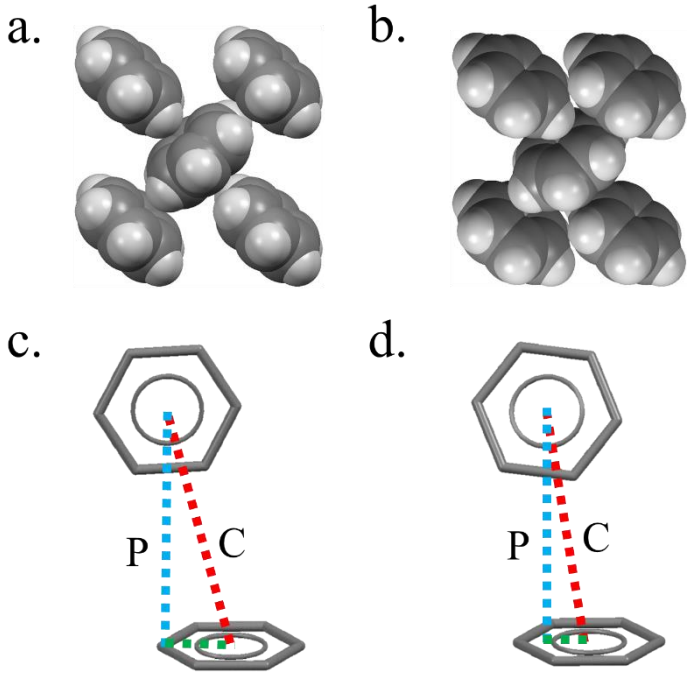

Figure 6.8. The benzene molecules in (a) benzene I and (b) benzene II crystals. The determination of inter-phenyl distances (*C*, *P*, and *d*) of (a) benzene I and (b) benzene II. The *d* distance is shown in green dashed line. Colour scheme: C – grey, H – white.

Table 6.2. The summary of the inter-phenyl distance in benzene I and benzene II crystal.

Crystals	Space group	*C* / Å	*P* / Å	*d* / Å	∠ / °
Benzene I [32]	*Pbca*	5.053	4.926	1.126	82.73
Benzene I [33]	*Pbca*	5.092	4.934	1.259	85.64
Benzene II [32]	$P2_1/c$	4.711	4.621	0.916	62.07

6.1.6 Excimer Formation

The benzene excimer is the simplest form of aromatic excimer and is observed in the gas phase, neat liquid and solutions.[35] As has been explained in **Chapter 2**, an excimer is formed from the interaction of an excited aromatic molecule with another aromatic molecule in the ground state. The fluorescence spectrum of the benzene excimer is

observed as broad and structureless peak at ~320 nm, which becomes more prominent at higher concentration.[36] The binding energy of the benzene excimer is ~33 kJ/mol, whereas the binding energy of the benzene dimer in the ground state is as low as ~10 kJ/mol.[37,38] Investigation of excimer formation by a linked benzene dimer in which the two benzenes were joined by $(CH_2)_4$ links, with interplanar distance of 3.73 Å, revealed that the distance between two benzenes shortened to 3.3 Å upon excitation, which accounts for ~0.4 Å decrease in inter-benzene distance on excimer formation.[39] In order for the benzene excimer to form, a parallel arrangement of the two benzene rings has to be fulfilled. However, in the ground state, the most favourable structure of the dimer is T-shaped, so that a structural reorganisation is required to form the benzene excimer. In the gas phase, the structural reorganisation can occur in the time scale of ~18 ps.[40] In liquid benzene, the formation of the excimer can happen as fast as ~2 ps, immediately after excitation, due to the readily available sandwich and displaced-stacked dimer with interplanar distance of 3.5–4.9 Å, precursors for the excimer formation.[35] In solid benzene, however, the closest neighbours form a T-shaped arrangement with crowded molecular packing, which is not favourable for excimer formation.

Although benzene is the simplest molecule to exhibit excimer formation, pyrene was the first molecule observed to form an excimer, with the first spectra reported by Förster in 1955.[41] Pyrene shows evidence of excimer fluorescence in cyclohexane, at a high concentration, at around 480 nm, as shown in **Figure 6.9**.[42] At lower concentration (10^{-4} M), the broad and structureless peak of the excimer disappears, while the structured peaks at shorter wavelength remain, which are the intrinsic molecular fluorescence.

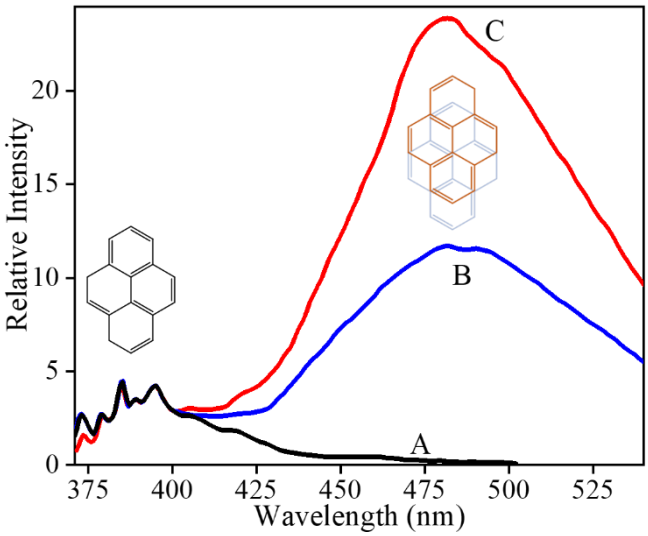

Figure 6.9. Fluorescence spectra of pyrene solutions in cyclohexane. Intensities normalised to a common value at 385 nm. A, 10^{-4} M; B, 5.5 x 10^{-3} M and C, 10^{-2} M. Figure is adapted after Birks and Christophorou.[42]

The pyrene crystal is dimeric in structure, with a displaced-stacked arrangement in the crystal lattice with interplanar distance in the ground state being 3.53 Å. The crystal absorption spectrum is structured, and it corresponds to the Franck-Condon excitation of individual molecules. In the pyrene crystal, the molecular separation is within the range of the attractive excimer interaction. Therefore, following excitation, the excimer is formed rapidly (<ns) between the excited molecule and its unexcited parallel neighbour, with a shortening of the interplanar distance by ~0.5 Å.

In a recent study by Pensack *et al.* using femtosecond transient absorption spectroscopy on a pyrene nanocrystal suspension, it was found that the excimer formation occurs in three steps, as shown in **Figure 6.10**.[43] First, absorption of light results in a vertical excitation of the molecular exciton to the Franck-Condon state. The vertical excitation also results in an excimer interaction force that drives intermolecular geometry changes, in both interplanar and lateral displacement distances, creating the intermediate excimer exciton, in ~4 ps time scale. The intermolecular geometry changes cause the electronic structure of the system to change. The last step is the excimer relaxation, which occurs in a time scale of ~17 ps. The excimer fluorescence then could be observed from the relaxed excimer structure.

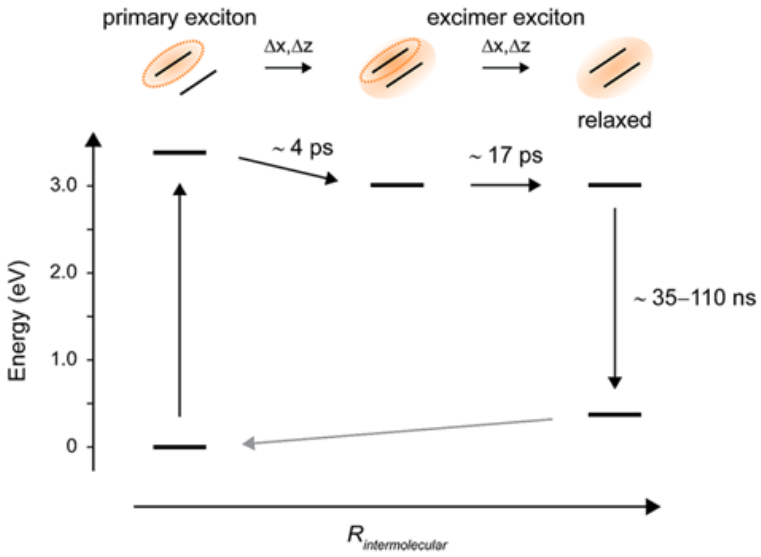

Figure 6.10. Schematic representation of excimer formation. Figure was taken from Pensack *et al.*[43]

In this chapter, combined measurements of single-crystal X-ray diffraction, UV-vis absorption and fluorescence emission spectroscopy were carried out on the Ph_7C_7H crystal to understand the relationship between the pressure-induced changes in the crystal structure and the electronic spectra. The optimised structures of the two benzene dimer conformations, ***Bz T*** and ***Bz DS***,[21] were used as reference for the inter-phenyl interactions found in Ph_7C_7H and Ph_5C_5H crystal structures. The study of pressure-dependent UV-visible absorption and fluorescence emission was also carried out to investigate the effect of pressure spectra on the Ph_5C_5H crystal as a comparison to the Ph_7C_7H, although only the ambient-pressure structure is available for the former. These two molecules were chosen as examples of phenyl-ring molecular rotors because of their distinct intermolecular interactions in the crystal and their intense fluorescence emission in the wavelength range that can be observed using the custom-built measurement setup.

6.2 Experimental

It should be noted that the synthesis and crystallisation of sym-heptaphenylcycloheptatriene (Ph_7C_7H) were carried out by Dr Paul McGonigal and co-workers (Durham University) as reported by Sturala et al.[18] The high-pressure X-ray diffraction data of Ph_7C_7H were collected in collaboration with Ms Gemma Turner and Dr Stephen Moggach of the University of Western Australia. The crystal structure of Ph_7C_7H at ambient pressure was collected and

solved by Ms Turner, and the crystal structures at high pressure were solved and refined by the author.

6.2.1 Synthesis

The *sym*-pentaphenylcyclopentadiene (Ph_5C_5H) were purchased from Sigma-Aldrich and purified by recrystallisation. The synthesis of *sym*-heptaphenylcycloheptatriene (Ph_7C_7H) was carried out in two steps, as reported by Sturala *et al*.[18] First is the synthesis of *sym*-triphenylcyclopropene (Ph_3C_3H), followed by the synthesis of the Ph_7C_7H.

Ph_3C_3H: diphenylacetylene (18.5 g, 104 mmol) and potassium tert-butoxide (KO^tBu, 35 g, 312 mmol) were placed in a dried 500 mL flask under N_2 atmosphere. Dry benzene (200 mL) was added ad the mixture was stirred. α,α-Dichlorotoluene (25 g, 155 mmol) was added to the reaction mixture uniformly for 30 min using a syringe pump. The mixture then heated to reflux for 3 h at 80 °C and were let to cool down. H_2O (200 mL) was added to dissolve the inorganic salts, then the layers were separated, and the aqueous layer was extracted with Et_2O (2 × 200 mL). The extract was combined with the benzene layer and dried over $MgSO_4$; the solvent removed under reduced pressure to give an orange powder. The powder then dissolved in a mixture of 2:1 Et_2O-CH_2Cl_2 (200mL) and then sparged with gaseous HCl, forming a colourless precipitate. The solid was dried under vacuum to yield $Ph_3C_3{\cdot}HCl_2$. The $Ph_3C_3{\cdot}HCl_2$ (18.6 g, 61.4 mmol) was then added to NaBH (9.3 g, 246 mmol) in ethanol (460). The mixture was stirred overnight at RT. The reaction was quenched with H_2O (500 mL) then extracted with Et_2O (3 × 200 mL). The organic layer was washed with H_2O (500 mL) and brine (500 mL) and then dried over $MgSO_4$, and the solvent was dried to give colourless Ph_3C_3H. The Ph_3C_3H was purified by recrystallisation in MeCN to form colourless crystals.

Ph_7C_7H: the Ph_3C_3H (1.2 g, 4.47 mmol), tetraphenylcyclopentadienone (1.79 g, 4.47 mmol) mixed with *p*-xylene (13.5 mL) in a sealed 20 mL microwave vial. The mixture was deoxygenated in N_2 gas, then stirred for 36 h at 140 °C in a microwave reactor. Upon cooling to RT, a crystalline solid formed then isolated using filtration through glass funnel, washed with Et_2O (3 × 10 mL). The solid was dried under vacuum to yield Ph_7C_7H, then purified by recrystallisation to form colourless crystals.

6.2.2 X-ray Crystallography of Ph_7C_7H

The structure at ambient pressure and room temperature were obtained on a Gemini R Ultra diffractometer using Mo Kα (λ = 0.7107 Å) radiation and integrated without rejection of the diamond shading. The data were indexed and integrated using CrysAlis PRO.[44] The crystal structure was solved using SHELXT[45] algorithm, and the refinements were carried out in Olex2 program.[46] The atoms in the structure were numbered and labelled using CRYSTALS.[47] The structure was refined isotropically against F^2. All 1,2 and 1,3 distances were restrained to ensure the aromatic geometry of the phenyl rings were not distorted. Vibrational and thermal similarity restraints were also applied to the carbon atoms. Hydrogen atoms were placed geometrically and constrained to ride on their host carbon atoms. The structure at ambient pressure was used as a template for the structure at the higher pressures.

For the high-pressure measurement, a single crystal of C_7Ph_7H was measured in a diamond anvil cell (DAC) with Daphne oil 7373 (Idemitsu Kosan Co., Ltd.) as a pressure transmitting medium, using synchrotron radiation as explained in **Chapter 3**. The crystal structures were refined isotropically against F^2 in Olex2[46] program with starting structure from the ambient pressure structure. All 1,2 and 1,3 distances were also restrained. Vibrational and thermal similarity restraints were applied, and the hydrogen atoms were added geometrically to ride the corresponding carbon atoms. Structure refinements were carried out to the maximum resolution of each sample as determined from the intensity statistics.

The inter-phenyl distances in the refined structures were identified as inter-centroid distance (***C***), centroid-to-plane distance (***P***) and inter-plane angle (∠), and were measured using a *Measure Distance* routine in Mercury.[48] The lateral displacement distance (***d***) was calculated using **Equation 6.1**.

$$\boldsymbol{d} = \boldsymbol{C} \sin\left(\cos^{-1}\frac{\boldsymbol{P}}{\boldsymbol{C}}\right)$$

Equation 6.1

6.2.3 High-pressure UV-Vis Absorption Spectroscopy

The high-pressure UV-vis absorption spectra of Ph_5C_5H and Ph_7C_7H were collected using a DAC with Daphne 7373 as hydrostatic medium, using the bespoke

measurement setup, as described in **Chapter 3**. The absorption spectra were measured at pressures up to 3.95 GPa and 3.03 GPa, for Ph_5C_5H and Ph_7C_7H, respectively.

The UV-vis absorption spectra of Ph_7C_7H were collected from a thin crystal (~10 μm). The crystal was colourless and transparent, making the absorption spectra collection easier than of Ph_5C_5H. However, the absorption spectra measurement can only be carried out from ~350 nm due to strong diamond absorption at a wavelength shorter than 350 nm. This does not discount the importance of measurements as the change (or shift) of the spectra can still be observed.

6.2.4 High-pressure Fluorescence Emission Spectroscopy

The high-pressure fluorescence emission spectra of Ph_5C_5H and Ph_7C_7H were collected using a DAC with Daphne 7373 as hydrostatic medium, using the bespoke measurement setup described in **Chapter 3**. A single wavelength Ocean Optics LS-LED 365 nm was used as the excitation light source. A band-pass filter (Semrock Brightline 370/36) was inserted in the excitation path to narrow the excitation bandwidth. The fluorescence emission spectra were collected at pressures that closely matched those used for the UV-vis absorption spectra. A correction for diamond absorption was applied for the Ph_7C_7H spectra, as the fluorescence peak coincides with a strong diamond absorption.

6.3 Results and Discussions

6.3.1 Effect of Pressure on Ph_5C_5H

6.3.1.1 Molecular Structure and Inter-phenyl Distances at Ambient Pressure

The Ph_5C_5H crystal structure from the Cambridge Crystallographic Database (Reference code: KUKDEZ)[49] was used for the measurement of the inter-phenyl distance, as this crystal structure has the same structure as that obtained, and used for structural analysis by Sturala *et al.*[18] The crystal was measured at room temperature and is crystallised in a monoclinic system with $P2_1/c$ space group (a = 15.954(4) Å, b = 6.267(1) Å, c = 24.517(8) Å, β = 93.94(2)°, V = 2445.51(108) Å3, Z = 4). **Figure 6.11** shows inter-phenyl interactions in Ph_5C_5H lattice at ambient pressure and temperature. The phenyl rings were numbered as Ph^1, Ph^2, Ph^3, Ph^4 and Ph^5, and the inter-phenyl interactions were also identified.

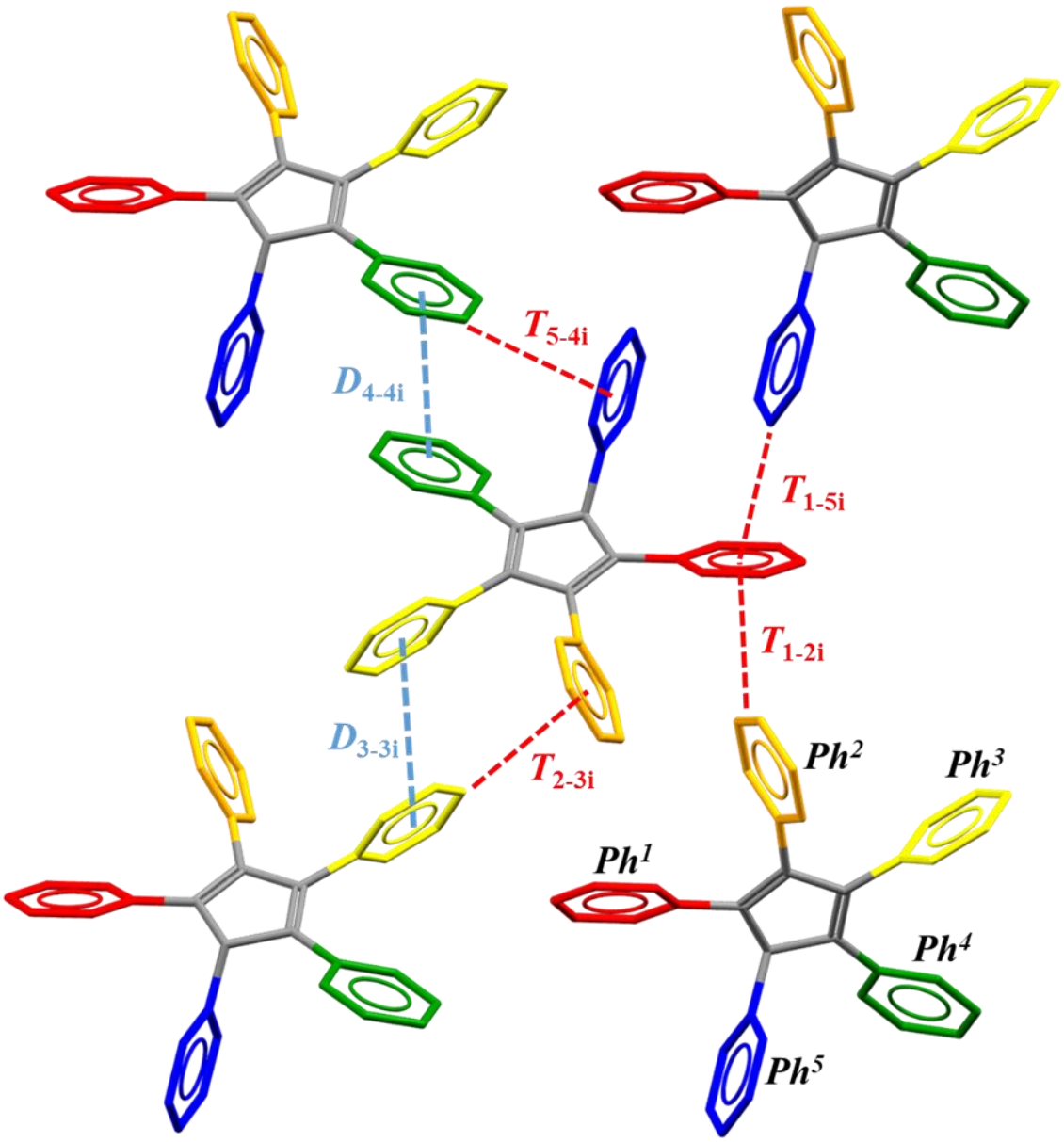

Figure 6.11. Crystal structure of Ph_5C_5H at ambient pressure and room temperature. Ph^1, Ph^2, Ph^3, Ph^4 and Ph^5, are depicted in red, orange, yellow, green and blue. The displaced-stacked inter-phenyl interaction (DS) is illustrated in the blue dashed line. The T shaped inter-phenyl interactions (*T*) are depicted as the red dashed line. The first number indicates the phenyl that makes up the top bar of the T; the letter i indicates an intermolecular interaction. Hydrogens were omitted for clarity.

The inter-phenyl centroid distance (***C***), centroid-to-plane distance (***P***) and inter-plane angle (∠) were measured and the lateral displacement distance (***d***) was calculated. From the inter-phenyl distances measurements, it was found that the Ph_5C_5H has no inter-phenyl interactions within the molecule, as the phenyls are spaced outwards from the centre of the molecule with ~70° angle between them. However, it was found that

all the phenyl groups are involved in intermolecular interactions, both in displaced-stacked (***D***) and T-shaped forms, as shown in **Figure 6.11**. At ambient pressure, two displaced-stacked dimer interactions were identified, between phenyls Ph^4-Ph^4 and Ph^3-Ph^3, denoted as $\boldsymbol{D_{4\text{-}4i}}$ and $\boldsymbol{D_{3\text{-}3i}}$, respectively, as depicted in **Figure 6.12**. The inter-phenyl parameters, as defined in **Figure 6.12** are listed in **Table 6.3**. The $\boldsymbol{D_{4\text{-}4i}}$ parameters are essentially identical to those of ***Bz DS***, and indicate that even at ambient pressure, a stable displaced-stacked dimer arrangement is found in the crystal.

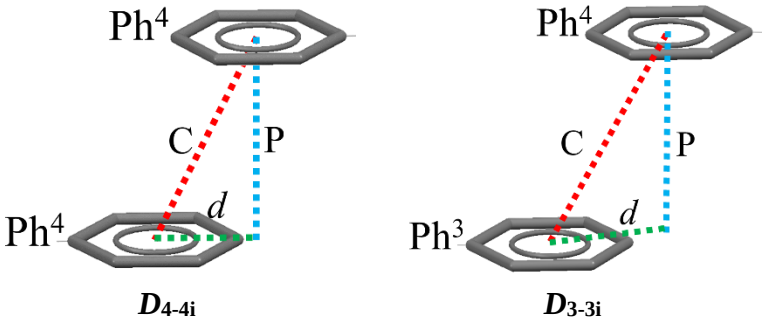

Figure 6.12. The intramolecular distance of the $D_{4\text{-}4i}$ and $D_{3\text{-}3i}$, consisted of *C*, *P* and *d* distances.

Table 6.3. The displaced-stacked intermolecular distances (*C*, *P* and *d*) and angle (∠) found in Ph_5C_5H. The parameters are compared to those of the displaced-stacked benzene dimer (*Bz DS*).

Interactions	*C* / Å	*P* / Å	*d* / Å	∠ / °
$\boldsymbol{D_{4\text{-}4i}}$	3.978	3.585	1.724	*0*
$\boldsymbol{D_{3\text{-}3i}}$	4.326	3.710	2.225	*0*
Bz DS	***3.95***	***3.54***	***1.74***	***0***

In addition to the displaced-stacked interactions, four significant T-shaped intermolecular phenyl interactions were also found between Ph^5-Ph^4, Ph^1-Ph^5, Ph^2-Ph^3 and Ph^1-Ph^2, identified as $\boldsymbol{T_{5\text{-}4i}}$, $\boldsymbol{T_{1\text{-}5i}}$, $\boldsymbol{T_{2\text{-}3i}}$ and $\boldsymbol{T_{1\text{-}2i}}$, respectively. The inter-phenyl distances, as shown in **Figure 6.13**, are listed in **Table 6.4**. Almost all T-shaped interactions closely resemble the ***Bz T*** structure. Moreover, $\boldsymbol{T_{1\text{-}2i}}$ has considerably shorter intermolecular phenyl distance than the ***Bz T***. Thus, it is evident that both displaced-stacked and T-shaped dimer interactions are present at ambient pressure.

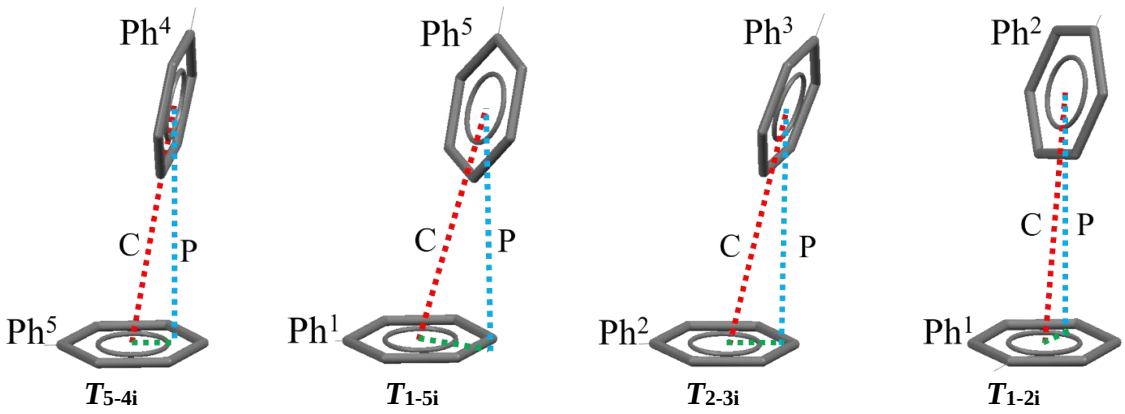

Figure 6.13. The intramolecular distance of the $T_{5\text{-}4i}$, $T_{1\text{-}5i}$, $T_{2\text{-}3i}$, and $T_{1\text{-}2i}$, consisted of *C* (red dashed line), *P* (blue dashed line) and *d* (green dashed line) distances.

Table 6.4. The T-shaped intermolecular distances (*C*, *P* and *d*) and angle (∠) found in Ph_5C_5H. The parameters are compared to those of the T-shaped benzene dimer (*Bz T*).

Interactions	*C* / Å	*P* / Å	*d* / Å	∠ / °
$T_{5\text{-}4i}$	5.079	4.997	0.909	81.43
$T_{1\text{-}5i}$	5.076	4.885	1.379	67.78
$T_{2\text{-}3i}$	5.043	4.901	1.188	76.69
$T_{1\text{-}2i}$	4.918	4.884	0.577	72.85
Bz T	***5.01***	***4.92***	***0.90***	***75.40***

6.3.1.2 UV-Vis Absorption Spectra

The UV-vis absorption spectra were collected at 0.00 GPa, 0.22 GPa, 0.55 GPa, 0.93 GPa, 1.26 GPa, 1.71 GPa, 2 GPa, 2.56 GPa, 3.37 GPa and 3.95 GPa, as shown in **Figure 6.14**. The absorption spectrum red-ssedge, obtained from half-maximum of the intensity, is used to quantify the spectral shift as function of pressure, due to the absence of the peak (saturation of absorption). The wavelength and wavenumber of the absorption red-edge (half-maximum intensity) as a function of pressure are given in **Table 6.5**. The red-edge of the 0 GPa absorption spectrum (408 nm) is considerably redshifted (> 2000 cm^{-1}) relative to that of the solution-phase spectrum (375 nm)[18], as a result of the dimer-like intermolecular phenyl interactions in the crystal. The absorption spectra show a bathochromic shift with increasing pressure, from 408 nm

(24530 cm^{-1}) at 0 GPa to 434 nm (23070 cm^{-1}) at 3.95 GPa, a 1460 cm^{-1} shift. This suggests that intermolecular interactions in the crystal become increasingly shorter with increasing pressure.

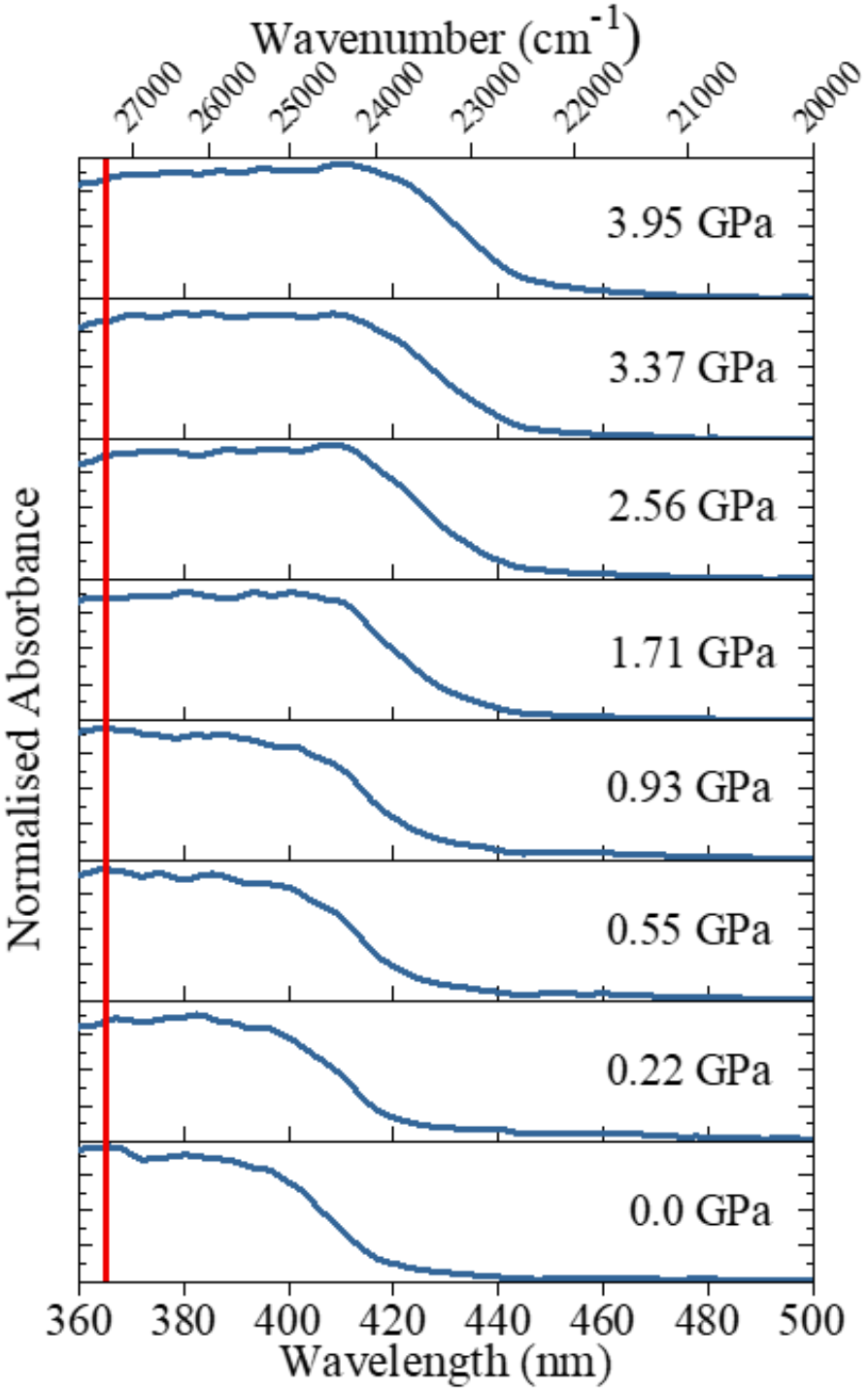

Figure 6.14. Absorption spectra of Ph_5C_5H at various pressure. The red line represents the excitation wavelength (365 nm) that was used for the fluorescence emission spectroscopy.

Table 6.5. Wavenumber and wavelength of absorption red-edge (half-maximum) as a function of pressure.

Pressure / GPa	Absorption Edge / nm	Absorption Edge / cm^{-1}
0.00	408	24530
0.22	411	24360
0.55	414	24180
0.93	415	24100
1.26	418	23920
1.71	422	23720
2.00	425	23560
2.56	427	23420
3.37	429	23340
3.95	434	23070

6.3.1.3 Fluorescence Spectra

Fluorescence emission spectra were measured at the 0.00 GPa, 0.25 GPa, 0.44 GPa, 1.02 GPa, 1.26 GPa, 1.57 GPa, 2.29 GPa, 2.62 GPa, 3.53 GPa and 3.95 GPa. These pressures were chosen to match the pressure from the UV-vis absorption measurement closely. The fluorescence spectra are depicted in **Figure 6.15**. The fluorescence maxima as a function of pressure are listed in **Table 6.6**. The fluorescence spectrum maximum is redshifted with increasing pressure, from 464 nm (21420 cm^{-1}) at 0 GPa to 489 nm (20160 cm^{-1}) at 3.95 GPa, a shift of 1260 cm^{-1}.

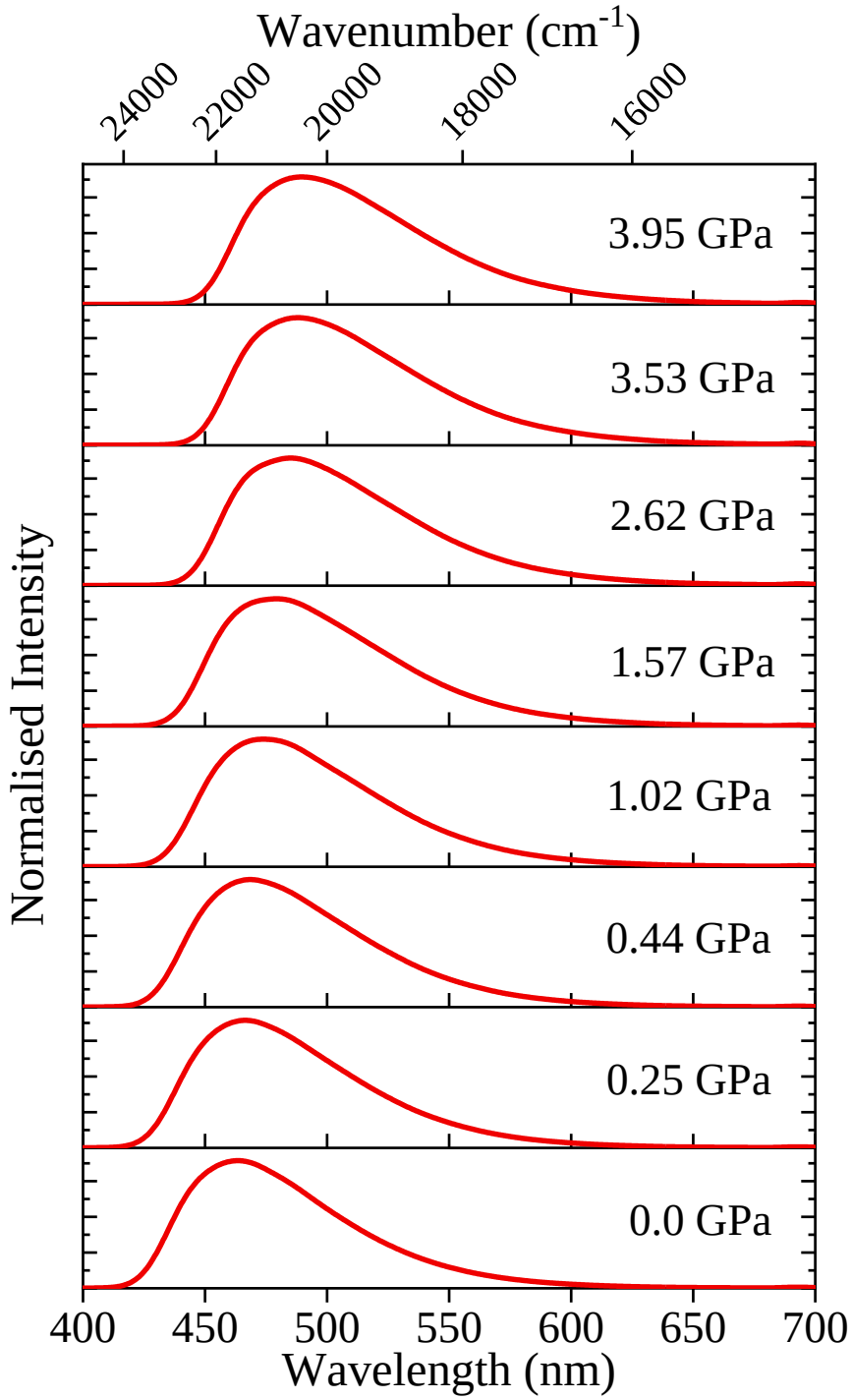

Figure 6.15. Fluorescence emission spectra of Ph_5C_5H at various pressure (λ_{ex} = 365 nm).

Table 6.6. Wavenumber and wavelength of fluorescence maximum as a function of pressure.

Pressure / GPa	Emission Maximum / nm	Emission Maximum / cm^{-1}
0.00	464	21420
0.25	466	21270
0.44	469	21130
1.02	474	20860
1.26	479	20770
1.57	480	20760
2.29	483	20560
2.62	486	20480
3.53	488	20280
3.95	489	20160

The UV-vis absorption red-edge and the fluorescence peak shift as a function of pressure are illustrated in **Figure 6.16**. It appears that there is a significant Stokes shift (~3100 cm^{-1}) between the absorption red-edge and the fluorescence maximum at 0 GPa, indicating a significant structural relaxation in the excited state. This can be attributed to excimer formation, where relaxation occurs to a more parallel closely stacked excited-state structure that resembles a benzene excimer which has a parallel stacked structure with an interplanar distance of ~3.3 Å. Unlike crystalline benzene, in the Ph_5C_5H crystal, displaced stacked arrangements (***D*****$_{4\text{-}4i}$** and ***D*****$_{3\text{-}3i}$**) are readily available as precursors for excimer formation. Excimer formation would require a decrease in interplanar distance of ~0.4 Å from the Franck-Condon geometry, and a similar structural relaxation has been observed to occur on the picosecond timescale in crystalline pyrene, as discussed in section **6.1.6**.

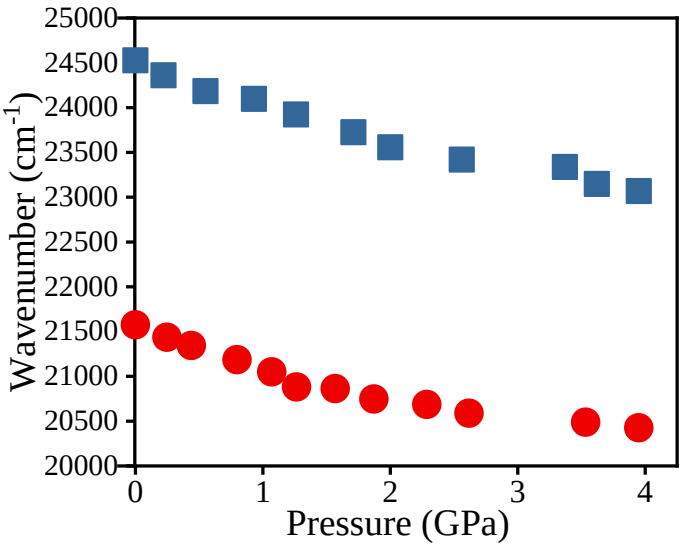

Figure 6.16. The summary of the UV-Vis absorption red-edge (blue rectangles) and the fluorescence emission maxima (red circles) of the Ph_5C_5H as a function of pressure.

The UV-vis absorption red-edge and the fluorescence emission spectrum maxima are redshifted proportionately with increasing pressure, with only a slight decrease in Stokes shift, by ~200 cm^{-1} at 3.95 GPa. This suggests that with increasing pressure, the geometry of the Franck-Condon state becomes slightly more similar to the geometry of the relaxed, emitting state.

6.3.2 Effect of pressure on Ph_7C_7H

6.3.2.1 High-Pressure Crystallography

The crystal structure reported in the Cambridge Crystallographic Database (Reference code: YOSWOS)[49] was measured at room temperature and is crystallised in a triclinic system with $P\bar{1}$ space group (a = 9.832(1) Å, b = 10.026(1) Å, c = 19.166(2) Å, α = 92.194(1)°, β = 90.57(1)°, γ = 108.94(1)°, V = 1785.20(33) Å3, Z = 2).[18] The crystal structures obtained in this chapter were also formed with the same crystal system and space group. The unit cell contents of Ph_7C_7H crystal is shown in **Figure 6.17**. The ambient pressure structure obtained from this work shows a good agreement with that from literature, but there is an increase in unit cell volume at 0.12 GPa, which is not expected to occur since the Ph_7C_7H crystal is non-porous and the PTM that was used is non-penetrating medium. At the time of writing of this chapter, the reason for the apparent increase in the unit cell volume at initial pressure has not been determined but may be due to a systematic error in the high-pressure crystallographic data obtained

from the measurement at synchrotron. However, this does not change the narrative regarding pressure-induced changes in the structure and their relation to the optical spectra. The crystal structure was refined using isotropic thermal parameters against F^2. Refinement using anisotropic displacement parameters caused the ellipsoid elongated in one direction, which could indicate the lack of data completeness in one of the axis directions. This is not surprising for a triclinic crystal system which has low symmetry ($P\bar{1}$) and is exacerbated by the shading of the DAC.

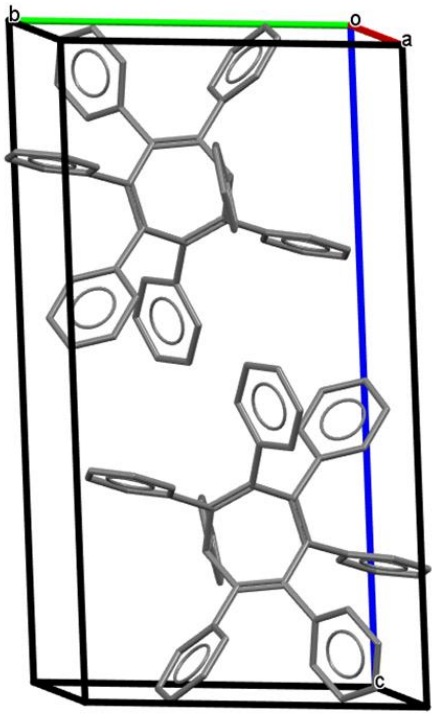

Figure 6.17. One unit cell snapshot of Ph_7C_7H within triclinic $P\bar{1}$ space group with Z=2. Two molecules per unit cell. Hydrogen atoms were omitted for clarity.

The crystal structures were obtained up to 3.39 GPa, and the unit cell volume decreased by 20% as illustrated in **Figure 6.18 a**. The unit cell parameters of the crystal at various pressure are listed in **Table 6.7**. It also can be seen from **Figure 6.18 b** that the unit cell parameters experienced anisotropic compression, with the *b*-axis decreased by ~8.3%, while *a* and *c* axes decreased by only ~5%. This pressure-induced anisotropic contraction is common in organic crystals with low symmetry and is caused by the shortening of the distance of the least repulsive interactions.[50]

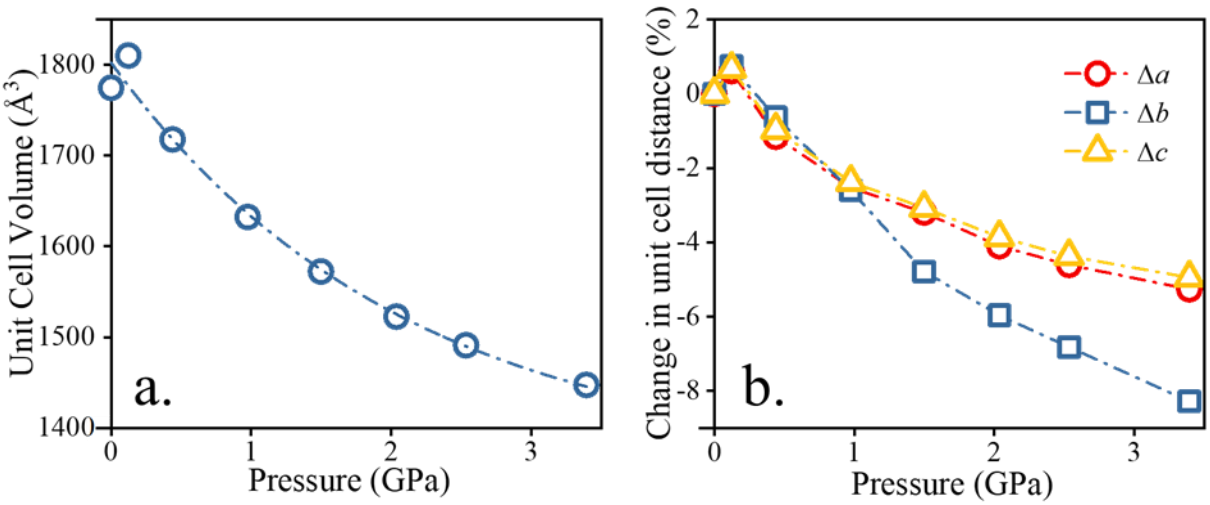

Figure 6.18. (a) Unit Cell Volume of Ph_7C_7H as a function of pressure. (Crystal structure could only be solved up to 3.4 GPa). (b)The change in unit cell dimension (%) as a function of pressure, along each axis.

Table 6.7. The summary of the unit cell parameters of the Ph_7C_7H crystal in various pressure.

Pressure / GPa	*a* / Å	*b* / Å	*c* / Å	α / °	β / °	γ / °	V / Å^3
Ambient	9.8130(20)	10.008(2)	19.126(4)	87.84(3)	90.56(3)	71.03(3)	1774.58(5)
0.12	9.8731(12)	10.0827(18)	19.2541(19)	87.770(14)	90.555(9)	70.978(16)	1810.2(5)
0.44	9.6994(13)	9.9444(16)	18.9410(20)	87.411(15)	90.594(10)	70.311(16)	1717.8(4)
0.98	9.5654(12)	9.7482(15)	18.6720(20)	86.645(15)	90.144(10)	69.954(16)	1632.3(4)
1.50	9.4996(10)	9.5292(13)	18.5388(17)	85.491(12)	89.348(8)	70.036(13)	1572.3(3)
2.04	9.4105(9)	9.4113(13)	18.3881(16)	84.854(11)	88.795(8)	69.860(13)	1522.7(3)
2.53	9.3610(8)	9.3258(12)	18.2905(14)	84.538(10)	88.427(7)	69.729(11)	1491.0(3)
3.39	9.2968(12)	9.1796(15)	18.180(2)	84.056(14)	88.039(1)	69.702(16)	1447.3(4)

6.3.2.2 Molecular Structure and Inter-phenyl Distances

6.3.2.2.1 Intramolecular Inter-Phenyl Interaction

In contrast to Ph_5C_5H, an intramolecular phenyl interaction can be identified between Ph^7 and Ph^3, this resembles a T-shaped dimer, and is labelled as $\boldsymbol{T_{7\text{-}3}}$, as shown in **Figure 6.19**. The inter-centroid distance (***C***), interplanar distance (***P***), displacement distance (***d***) and interplanar angle (∠) are listed in **Table 6.8**. Intramolecular interaction between two phenyl rings linked by aliphatic chains separated by three carbon atoms, like this Ph^7-Ph^3 interaction, is well known to exist.[51] In Ph_5C_5H,

however, two phenyl rings can only be separated by a maximum of 2 carbon atoms. Therefore, there is no intramolecular interaction in Ph_5C_5H.

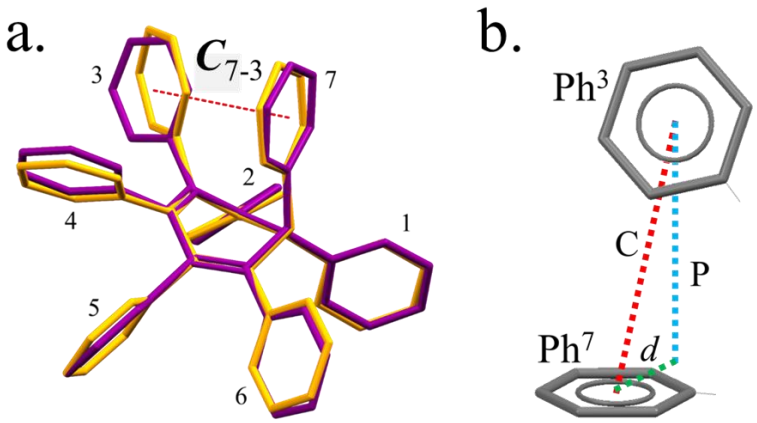

Figure 6.19. (a) Comparison of molecular structures of Ph_7C_7H at 0.12 GPa (purple) and 3.4 GPa (orange). The phenyl rings are numbered as shown. The intramolecular inter-centroid distance (*C*) between Ph^7 and Ph^3, $C_{7\text{-}3}$, is indicated. (b) The intramolecular phenyl distances of $T_{7\text{-}3}$.

Table 6.8. The T-shaped inter-phenyl distances (*C*, *P* and *d*) and angle (∠) of the $T_{7\text{-}3}$ in various pressure. The parameters are compared to those of the T-shaped (*Bz T*) and the displaced-stacked (*Bz DS*) benzene dimers.

Pressure / GPa	$C_{7\text{-}3}$ / Å	$P_{7\text{-}3}$ / Å	$d_{7\text{-}3}$ / Å	$\angle_{7\text{-}3}$ / °
Ambient	5.136	4.726	2.010	68.68
0.12	5.118	4.670	2.094	67.67
0.44	5.035	4.611	2.022	66.98
0.98	4.860	4.466	1.917	62.13
1.50	4.729	4.289	1.992	53.49
2.04	4.698	4.227	2.050	51.01
2.53	4.673	4.183	2.083	49.65
3.39	4.639	4.092	2.185	47.14
Bz T	***5.01***	***4.92***	***0.90***	***75.40***
Bz DS	***3.95***	***3.54***	***1.74***	***0***

It can be seen from **Table 6.8** that although the $T_{7\text{-}3}$ interplanar distance (***P***) is similar to that of ***Bz T,*** the lateral displacement is much greater. Moreover, the lateral displacement distance (***d***) is essentially unchanged with increasing pressure. This

could be caused by the restriction of the phenyl lateral movement by the rigid main cycloheptatriene core. With increasing pressure, the interplanar angle of $\boldsymbol{T_{7\text{-}3}}$ decreases, deviating more from the ***Bz T*** structure. Although the rings become more parallel with increasing pressure, the structure remains significantly different from that of ***Bz DS*****.**

According to the TDDFT calculation of Sturala *et al.*[18], the relaxed excited state structure (see **Figure 6.6**), shows a reorientation of the Ph^3 and Ph^7 to give ***C***, ***P***, ***d*** and ∠ parameters decreased to 3.96 Å, 3.74 Å, 1.3 Å and 25º, respectively. It is interesting that ground-state molecular structure at high pressure becomes more similar to the predicted relaxed excited state structure. Thus, at a higher pressure, relaxation from the Franck-Condon state to the relaxed excited state would be expected to require less structural change.

6.3.2.2.2 Intermolecular Inter-Phenyl Interactionss

The noteworthy intermolecular phenyl interactions in the Ph_7C_7H lattice were identified and are shown in **Figure 6.20**. Each phenyl ring attached to the cycloheptatriene core is labelled as Ph^1, Ph^2, Ph^3, Ph^4, Ph^5, Ph^6 and Ph^7. Two inter-phenyl interactions showing displaced stacked structures are evident, $\boldsymbol{D_{5\text{-}5i}}$ and $\boldsymbol{D_{6\text{-}3i}}$, and five interactions involving T-shaped geometries, $\boldsymbol{T_{1\text{-}3i}}$, $\boldsymbol{T_{3\text{-}1i}}$, $\boldsymbol{T_{4\text{-}6i}}$, $\boldsymbol{T_{6\text{-}4i}}$ and $\mathbf{T_{7\text{-}3}}$, can be identified.

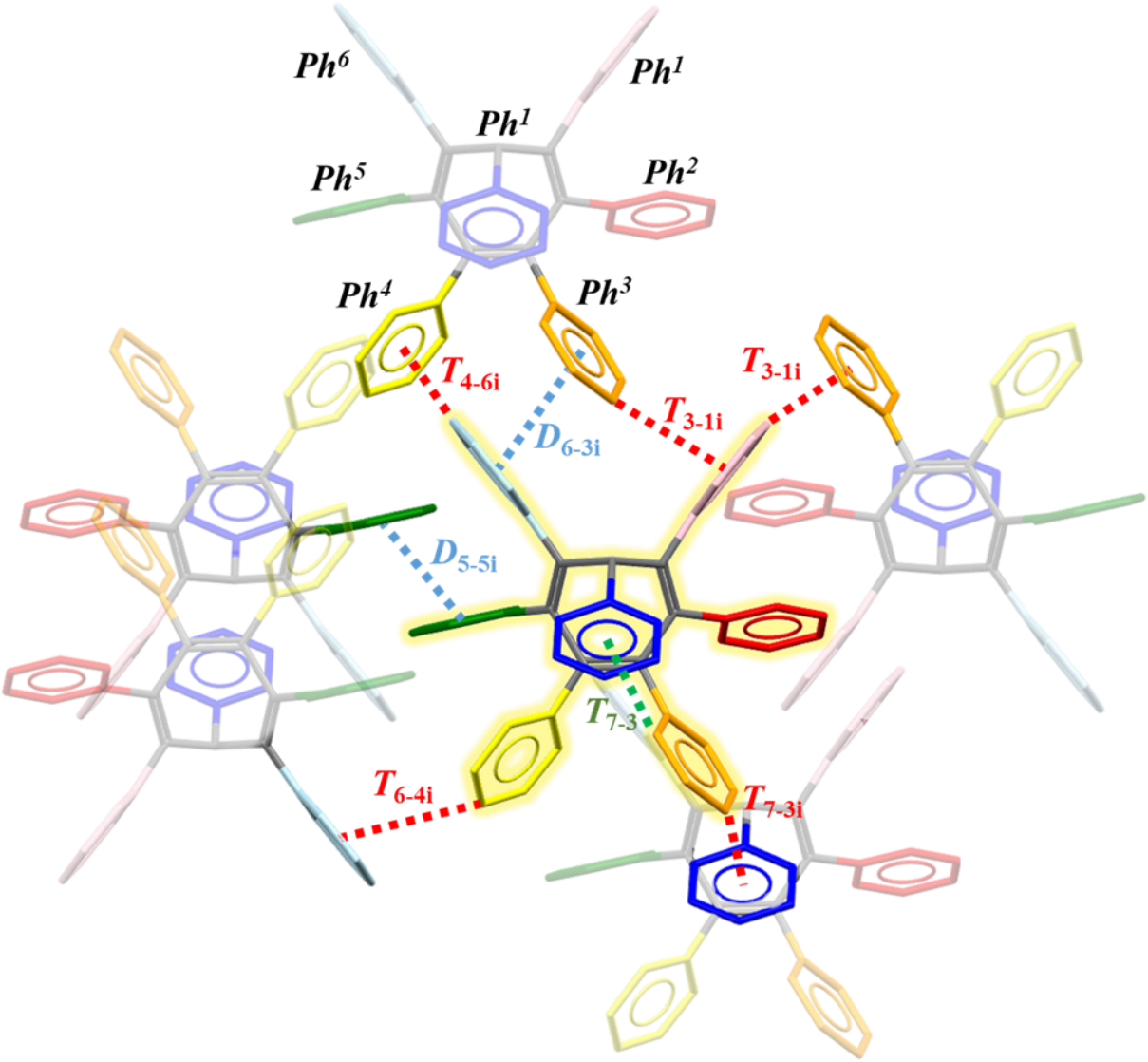

Figure 6.20. Crystal structure of Ph_7C_7H at 0.12 GPa. The Ph^1, Ph^2, Ph^3, Ph^4, Ph^5, Ph^6 and Ph^7 are shown in pink, red, orange, yellow, green, light blue and dark blue colours. The blue dashed-line depicts displaced stacked inter-phenyl interaction (*D*). The red dashed-line indicates the intermolecular T-shape inter-phenyl interactions (*T*). The intramolecular T-shape inter-phenyl interaction ($T_{7\text{-}3}$) is illustrated by the green dashed line. The first number indicates the phenyl that makes up the top bar of the T, and the letter i indicates an intermolecular interaction. Hydrogen atoms were omitted for clarity.

The $D_{6\text{-}3i}$ and $D_{5\text{-}5i}$ interactions are illustrated more clearly in **Figure 6.21,** and the corresponding intermolecular parameters are given in **Table 6.9** and **Table 6.10**, respectively. The pressure-dependence of the inter-phenyl parameters is shown graphically in **Figure 6.22.** It can be seen that at pressures of ~2 GPa and above, the $D_{6\text{-}3i}$ interaction parameters closely resemble those of ***Bz DS***, although the two rings

are not completely parallel. On the other hand, for $D_{5\text{-}5i}$ the lateral displacement (***d***) remains much higher than that of ***Bz DS***, preventing significant electronic interaction even at 3.39 GPa.

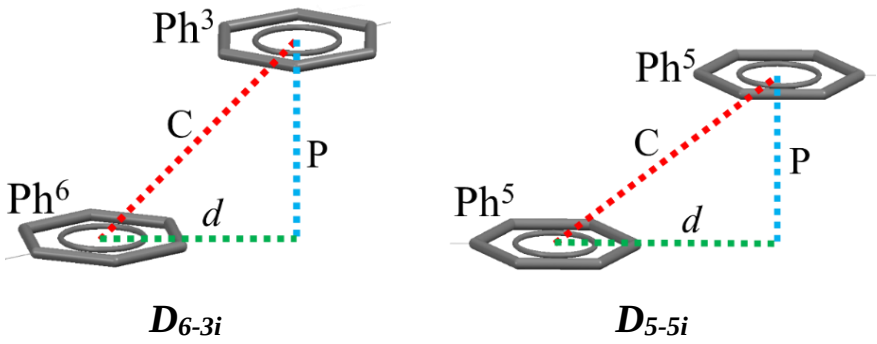

$D_{6\text{-}3i}$ $D_{5\text{-}5i}$

Figure 6.21 The intermolecular parameters of $D_{6\text{-}3i}$ and $D_{5\text{-}5i}$.

Table 6.9. The inter-phenyl distances (*C*, *P* and *d*) and angle (∠) of $D_{6\text{-}3i}$ as a function of pressure. The highlighting indicates structures that resemble that of *Bz DS*.

Pressure / GPa	**$C_{6\text{-}3i}$ / Å**	**$P_{6\text{-}3i}$ / Å**	**$d_{6\text{-}3i}$ / Å**	**$\angle_{6\text{-}3i}$ / °**
Ambient	4.711	3.474	3.182	2.53
0.12	4.786	3.535	3.226	1.88
0.44	4.486	3.493	2.815	2.09
0.98	4.235	3.393	2.534	8.55
1.50	4.141	3.565	2.107	16.21
2.04	4.075	3.553	1.995	18.36
2.53	4.022	3.533	1.922	19.79
3.39	3.992	3.532	1.860	22.33
Bz DS	***3.95***	***3.54***	***1.74***	***0***

Table 6.10. The inter-phenyl distances (*C, P* and *d*) and angle (∠) of $D_{5\text{-}5i}$ as a function of pressure.

Pressure / GPa	$C_{5\text{-}5i}$ / Å	$P_{5\text{-}5i}$ / Å	$d_{5\text{-}5i}$ / Å	$\angle_{5\text{-}5i}$ / °
Ambient	4.912	3.137	3.780	0
0.12	4.932	3.138	3.805	0
0.44	4.734	3.073	3.601	0
0.98	4.548	3.040	3.383	0
1.50	4.411	2.987	3.246	0
2.04	4.314	2.966	3.133	0
2.53	4.256	2.919	3.097	0
3.39	4.197	2.843	3.087	0
Bz DS	***3.95***	***3.54***	***1.74***	***0***

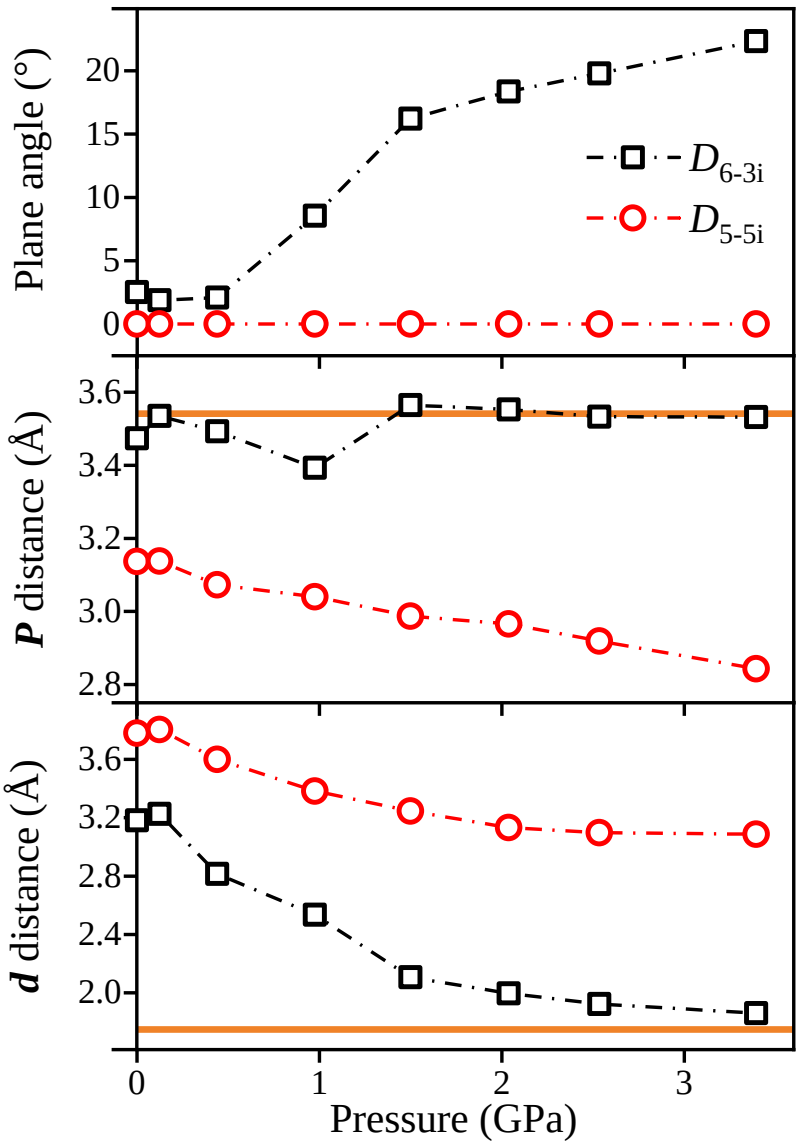

Figure 6.22. The inter-phenyl parameters for displaced-stacked interactions plotted as a function of pressure. The bold orange line indicates the value of each parameter for *Bz DS* dimer.

The significant T-shaped intermolecular phenyl interactions are shown in **Figure 6.23** and their respective parameters listed in **Table 6.11** to **Table 6.15**. In the tables, the pressures where the parameters closely resemble those of the ***Bz T*** dimer are highlighted in yellow. The pressure-dependence of the inter-phenyl parameters is also shown graphically in **Figure 6.24**.

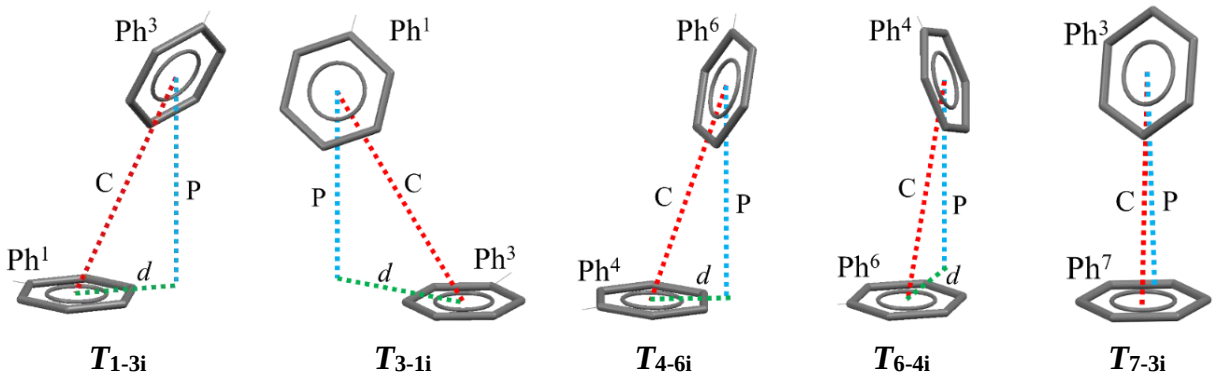

Figure 6.23. The inter-phenyl parameters of $T_{1\text{-}3i}$, $T_{3\text{-}1i}$, $T_{4\text{-}6i}$, $T_{6\text{-}4i}$ and $T_{7\text{-}3i}$.

Table 6.11. The inter-phenyl distances (*C*, *P* and *d*) and angle (∠) of the $T_{1\text{-}3i}$ as a function of pressure. The highlighting indicates structures that resemble that of *Bz T*.

Pressure / GPa	**$C_{1\text{-}3i}$ / Å**	**$P_{1\text{-}3i}$ / Å**	**$d_{1\text{-}3i}$ / Å**	**$\angle_{1\text{-}3i}$ / °**
Ambient	5.533	4.949	2.474	63.64
0.12	5.626	5.069	2.441	65.25
0.44	5.387	5.03	1.928	66.40
0.98	5.202	4.984	1.490	69.55
1.50	5.12	4.929	1.385	75.60
2.04	5.016	4.853	1.268	76.80
2.53	4.92	4.759	1.248	77.36
3.39	4.816	4.667	1.189	77.83
Bz T	***5.01***	***4.92***	***0.90***	***75.40***

Table 6.12. The inter-phenyl distances (*C, P* and *d*) and angle (∠) of the $T_{3\text{-}1i}$ as a function of pressure. The highlighting indicates structures that resemble that of *Bz T*.

Pressure / GPa	$C_{3\text{-}1i}$ / Å	$P_{3\text{-}1i}$ / Å	$d_{3\text{-}1i}$ / Å	∠3-1i / °
Ambient	5.935	4.762	3.542	63.64
0.12	5.941	4.768	3.544	65.25
0.44	5.664	4.62	3.277	66.4
0.98	5.318	4.696	2.496	69.55
1.50	5.014	4.741	1.632	75.6
2.04	4.885	4.668	1.440	76.8
2.53	4.814	4.629	1.322	77.36
3.39	4.736	4.586	1.183	77.83
Bz T	***5.01***	***4.92***	***0.90***	***75.4***

Table 6.13. The inter-phenyl distances (*C, P* and *d*) and angle (∠) of the $T_{4\text{-}6i}$ as a function of pressure. The highlighting indicates structures that resemble that of *Bz T*.

Pressure / GPa	$C_{4\text{-}6i}$ / Å	$P_{4\text{-}6i}$ / Å	$d_{4\text{-}6i}$ / Å	$\angle_{4\text{-}6i}$ / °
Ambient	5.261	5.000	1.637	69.9
0.12	5.349	5.108	1.587	70.82
0.44	5.152	5.000	1.242	73.98
0.98	4.994	4.884	1.042	77.14
1.50	4.922	4.824	0.977	80.56
2.04	4.847	4.757	0.930	82.02
2.53	4.785	4.694	0.929	82.98
3.39	4.747	4.644	0.984	84.22
Bz T	***5.01***	***4.92***	***0.90***	***75.4***

Table 6.14. The inter-phenyl distances (*C, P* and *d*) and angle (∠) of the $T_{6\text{-}4i}$ as a function of pressure.

Pressure / GPa	$C_{6\text{-}4i}$ / Å	$P_{6\text{-}4i}$ / Å	$d_{6\text{-}4i}$ / Å	$\angle_{6\text{-}4i}$ / °
Ambient	5.397	4.921	2.216	69.9
0.12	5.453	4.962	2.261	70.82
0.44	5.259	4.895	1.923	73.98
0.98	5.125	4.811	1.766	77.14
1.50	5.06	4.742	1.766	80.56
2.04	4.988	4.692	1.693	82.02
2.53	4.947	4.672	1.626	82.98
3.39	4.894	4.643	1.547	84.22
Bz T	***5.01***	***4.92***	***0.90***	***75.40***

Table 6.15. The inter-phenyl distances (*C, P* and *d*) and angle (∠) of the $T_{7\text{-}3i}$ as a function of pressure. The highlighting indicates structures that resemble that of *Bz T*.

Pressure / GPa	$C_{7\text{-}3i}$ / Å	$P_{7\text{-}3i}$ / Å	$d_{7\text{-}3i}$ / Å	$\angle_{7\text{-}3i}$ / °
Ambient	4.957	4.899	0.756	68.68
0.12	5.052	4.981	0.844	67.67
0.44	4.984	4.883	0.998	66.98
0.98	4.960	4.823	1.158	62.13
1.50	4.877	4.697	1.313	53.49
2.04	4.787	4.601	1.321	51.01
2.53	4.728	4.54	1.320	49.65
3.39	4.617	4.419	1.338	47.14
Bz T	***5.01***	***4.92***	***0.90***	***75.40***

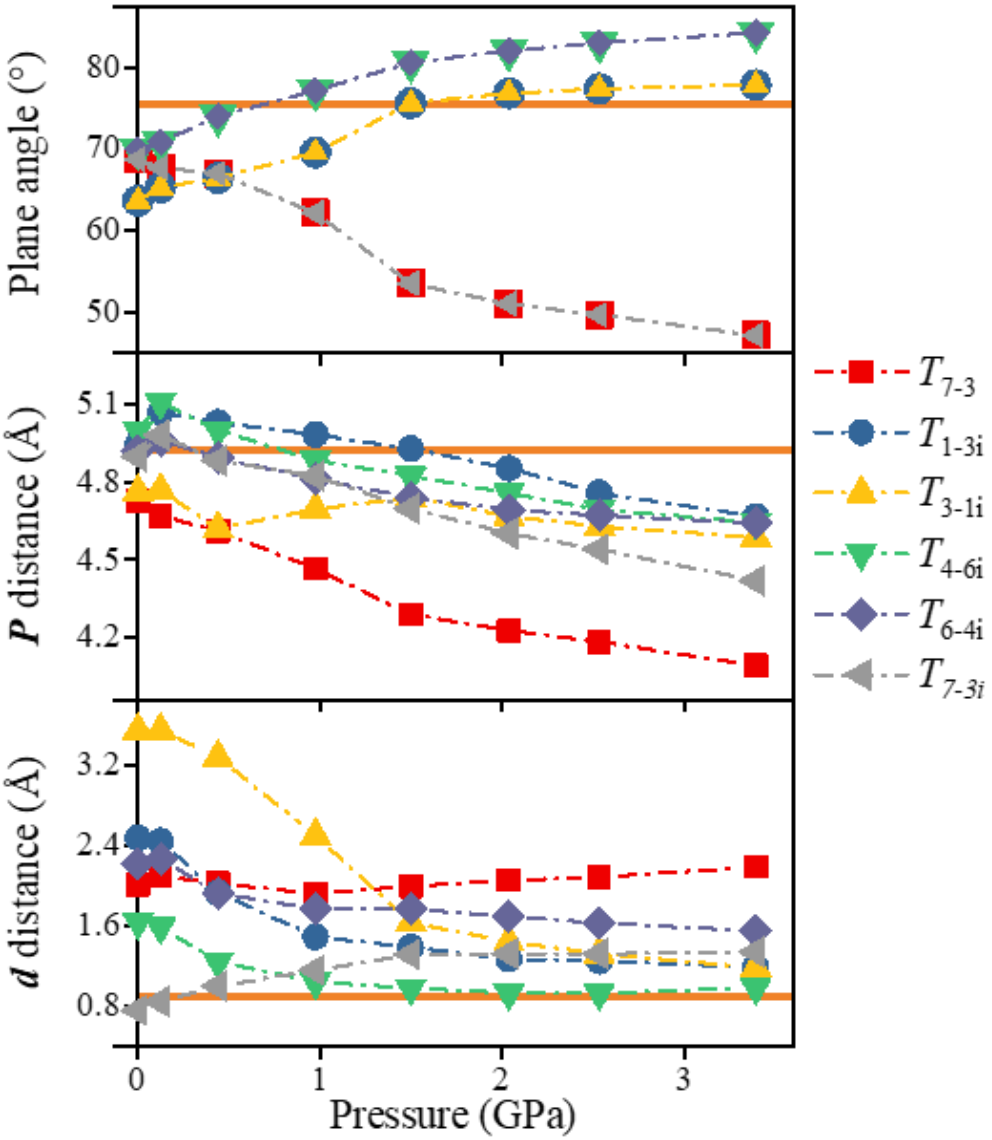

Figure 6.24. The T-shaped intermolecular inter-phenyl interactions plotted as a function of pressure. The intramolecular $T_{7\text{-}3}$ interaction is also shown—the bold orange lines indicate the value of each parameter of the *Bz T* dimer.

From **Figure 6.24** and **Table 6.13**, it can be seen that $T_{4\text{-}6i}$ closely resembles **Bz T** at a pressure higher than 1 GPa. On the other hand, $T_{7\text{-}3i}$ (**Table 6.15**) closely resembles **Bz T** at ambient pressure but deviates from this structure at pressures higher than 1 GPa. Moreover, the $T_{1\text{-}3i}$ and $T_{3\text{-}1i}$ (**Table 6.11** and **Table 6.12**) only become similar to the **Bz T** structure at pressures higher than 2 GPa. In the case of $T_{6\text{-}4i}$, the structure does not approach that of **Bz T** at any pressure.

It should be noted that Ph^7 and Ph^3 experience both intramolecular and intermolecular interactions, $T_{7\text{-}3}$ and $T_{7\text{-}3i}$, creating an extended chain of T-shaped Ph^7-Ph^3

interactions. The phenyl interplane angles are the same for both interactions, and the angle shows the same pressure-dependent behaviour. However, at all pressures, the values of ***P*** and ***d*** for the intermolecular $\boldsymbol{T_{7\text{-}3i}}$ are much closer to those of ***Bz T*** than are those of intramolecular $\boldsymbol{T_{7\text{-}3}}$.

6.3.2.3 UV-Vis Absorption Spectra

The UV-vis absorption spectra were collected at 0.00 GPa, 0.27 GPa, 0.69 GPa, 1.13 GPa, 1.71 GPa, 2.12 GPa, 2.65 GPa, and 3.06 GPa, as shown in **Figure 6.25**. The absorption spectrum red-edge, obtained from half-maximum of the intensity, is used to quantify the spectral shift as a function of pressure, as listed in **Table 6.16**. At 0 GPa, the wavelength of the absorption spectrum red-edge of the crystal matches the absorption spectrum in solution reported by Sturala *et al.* (Figure S26 d)[18]. This suggests that the only significant intermolecular interaction at low pressure, $\boldsymbol{T_{7\text{-}3i}}$, has little effect on the electronic transition energy.

As pressure is increased, the spectrum is redshifted as a result of a more significant inter-phenyl interaction. At pressures above 1.1 GPa, there is a noticeable broadening to the longer wavelength and the development of an increasingly intense long-wavelength tail. The UV-vis absorption red-edge shifts by ~1470 cm^{-1}, from 359 nm to 379 nm from 0 GPa to 3.06 GPa. It can be seen from **Figure 6.25** that there is a change in spectral profile at higher pressures, which can be attributed to the formation of pair-wise, intermolecular interactions between phenyl groups with structures resembling the equilibrium geometries of benzene dimers. The formation of displaced-stacked structures, $\boldsymbol{D_{6\text{-}3i}}$, at pressures above 2 GPa is particularly significant in terms of the formation of excitonic interactions and is likely the cause of the increased absorption at longer wavelengths. Unlike Ph_5C_5H, where displaced-stacked dimer interactions are already present at ambient pressure, these interactions only develop at high pressure in Ph_7C_7H.

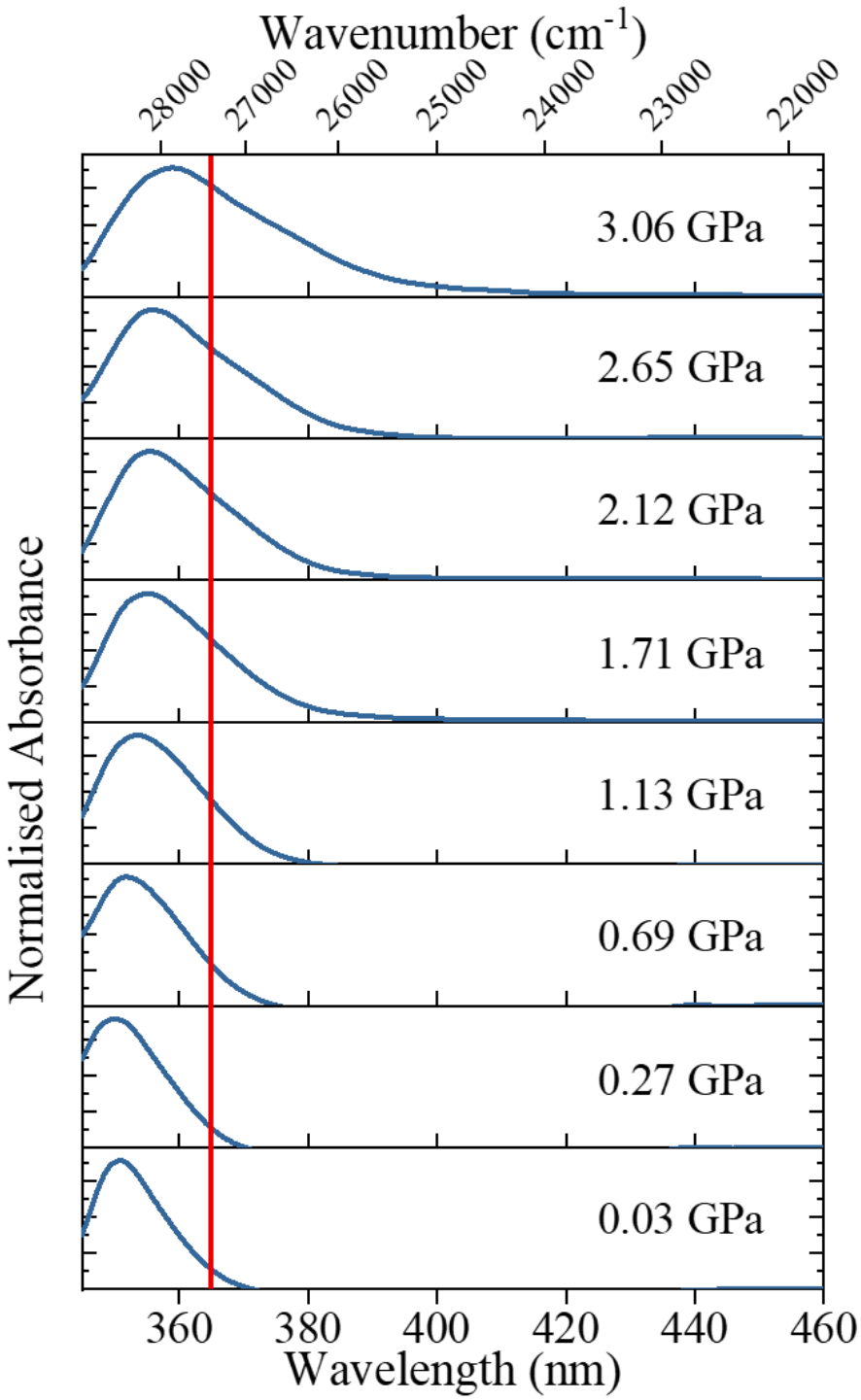

Figure 6.25. UV-vis absorption spectra of Ph_7C_7H in the various function of pressures. The wavelength at which fluorescence spectra were excited, 365 nm, is shown in a red line.

Table 6.16. Wavelength and wavenumber of absorption red-edge (half-maximum) as a function of pressure.

Pressure / GPa	Absorption Edge / nm	Absorption Edge / cm^{-1}
0.00	359	27860
0.27	360	27780
0.69	362	27620
1.13	365	27400
1.71	369	27100
2.12	370	27030
2.65	372	26880
3.06	379	26390

6.3.2.4 Fluorescence Spectra

Fluorescence emission spectra were measured at 0.00 GPa, 0.27 GPa, 0.52 GPa, 1.07 GPa, 1.82 GPa, 2.12 GPa, 2.65 GPa and 3.03 GPa. These pressures were chosen to match those of the UV-vis absorption measurements closely. The fluorescence spectra are depicted in **Figure 6.26**. The wavelength and wavenumber of the fluorescence maximum as a function of pressure are listed in **Table 6.17**.

The emission spectrum at 0 GPa is in a good agreement with that previously reported by Sturala *et al.* (**Figure 6.5**) for the crystalline Ph_7C_7H.[18] It also resembles the relaxed emission from Ph_7C_7H in solution, reported in the same study.[18] The significant Stokes shift of 3300 cm^{-1} between the absorption spectrum red-edge and the fluorescence emission maximum indicates that there is structural relaxation in the excited state prior to emission, in the crystalline state.

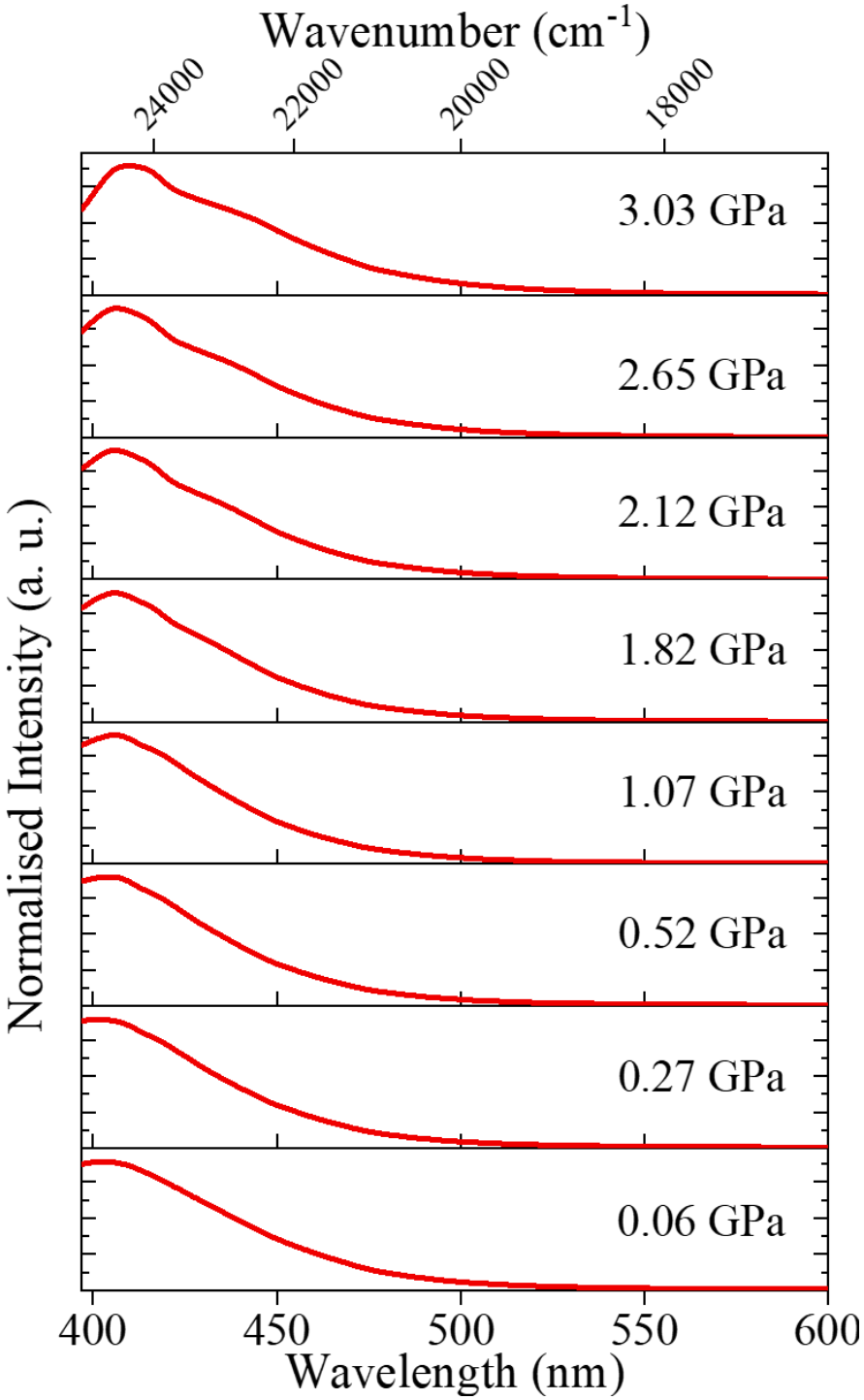

Figure 6.26. Fluorescence spectra of Ph_7C_7H in various pressures (λ_{ex} = 365 nm).

Table 6.17. Wavenumber and wavelength of fluorescence maximum as a function of pressure.

Pressure / GPa	Fluorescence Peak / nm	Fluorescence Peak / cm^{-1}
s0.06	407	24550
0.27	407	24550
0.52	407	24550
1.07	407	24550
1.82	407	24550
2.12	407	24550
2.65	408	24500
3.03	412	24250

The wavelength of the fluorescence maximum is essentially unchanged throughout the increase of pressure, in contrast to the observed regular red shift in the absorption spectrum. This is further evidence that the emission arises from a relaxed excited state. This also suggests that the relaxed excited state structure is essentially independent of pressure. At pressures above 1.8 GPa, however, a shoulder becomes apparent on the long-wavelength side of the fluorescence maximum. The intensity of this shoulder increases with increasing pressure. At 3 GPa there is a small redshift in the emission maximum, as a result of the increasing relative intensity of the shoulder band. This change in the emission spectral profile corresponds to a similar change in the profile of the absorption spectrum. Thus, the long-wavelength emission can be linked to the excitation of displaced-stacked structures, $\boldsymbol{D_{6\text{-}3i}}$.

At pressures below 1 GPa, the Stokes shift can be attributed to the increase in interaction between Ph^3 and Ph^7, due to intra- or intermolecular relaxation. At higher pressures, however, other intermolecular inter-phenyl interactions become more significant. The long-wavelength emission shoulder that appears at the highest pressures can be attributed to the relaxation of displaced-stacked Franck-Condon structures of $\boldsymbol{D_{6\text{-}3i}}$ to more closely stacked excimer-like structures. Such structures will not be accessible from T-shaped dimers in the crystalline state.

The decrease in Stokes shift with increasing pressure is illustrated in **Figure 6.27**. The decrease in Stokes shift indicates that the relaxed emitting structure becomes more closely resembles the structure of the Franck-Condon excited state (i.e. the ground-state structure) as pressure increases, which consistent with the formation of more closely interacting inter-phenyl dimers. Furthermore, relaxation may be inhibited in the crystal, so that emission may not occur fully relaxed structures but rather from a range of structures on the relaxation pathway between the Franck-Condon state and the lowest energy emitting state.

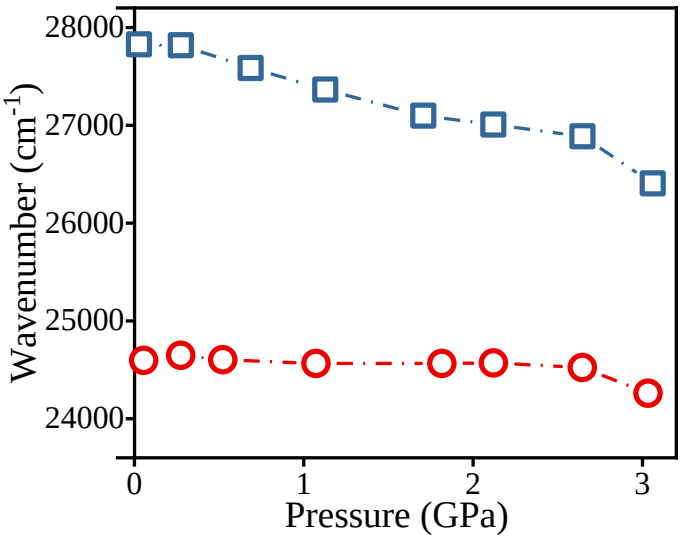

Figure 6.27. Pressure-dependence of the red edge (half maximum) of the absorption spectrum (blue rectangle) and the maximum of the fluorescence spectrum (red circle).

The maximum of the fluorescence intensity was observed to increase with increasing pressure, but this is not due to an influence of intermolecular interactions on quantum yield. The increase in fluorescence intensity is due to an increase in absorbance at the excitation wavelength (365 nm), that occurs as a result of the pressure-induced red shift in the absorption spectrum (as shown in **Figure 6.25**). As shown in **Figure 6.28**, there is a linear correlation of fluorescence intensity with the relative absorbance, up to 2.6 GPa. This may suggest that up to 2.6 GPa the quantum yield is unchanged. However, the fluorescence intensity at 3 GPa deviates from linearity, suggesting that there may be a decrease in the quantum yield at this pressure, corresponding to an increase in the contribution from long-wavelength emitting excimers. This is an example of aggregation-caused quenching.

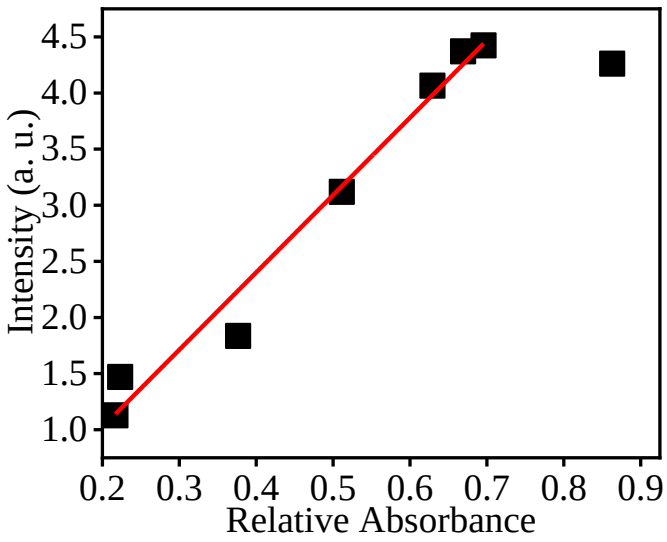

Figure 6.28. Correlation between maximum emission intensity and absorbance at the excitation wavelength, 365 nm.

6.4 Conclusions and Future Work

Inter-phenyl interactions in crystalline Ph_5C_5H at ambient pressure were identified using a crystal structure available from the literature.[49] At ambient pressure, significant T-shape and displaced-stacked intermolecular phenyl interactions were identified which resemble the known structures of stable benzene dimers. High-pressure UV-vis absorption spectra and fluorescence emission spectra were measured up to 3.95 GPa to investigate the effect of these interactions. At 0 GPa, the UV-vis absorption red-edge occurred at longer wavelength than in solution phase, indicating strong intermolecular interactions within the crystal. Moreover, the fluorescence spectrum was structureless and found at longer wavelength (464 nm) compared to the solution phase with a large Stokes shift. This indicates emission from an excimer state in the crystal, that is readily accessible even at ambient pressure. With increasing pressure, both absorption and emission spectra were redshifted with the same trend with a slight decrease in Stokes shift. This indicates that relaxation from the excited Franck-Condon structure to the relaxed emitting structure is rather unchanged as a function of pressure.

A high-pressure single-crystal diffraction experiment to determine the structure of Ph_7C_7H has been successfully carried at pressures up to 3.39 GPa, in a DAC with Daphne oil 7373 as a hydrostatic medium using synchrotron radiation. The Ph_7C_7H crystallises in a triclinic crystal system with $P\bar{1}$ space group. Upon increasing pressure,

the unit cell volume is decreased by ~18% at 3.39 GPa. However, the unit cell parameters experienced anisotropic compression with the *b*-axis decreased by ~8.3%, while *a* and *c* axes only decreased by ~5%. From the crystal structure, inter-phenyl interactions were identified with the intermolecular T-shaped, $\boldsymbol{T_{7\text{-}3i}}$, the most prominent interaction at ambient pressure. As pressure increase, however, the $\boldsymbol{T_{7\text{-}3i}}$ interaction becomes less prominent, while other interactions such as $\boldsymbol{T_{1\text{-}3i}}$, $\boldsymbol{T_{3\text{-}1i}}$, $\boldsymbol{T_{4\text{-}6i}}$, and displaced-stacked $\boldsymbol{D_{6\text{-}3i}}$ becomes dominant at ~2 GPa.

High-pressure UV-vis absorption and fluorescence emission spectral measurements were also successfully carried out for the Ph_7C_7H crystal up to ~3 GPa. The UV-vis absorption spectrum red-edge is redshifted with increasing pressure with a shoulder at longer wavelength become evident at ~2 GPa, indicating a newly formed chromophore. On the other hand, the fluorescence maximum is essentially unchanged throughout the pressure, indicating a relaxed emitting structure that is essentially the same. The emission spectrum at ~2 GPa also shows a long-wavelength shoulder, arising from a new emitting species, the intensity of which increases at higher pressures. This emission can be attributed to excimers resulting from excitation of displaced-stacked inter-phenyl dimers, $\boldsymbol{D_{6\text{-}3i}}$. The fluorescence intensity increases with increasing pressure up to 2.6 GPa and shows a linear correlation to the increase in the relative absorbance at the excitation wavelength (365 nm) that arises from the pressure-induced redshift in the latter. This indicates an unchanged quantum yield up to 2.6 GPa, but there is evidence of aggregation-caused quenching at higher pressure.

These experiments have revealed the influence of intermolecular interactions on the absorption and emission spectra of phenyl-ring molecular rotors. Moreover, specific inter-phenyl interactions have been identified as being particularly significant.

Follow-up experiments, such as time-resolved fluorescence spectroscopy could be carried out to further investigate excimer formation for Ph_7C_7 at higher pressure. The acquisition of a better-quality diamond and a shorter wavelength excitation source would enable the detection of the fluorescence spectrum of Ph_7C_7H below 400 nm. Moreover, measurements could also be carried out on the related molecular rotor Ph_6C_6 in the crystal state. This molecule differs from Ph_7C_7H and Ph_5C_5H in that it has

been observed to exhibit aggregation-induced emission without a change in its emission spectrum.

6.5 References

1. Kuimova, M. K., *Phys. Chem. Chem. Phys.* **2012,** *14* (37), 12671-12686.
2. Lee, S. C.; Heo, J.; Woo, H. C.; Lee, J. A.; Seo, Y. H.; Lee, C. L.; Kim, S.; Kwon, O. P., *Chem. Eur. J.* **2018,** *24* (52), 13706-13718.
3. Bennet, M. A.; Richardson, P. R.; Arlt, J.; Mccarthy, A.; Buller, G. S.; Jones, A. C., *Lab Chip* **2011,** *11* (22), 3821.
4. Li, Z.; Qin, A. J., *Natl. Sci. Rev.* **2014,** *1* (1), 22-24.
5. Birks, J. B., *Photophysics of aromatic molecules*. Chichester Wiley-Interscience: Chichester, **1970**.
6. Ahn, D. H.; Jeong, J. H.; Song, J.; Lee, J. Y.; Kwon, J. H., *ACS Appl. Mater. Inter.* **2018,** *10* (12), 10246-10253.
7. Xie, Z. L.; Chen, C. J.; Xu, S. D.; Li, J.; Zhang, Y.; Liu, S. W.; Xu, J. R.; Chi, Z. G., *Angew. Chem. Int. Ed.* **2015,** *54* (24), 7181-7184.
8. Moorthy, J. N.; Natarajan, P.; Venkatakrishnan, P.; Huang, D. F.; Chow, T. J., *Org. Lett.* **2007,** *9* (25), 5215-5218.
9. Li, H.; Wang, J. X.; Lin, H.; Xu, L.; Xu, W.; Wang, R. M.; Song, Y. L.; Zhu, D. B., *Adv. Mater.* **2010,** *22* (11), 1237-+.
10. Hong, Y. N.; Lam, J. W. Y.; Tang, B. Z., *Chem. Soc. Rev.* **2011,** *40* (11), 5361-5388.
11. Luo, J. D.; Xie, Z. L.; Lam, J. W. Y.; Cheng, L.; Chen, H. Y.; Qiu, C. F.; Kwok, H. S.; Zhan, X. W.; Liu, Y. Q.; Zhu, D. B.; Tang, B. Z., *ChemComm.* **2001,** (18), 1740-1741.
12. Ng, J. C. Y.; Liu, J. Z.; Su, H. M.; Hong, Y. N.; Li, H. K.; Lam, J. W. Y.; Wong, K. S.; Tang, B. Z., *J.Mater. Chem. C* **2014,** *2* (1), 78-83.
13. Ceballos, S. A.; Gil, S.; Costero, A. M., *RSC Adv.* **2017,** *7* (23), 14279-14282.
14. Dong, H.; Luo, M.; Wang, S.; Ma, X., *Dyes Pigm.* **2017,** *139*, 118-128.
15. Li, X.; Yin, Y. H.; Yan, H.; Lu, C. S., *Chem. Asian J.* **2017,** *12* (17), 2207-2210.
16. Zhang, C. J.; Yao, X. Y.; Xiang, J. W.; Ma, X., *Polym. Chem.* **2017,** *8* (33), 4835-4841.

17. Mei, J.; Leung, N. L. C.; Kwok, R. T. K.; Lam, J. W. Y.; Tang, B. Z., *Chem. Rev.* **2015,** *115* (21), 11718-11940.
18. Sturala, J.; Etherington, M. K.; Bismillah, A. N.; Higginbotham, H. F.; Trewby, W.; Aguilar, J. A.; Bromley, E. H. C.; Avestro, A. J.; Monkman, A. P.; McGonigal, P. R., *J. Am. Chem. Soc.* **2017,** *139* (49), 17882-17889.
19. Gu, Y. R.; Liu, H. C.; Qiu, R.; Liu, Z. D.; Wang, C. Y.; Katsura, T.; Zhang, H.; Wu, M.; Yao, M. G.; Zheng, H. Y.; Li, K.; Wang, Y. J.; Wang, K.; Yang, B.; Ma, Y. G.; Zou, B., *J. Phys. Chem. Lett.* **2019,** *10* (18), 5557-5562.
20. Li, N.; Gu, Y. R.; Chen, Y. P.; Zhang, L.; Zeng, Q. X.; Geng, T.; Wu, L. W.; Jiang, L. N.; Xiao, G. J.; Wang, K.; Zou, B., *J. Phys. Chem. C* **2019,** *123* (11), 6763-6767.
21. Lee, E. C.; Kim, D.; Jurecka, P.; Tarakeshwar, P.; Hobza, P.; Kim, K. S., *J. Phys. Chem. A* **2007,** *111* (18), 3446-3457.
22. Steed, J. M.; Dixon, T. A.; Klemperer, W., *J. Chem. Phys.* **1979,** *70* (11), 4940-4946.
23. Janda, K. C.; Hemminger, J. C.; Winn, J. S.; Novick, S. E.; Harris, S. J.; Klemperer, W., *J. Chem. Phys.* **1975,** *63* (4), 1419-1421.
24. Scherzer, W.; Krätzschmar, O.; Selzle, H. L.; Schlag, E. W., *Z. Naturforsch. A* **1992,** *47* (12).
25. Kiermeier, A.; Ernstberger, B.; Neusser, H. J.; Schlag, E. W., *J. Phys. Chem.* **1988,** *92* (13), 3785-3789.
26. Börnsen, K. O.; Selzle, H. L.; Schlag, E. W., *J. Chem. Phys.* **1986,** *85* (4), 1726-1732.
27. Fung, K. H.; Selzle, H. L.; Schlag, E. W., *J. Phys. Chem.* **1983,** *87* (25), 5113-5116.
28. Felker, P. M.; Maxton, P. M.; Schaeffer, M. W., *Chem. Rev.* **1994,** *94* (7), 1787-1805.
29. Henson, B. F.; Hartland, G. V.; Venturo, V. A.; Felker, P. M., *J. Chem. Phys.* **1992,** *97* (4), 2189-2208.
30. Arunan, E.; Gutowsky, H. S., *J. Chem. Phys.* **1993,** *98* (5), 4294-4296.
31. Krause, H.; Ernstberger, B.; Neusser, H. J., *Chem. Phys. Lett.* **1991,** *184* (5-6), 411-417.

32. Konovalova, I. S.; Shishkina, S. V.; Bani-Khaled, G.; Muzyka, E. N.; Boyko, A. N., *Crystengcomm* **2019,** *21* (18), 2908-2919.
33. Nayak, S. K.; Sathishkumar, R.; Row, T. N. G., *Crystengcomm* **2010,** *12* (10), 3112-3118.
34. Wright, J. D., *Molecular Crystals*. Second ed.; Cambridge University Press: Cambridge, **1995**.
35. Iyer, E. S. S.; Sadybekov, A.; Lioubashevski, O.; Krylov, A. I.; Ruhman, S., *J. Phys. Chem. A* **2017,** *121* (9), 1962-1975.
36. Hirayama, F.; Lipsky, S., *J. Chem. Phys.* **1969,** *51* (5), 1939-1951.
37. Cundall, R. B.; Robinson, D. A., *J. Chem. Soc., Faraday Trans. 2* **1972,** *68* (0), 1133-1144.
38. Sinnokrot, M. O.; Sherrill, C. D., *J. Phys. Chem. A* **2006,** *110* (37), 10656-10668.
39. Birks, J. B., *Rep. Prog. Phys.* **1975,** *38* (8), 903-974.
40. Miyazaki, M.; Fujii, M., *Phys. Chem. Chem. Phys.* **2015,** *17* (39), 25989-25997.
41. Förster, T.; Kasper, K., *Elektrochem.* **1955,** *59* (10), 976-980.
42. Birks, J. B.; Christophorou, L. G., *Spectrochim. Acta* **1963,** *19* (2), 401-410.
43. Pensack, R. D.; Ashmore, R. J.; Paoletta, A. L.; Scholes, G. D., *J. Phys. Chem. C* **2018,** *122* (36), 21004-21017.
44. Agilent *CrysaAlis PRO*, Agilent Technologies Ltd: Yarnton, Oxfordshire, England, **2014**.
45. Sheldrick, G. M., *Acta Crystallogr. A* **2015,** *71*, 3-8.
46. Dolomanov, O. V.; Bourhis, L. J.; Gildea, R. J.; Howard, J. A. K.; Puschmann, H., *J. Appl. Crystallogr.* **2009,** *42*, 339-341.
47. Betteridge, P. W.; Carruthers, J. R.; Cooper, R. I.; Prout, K.; Watkin, D. J., *J. Appl. Crystallogr.* **2003,** *36*, 1487-1487.
48. Macrae, C. F.; Sovago, L.; Cottrell, S. J.; Galek, P. T. A.; McCabe, P.; Pidcock, E.; Platings, M.; Shields, G. P.; Stevens, J. S.; Towler, M.; Wood, P. A., *J. Appl. Crystallogr.* **2020,** *53*, 226-235.
49. Field, L. D.; Hambley, T. W.; Lindall, C. M.; Masters, A. F., *Inorg. Chem.* **1992,** *31* (12), 2366-2370.
50. Boldyreva, E. V., *J. Mol. Struct.* **2003,** *647* (1-3), 159-179.
51. Förster, T., *Angew. Chem. Int. Ed.* **1969,** *8* (5), 333-336.

Chapter 7
Solution Phase and High-pressure Solid-state Optical Spectroscopy of BCPEB

7.1 Introduction

A combination of UV-vis absorption, excitation and emission spectroscopy has been carried out for 1,4-bis(4-carbomethoxyphenylethynyl)benzene (BCPEB) (**Figure 7.1**) in various solvents, to investigate the photophysical properties of the molecule. Low-temperature excitation and emission spectral measurements have also been collected for BCPEB at 77K in ethanol, to observe more clearly the vibronic transitions. It was found that the photophysical properties are very similar to those of 1,4-bis-(phenylethynyl)benzene (BPEB) (**Figure 7.1**) as reported in the literature .[1-3]

A combination of high-pressure single-crystal X-ray diffraction, UV-vis absorption and fluorescence emission spectroscopy has also been carried out to study the effect of pressure on the BCPEB in the crystalline state. The results reported in this chapter reveal that upon increasing pressure, the intermolecular distance becomes shorter, and the UV-vis absorption and fluorescence emission spectra show a red-shift, with more resolved vibronic structure evident at high pressure. The effect of pressure on the spectroscopic properties can be related to increasing intermolecular interactions and more restricted vibrational motion within the crystal.

7.1.1 1,4-bis-(phenylethynyl)benzene (BPEB)

Molecules that have the form of a linear, conjugated, rigid molecular rod containing aryl and acetylenic groups, have been gaining interest from scientists due to their bright photoluminescence and electroluminescence properties.[1,4-6] These properties make molecules of this type particularly attractive as candidates for organic light-emitting diodes (OLEDs) and molecular wires.[7-9]

One of the simplest of this class of molecules to study is 1,4-bis-(phenylethynyl)-benzene (BPEB), as shown in **Figure 7.1**. It consists of three phenyl rings, linked by acetylene bridges extending the π-conjugation. Multiple derivatives of BPEB, with

substituted terminal and middle rings have also been synthesised and studied, to gain a better understanding of the photophysics of this type of molecule.[10,11] This chapter, is concerned a derivative of BPEB, 1,4-bis(4-carbomethoxyphenylethynyl)benzene (BCPEB), which has a carbomethoxy group attached to each of terminal phenyl rings, in the *para* position, as shown in **Figure 7.1**.

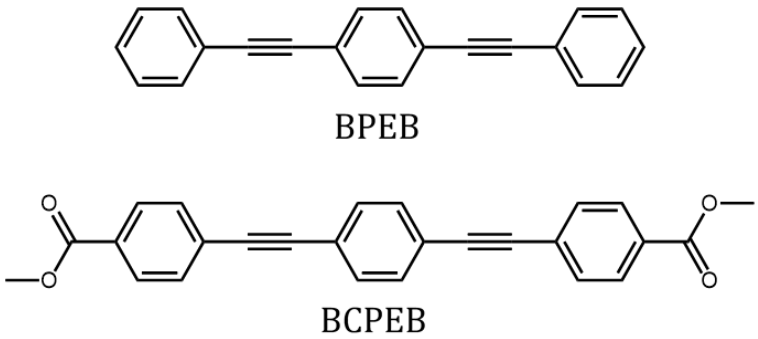

Figure 7.1. The structure of the 1,4-bis-(phenylethynyl)benzene (BPEB) and 1,4-bis(4-carbomethoxyphenylethynyl)benzene (BCPEB).

The BPEB molecule has free rotation of both terminal and central phenyl rings. The torsional rotation of the rings can be assigned to the asymmetrical terminal ring twisting (TRT) and the symmetrical middle-ring twisting (MRT).[12,13] Greaves *et al.* reported that the calculated energy barrier to twisting of the central phenyl, ring from its planar conformation, is ~2.7 kJ mol^{-1} which is comparable to thermal energy at room temperature. Therefore, about 30% of BPEB molecules in a sample will have sufficient energy for free rotation of the phenyl rings, at ambient temperature.[12] This means that, in solution at room temperature, all possible torsional conformers will be present and can interact with the light upon irradiation, with the result that the absorption spectrum represents a mixture of conformers. Levitus *et al*. reported that in the excited state, the barrier for torsion of the middle is ~15 kJ mol^{-1}, so that the molecule experiences planarisation following excitation, and the emission arises from the planar conformer, which has a high fluorescence quantum yield.[14]

The photophysical properties of BPEB have been studied in various solvents and temperatures.[2,14] Beeby *et al.* reported[2] that in cyclohexane, the excitation and emission spectra were independent of concentration between 10^{-6} and 2.5×10^{-4} M. Moreover, the steady-state excitation and emission spectra were found to be essentially independent of collection wavelength and excitation wavelength, respectively. These

findings are contrary to those reported previously by Levitus *et al.*,[14] who reported evidence of aggregation and the dependence of the emission spectrum on excitation wavelength, which later confirmed as the fluorescence from impurity. The absorption and emission spectra in methanol at ambient temperature, and in EPA at ambient temperature and 77 K are shown in **Figure 7.2**. [2,14]

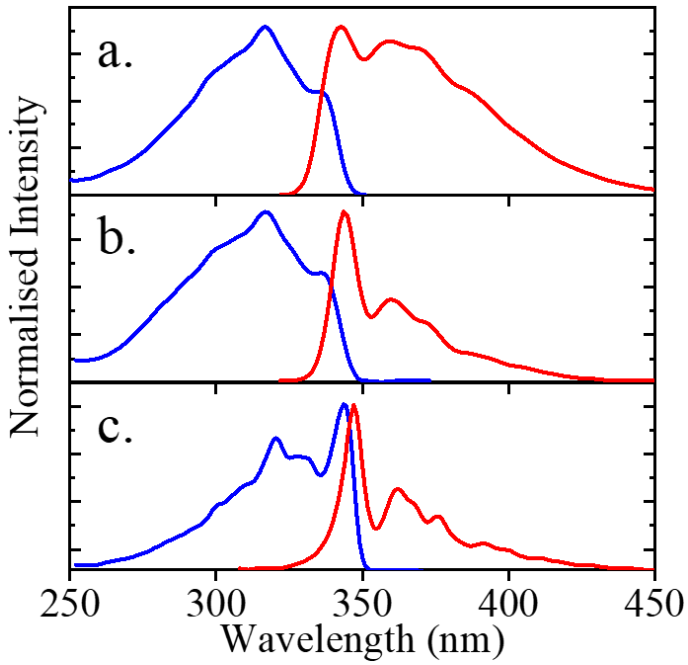

Figure 7.2. (a) Absorption and emission spectra of BPEB in methanol.[3] (b) Excitation and emission spectra of BPEB in EPA at ambient temperature and (c) 77K, determined with emission at 360 nm and excitation at 320 nm, respectively.[2]

It can be seen that, at ambient temperature, the vibronic structures in the emission spectrum is more clearly resolved in the less polar solvent. At 77K, the vibronic structure in both excitation and emission spectra becomes clear, with a mirror-image relationship. Moreover, the shoulder at ~336 nm, the 0-0 band, in the absorption/excitation spectrum at ambient temperature becomes the most intense peak, with a slight red-shift at low temperature. These observations can be taken to indicate that, at low temperature, the planar conformer is preferred over other conformers. Calculation of the torsional-angle-dependence of the vibrationally resolved electronic spectra also confirmed that the greater the torsional rotation of the phenyl ring, the less intense becomes the 0-0 band.[13] Thus, the different wavelength regions of the absorption spectrum at ambient temperature can be identified with different

conformational populations, as illustrated in **Figure 7.3**. MRT conformers absorb at the extreme blue end of the spectrum, TRT conformers around the peak, and the planar conformer on the red edge of the spectrum.[13]

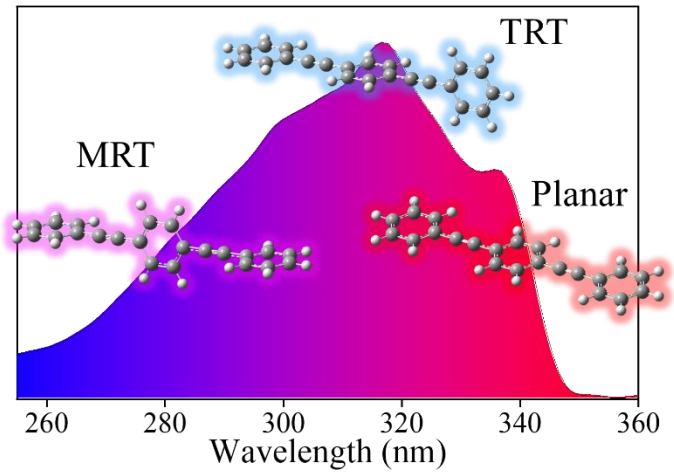

Figure 7.3. Room temperature absorption spectrum of BPEB with its predominant population of conformers at the specific wavelength regions. Redrawn from Roy et al.13

A femtosecond transient absorption study was carried out on BPEB, using two different excitation wavelengths, 285 nm to excite the MRT conformer, and at 347 nm to excite the planar conformer.[13] For excitation at 285 nm, it was found that the blue part of the absorption spectrum experienced a red-shift with increasing delay time up to 2 ps. However, for excitation at 347 nm, the absorption spectrum was essentially unchanged with delay time. This indicates that upon excitation of the MRT conformer relaxation occurs in excited state to reach the planar conformation, while excitation of the planar conformer did not result in structural change. This also indicates that the planar conformer is the most preferred conformation in the excited state, confirming the computational study in the same paper and that reported by Levitus *et al*.[13, 14]

7.1.2 1,4-bis(4-carbomethoxyphenylethynyl)benzene (BCPEB)

The absorption and emission spectra of BCPEB at ambient temperature in various solvents have been reported by Fasina *et al.*, as summarised in **Table 7.1**.[10] The absorption and emission maxima were observed at ~335 nm and ~365 nm, respectively. Both maxima are shifted to the red by ~20 nm compared with BPEB, which can be attributed to more delocalised π-conjugation within the molecule, involving the carbomethoxy groups. The absorption spectrum in DMF was reported

by Marshall *et al.* and showed a very similar absorption maximum at ~336 nm.[15] The electronic spectra at low temperature have not been reported.

Table 7.1. Absorption and emission data for BCPEB in various solvents.[10]

Solvent	λ_{abs} / nm	ε /cm^{-1} M^{-1}	λ_{em} / nm	Stokes shift /cm^{-1}	Φ	τ / ns
MeCN	331	n/a	364	2650	0.87	0.67
C_6H_{12}	335	n/a	362	2200	0.81	n/a
CH_2Cl_2	335	65600	367	2600	0.91	0.68

The BCPEB molecule has been synthesised and incorporated into Zr- and Hf-based UiO-family metal-organic frameworks (MOFs) by Marshall *et al*.[15] The MOF system has been discussed in **Chapter 4**. The BCPEB molecule crystallised in an orthorhombic crystal system with *Pbca* space group; the data can be found in Cambridge Crystallographic Database (Reference code = GEDPUD). The solid-state UV-vis absorption and emission spectra of BCPEB are shown in **Figure 7.4**. The absorption spectrum of the powder was collected using diffuse reflectance, with the sample mixed with $BaSO_4$. The extended long-wavelength tail of the absorption spectrum may be caused by the scattering of the light by the powder. Both absorption and emission spectra occur at significantly longer wavelength than those in solution, which could be due to an increase in intermolecular interaction in the solid-state. The quantum yield of the BCPEB crystal has not been measured, but it is likely that it is lower than that of the Zr-based BCPEB MOF at ~17.3%.[15]

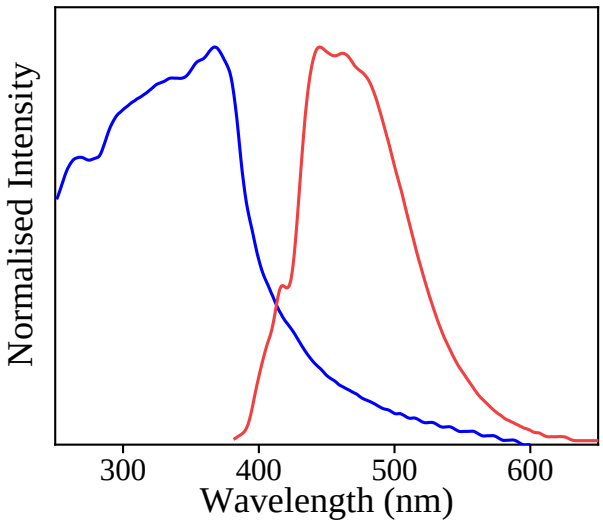

Figure 7.4. Solid-state absorption (blue) and emission (red) spectra (λ_{ex} = 367 nm) of BCPEB. Redrawn from Marshall *et al.*[15]

In this thesis, UV-vis absorption, excitation, and fluorescence emission spectra of BCPEB were investigated in various solvents at ambient temperature and also at 77 K. A combination of single-crystal X-ray diffraction, UV-vis absorption and emission spectroscopy as a function of pressure in a diamond anvil cell (DAC) were also carried out for the BCPEB crystal to understand the effect of pressure on the crystal structure and its electronic spectra, in relation to the intermolecular interactions within the crystal.

7.2 Experimental

It should be noted that the BCPEB crystal was synthesised and provided by Dr Ross Marshall and Prof Ross Forgan of the University of Glasgow. The X-ray diffraction data were collected in collaboration with Ms Gemma Turner and Dr Stephen Moggach of the University of Western Australia. The crystal structures were solved and refined by the author.

7.2.1 Synthesis of BCPEB

Methyl 4-ethynylbenzoate (15.59 mmol, 2.5 eq.) was dissolved in triethylamine (160 mL) by stirring. The solution was then degassed for 10 minutes, then 1,4-diiodobenzene (6.24 mmol, 1 eq), bis(triphenylphosphine)palladium(II) dichloride (0.42 mmol) and CuI (0.38 mmol) were added. The mixture was left to stir at 50ºC overnight under N_2 atmosphere. The mixture was removed from the heat and cooled to room temperature then the product was collected by vacuum filtration and washed

with hexane until washing were colourless. The product was then stirred overnight in water (300 mL) then collected by vacuum filtration. The product was stirred using as small as a possible volume of dichloromethane, then collected by vacuum filtration until dried. The single crystals were grown by slow evaporation in $CDCl_3$.

7.2.2 Solution-phase Sample Preparation

Crystalline BCPEB was dissolved in analytical grade toluene, $CHCl_3$, dimethylformamide (DMF) or ethanol to obtain a concentration of 1.52 μM, 1.62 μM, 1.42 μM and 1.25 μM, respectively. These solvents were chosen as they have different relative polarities of 0.099, 0.259, 0.386 and 0.654, respectively. The concentration of solutions was adjusted to obtain an absorbance of less than 0.1 at 336 nm for fluorescence measurement.

7.2.2.1 UV-Vis Absorption Spectroscopy

Absorption spectra of the BCPEB solutions were collected using a CARY 300 UV-visible Spectrophotometer. Optically identical 0.8 mL cuvettes with 10 mm path length (Starna Scientific Ltd) were used for all measurements.

7.2.2.2 Fluorescence *S*pectroscopy

Fluorescence spectra were collected using a FluoroMax®-P Spectrofluorimeter (Jobin-Yvon HORIBA) with FluorEssence™ v.3.5 software. Excitation and emission slit bandwidths of 3 nm were used. The spectra were corrected for the wavelength-dependence and variation of the excitation lamp intensity. As for room-temperature measurements, solutions were contained in a 0.8 mL fused-silica fluorescence cuvette with 10 mm path length.

The fluorescence spectroscopy at 77K was carried using the FL-1013 Liquid Nitrogen Dewar Assembly (Jobin-Yvon HORIBA) with the FluoroMax®-P Spectrofluorimeter. The low-temperature sample device is illustrated in **Figure 7.5**. Ethanol was used as a solvent as it forms a transparent glass at 77 K. The solution was contained in a fused-silica NMR tube which was immersed in liquid N_2 in the fused silica dewar.

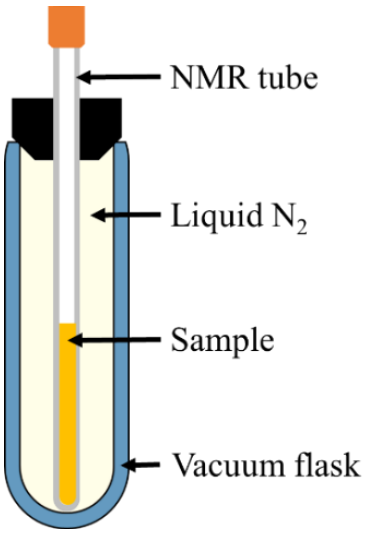

Figure 7.5. Schematic of the low-temperature sample setup that is placed in the sample chamber of Fluoromax-P instrument.

7.2.3 High-pressure Crystallography

A single crystal of BCPEB was measured with a diamond anvil cell (DAC) in Daphne oil 7373 (Idemitsu Kosan Co., Ltd.) as a pressure transmitting medium, using synchrotron radiation, as explained in **Chapter 3**. The X-ray diffraction measurements were carried out from 0.18 GPa to 5.96 GPa, but the crystal structure could only be obtained up to ~3.51 GPa.

The crystal structure at 0.18 GPa was solved using SHELXT[16] algorithm within Olex2[17] software. The atoms within the structure were then labelled and numbered using CRYSTALS[18]. The structure was then refined isotropically against F^2. All atomic bonds between two atoms (1,2 distances) and bonds of two atoms connected to the same atom (1,3 distances) were restrained to ensure the phenyl ring was not distorted. Vibrational and thermal similarity restraints were also applied to the carbon atoms. Hydrogen atoms were added geometrically and left to ride the host atom during the refinement.

The crystal structures at higher pressure were also refined isotropically against F^2 using the crystal structure at 0.18 GPa as a starting structure. All 1,2 and 1,3 distances were also restrained. Vibrational and thermal similarity restraints were also applied, and hydrogen atoms were placed geometrically and to ride the host atoms. Structure refinements were carried out to the maximum resolution of each sample as determined from the intensity statistics.

7.2.4 High-pressure UV-Vis absorption spectroscopy

A crystal of BCPEB was loaded into a DAC alongside to a ruby chip with Daphne oil 7373 as the hydrostatic pressure medium, and the DAC then placed in the bespoke measurement setup, as described in **Chapter 3**. The absorption spectra were collected at a pressure series up to 4.37 GPa.

7.2.5 High-pressure Fluorescence emission spectroscopy

Multiple crystals of BCPEB were loaded into a DAC alongside a ruby chip with Daphne oil 7373 as pressure transmitting medium (PTM). The DAC was then placed in the custom-built measurement setup, as described in **Chapter 3**. A single wavelength 365-nm Ocean Optics LS-LED was used as the excitation source. A band-pass filter (Semrock Brightline 370/36) was inserted in the excitation path to narrow the excitation bandwidth. The fluorescence emission spectra were collected at a pressure series closely matched those used for the UV-vis absorption measurements, up to 4.26 GPa. A correction for the diamond absorption was applied to all spectra.

7.3 Results and Discussions

7.3.1 Solution-phase spectra at room temperature

UV-vis absorption, excitation and emission spectra of BCPEB in toluene, chloroform, DMF and ethanol are displayed in **Figure 7.6**. The absorption spectra show similar spectral profiles in the different solvents, with a small difference in the position of the absorbance maximum. In toluene and chloroform, the absorbance maxima were found at 337 nm, while in DMF and ethanol the maxima were found at 335 nm and 333 nm, respectively. The absorption and emission spectra show a very similar profile to that observed for BPEB (see **Figure 7.2**), but with a ~20 nm shift to longer wavelength, in agreement with previous reports.[2]

The excitation spectra closely resemble the absorption spectra, but the long-wavelength shoulder has higher relative intensity in the excitation spectra, suggesting that the quantum yield is dependent on the excitation wavelength. (Distortion of the excitation spectral profile by the inner-filter effect is unlikely, given that the maximum absorbance was less than 0.1).

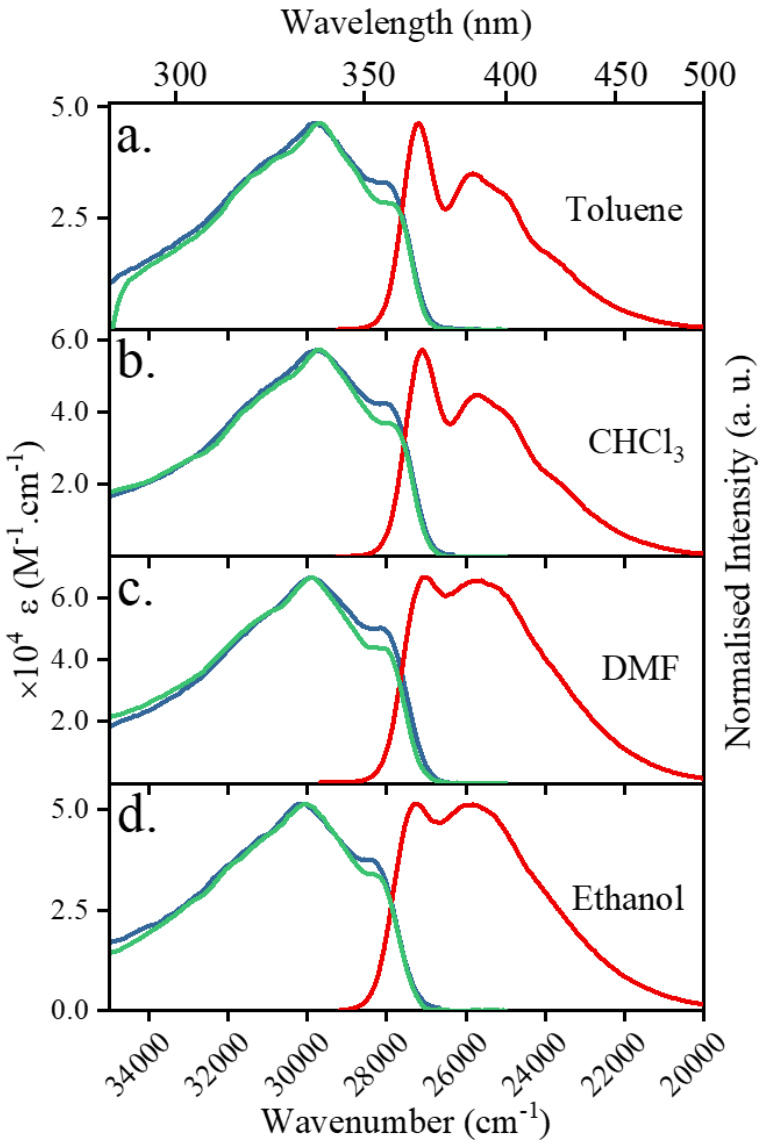

Figure 7.6. The UV-vis absorption (green), excitation (blue, λ_{ex} = 365 nm) and fluorescence (red, λ_{em} = 386 nm) spectra of BCPEB solutions in (a) toluene, (b) chloroform, (c) DMF and (d). The figure is arranged as the solution with at the topmost having the lowest relative polarity.

The emission spectral profile depends on solvent, with more clearly resolved vibronic structures evident in less polar solvents. This is similar to BPEB, which showed more resolved vibronic structure in cyclohexane compared to methanol.[2, 3]

In all solvents, the emission spectra were found to be independent of excitation wavelength, and the excitation spectra independent of emission wavelength, as illustrated in **Figure 7.7**. This is consistent with the behaviour reported for BPEB by Beeby *et al.*[2] that there is only one emitting species. As for BPEB, this can be explained by a higher rotational barrier in the excited state, which guides the twisted Franck-

Condon species to relax to the lower energy planar conformation from which emission occurs. That is to say that although the absorption arises from multiple conformers, emission only arises from the planar conformer.

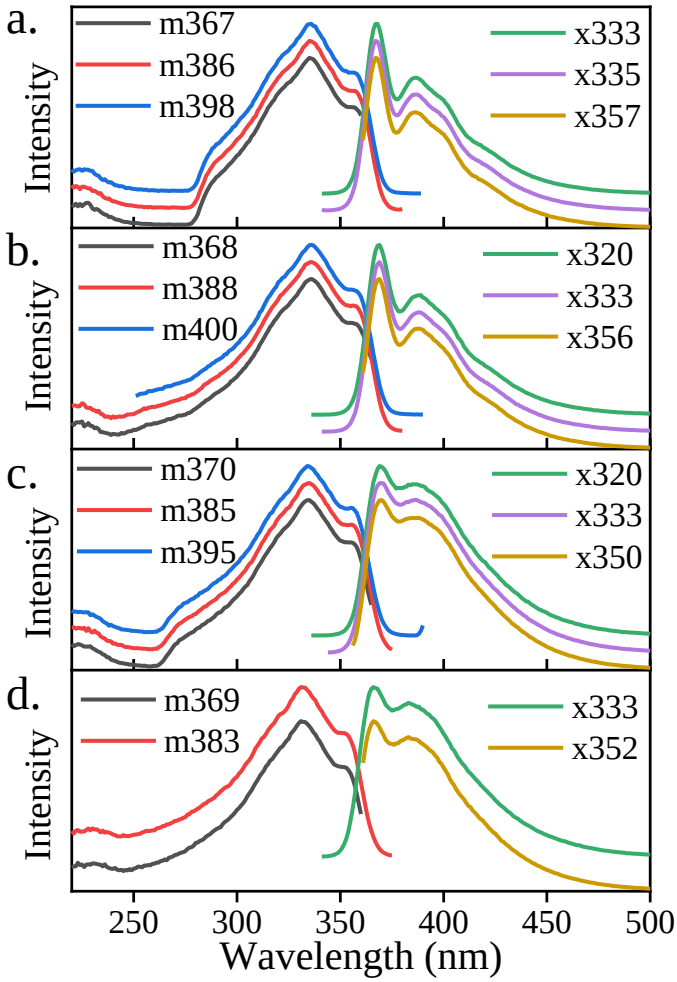

Figure 7.7. The excitation and emission spectra of BCPEB, at various emission and excitation wavelengths, respectively, in (a) Toluene, (b) $CHCl_3$, (c) DMF and (d) Ethanol. The intensity is normalised, and an offset was applied for clarity.

7.3.2 Fluorescence Spectra at 77 K

The excitation and emission spectra of the BCPEB in ethanol at 77 K, are shown in **Figure 7.8**. The vibronic structure is resolved much more clearly than at room temperature. The lowest energy excitation peak at ~360 nm at room temperature, seen as shoulder at room temperature, becomes the most intense band at low temperature. The excitation and emission spectra show a mirror-image relationship in their vibronic structure, although the relative intensities of the vibronic bands are not identical.

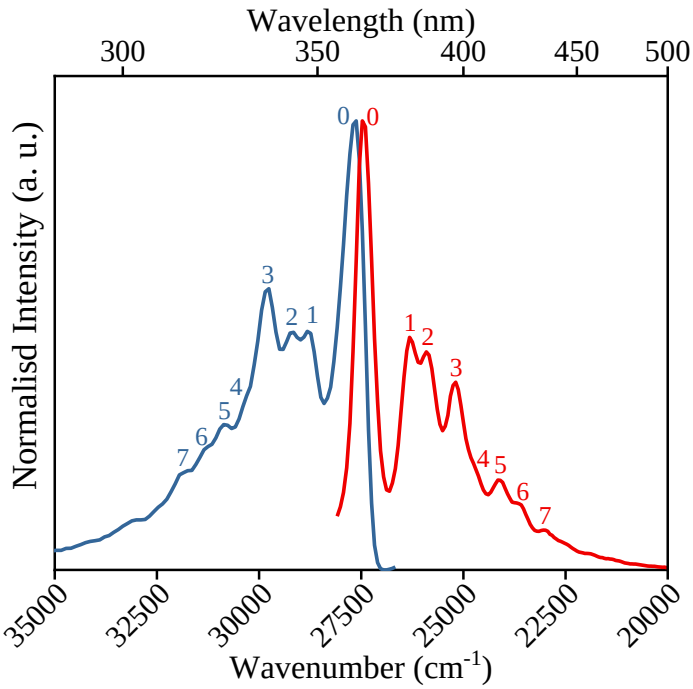

Figure 7.8. The excitation (blue) and emission (red) spectra of BCPEB in ethanol at 77K.

The highest energy emission (27445 cm^{-1}) and lowest energy excitation (27654 cm^{-1}) bands, the 0-0 transitions, show a significant degree of overlap, indicating a small or negligible relaxation of the Franck-Condon structure. As for BPEB, it can be inferred that the planar conformer is preferentially populated at 77 K.

The vibronic transitions, as numbered in **Figure 7.8**, are listed in **Table 7.2** and compared with those for the computed absorption spectrum of BPEB reported by Roy *et al.*,[13] together with their assignments. There is excellent agreement, indicating that apart from the additional, terminal carbomethoxy groups, the vibrational properties of BCPEB are virtually identical to BPEB.

As shown in **Figure 7.9**, the excitation and emission spectra are independent of emission and excitation wavelengths, respectively. This suggests that it is possible that, at 77K, only the planar conformer is present.

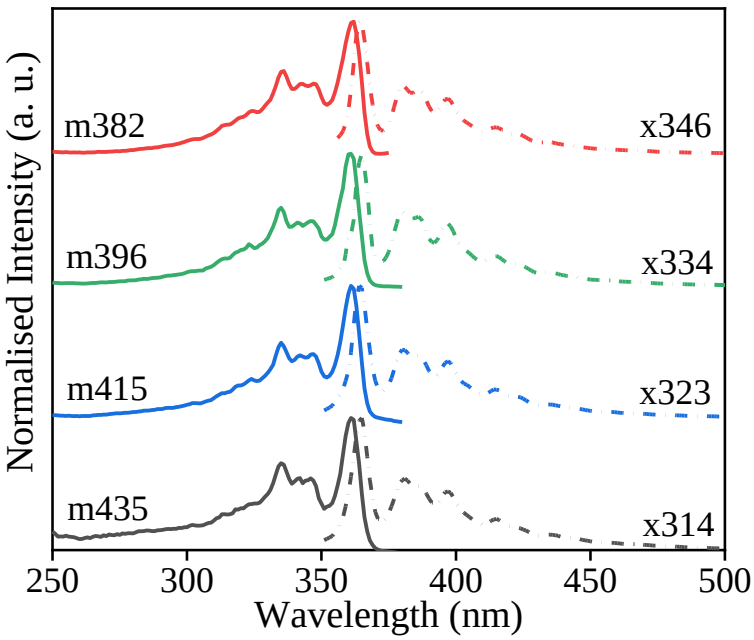

Figure 7.9. The excitation and emission spectra of BCPEB in ethanol at 77K, collected at various emission and excitation wavelengths, respectively.

Table 7.2. Vibronic bands of BCPEB in frozen ethanol compared to the computed values for BPEB and their assignments from literature.[13]

Transitions	Excitation		Emission		BPEB	Mode assignment[13]
	$\bar{\nu}_x$ / cm^{-1}	$\Delta\bar{\nu}_x$ / cm^{-1}	$\bar{\nu}_m$ / cm^{-1}	$\Delta\bar{\nu}_m$ / cm^{-1}	$\Delta\bar{\nu}$[13] /cm^{-1}	
0	27654	-	27445	-	-	0-0 transition
1	28789	1135	26293	1152	**1096**	Central ring C-H scis.
2	29186	1532	25896	1549	**1601**	Central ring C=C str.
3	29809	2155	25198	2247	**2169**	C≡C str. & [(central ring C-H scis.) + 2 quanta] (progression)
4	30393	2739	24706	2739	**2744**	Central ring C=C str. + central ring C-H scissoring (combination)
5	30865	3211	24101	3344	**3242**	C≡C str. + central ring C-H scs., (combination) & 2 quanta of C=C (progression)
6	31341	3687	23612	3833	**3770**	C≡C str. + central ring C=C str. (combination)
7	31850	4196	23006	4439	**4338**	C≡C str. + (2 quanta) (progression)

*str. = stretching, scis. = scissoring

7.3.3 High-Pressure X-ray Crystallography

It was reported previously by Marshall *et al.* the BCPEB crystal formed in orthorhombic crystal system with *Pbca* space group (*a*=7.186(2) Å, *b*=5.9324(19) Å, *c*=45.765(14) Å, V = 1950.8(11) Å^3, Z = 4).[15] The crystal structures obtained in the present work were found in the same crystal system and space group, but with different value of lattice parameters (**Table 7.3**). Moreover, the unit cell volume of the 0.18 GPa structure is significantly larger than the structure of ambient pressure, reported by Marshal *et al.*[15] As has been discussed in **Chapter 6**, the reason for this larger unit cell volume is likely due to systematic error in the high-pressure crystallographic data. However, this does not change the narrative. The content of the unit cell of the BCPEB crystal is shown in **Figure 7.10**.

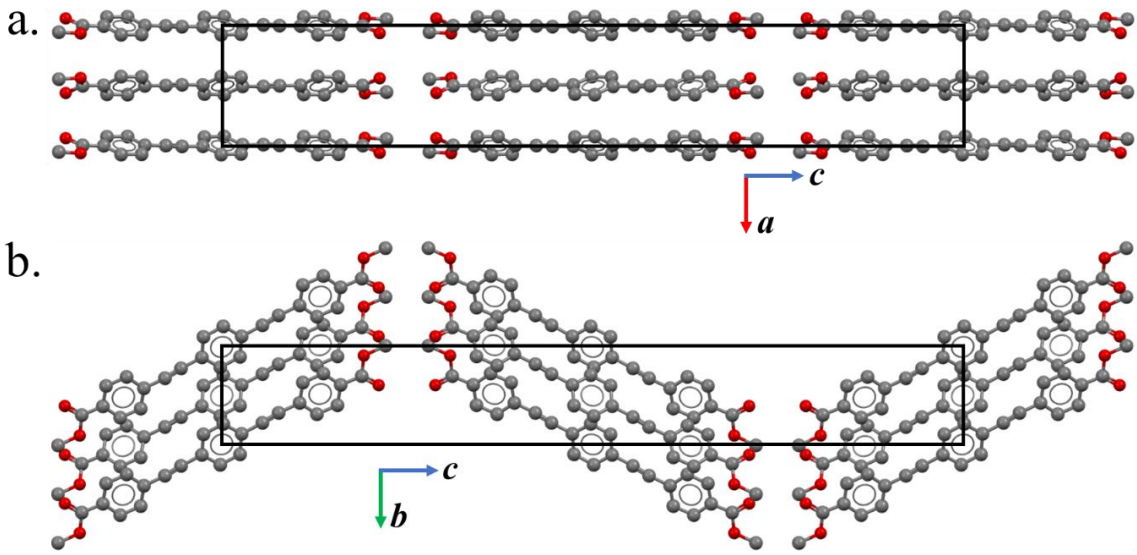

Figure 7.10 The unit cell of the BCPEB crystal seen from (a) b-axis and (b) a-axis. Colour scheme: O – red and C – grey. Hydrogen atoms were omitted for clarity

The unit cell dimensions were obtained up to 5.96 GPa, but the crystal structure can only be obtained up to 3.51 GPa, due to worsening of quality of data at higher pressure. The unit cell parameters at various pressures are given in **Table 6.7**. The unit cell volume appears to shrink by ~19% at 3.51 GPa, as illustrated in **Figure 7.11 a**. It can also be seen from **Figure 7.11 b** that the crystal contracts anisotropically, with the *a*-axis shortening by ~10% at 3.51 GPa, while *b* and *c* axes contracted only by ~6% and

4%, respectively. The *a*-axis is the direction of the molecular stacking, which could indicate that pressure will affect strongly to the stacking interactions of the molecules.

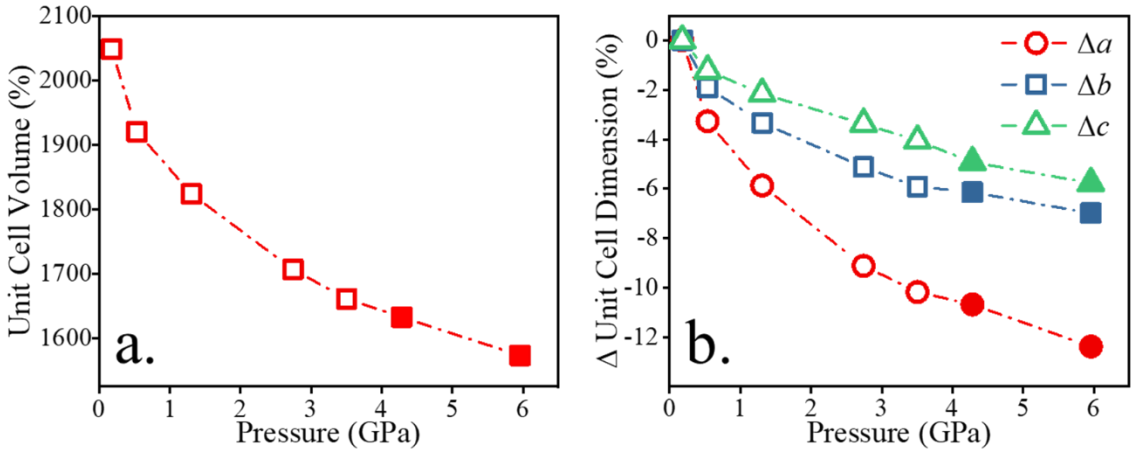

Figure 7.11. (a) Unit Cell Volume and (b) the change in unit cell dimensions (%) as a function of pressure. The crystal structure c only be obtained at pressures shown by the hollow symbols.

Table 7.3. The unit cell parameters of the Ph_7C_7H crystal at various pressures. The pressures where the structure unresolved are highlighted in yellow.

Pressure / GPa	***a*** **/ Å**	***b*** **/ Å**	***c*** **/ Å**	**V / Å³**
0.18	7.4006(11)	6.0292(12)	45.91(7)	2048.9(3)
0.54	7.1587(8)	5.9147(9)	45.35(4)	1920.4(12)
1.31	6.9663(7)	5.8281(7)	44.92(3)	1824.0 (13)
2.74	6.7257(8)	5.7204(8)	44.36(4)	1706.6(15)
3.51	6.6475(8)	5.6727(8)	44.05(4)	1661.1(15)
4.28	6.6102(11)	5.6588(10)	43.65(5)	1632.7(17)
5.96	6.4844(9)	5.608(1)	43.26(4)	1573.1(16)

The crystal structure was refined using isotropic thermal parameters due to the lack of data completeness caused by the shading from the DAC. The overall atomic displacement parameters amplitudes (i.e. thermal motion of atoms, see **Figure 7.12**) were decreasing with increasing pressure, which indicates the thermal motion of the BCPEB molecule become more restricted. Moreover, with increasing pressure, the

molecular arrangement became more packed, as can be seen in **Figure 7.13**. From **Figure 7.13**, at 0.18 GPa, void can be seen clearly in between molecules, which could allow the phenyl rings of the molecule to perform torsional vibrations. At higher pressure, however, the void disappeared, causing more restricted motion of the molecules.

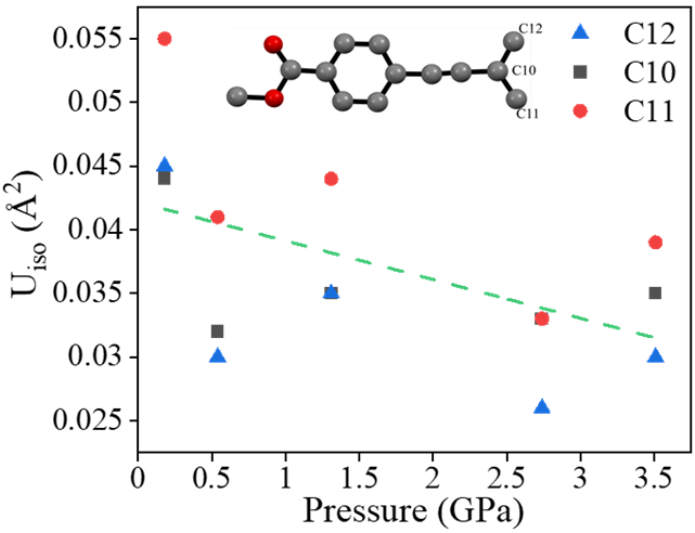

Figure 7.12. The isotropic atomic displacement parameters (U_{iso}) of the central aromatic ring (C10 (black), C11(red) and C12(blue)) of BCPEB in a crystal. Green line indicates that overall ADP is decreasing with increasing pressure.

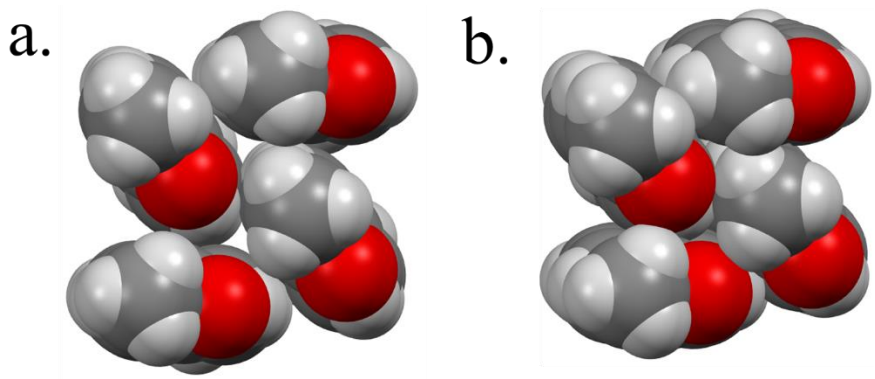

Figure 7.13. The packing of BCPEB molecules at (a) 0.18 GPa and (b) 3.51 GPa. Colour scheme: O – red, C – grey and H – white.

7.3.4 Measurement of Intermolecular Distances

From the crystal structure, it is found that the molecules are arranged in a distorted T-shaped arrangement, as seen from the molecular length direction. The T-shaped arrangement is typical in a crystal of aromatic molecules that have a long and short

axis, such as naphthalene, anthracene and phenanthrene.[19] On the other hand, disc-like aromatic molecules such as pyrene and perylene tend to adopt a stacked molecular arrangement. The T-shaped arrangement is effective to avoid π-π orbitals repulsion while preferring the CH···π interactions.

The intermolecular distance parameters were measured to quantify the change of intermolecular interactions with increasing pressure. The intermolecular distance parameters between central phenyl rings consisted of centroid distance ($\boldsymbol{C}_{PP}$), centroid-to-plane distance ($\boldsymbol{P}_{PP}$) and intermolecular plane angle (∠) were measured using a *Measure Distance* routine in Mercury.[20] Displacement distance ($\boldsymbol{d}_{PP}$) was calculated using **Equation 7.1**.

$$\boldsymbol{d} = \boldsymbol{C} \sin\left(\cos^{-1}\frac{\boldsymbol{P}}{\boldsymbol{C}}\right)$$

Equation 7.1

The phenyl-ethynyl centroid distance ($\boldsymbol{C}_{PE}$) were measured, and the phenyl-ethynyl displacement distance ($\boldsymbol{d}_{PE}$) were calculated using the same method as the $\boldsymbol{d}_{PP}$ using the same value of $\boldsymbol{P}_{PP}$. The schematic of the intermolecular distances is illustrated in **Figure 7.14**. The change in the distances as a function of pressure is summarised in **Table 7.4** and also depicted graphically in **Figure 7.15**.

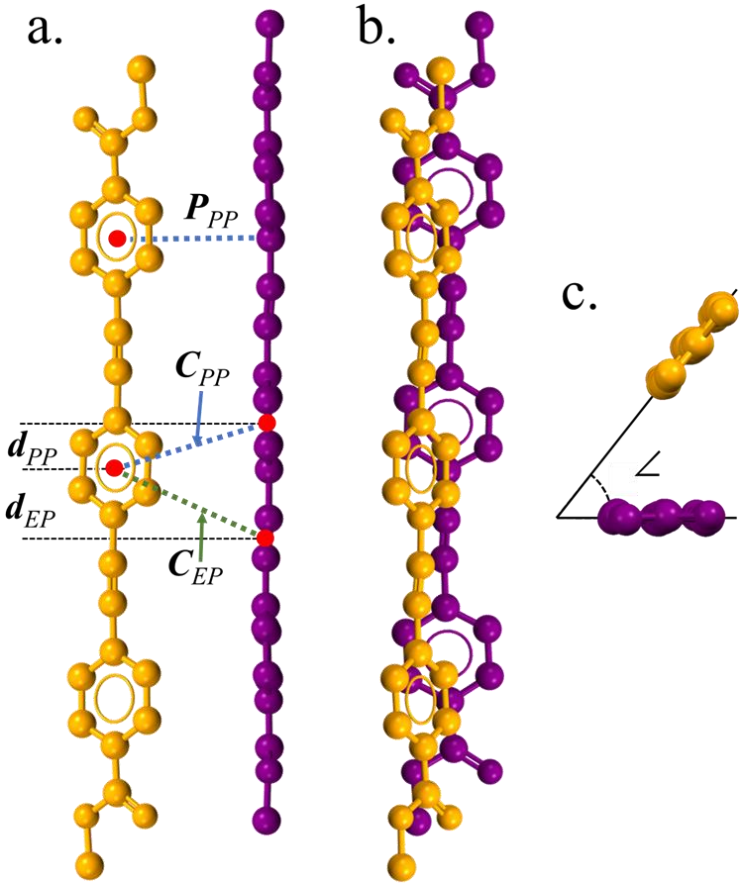

Figure 7.14. The stacking arrangement of neighbouring molecules and the definition of the parameters used to measure intermolecular distance. (a) The inter-phenyl centroid distance (C_{PP}), phenyl-ethynyl centroid distance (C_{EP}), plane to centroid distance (P_{PP}), lateral displacement of the phenyl-phenyl (d_{PP}) and ethynyl-phenyl (d_{EP}) distances, viewed along the direction of the plane. (b) Viewed from the perpendicular direction. (c) The intermolecular plane angle (∠) viewed along the length of the molecules.

Table 7.4. The inter-phenyl and phenyl-ethynyl distances of the BCPEB central phenyl ring at various pressures.

Pressure / GPa	C_{PP} / Å	P_{PP} / Å	d_{PP} / Å	∠ / °	C_{PE} / Å	d_{PE} / Å
0.18	4.773	4.508	1.568	52.63	4.994	2.149
0.54	4.643	4.353	1.615	51.6	4.815	2.058
1.31	4.541	4.234	1.641	50.35	4.685	2.006
2.74	4.415	4.081	1.685	48.38	4.532	1.971
3.51	4.369	4.03	1.687	47.71	4.476	1.948

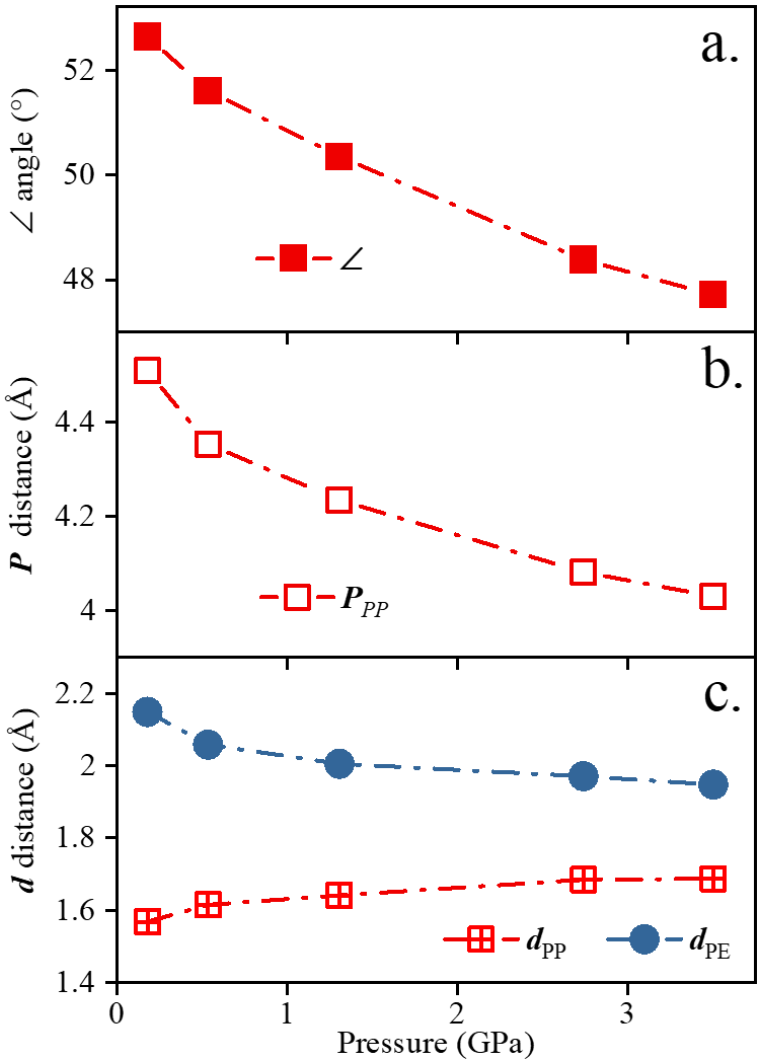

Figure 7.15. (a) the intermolecular plane angle, (∠, red square), (b) centroid-to-plane distance (P_{PP}, red square) and (c) the displacement distance of the inter-phenyl (d_{PP}, red square) and phenyl-ethynyl (d_{PE}, blue circle).

Figure 7.15 shows that the intermolecular planar angle (∠) and interplanar distance (***P***) decrease with increasing pressure by ~5° and ~0.5 Å, respectively, with a change in the lateral displacement distances of only ~0.2 Å. This suggests that with increasing pressure, the molecules are moving towards a more packed arrangement, which increases intermolecular interactions. This has been illustrated visually in **Figure 7.13**. However, it is unlikely that there is a strong π-π electronic interaction due to large intermolecular angle and distances. The molecular structure at higher pressure shows a slight in-plane twist, causing the molecule to become slightly more S-shaped within

the plane, as shown in **Figure 7.16**. This change is caused by the pressure along c-axis, which compress the length of the molecule.

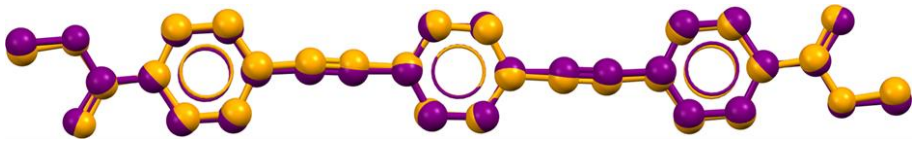

Figure 7.16. Comparison of the molecular structure at 0.18 Gpa (purple) and 3.51 GPa (orange).

7.3.5 High-Pressure Electronic Spectra

The UV-vis absorption spectra were collected from thin and colourless crystal (~10 μm). The absorption spectra measurements could only be carried out for wavelengths greater than ~350 nm due to strong absorption by diamond at shorter wavelengths. The UV-vis absorption spectra were collected at 0.03 GPa, 0.25 GPa, 0.41 GPa, 1.04 GPa, 2.01 GPa, 3.32 GPa, 3.76 GPa, and 4.37 GPa, as shown in **Figure 7.17**. The absorption spectrum at ambient pressure occurs at a longer wavelength than that measured in solution by ~13 nm (~1000 cm^{-1}), measured from the shoulder of the spectrum. This due to the presence of intermolecular interactions in the crystal, which lowers the potential energy of the excited state relative to the ground state, similar to the solvent effects.

Fluorescence emission spectra were measured at the ambient pressure, 0.27 GPa, 0.49 GPa, 1.02 GPa, 2.07 GPa, 2.98 GPa, 3.70 GPa and 4.26 GPa. These pressures were chosen to be close to those used in the UV-vis absorption measurements. The fluorescence spectra with normalised intensity at various pressures are displayed in **Figure 7.17** alongside the UV-vis absorption spectra. The fluorescence spectrum at ambient pressure is found at longer wavelength compared to that in solution-phase by ~75 nm (~4600 cm^{-1}), measured from the emission peak. The fluorescence spectrum at ambient pressure also shows a smaller peak at shorter wavelength ~415 nm but disappeared at higher pressure.

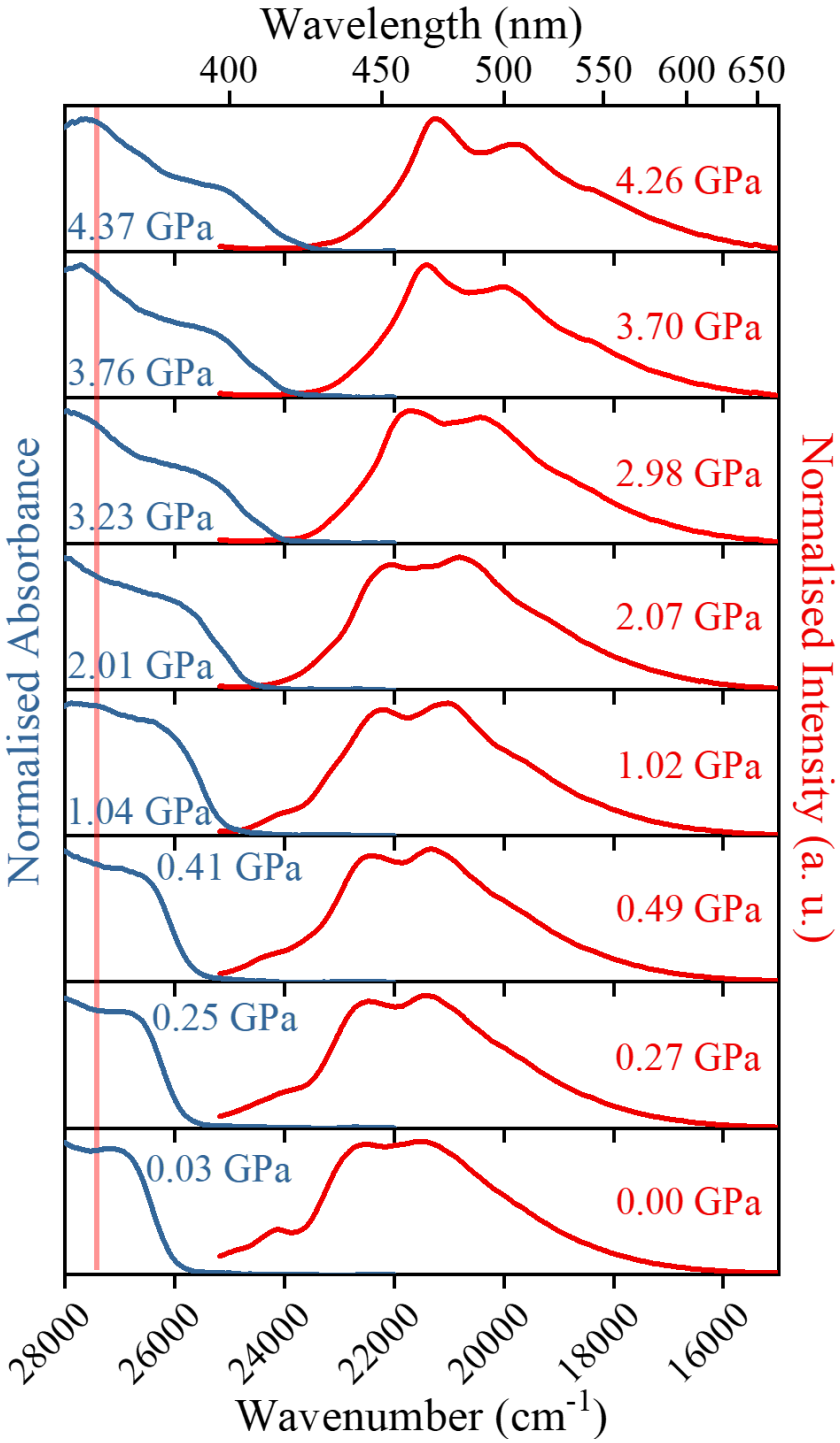

Figure 7.17. The UV-vis absorption spectra (blue) and emission spectra (red) of BCPEB in various pressures. The pink line indicates the excitation wavelength for the emission measurement.

Table 7.5. Wavelength and wavenumber of absorption red-edge (half-maximum) of BCPEB as a function of pressure.

Pressure / GPa	Absorption Edge / nm	Absorption Edge / cm^{-1}
0.03	379	26410
0.25	381	26250
0.41	384	26060
1.04	391	25580
2.01	398	25160
3.23	404	24760
3.76	406	24630
4.37	410	24390

At the highest pressure, ~4.3 GPa, it is notable that both absorption and emission spectra resemble the solution-phase spectra (**Figure 7.6**), with clear vibronic structure in the emission spectrum. According to the emission phenomenon in solution-phase, the emission spectrum of the crystal at this pressure can be assigned as the emission from the planar conformer. The absorption spectrum also resembles the shape of the spectrum in solution-phase, where the long-wavelength shoulder arises from the planar conformer, while the absorption at shorter wavelength is due to the thermally populated twisted conformers. The absorption spectrum shoulder is found at 396 nm (~25200 cm^{-1}) in the crystal, at longer wavelength than that in solution phase, at 365 nm (~27400 cm^{-1}). Moreover, the 0-0 emission band is found at ~21200 cm^{-1}, compared to ~27200 cm^{-1} in solution phase, which indicates significant stabilisation of the excited state relative to the ground-state by intermolecular interactions in crystal. In the crystal, the Stokes shift is ~3200 cm^{-1}, compared to merely ~1000 cm^{-1} in solution. This indicates that much greater relaxation occurs from the Franck-Condon state to the emitting state in crystal. This is due to relaxation of the local environment

about the excited molecule, as a result of the change in the electronic structure on excitation. Computational studies[13] have shown that in the planar ground state the three phenyl rings have a benzenoid structure, with the electron cloud delocalised over the rings, whereas in the excited state the central phenyl ring adopts a much more quinoidal structure.

At 3.7 GPa, there is little change in the absorption and emission spectra, but at ~3 GPa, the vibronic structure in the emission spectrum starts to broaden and become less distinct. The absorption spectral profile little-changed, but there is a slight blue-shift of ~350 cm^{-1} compared to the spectrum at ~4.3 GPa.

At pressure below 3 GPa, the long-wavelength shoulder on absorption spectrum becomes less distinct with decreasing pressure and is not apparent below 1 GPa. The red-edge of the absorption is shifted to shorter wavelength by ~1700 cm^{-1} at ambient pressure. However, the magnitude of the shift is the most significant at pressures between 1 GPa and ambient pressure, which shifted by ~850 cm^{-1}. The change in absorption spectrum with decreasing pressure is consistent with an increase in the torsional mobility and increased relative population of twisted conformers that absorb at shorter wavelength, as reported by Roy *et al*.[13] This is consistent with the relatively large increase in the interplanar distance in the crystal between 0.54 GPa and 0.18 GPa (see **Figure 7.15**). At the lower pressures, the torsional motion may be less hindered in the crystal than in solution. With decreasing pressure, the vibronic structure of emission spectrum broadens and becomes unresolved, but between 1 GPa and ambient pressure, there is little shift in the emission wavelength, only a small shift to the blue by ~350 cm^{-1}. The difference in magnitude of the blue-shifts of the absorption and emission spectra indicates that the emission spectrum is dominated by relaxed planar conformation. However, the change in emission spectral profile suggests an increase in conformational heterogeneity of the emitting species with decreasing pressure. The appearance of a short-wavelength tail on the emission spectrum at lower pressures may be indicative of the emission from unrelaxed twisted structures, which deviate significantly from planarity.

To better analyse the change in vibronic structure of the emission spectrum as a function of pressure, deconvolution of the spectra was carried out. The deconvolution

was done with Lorentzian peak function using the *Fitting* routine within the Origin® program. The emission spectrum at 4.26 GPa was deconvoluted first, and the peak parameters were used as starting parameters for the emission spectra at lower pressures. The full-width half-maxima were fixed, while the wavelength maxima and area under the curve were let to be refined freely. (The deconvolution, did not consider the short-wavelength tail at ~415 nm (~24100 cm^{-1}) that was found at lower pressure.)

The results of the deconvolution are shown in **Figure 7.18**. The wavelength maxima of the deconvoluted bands at various pressure are listed in **Table 7.6** and illustrated graphically in **Figure 7.19 a**. The ratio of the intensity between the shortest-wavelength band (Peak 1) and the second vibronic band (Peak 2) is shown as a function of pressure in **Figure 7.19 b**.

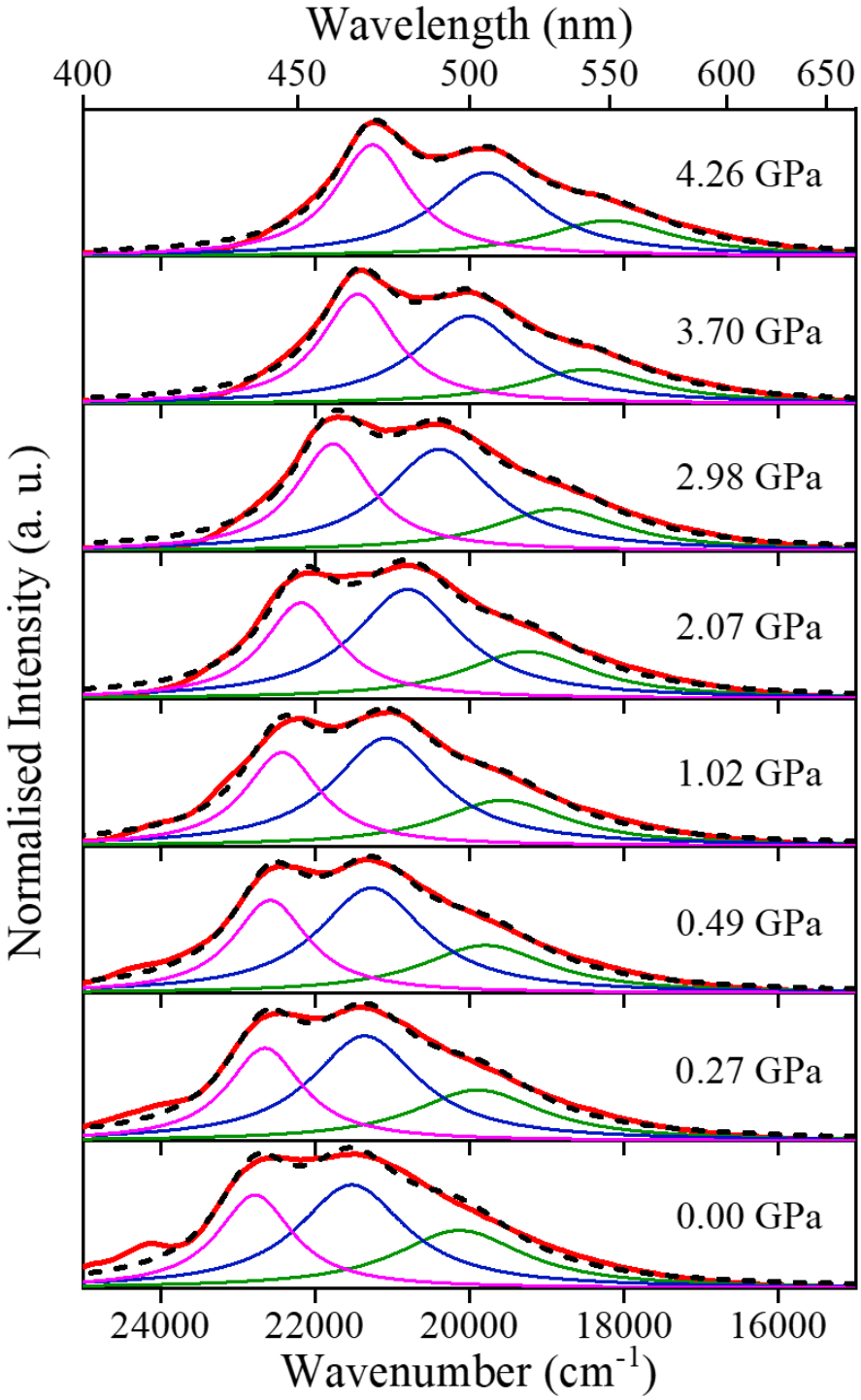

Figure 7.18. The deconvolution of the fluorescence emission spectra of BCPEB in various pressure. The red line is the actual fluorescence spectrum; the dashed black line is the cumulative fitted spectrum. The pink, blue and green peaks are labelled as Peak 1, 2 and 3 respectively.

Table 7.6. Wavelength and wavenumber of deconvoluted fluorescence peaks of BCPEB.

Pressure / GPa	Peak 1		Peak 2		Peak 3	
	/ nm	/ cm^{-1}	/ nm	/ cm^{-1}	/ nm	/ cm^{-1}
0.00	439	22780	465	21520	497	20130
0.27	442	22650	468	21350	503	19890
0.49	443	22580	470	21270	505	19790
1.02	446	22430	475	21070	511	19570
2.07	451	22180	481	20800	519	19260
2.98	459	21770	490	20390	530	18860
3.70	466	21440	500	20010	542	18460
4.26	470	21260	506	19780	550	18200

From **Figure 7.19 b**, it can be seen that the intensity ratio of Peak 1 and Peak 2 decreases considerably with decreasing pressure. This can be compared with the simulated absorption spectra of BPEB reported by Roy *et al*,[13] which showed that the 0-0 band becomes less intense, relative to the other vibronic bands, with increase in the torsional angle of the central ring. The change in vibronic intensity distribution in the fluorescence spectrum of BCPEB as a function of pressure, thus confirms that there is an increased contribution to the emission from twisted conformers as the pressure is decreased.

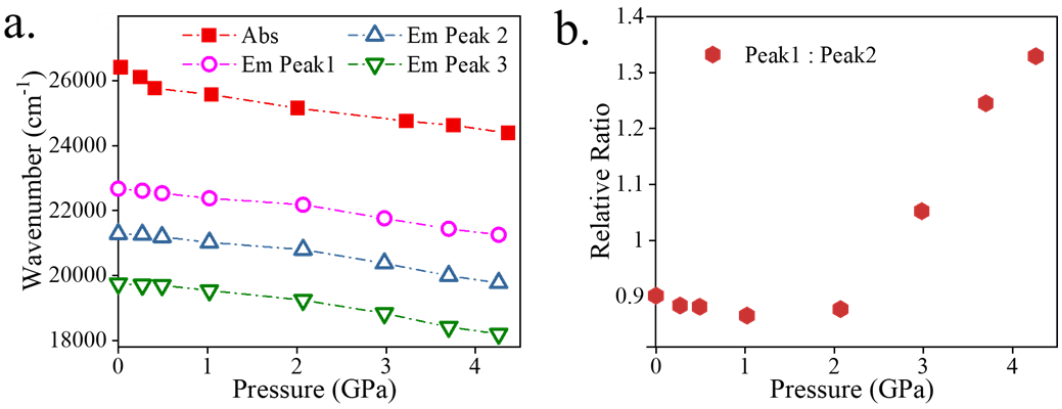

Figure 7.19. (a) Pressure-dependence of the red edge (half maximum) of the absorption spectrum (red rectangle) and the deconvoluted fluorescence spectrum peaks (pink circle, blue triangle and green flipped-triangle). (b) The pressure-dependent relative intensity ratio of the Peak 1:2.

7.4 Conclusions and Further Work

Solution-phase UV-vis absorption, excitation, and emission spectra of BCPEB have been measured in various solvents. Both absorption and emission spectra of the BCPEB were found at a longer wavelength than the analogue molecule, BPEB, caused by more delocalised conjugation of π-electrons across the terminal carbomethoxy groups. Excitation and fluorescence spectra at 77K reveal well-defined vibronic bands, showing a mirror image relationship between excitation and emission, with the 0-0 transition at ~27550 cm^{-1}. The vibronic wavenumbers are in excellent agreement those reported for BPEB molecule. Therefore, it can be concluded that, as in the case of BPEB, the emitting species of BCPEB in solution is the planar conformer.

High-pressure single-crystal X-ray diffraction has been successfully carried out for BCPEB in a DAC with Daphne oil 7373 as the pressure-transmitting medium (PTM), using synchrotron radiation. The crystal structure was obtained from 0.18 GPa to 3.51 GPa. The BCPEB molecules crystallise in orthorhombic crystal system with *Pbca* space group. The structure experienced anisotropic compression with increasing pressure. Also, the intermolecular distances shortened, and intermolecular angle narrowed, causing a more stacked arrangement of molecules. Moreover, at higher pressure, the intermolecular void getting smaller, which caused thermal motion became more hindered with increasing pressure.

High-pressure UV-vis absorption and fluorescence emission were also successfully carried out. At the highest pressures, around 4 GPa, both absorption and emission

spectra resemble those seen in solution, indicating absorption by both planar and twisted conformers, and emission from a relaxed planar state. There is significant stabilisation of the excited state relative to the ground state by intermolecular interactions.

As pressure decreased, both absorption and emission spectra experienced blue-shifts. The vibronic structure of the emission spectra also became less resolved, but fluorescence is still dominated by a relaxed planar conformation, although with an increase in conformational heterogeneity. This caused by the increase in free space/void within the crystal, which makes it possible for the BCPEB molecule to experience torsional motion of its phenyl rings. Change in relative intensities of vibronic bands in the emission spectra confirms that the phenyl rings of the BCPEB experience increasing torsional motion at lower pressure. A short-wavelength tail that can be observed on the emission spectrum at lower pressure may be indicative of unrelaxed twisted structures which deviate significantly from planarity.

This work has shown that the absorption and emission properties of BCPEB in the crystalline state can be interpreted in terms of the torsional dynamics of the molecule, analogous to the previous interpretation of the photophysics of BPEB in solution phase presented by Beeby and coworkers.[2,12,13]

Follow-up experiments, such as solid-state quantum yield measurement, time-resolved absorption, and fluorescence spectroscopy, could be carried out to get a better understanding of the effect of molecular interaction on the molecular dynamics and photophysics within the crystal. A better-quality diamond could be used to extend the excitation wavelength range to shorter wavelengths, and the use of a range of excitation wavelengths would enable the selective excitation of different conformational populations.

7.5 References

1. Levitus, M.; Schmieder, K.; Ricks, H.; Shimizu, K. D.; Bunz, U. H.; Garcia-Garibay, M. A., *J. Am. Chem. Soc.* **2001,** *123* (18), 4259-65.
2. Beeby, A.; Findlay, K.; Low, P. J.; Marder, T. B., *J. Am. Chem. Soc.* **2002,** *124* (28), 8280-8284.
3. Roy, K.; Kayal, S.; Ariese, F.; Beeby, A.; Umapathy, S., *J. Chem. Phys.* **2017,** *146* (6).
4. Li, H.; Powell, D. R.; Firman, T. K.; West, R., *Macromolecules* **1998,** *31* (4), 1093-1098.
5. Beeby, A.; Findlay, K. S.; Low, P. J.; Marder, T. B.; Matousek, P.; Parker, A. W.; Rutter, S. R.; Towrie, M., *Chem. Commun.* **2003,** (19), 2406-2407.
6. Grummt, U. W.; Birckner, E.; Al-Higari, M.; Egbe, D. A. M.; Klemm, E., *J. Fluoresc.* **2001,** *11* (1), 41-51.
7. Mikroyannidis, J. A., Blue light-emitting poly(p-phenylenevinylene) derivative with oxadiazole and carbazole pendant groups. *J. Appl. Polym. Sci.* **2006,** *101* (6), 3842-3849.
8. Terao, J.; Homma, K.; Konoshima, Y.; Taniguchi, M.; Kiguchi, M.; Komoto, Y.; Horikawa, M.; Naito, Y.; Fujihara, T.; Tsuji, Y., *Bull. Chem. Soc. Jpn.* **2014,** *87* (8), 871-873.
9. Terao, J.; Homma, K.; Konoshima, Y.; Imoto, R.; Masai, H.; Matsuda, W.; Seki, S.; Fujihara, T.; Tsuji, Y., *Chem. Commun.* **2014,** *50* (6), 658-660.
10. Fasina, T. M.; Collings, J. C.; Burke, J. M.; Batsanov, A. S.; Ward, R. M.; Albesa-Jove, D.; Porres, L.; Beeby, A.; Howard, J. A. K.; Scott, A. J.; Clegg, W.; Watt, S. W.; Viney, C.; Marder, T. B., *J. Mater. Chem.* **2005,** *15* (6), 690-697.
11. Fasina, T. M.; Collings, J. C.; Lydon, D. P.; Albesa-Jove, D.; Batsanov, A. S.; Howard, J. A. K.; Nguyen, P.; Bruce, M.; Scott, A. J.; Clegg, W.; Watt, S. W.; Viney, C.; Marder, T. B., *J. Mater. Chem.* **2004,** *14* (15), 2395-2404.
12. Greaves, S. J.; Flynn, E. L.; Futcher, E. L.; Wrede, E.; Lydon, D. P.; Low, P. J.; Rutter, S. R.; Beeby, A., *J. Phys. Chem. A* **2006,** *110* (6), 2114-2121.
13. Roy, K.; Kayal, S.; Kumar, V. R.; Beeby, A.; Ariese, F.; Umapathy, S., *J. Phys. Chem. A* **2017,** *121* (35), 6538-6546.

14. Levitus, M.; Schmieder, K.; Ricks, H.; Shimizu, K. D.; Bunz, U. H. F.; Garcia-Garibay, M. A., *J. Am. Chem. Soc.* **2001,** *123* (18), 4259-4265.
15. Marshall, R. J.; Kalinovskyy, Y.; Griffin, S. L.; Wilson, C.; Blight, B. A.; Forgan, R. S., *J. Am. Chem. Soc.* **2017,** *139* (17), 6253-6260.
16. Sheldrick, G. M., *Acta Crystallogr. A* **2015,** *71*, 3-8.
17. Dolomanov, O. V.; Bourhis, L. J.; Gildea, R. J.; Howard, J. A. K.; Puschmann, H., *J. Appl. Crystallogr.* **2009,** *42*, 339-341.
18. Betteridge, P. W.; Carruthers, J. R.; Cooper, R. I.; Prout, K.; Watkin, D. J., *J. Appl. Crystallogr.* **2003,** *36*, 1487-1487.
19. Stevens, B., *Spectrochim. Acta* **1962,** *18* (4), 439-448.
20. Macrae, C. F.; Sovago, L.; Cottrell, S. J.; Galek, P. T. A.; McCabe, P.; Pidcock, E.; Platings, M.; Shields, G. P.; Stevens, J. S.; Towler, M.; Wood, P. A., *J. Appl. Crystallogr.* **2020,** *53*, 226-235.

Chapter 8
The Effect of Pressure on Crystal Structures and Optical Properties of 4CzIPN and 4CzIPN-$^{t}Bu_8$

8.1 Introduction

A combination of high-pressure single-crystal diffraction, steady-state UV-vis absorption and fluorescence emission and time-resolved fluorescence emission spectroscopy have been used to study the response of 4CzIPN and 4CzIPN-$^{t}Bu_8$ to pressure. The results in this chapter reveal that both compounds showed a different response to pressure, particularly in their crystal structure and electronic spectra. 4CzIPN showed a gradual decrease in both intensity and delayed lifetime with increasing pressure. While 4CzIPN-$^{t}Bu_8$ show more complicated processes where the delayed lifetime starts to increase at ~0.8 GPa before experiencing a decrease at ~2 GPa. This phenomenon can be linked to the pressure-dependent singlet-triplet energy gap (ΔE_{ST}) of the compounds.

8.1.1 Delayed Fluorescence

The most common fluorescence phenomenon that occurs after a molecule is irradiated by light is prompt fluorescence. This is where the emission occurs immediately after the excitation and from the direct vertical conversion of $S_1 \rightarrow S_0$ without experiencing intersystem crossing (ISC). Delayed emission could occur without the presence of ISC such as in excimer emission, as has been explained in **Chapter 6**.[1] Delayed emission could also occur with the presence of ISC such as in phosphorescence, triplet-triplet annihilation (TTA) and thermally activated delayed fluorescence (TADF).

Phosphorescence typically occurs when the solution is cooled down, and the observed spectrum is redshifted with respect to the fluorescence spectrum, as has been mentioned in **Chapter 2**. The lifetime is prolonged to millisecond rate because the $T_1 \rightarrow S_0$ transition is symmetry forbidden.

Triplet-triplet annihilation also referred to as P-type delayed fluorescence, is observed mainly in aromatic crystals, concentrated rigid solutions and from fluid solutions of disc-type aromatic molecules.[2] TTA is a bimolecular process that occurs from the collision of two molecules in the triplet state.[3] The outcome of the triplet annihilation can result in one molecule at S_1 and another at S_0. The emission from the S_1 as a product of TTA has delayed fluorescence characteristics with a prolonged lifetime. The production of the emitting state, S_1, however, only achieves 62.5% efficiency, which is pale in comparison to the 100% that is obtained from TADF. Due to the nature of bimolecular processes, TTA is less likely to occur in dilute solution.

TADF occurs at room temperature and gets more intense with increasing temperature. It has an emission spectrum identical to the prompt fluorescence spectrum. This delayed fluorescence is also known as E-type delayed fluorescence, named after eosin, in which it was first observed. TADF intensity, however, decreases with a decrease in temperature. The molecule is less able to carry out triplet-singlet reverse intersystem crossing at low temperature due to the thermal energy required to bridge the singlet-triplet energy gap. TADF will be discussed further in **8.1.2**.

8.1.2 Thermally Activated Delayed Fluorescence

The schematic of the TADF process is shown in **Figure 8.1**. TADF is a monomolecular process which means it can occur in the absence of triplet-triplet (T_1-T_1) interaction, and at low molecule concentrations. Upon excitation of the molecule, the triplet state can be occupied when the rate of fluorescence decay (k_F) is much lower than the rate of ISC (k_{ISC}). When the excited triplet state is formed from the $S_1 \rightarrow T_1$ ISC, three processes can compete; first is the phosphorescence or the radiative $T_1 \rightarrow S_0$ transition with k_P decay rate, second is the non-radiative $T_1 \rightarrow S_0$ transition with k_{nr} decay rate and the last is the thermally activated $T_1 \rightarrow S_1$ reverse intersystem crossing (rISC) with k_{rISC} decay rate. In order for the TADF to occur $k_{rISC} \gg (k_P + k_{nr})$ must be fulfilled.

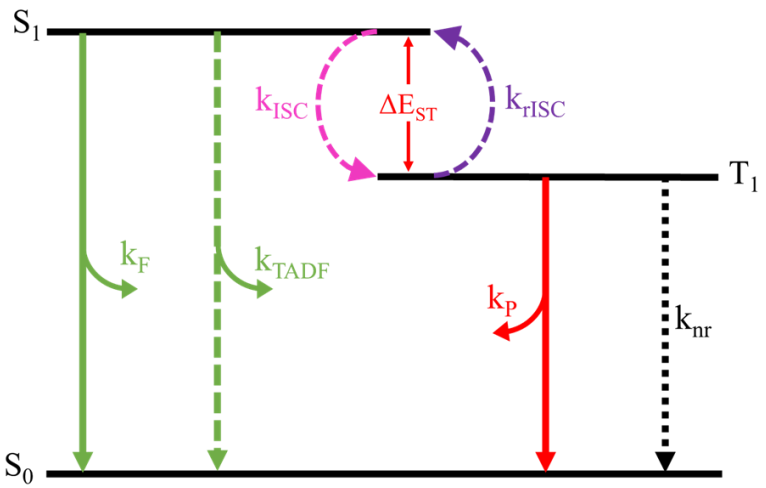

Figure 8.1. The schematic diagram of the processes following excitation and the thermally activated delayed fluorescence.

Organic molecules that show efficient TADF have shared properties, the most important amongst all are the small energy gap between the S_1 and T_1, also known as ΔE_{ST}, and slow k_{nr}. This could also mean that the molecular geometry between S_1 and T_1 should not differ by much. Both conditions are essential to achieve the maximum rate of conversion of the excited triplet state to the emissive excited singlet state due to the thermally activated rISC mechanism. TADF can be described using thermal equilibrium between S_1 and T_1. Upon an assumption that $k_F \ll k_{rISC}$ allowing sufficient time for an equilibrium, K, to form, the steady-state populations of the emitting singlet and triplet states are determined by Boltzmann distribution statistics as described in **Equation 8.1**.[3,4]

$$K = \frac{[S_1]}{[T_1]} = \frac{k_{rISC}}{k_{ISC}} = \frac{1}{3}\, e^{\left(-\frac{\Delta E_{ST}}{k_B T}\right)}$$

Equation 8.1

where the k_B and T are the Boltzmann constant and temperature, respectively, it is possible to express the rate of the whole TADF process, as the rISC followed by fluorescence, as the product of the amount of population in the S_1 state and the rate-limiting step, k_F, as written in **Equation 8.2**.

$$k_{TADF} = \frac{1}{3}\, k_F\, e^{\left(-\frac{\Delta E_{ST}}{k_B T}\right)}$$

Equation 8.2

This approach means the TADF process depends only on the $\Delta E_{ST,}$ which triggers the race on the design of molecules with small ΔE_{ST}. Typically, the ΔE_{ST}, in order to get an efficient TADF has to be no higher than 0.2 eV (19.3 kJ/mol); otherwise, the radiative ISC will occur as phosphorescence or non-radiative decay. Eosin, as the prototype molecule for TADF phenomenon, has a ΔE_{ST} of 0.37 eV (35.7 kJ/mol), which made it an ineffective TADF material.[5]

An organic molecule that has TADF also has prompt fluorescence component, and the overall fluorescence quantum yield (Φ_F) consists of prompt (Φ_{PF}) and delayed (Φ_{DF}) component, as shown in **Equation 8.3**.

$$\Phi_F = \Phi_{PF} + \Phi_{DF}$$

Equation 8.3

Fluorescence intensity (I_{fl}) at a given time is considered as the sum of the intensity from the prompt and delayed fluorescence component, as shown in **Equation 8.4**.

$$I_{fl}(t) = A_{PF}\, e^{\left(-\frac{t}{\tau_{PF}}\right)} + A_{DF}\, e^{\left(-\frac{t}{\tau_{DF}}\right)}$$

Equation 8.4

Where the A_{PF} and A_{DF}, are the prompt and delayed fluorescence pre-exponential factor, respectively. The A_{PF} and A_{DF} represent the intensity fraction at the immediate time after the excitation, or at t=0. The τ_{PF} and τ_{DF} are the prompt and delayed fluorescence lifetime, respectively. The τ_{PF} is the typical fluorescence lifetime with nanosecond timescale, while the τ_{DF} has microsecond timescale.

In terms of molecular design, optimum TADF compounds can be achieved in several ways, such as minimising the singlet-triplet energy gap (ΔE_{ST}) and suppressing the internal conversion pathways.[3] Control of ΔE_{ST} could be achieved by varying the electron donor-acceptor conformations and often isomerisation. Modification of the polarity of the solvent can also alter the conformations and therefore the ΔE_{ST}. The control of internal conversion pathways, however, is not considered a straightforward task. The challenge is to obtain a photoluminescence quantum yield (PLQY) close to unity with a short emissive lifetime to ensure the exciton returning to the singlet state via rISC does not return to the triplet state which will have a potential of decay through non-radiative pathways. Despite effort, it is also challenging to obtain an excellent red

TADF active molecule, due to increase in non-radiative deactivation as a consequence of the narrowing of S_1-S_0 energy gap as wavelength is increased.[6]

In a device, the external quantum efficiency (η_{EQE}) can be introduced as the ratio of extracted photons over injected charges.[7] The EQE can be expressed in **Equation 8.5**.[8]

$$\eta_{EQE} = \gamma . \Phi_{PL} . \eta_{S/T} . \eta_{out}$$

Equation 8.5

Where the γ is charge balance factor, $\eta_{S/T}$ is the singlet-triplet factor (1/4 for fluorescent and 1 for phosphorescent emitter), Φ_{PL} is the PLQY and the η_{out} is the out-coupling efficiency of the emitted light.

8.1.3 4CzIPN and 4CzIPN-^{t}Bu$_8$

The concept of TADF is interesting in terms of organic light-emitting diode (OLED) applications, as it promises high electroluminescence efficiency. OLEDs have been a preferred form of light-generating device due to excellent characteristics such as; self-luminescence without involving energy transfers between molecules or metal ions, surface luminescence where the emission can occur from a thin layer of device which means they have high flexibility and resolution.[9]

In order to achieve electroluminescence, the charge carriers, such as electrons or holes, have to be injected into the light-emitting material. According to spin-statistics, carrier recombination is expected to produce singlet and triplet excitons with the ratio of 1:3, respectively.[10] In a conventional fluorescent compound, only the energy in the singlet state can be converted to light, which comprises of only 25%. On the other hand, in a phosphorescent compound, where spin-orbit coupling is utilised, triplet excitons, can emit and thus 100% can be harvested as light. Devices that utilise phosphorescence are often referred to as phosphorescent OLED or PhOLED.[11] However, the spin-orbit coupling usually involves precious metal such as Pt, Ir and Rh, making the PhOLED costly.[12, 13]

In TADF materials where rISC can occur, a potentially 100% energy from singlet and triplet state energy can be harvested. This type of materials often referred to as the third-generation organic electroluminescence materials.[9] For example, carbazole-triazine substituted benzene show a blue emission with an up-conversion ($T_1 \rightarrow S_1$)

efficiency near 100%, with the photoluminescence quantum yield (PLQY) of 56% in toluene, making the η_{EQE} of 25%.[14] Phenyl, pyridine and anthracene substituted 3,5-dicyanopyridine show ~540 nm emission with PLQY ranged from 56%-89% and maximum η_{EQE} of ~29%.[15]

One of the most widely popular and the very first compounds studied to exhibit TADF is the 1,2,3,5-tetrakis(carbazol-9-yl)-4,6-dicyanobenzene, 4CzIPN, and its derivatives, as shown in **Figure 8.2**. It first came into attention as reported by Uoyama *et al.* in 2012.[10] It attracted scientists attention not only due to its excellent PLQY but also its metal-free nature of the compound, making it an excellent candidate for an environmentally friendly option of the light-emitting device, which as mentioned previously, usually contains precious metals.[16, 17]

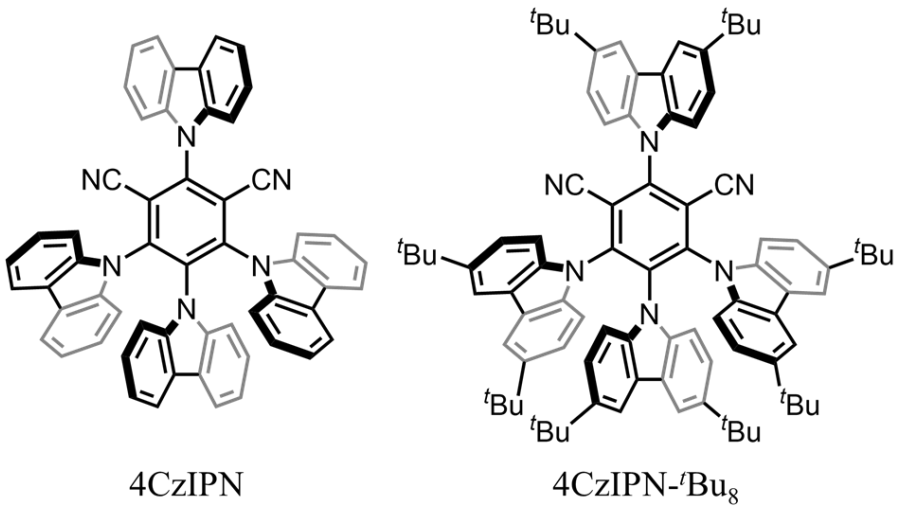

Figure 8.2. The structural formula of the 4CzIPN and 4CzTPN-^{t}Bu$_8$.

As seen from **Figure 8.2**, the 4CzIPN molecule comprises of four carbazole molecules attached to a dicyanobenzene core. Due to steric hindrance, the carbazoles could not form a coplanar geometry with the dicyanobenzene core or with other carbazoles. This prohibition of the coplanar structure provided the localisation of donor and acceptor moieties, leading to a small ΔE_{ST}. The variation of the number of the carbazoles and the substitution to the carbazole or the dicyanobenzene core could lead to a wide range of emission colour of the compounds, ranging from 450 nm to 600 nm. It is also known that the cyano groups take part in reducing the non-radiative deactivation and changes in the geometry of the singlet and triplet excited state by changing the C≡N bond length. The fluorescence emission of the 4CzIPN could be found at 507 nm with PLQY

as high as ~94% in toluene and with the device η_{EQE} of ~19.3%.[10] The Stokes shift of the 4CzIPN is known to be small (see **Figure 8.3**), indicating a small relaxation of the Franck-Condon geometry, due to its rigid structure, thanks to the steric hindrance between carbazoles. This concept of utilising steric hindrance to minimise non-radiative deactivation, referred to restriction of intramolecular rotation (RIR), is not specific to this molecule, but could also be found in some rigid molecular rotors as discussed in **Chapter 6**.[18]

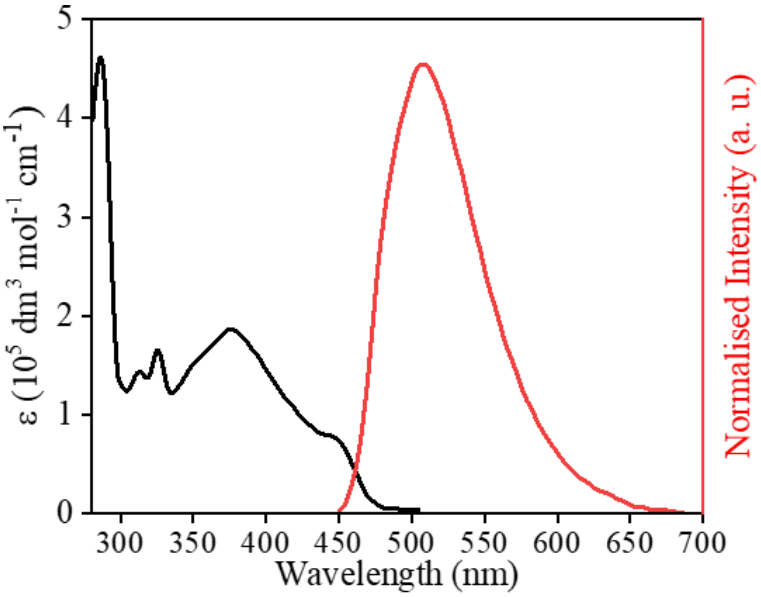

Figure 8.3. UV-vis absorption and photoluminescence spectra of 4CzIPN in toluene at concentration of 10 μM. Redrawn from Uoyama *et al.*[10]

The delayed lifetime of the 4CzIPN solution in toluene was found at ~5.1 μs, two orders of magnitude longer than the prompt component of only ~17.8 ns.[10] Under the presence of oxygen, the delayed component becomes only ~91 ns and the prompt to ~6.9 ns, which is a sign of the quenching of the triplet state by oxygen. A DFT calculation on the 4CzIPN in the gas phase, performed by Uoyama *et al.*, predicted that the highest occupied molecular orbital is around the carbazole, while the lowest unoccupied molecular orbital is around the dicyanobenzene core, characteristics of donor-acceptor localisation.[10]

The photophysics of some TADF materials, including 4CzIPN and 4CzIPN-$^{t}Bu_8$ in various solutions and in solid-state, has also been studied recently by Etherington *et al.*[19] It is suggested that the intermolecular interactions caused emission at a longer wavelength on the 4CzIPN crystal compared to the one in toluene, as shown in **Figure**

8.4 a. The concept of intermolecular interactions is different from what has been previously suggested, such as that the redshift arises from the solid-state solvation effect.[20] This intermolecular interaction came in the form of dimer between the carbazoles.

The time-resolved fluorescence emission measurement of sublimated crystals, listed in the literature as Fraction 1 and 2, which depend on the sublimation temperature, revealed that the fluorescence comprises of monomer prompt fluorescence, monomer delayed fluorescence and dimer delayed fluorescence with a lifetime of ~5 ns, ~400 ns and ~2.5 μs, respectively. The Fraction 1, however, lacked in the delayed fluorescence component from the monomer, which was suggested came from its more crystalline structure, providing more stacked-carbazole populations.

It is also reported that the presence of the monomer and dimer prompt and delayed component is dependent on how the sample was prepared, such as in solution-growth, evaporated films, annealed films, or sublimation. Unfortunately, the 4CzIPN-$^{t}Bu_8$ has not been studied as extensively as the original 4CzIPN, making the information about it limited.

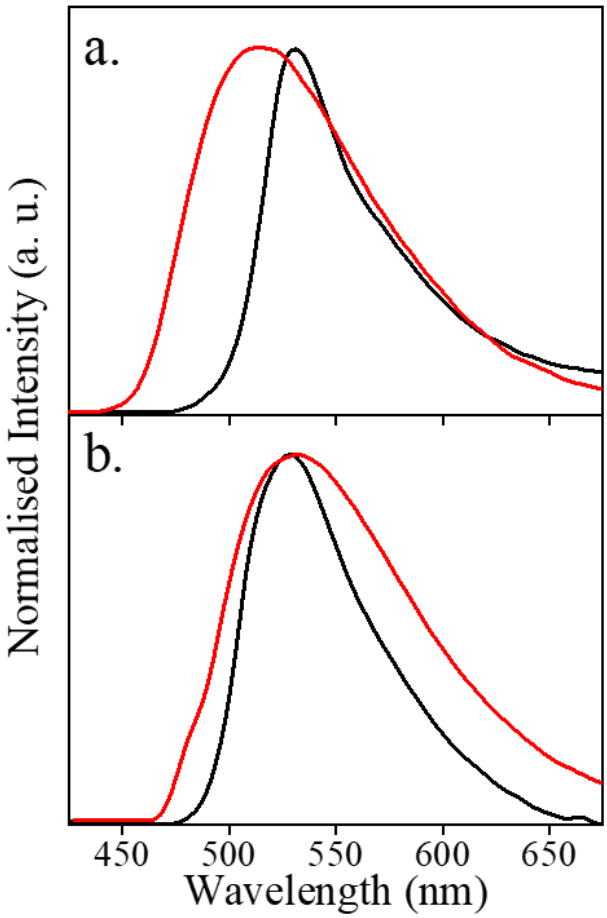

Figure 8.4. Steady-state fluorescence emission of (a) 4CzIPN and (b) 4CzIPN-$^{t}Bu_8$ in crystal form (black) and in toluene (red). Reproduced from Etherington *et al.*[19]

In order to better understand the connection between molecular interactions and the spectroscopic properties of these compound, hydrostatic pressure will be applied to these compounds *in situ* using a diamond anvil cell (DAC). Introducing high-pressure to a single crystal will potentially force the dimer distance closer together, giving a new insight to explore rISC and TADF performance.

8.1.4 Fluorescence Stretched Mono-Exponential Decay

The detailed time-resolved fluorescence emission spectroscopy of a molecule has been discussed in **Chapter 2** on an assumption of non-interacting environments.[21] However, the presence of random sinks that capture the excitations can modify the decay process in which the decay rate itself is dependent on time.[21] Sinks are lower energy states that could trap the exciton within a certain distance, which make it shorter-lived.[22] The presence of the random sinks has previously been reported in the

Förster resonance energy transfers (FRET) after previously predicted also by Förster in 1948 for the intensity decay of a donor molecule caused by trap sites with lower energy states than the emitting species. The presence of the trap sites increases non-radiative relaxation. This intensity decay of the donor molecule in the presence of FRET follow a stretched-exponential law. This stretched-exponential decay provides a better fit to the intensity decay data than the mono-exponential decay, while multiple independent components (multiple-exponential fit) could result in arbitrary and erroneous parameters, which could cause a misinterpretation. The stretched mono-exponential decay can be introduced as **Equation 8.6**.

$$-\frac{d[^1\mathrm{M}^*]}{dt} = (\Gamma + k_{nr})^{\gamma}[^1\mathrm{M}^*]$$

Equation 8.6

where the $[^1\mathrm{M}^*]$ is the concentration of the singlet emitting species. The Γ and k_{nr} are the radiative and non-radiative decay rates, respectively. The γ is the characteristic constant. Under the assumption that the fluorescence intensity is proportional to the decay rate, a stretched-exponential function can be written in **Equation 8.7**.

$$I_t = I_0\, e^{-\left(\frac{t}{\tau_f}\right)^{1/h}}$$

Equation 8.7

where I_t is the fluorescence intensity a time *t*, I_0 the fluorescence intensity a time 0. The τ_f is the fluorescence lifetime, and the *h* is the heterogeneity parameter of the sample, (*h* is greater than 1, with h = 1 is homogenous). The delayed-fluorescence measured in this chapter were fitted using the **Equation 8.7** as well as mono- and biexponential function as comparison, as it is likely that there is a significant perturbation to the emitting species in the DAC with increasing pressure.

8.2 Experimental

It should be noted that the crystals were provided by Dr Marc Etherington of Northumbria University. The time-resolved fluorescence spectroscopy measurements were done in collaboration with Dr Marc Etherington and Prof Andrew Monkman of Durham University. The X-ray diffraction was collected in collaboration with Ms

Gemma Turner and Dr Stephen Moggach of the University of Western Australia. The crystal structures at high-pressure were solved and refined by the writer.

8.2.1 Synthesis

The synthesis of the 4CzIPN and 4CzIPN-$^{t}Bu_8$ was carried out according to Etherington *et al*.[19] ss

4CzIPN: NaH (0.36 g, 15 mmol) was added and stirred into a solution of carbazole (1.67 g, 10 mmol) in anhydrous THF (40 mL) under argon atmosphere at room temperature for 30 minutes, and then tetrafluoroisophthalonitrile (0.4 g, 2 mmol) was added and stirring continued. After stirring for 12 hours, 2 mL H_2O was added to the solution to stop the reaction by quenching the excess NaH. The mixture was concentrated under reduced pressure and washed using H_2O and ethanol. The powder then recrystallised from chloroform/hexane (1:4) mixture to obtain the yellow crystals. The 4CzIPN was then evaporated and sublimated onto a sapphire substrate using a Kurt J. Lesker deposition chamber at a vacuum below 10^{-6} mbar. This sublimated crystal was used for the measurements throughout this chapter.

4CzIPN-tBu8: the synthesis of this compound follows the synthesis of the 4CzIPN with 3,6-di-tert-buthylcarbazole (3,6-Di^{t}BuCz) used instead of carbazole.

8.2.2 High-pressure Crystallography

Both 4CzIPN and 4CzIPN-$^{t}Bu_8$ diffraction data were collected using a diamond anvil cell (DAC) with Daphne oil 7373 (Idemitsu Kosan Co., Ltd) as a pressure transmitting medium, using synchrotron radiation as explained in **Chapter 3**. The diffraction data of 4CzIPN were collected from 0.08 GPa to 7.42 GPa, but the crystal structure could only be solved up to 4.16 GPa, due to the deterioration of crystallinity as pressure increase. The crystal structure at the lowest pressure was solved using SHELXT[23] within Olex2[24] program. The structure was then numbered in CRYSTALS.[25] The structure was then refined isotropically against F^2, still within Olex2 program. All 1,2 and 1,3 distances were restrained. Vibrational and thermal similarity were also restrained, and the hydrogen atoms were added geometrically to ride its host atoms. The structure at the lowest pressure then used as a starting structure for the refinement of the crystal structure at higher pressure.

The diffraction data of the 4CzIPN-$^{t}Bu_8$ were collected from 0.11 GPa to 4.20 GPa with the same method as the 4CzIPN. However, none of the crystal structure could be solved due to low crystallinity. The low crystallinity may be a feature of the compound in which the crystal growth was more challenging compared to other compounds.[26] It is also hinted in the literature[19] that the 4CzIPN-$^{t}Bu_8$ crystal could only form with the presence of C_6H_{14} cocrystal. Nevertheless, the unit cell parameters could be obtained.

The intermolecular distances on the refined structure of the 4CzIPN were measured using a *Measure Distance* routine within Mercury.[27]

8.2.3 High-Pressure Steady-State Electronic Spectroscopy

8.2.3.1 High-pressure UV-Vis Absorption Spectroscopy

The high-pressure UV-vis absorption spectra of 4CzIPN and 4CzIPN-$^{t}Bu_8$ were collected using a DAC with Daphne oil 7373 as a hydrostatic medium, following the X-ray crystallography measurement, with the custom-built measurement setup, as explained in **Chapter 3**. The absorption spectra of 4CzIPN and 4CzIPN-tBu8 were measured up to 4.31 GPa and 4.26 GPa, respectively.

8.2.3.2 High-pressure UV-Vis Fluorescence Emission Spectroscopy

The high-pressure fluorescence emission spectra of 4CzIPN and 4CzIPN-$^{t}Bu_8$ were collected using the same DAC as mentioned in **8.2.3.1**. A single wavelength Ocean Optics LS-LED 365 nm was used as the excitation light source. A band-pass filter (Semrock Brightline 370/36) was inserted in the excitation path to narrow the excitation bandwidth. A 409 nm long-pass filter was used to remove the excitation light before reaching the detector. The fluorescence emission spectra were collected at a pressure series to match the UV-vis absorption measurement for up to 4.26 GPa for 4CzIPN and 3.95 GPa for 4CzIPN-$^{t}Bu_8$.

8.2.4 High-pressure Time-Resolved Fluorescence Emission Spectroscopy

The high-pressure time-resolved fluorescence emission spectra of both 4CzIPN and 4CzIPN-tBu8 were also measured in a DAC using a modified custom-built setup, coupled with the instruments available in the Organic Electroactive Materials (OEM) group of Prof Andrew Monkman at Durham University. **Figure 8.5** Show the schematic of the measurement setup. From the custom-built measurement setup (see

Chapter 3), the first reflective objective lens had to be removed to accommodate the 3rd harmonic 355 nm Nd:YAG laser with ~1 mm beam diameter by EKSPLA®. The fluorescence light from the sample then collected by the second reflective objective lens and then guided into a monochromator before detected by 4 Quik Edig nanosecond high-speed Intensified Charge-Coupled Device (iCCD) streak camera by Stanford Computer Optics.

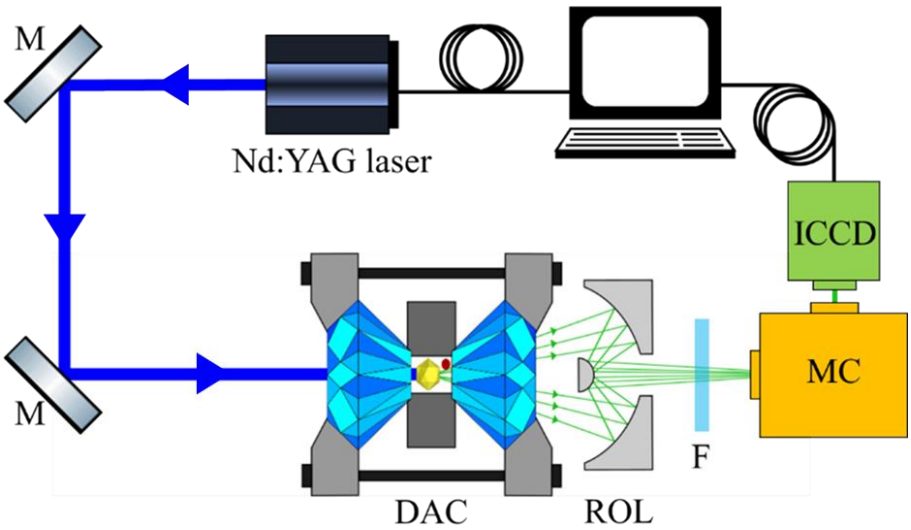

Figure 8.5. High-pressure time-resolved spectroscopy setup consisted of Nd:YAG laser, mirrors (M), diamond anvil cell (DAC), reflective objective lens (ROL), filter (F), monochromator (MC) and streak camera (iCCD).

The fluorescence emission spectra of the samples were measured from 7.5 ns to 0.1 ms delayed time, then the spectra at each delayed time were integrated using a MATLAB code. The averaged intensity between 365 nm and 390 nm was used as a baseline. Unfortunately, the integrated fluorescence intensity between 7.5 ns and 200 ns delayed time could not be included in the intensity decay fit due to a scaling problem on the iCCD camera. Nevertheless, the emission spectrum at a delayed time earlier than 200 ns can still be used to see the evolution of the emission spectrum as a function of time. As a consequence of this problem, the prompt fluorescence emission, which is ~10 ns, could not be observed.

The pressure in the DAC was approximated using the fluorescence spectra peak from the steady-state fluorescence emission measurement. The comparison between the emission spectra of 4CzIPN and 4CzIPN-$^{t}Bu_8$ that were measured using the USB2000+ and streak camera is shown in **Figure 8.6 a** and **b**, respectively, and show

a good agreement. **Figure 8.6 c** and **d** show the steady-state emission maxima of the 4CzIPN and 4CzIPN-$^{t}Bu_8$ as a function of pressure with the approximated pressure for the time-resolved emission spectra peaks.

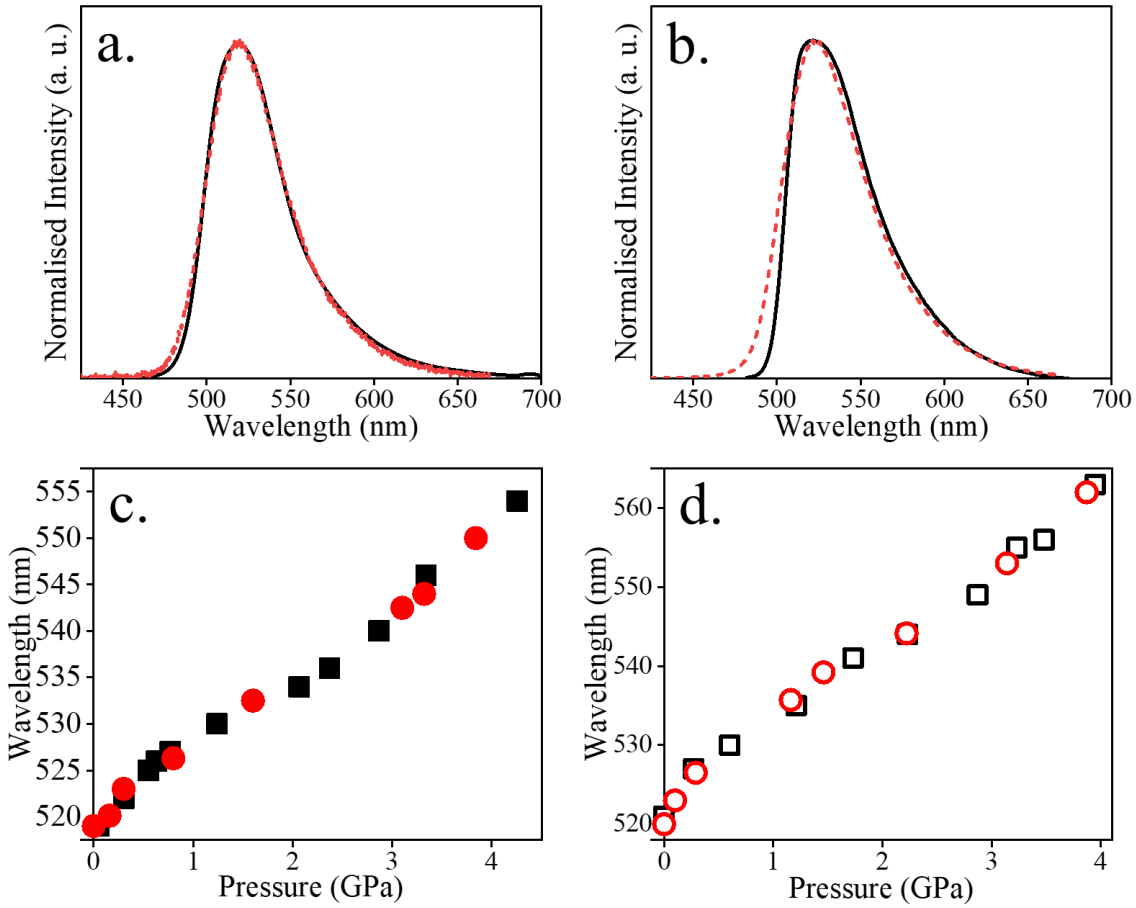

Figure 8.6. The fluorescence spectra of (a) 4CzIPN and (b) 4CzIPN-$^{t}Bu_8$ measured with USB2000+ spectrometer (black) and ICCD (red). The pressure-dependent fluorescence maxima of the (c) 4CzIPN and (d) 4CzIPN-$^{t}Bu_8$ measured with USB2000+ spectrometer (black) and ICCD (red).

8.3 Results and Discussions

8.3.1 Effect of Pressure on 4CzIPN

8.3.1.1 High-Pressure X-ray Crystallography

The 4CzIPN crystal structure that was reported by Etherington *et al.* (CCDC reference code: YUGDOV01), was collected at 120 K and found in a triclinic system with $P\bar{1}$ space group (a = 8.9077(6) Å, b = 19.4451(13) Å, c = 23.7968(15) Å, α = 78.143(3)°, β = 84.235(3)°, γ = 89.989(3)°, V = 4012.6(5) Å3, Z = 4).[19] The crystal structures discussed in this chapter were found in the space group, as reported by Etherington *et al.* The unit cell content of 4CzIPN is depicted in **Figure 8.7**. The unit cell parameters

of the 4CzIPN in various pressure is also listed in **Table 8.1** and shown graphically in **Figure 8.8**. The unit cell volume at 0.08 GPa is significantly larger than what was observed from the literature, which could be due to systematic error caused by an error in the calibration of the diffractometer at the Synchrotron, as has also been mentioned in **Chapter 6** and **Chapter 7**. However, this will not change the narrative. Although the diffraction data were collected up to 7.42 GPa, the crystal structure could only be obtained up to 4.16 GPa. At pressure higher than 4.16 GPa, only the unit cell parameters can be obtained.

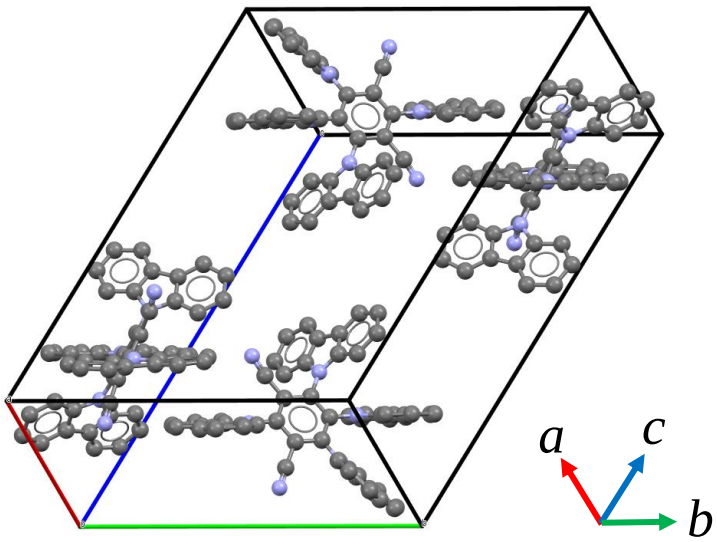

Figure 8.7. One unit cell of 4CzIPN within a triclinic $P\bar{1}$ space group with Z=4. The purple and grey spheres represent nitrogen and carbon atoms, respectively. Colour scheme: N – purple, C – grey. Hydrogen atoms were omitted for clarity.

Table 8.1. Unit cell parameters and unit cell volume (V_{UC}) of the 4CzIPN crystal in various pressure. The crystal structure in the yellow-highlighted rows could not be obtained.

Pressure / GPa	*a* / Å	*b* / Å	*c* / Å	α / °	β / °	γ / °	V_{UC} / Å^3
0.08	9.0601(7)	19.7246(19)	24.126(2)	77.837(8)	83.707(8)	89.9269(8)	4188.3(7)
0.58	8.7428(6)	19.2806(16)	23.668(2)	77.927(7)	84.827(7)	89.809(6)	3885.0(5)
1.24	8.5345(6)	19.0304(7)	23.449(2)	78.103(7)	85.580(7)	89.736(6)	3715.4(5)
1.55	8.4736(5)	18.9639(14)	23.3904(18)	78.144(7)	85.820(7)	89.730(6)	3668.5(5)
2.00	8.3736(5)	18.8449(15)	23.284(19)	78.245(7)	86.196(7)	89.706(6)	3589.1(5)
2.53	8.2743(5)	18.7086(14)	23.1889(19)	78.265(7)	86.522(6)	89.680(6)	3508.1(4)
3.23	8.2173(5)	18.6072(15)	23.099(2)	78.323(7)	86.738(7)	89.728(6)	3453.1(5)
3.76	8.1553(5)	18.4739(14)	23.0273(19)	78.377(7)	86.932(6)	89.773(6)	3393.2(4)
4.16	8.1480(8)	18.453(2)	23.023(3)	78.365(11)	86.986(11)	89.841(9)	3385.6(7)
5.71	8.054(3)	18.168(6)	23.137(7)	78.70(3)	86.98(3)	89.95(3)	3315.4(19)
7.42	7.9588(12)	17.843(2)	22.626(3)	79.343(14)	87.57(2)	90.264(15)	3154.5(8)

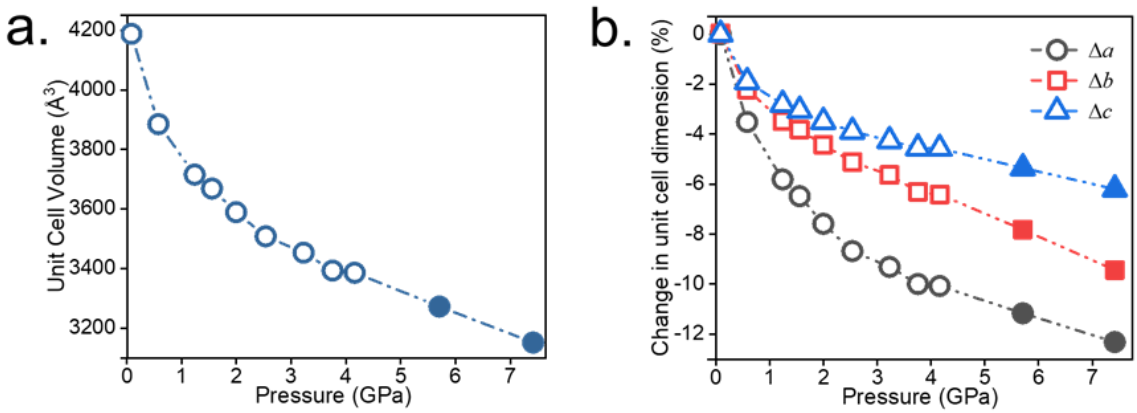

Figure 8.8. (a) The unit cell volume of the 4CzIPN single crystal and (b) the change in unit cell parameters as a function of pressure. The hollow symbols represent the pressure point with a solved structure.

From **Table 8.1** and **Figure 8.8**, it can be seen that the unit cell volume is contracted by ~19% up to 4.16 GPa. The compression of the unit cell occurred anisotropically, which is common in crystal system with low symmetry[28], with the *a*-axis become the most compressed by ~10%, followed by *b* and *c* axes by ~6% and ~5%, respectively. The most compressed axis of the crystal often associated with the direction of the

weakest intermolecular repulsion[28], in this case, the stacking direction of the intermolecular carbazoles.

Throughout the crystal structure, a series of noteworthy interactions were identified and is presented in **Figure 8.9**. Two inter-phenyl distances of the intermolecular carbazole were identified as $\mathbf{C_{I\text{-}PiA}}$, and $\mathbf{C_{I\text{-}PiA}}$. Additionally, two intramolecular carbazoles distances were identified as $\mathbf{C_{I\text{-}c45}}$ and $\mathbf{C_{I\text{-}c56}}$. The change in the intra- and intermolecular distances as a function of pressure are listed in **Table 8.2** and depicted graphically in **Figure 8.10**.

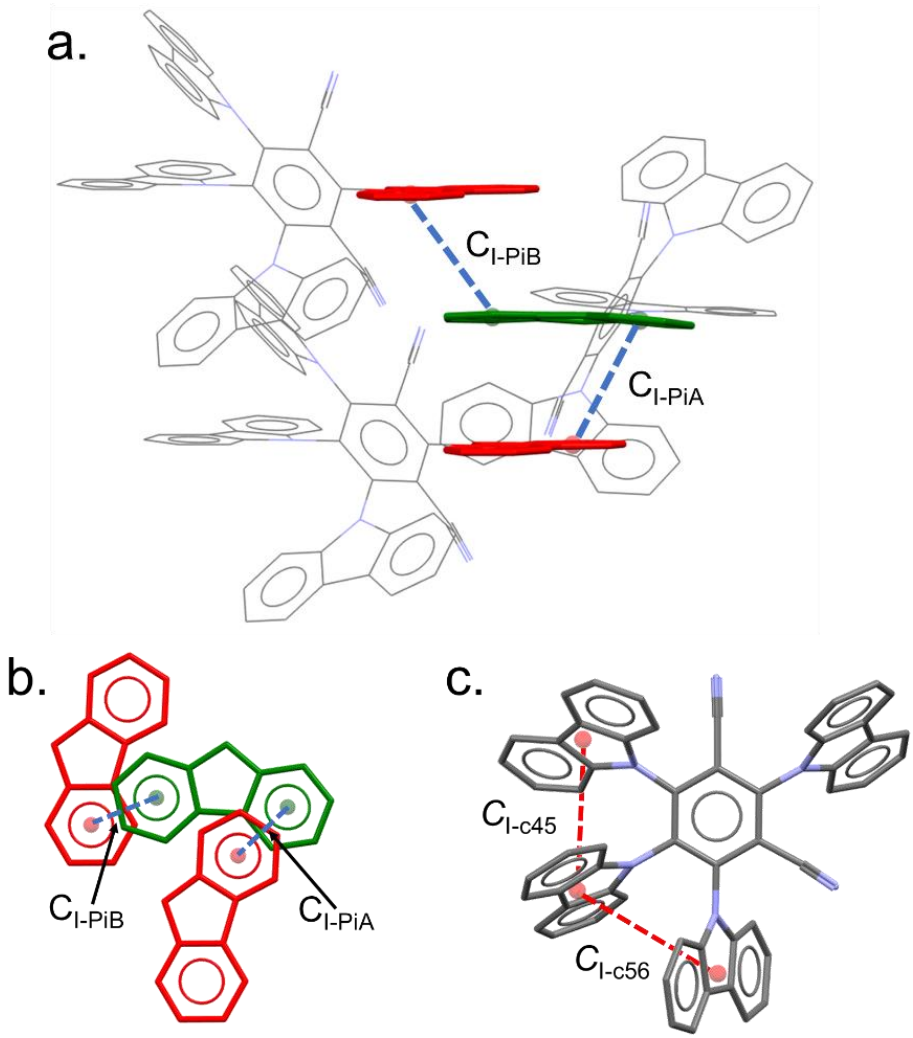

Figure 8.9. (a) Intermolecular stacking of the carbazole seen from the parallel and (b) perpendicular direction of the stacking plane. The capital C represent the centroids. The subscripted capital I represents the 4CzIPN compound. The P represents phenyl ring, small i represents the intermolecular interactions and the letter A and B represent the numbering of the interactions. (c) The intramolecular carbazole arrangement in a 4CzIPN molecule. The capital C represent the centroids. The subscripted lowercase c represents the carbazole, the number 45 and 56 represent the number of the carbon on the dicyanobenzene core, where the carbazole groups are attached.

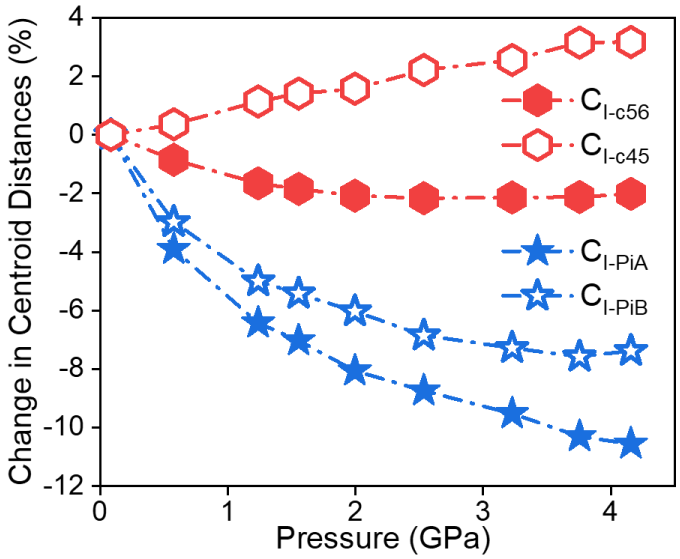

Figure 8.10. The change in the intramolecular carbazole distances ($C_{I\text{-}c56}$ and $C_{I\text{-}c45}$, filled and hollow red hexagon, respectively) and intermolecular phenyl distance ($C_{I\text{-}PiA}$ and $C_{I\text{-}PiB}$, filled and hollow blue pentagram) of 4CzIPN as a function of pressure.

Table 8.2. The summary of the intermolecular phenyl distances ($C_{I\text{-}PiA}$ and $C_{I\text{-}PiB}$) and intramolecular carbazole distances ($C_{I\text{-}c56}$ and $C_{I\text{-}c45}$) of 4CzIPN in various pressure.

Pressure / GPa	Intermolecular Phenyl Distances / Å		Intramolecular Carbazole Distances / Å	
	$C_{I\text{-}PiA}$	$C_{I\text{-}PiB}$	$C_{I\text{-}c56}$	$C_{I\text{-}c45}$
0.08	3.970	3.998	4.719	4.377
0.58	3.815	3.879	4.679	4.393
1.24	3.715	3.798	4.641	4.427
1.55	3.691	3.781	4.632	4.439
2.00	3.650	3.757	4.621	4.446
2.53	3.623	3.724	4.617	4.474
3.23	3.592	3.707	4.618	4.489
3.76	3.561	3.695	4.619	4.515
4.16	3.551	3.703	4.624	4.516

From **Figure 8.10**, it could be seen that the pressure caused a decrease in the intermolecular distances while the overall intramolecular distance appears to be only slightly affected.

8.3.1.2 High-Pressure Steady-State Electronic Spectroscopy

The UV-vis absorption spectra were measured from a 4CzIPN crystal with ~20 μm thickness. The absorption spectra were collected up to 4.31 GPa, as shown in **Figure 8.11**. Similar to what has been observed throughout this thesis, the peak of absorption spectra could not be observed, due to a high concentration of chromophore within the crystal. Due to this reason, the absorption red edge, collected from half-maximum of the spectrum, was used to quantify the shift as a function of pressure. The absorption red-edge as a function of pressure is summarised in **Table 8.3**.

The fluorescence emission spectra were measured up to 4.26 GPa from a number of crystals within the DAC. The emission spectra in various pressures are also shown in **Figure 8.11**. The emission peak could be identified; therefore, the peak was used to quantify the shift as a function of pressure. The emission spectra peak as a function of pressure is also summarised in **Table 8.4**. The change of absorption red-edge and fluorescence emission peak as a function of pressure is also depicted graphically in **Figure 8.12.**

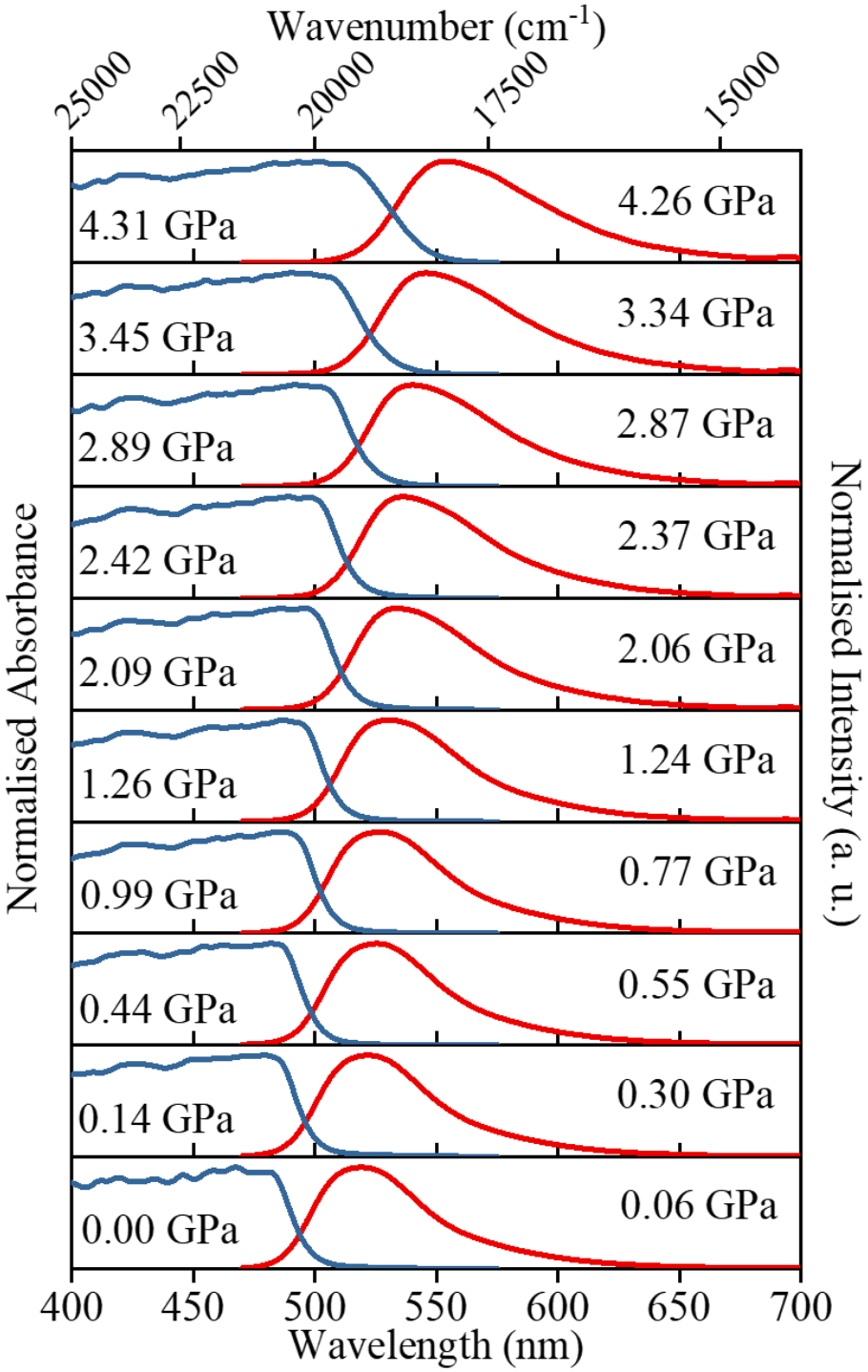

Figure 8.11. Normalised UV-vis Absorption (blue) and fluorescence emission (red) spectra of the 4CzIPN in various pressure.

Table 8.3. Summary of the wavelength and wavenumber of UV-vis absorption red-edge of the 4CzIPN in various pressure.

Pressure / GPa	Absorption Edge / nm	Absorption Edge / cm^{-1}
0.00	491	20370
0.13	493	20270
0.44	495	20190
0.99	501	19960
1.26	504	19850
1.73	506	19760
2.09	509	19660
2.42	511	19590
2.89	516	19400
3.45	520	19240
4.31	532	18800

Table 8.4. Summary of wavelength and wavenumber of fluorescence emission peak of 4CzIPN in various pressure.

Pressure / GPa	Emission Peak / nm	Emission Peak / cm^{-1}
0.06	519	19160
0.30	522	19070
0.55	525	18950
0.63	526	18940
0.77	527	18880
1.24	530	18730
2.06	534	18610
2.37	536	18540
2.87	540	18400
3.34	546	18210
4.26	554	17940

From **Figure 8.12**, it can be seen that both absorption and emission spectra were redshifted as a function of pressure by 1570 cm^{-1} and 1220 cm^{-1}, respectively, up to ~4.3 GPa. This redshift caused by the increase of the intermolecular stacking of the carbazoles in the crystal. The absorption and emission spectra also shifted proportionally, with a small decrease in Stokes shift from 1210 cm^{-1} at 0 GPa, to 860 cm^{-1} at 4.3 GPa, which can also be seen in **Figure 8.11** as the absorption and emission spectra experienced more spectral overlap with increasing pressure. This could also mean that at 0 GPa there was a geometry relaxation from the Franck-Condon state, S_1 to the relaxed excited state, S_1^*. However, at higher pressure, the S_1-S_1^* gap became narrower, indicating a more similar geometry between the Franck-Condon and relaxed excited state. The more similar geometry at the Franck-Condon state and relaxed excited state could be a consequence of a tighter space in the crystal at a higher pressure, preventing a significant molecular relaxation. Due to the somewhat consistent redshift of both absorption and emission spectra, it could be implied that S_1-S_0 and S_1^*-S_0 and possibly T_1-S_0 gaps were getting narrower with increasing pressure, also proportionally.

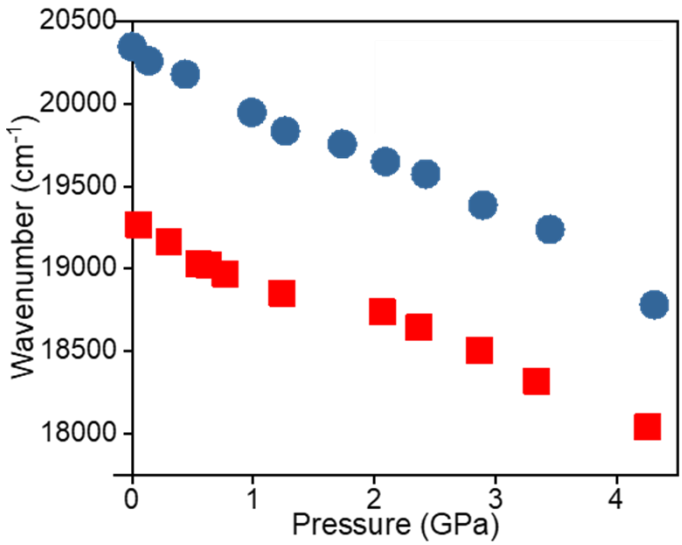

Figure 8.12. The absorption red-edge (blue circle) and fluorescence emission peak (red square) of 4CzIPN as a function of pressure.

8.3.1.3 High-Pressure Time-Resolved Fluorescence Emission Spectroscopy

The time-resolved fluorescence emission spectra were collected at 0 GPa, 0.16 GPa, 0.3 GPa, 0.8 GPa, 1.6 GPa, 3.1 GPa, 3.32 GPa, and 3.8 GPa. A second measurement

was also carried out at 0 GPa, 0.3 GPa, 0.5 GPa, 1.43 GPa, 2.9 GPa, 4.3 GPa. The emission spectra were redshifted with increasing pressure, similar to what has been observed in the steady-state measurement. **Figure 8.13** shows that at each pressure, the emission peak was essentially unchanged as a function of delayed time, which may suggest that the emission arises from single species. The integrated fluorescence intensity decay was fitted with stretched mono-exponential and bi-exponential decay functions for comparison.

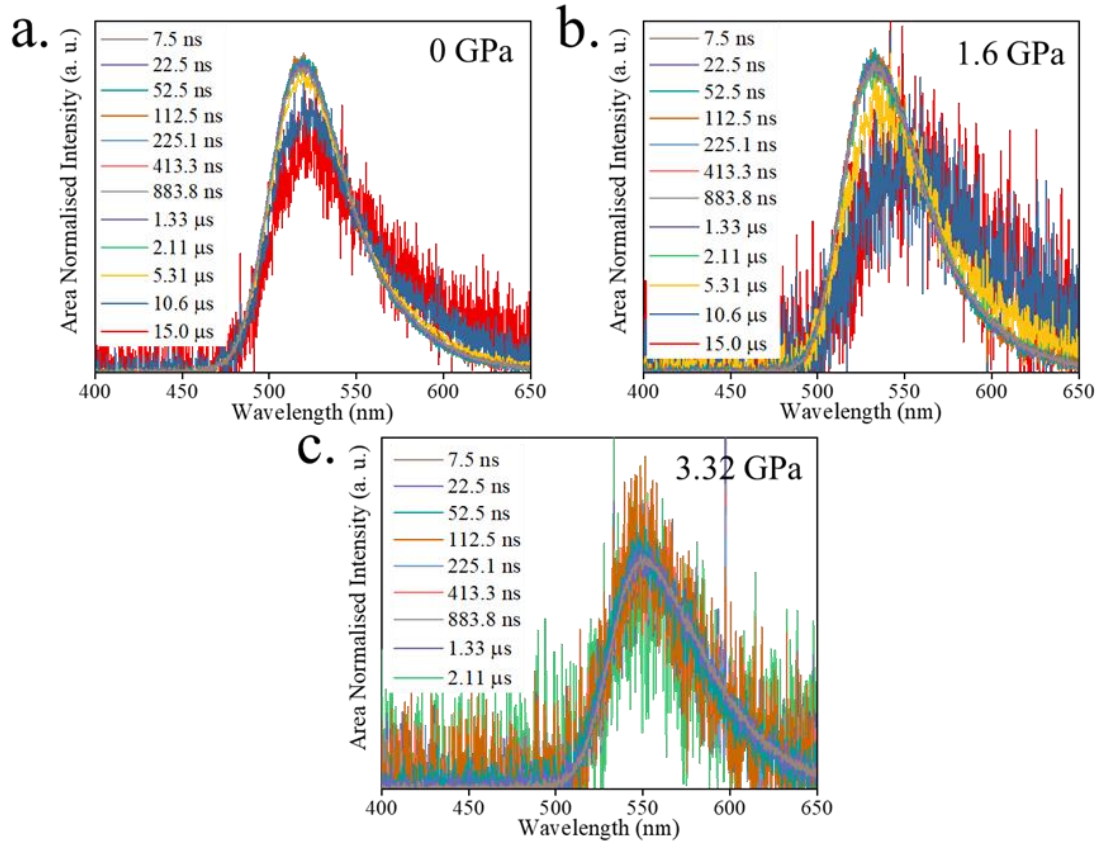

Figure 8.13. The spectra of 4CzIPN at (a) 0 GPa, (b) 1.6 GPa and (c) 3.32 GPa at various delayed time.

8.3.1.3.1 Stretched Mono-Exponential Decay Fit

The stretched mono-exponential decay fit is used under a presumption that it is likely that in the crystal, the emitting species was interacting with its surrounding environment, making the decay not only arise from the population of the emitting species but also other factors, which resulted in the time-dependent decay lifetime.

The integrated fluorescence intensity decay and its decay fit at various pressures are plotted in logarithmic-linear scale, as shown in **Figure 8.14 a**. The pre-exponential

factor (A-factor) and the delayed lifetime (τ) are also plotted as a function of pressure, as shown in **Figure 8.14b** and **Figure 8.14c**, respectively. The fitted parameters are also listed in **Table 8.5**.

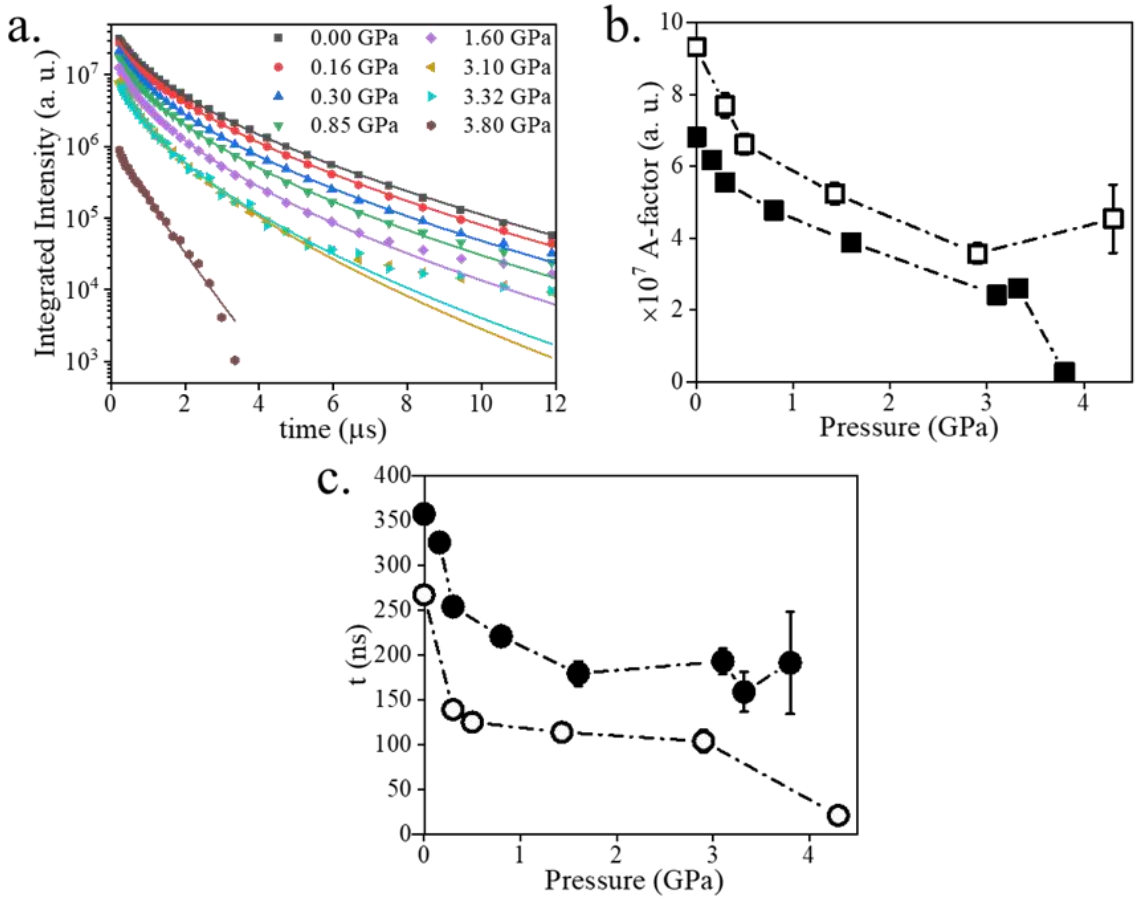

Figure 8.14. (a) The logarithmic-linear plot of integrated fluorescence intensity decay of 4CzIPN fitted with stretched mono-exponential decay fit at various pressure. (b) The A-factor and (c) the lifetime of the fitted fluorescence decay as a function of pressure. The filled and hollow symbols represent the first and second measurements, respectively.

Table 8.5. Summary of fluorescence decay fitted parameters (A-factor and lifetime) of 4CzIPN fitted with mono-exponential decay function at various pressure.

1st measurement				2nd measurement			
Pressure / GPa	**A / a. u.**	**τ / ns**	**h**	**Pressure / GPa**	**A / a. u.**	**τ / ns**	**h**
0.00	6.82E7	358	1.79	**0.00**	9.32E7	267	1.85
0.16	6.17E7	326	1.81	**0.3**	7.70E7	139	2.06
0.3	5.55E7	254	1.88	**0.5**	6.62E7	125	2.07
0.8	4.78E7	221	1.92	**1.43**	5.24E7	114	2.05
1.6	3.88E7	179	1.94	**2.9**	3.57E7	104	1.99
3.1	2.42E7	193	1.8	**4.3**	4.54E7	21	2.61
3.32	2.60E7	159	1.91				
3.8	2.607E7	191	1.12				

It can be seen from **Figure 8.14 a** that the integrated emission intensity at 200 ns delayed time decreased significantly with increasing pressure. This can also be seen from the decrease in A-factor by more than half the original value at ~ 4 GPa. The delayed lifetime experienced a rapid decrease from ~300 ns to ~200 ns up to 0.5 GPa, followed by a slighter decrease at higher pressure. The origin of the delayed lifetime, however, is unclear due to the value is not similar to neither delayed emission of monomer or dimer species, as reported by Etherington *et al.*[19], with the value of heterogeneity parameter closer to 2, which suggests a high level of disorder. The first and second measurements showed similarity in the trends for both A-factor and delayed fluorescence as a function of pressure, with significant discrepancy at higher than 3 GPa which could be caused by low emission intensity or more random amorphisation of the crystal, as the measurements were carried out around the hydrostatic limit of the PTM.

8.3.1.3.2 Bi-Exponential Decay Fit

The integrated emission intensity was also fitted with biexponential function as a comparison to the stretched mono-exponential fit, as shown in **Figure 8.15**. The decay was fitted with bi-exponential decay function due to the unclear origin of the delayed

lifetime present in the stretched mono-exponential fit. The A-factors and delayed lifetime are also summarised in **Table 8.6**.

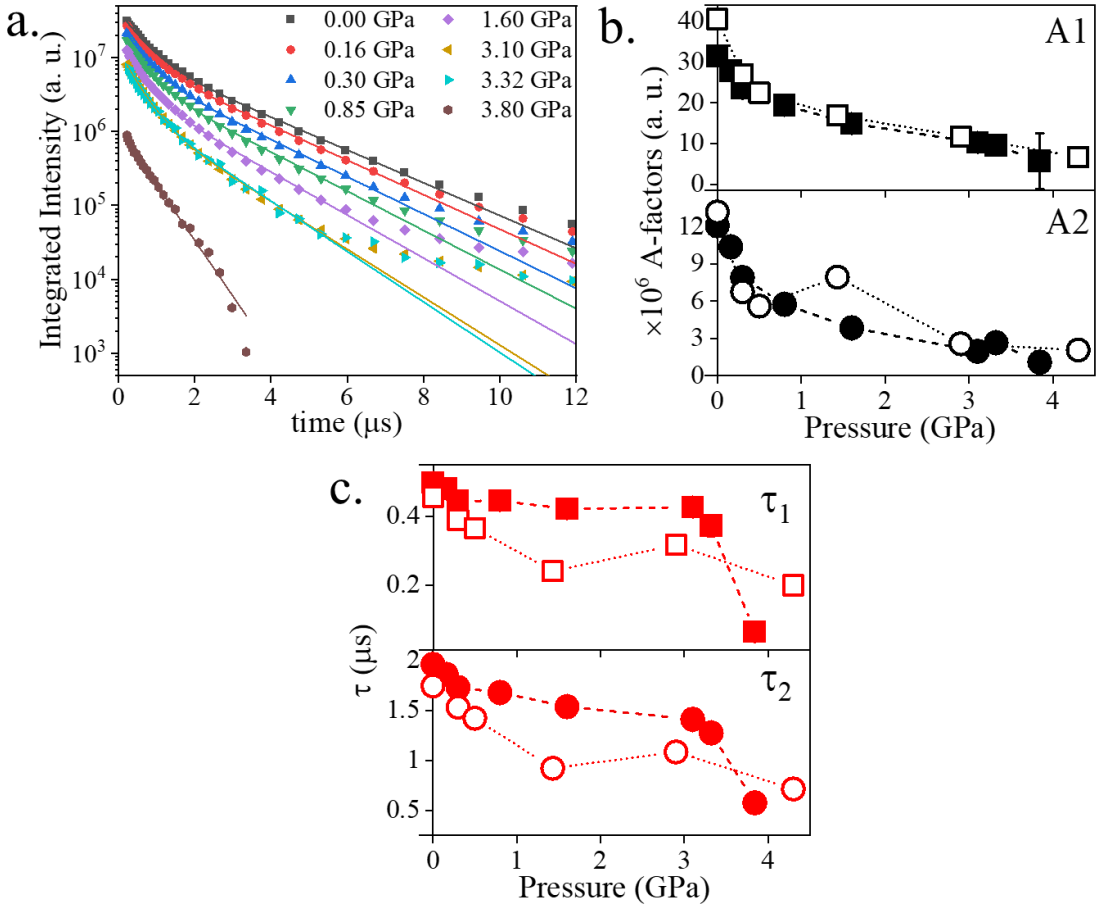

Figure 8.15. (a) The logarithmic-linear plot of integrated fluorescence intensity decay of 4CzIPN fitted with bi-exponential decay function at various pressure. (b) The A-factor and (c) the lifetime of the fitted fluorescence decay as a function of pressure. The filled and hollow symbols represent the first and second measurements, respectively.

Table 8.6. Summary of fluorescence decay fitted parameters (A-factor and lifetime) of 4CzIPN fitted with bi-exponential decay function at various pressure.

1st measurement						
Pressure / GPa	**A1 / a. u.**	**τ_1 / ns**	**A2 / a. u.**	**τ_2 / ns**	**True A1**	**True A2**
0.00	3.14E7	498	1.21E7	1956	0.78	0.22
0.16	2.78E7	479	1.04E7	1857	0.79	0.21
0.30	2.35E7	444	7.89E6	1726	0.81	0.19
0.80	1.94E7	444	5.73E6	1676	0.83	0.17
1.60	1.49E7	421	3.85E6	1535	0.85	0.15
3.10	1.03E7	426	1.96E6	1408	0.88	0.12
3.32	9.55E6	372	2.65E6	1273	0.85	0.15
3.80	5.66E6	63	1.09E6	576	0.99	0.01
2nd measurement						
0.00	4.06E7	456	1.32E7	1742	0.82	0.18
0.30	2.70E7	389	6.74E6	1529	0.86	0.14
0.50	2.24E7	365	5.59E6	1419	0.86	0.14
1.43	1.69E7	240	7.92E6	920	0.81	0.19
2.90	1.18E7	316	2.57E6	1084	0.88	0.12
4.30	6.66E6	199	2.07E6	713	0.88	0.12

From **Figure 8.15 b** and **c**, it can be distinguished clearly from the biexponential decay fit that at 0 GPa, the emission emerged from contributions of the monomer and dimer, with delayed lifetimes of ~500 ns and ~2 μs, respectively. As can also be seen in **Figure 8.15 b**, the decrease of both A-factors and the delayed lifetimes, follow the same trends as one fitted with the stretched mono-exponential function, in which the A-factor and delayed fluorescence decreased rapidly up to 0.5 GPa, but experienced a slower decay at higher pressure.

The proportion of true A1 and A2 (**Table 8.6**) shows that overall intensity was mostly contributed by the monomer species (~80%) at 0 GPa, and the monomer intensity fraction increasing as pressure increased. This means, although the 4CzIPN sample was labelled as Fraction 1, it appears that the kinetics followed more of the Fraction 2,

with the presence of a significant amount of monomer species.[19] Moreover, the emission spectra onset from this chapter is found at ~2.57 eV (483 nm), which is in a good agreement with the emission spectral onset of the 4CzIPN Fraction 2 from what reported by Etherington *et al.*[19] The emission maximum of the sample that was measured in this chapter is found at 519 nm, shorter than the 4CzIPN Fraction 1 from the literature at 532 nm,[19] which may be a sign of the lack of dimer emission. This must be a real phenomenon, since the measurement of the sample using the same method with the same custom-built setup, but with different light source and detectors resulted in a matched spectra, as shown in **Figure 8.6**. Sample transformation from Fraction 1 to Fraction 2 could be the reason for this difference, as the sample that was measured in this chapter was not as fresh as the one in literature. Also, the difference in the measurement technique could cause this distinction, which somehow prefers different species to excite or to emit. As a comparison, this chapter using colinear arrangement of light source and detector, while Etherington *et al.*[19] used front surface excitation with 90° angle between the light source (EKSPLA Nd:YAG laser 355 nm) and the detector (iCCD).

8.3.1.3.3 Decay Fits Comparison

The fluorescence intensity decay of 4CzIPN can be explained better using bi-exponential decay fit, due to both consistent value of A-factors and the delayed lifetime for two sets of measurements. Moreover, the delayed lifetimes of τ_1 (~500 ns) and τ_2 (~2 μs) can be identified to arise from monomer and dimer contributions, respectively. The value of the τ_1 and τ_2 also in a great agreement with the value of delayed lifetimes of monomer (~400 ns) and dimer (~2.6 μs) of Fraction 2, reported by Etherington *et al.*[19] The decrease in A-factors and delayed lifetimes with increasing pressure from both stretched mono-exponential and biexponential show very similar trends and can be used to explain the change in energy levels as a function of pressure.

The decrease in A-factor and delayed lifetime along with spectral redshift with increasing pressure in both absorption and emission spectra could be interpreted as a consequence of the decrease in S_1^*-S_0 and possible T_1-S_0, as illustrated in **Figure 8.16**. The decrease in both S_1^* and T_1 relative to the S_0 with increasing pressure caused the increase in the non-radiative decay which is evident from the decrease in A-factor (i.e.

emission intensity) and a shorter-lived emitting species, which could be seen from the shortening of the delayed lifetime. The pressure, however, did not cause an apparent change in the S_1^*-T_1 energy gap (ΔE_{ST}).

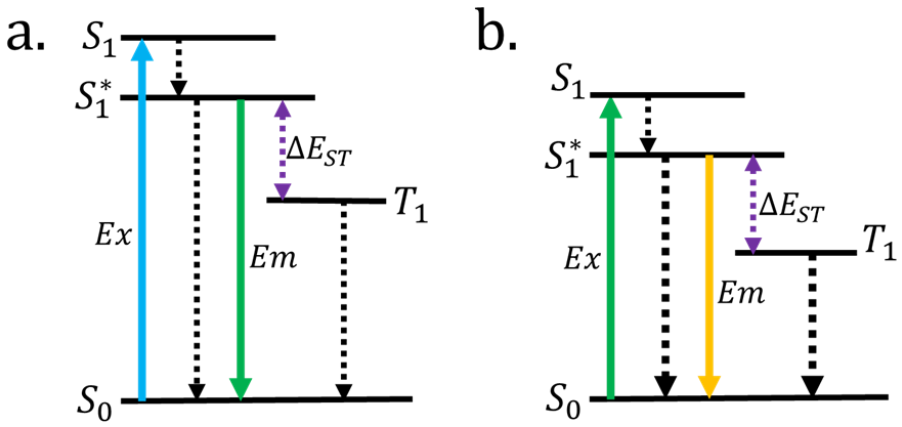

Figure 8.16. The simplified Jablonski diagram of 4CzIPN at (a) lower pressure and (b) at higher pressure. The black dashed lines represent a non-radiative decay.

8.3.2 Effect of Pressure on 4CzIPN-^{t}Bu$_8$

8.3.2.1 High-Pressure X-ray Crystallography

The X-ray diffraction data of the 4CzIPN-^{t}Bu$_8$ were collected up to 4.2 GPa, but none of the crystal structures could be solved. However, the unit cell parameters can still be obtained. The crystal crystallised in a triclinic $P\bar{1}$ space group with the unit cell parameters are summarised in **Table 8.7**. The effect of pressure on the change in unit cell parameters also shown in **Figure 8.17**.

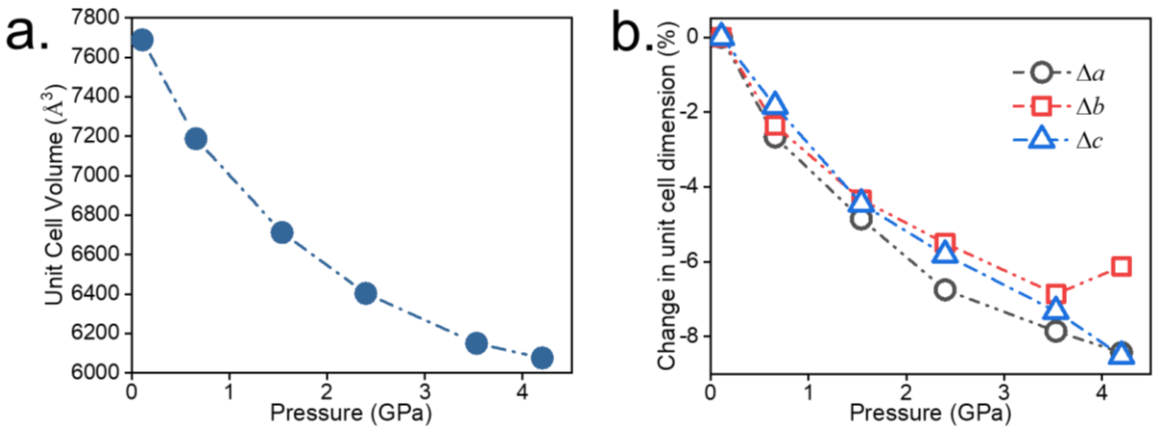

Figure 8.17. (a) The unit cell volume of the 4CzIPN-^{t}Bu$_8$ single crystal and (b) the change in unit cell parameters as a function of pressure.

Table 8.7. Unit cell parameters and unit cell volume (V_{UC}) of the 4CzIPN-$^{t}Bu_8$ single crystal as a function of pressure.

Pressure / GPa	*a* / Å	*b* / Å	*c* / Å	α / °	β / °	γ / °	V_{UC} / Å^3
0.11	11.976(3)	21.180(5)	31.616(10)	74.41(3)	84.71(4)	89.86(2)	7688(4)
0.66	11.657(3)	20.681(4)	31.033(8)	74.82(2)	84.69(3)	89.911(18)	7187(3)
1.54	11.395(3)	20.260(6)	30.209(9)	75.17(3)	84.73(3)	89.90(2)	6712(3)
2.40	11.168(4)	20.014(7)	29.776(13)	75.18(4)	84.48(6)	89.87(3)	6403(4)
3.53	11.035(5)	19.726(10)	29.300(14)	75.63(5)	84.69(6)	89.98(4)	6150(5)
4.20	10.967(4)	19.882(8)	28.921(12)	75.52(4)	84.53(5)	89.79(3)	6076(4)

From **Figure 8.17**, it can be seen that the unit cell volume is compressed by ~21% at a pressure of 4.2 GPa, comparable to the unit cell volume decrease of the 4CzIPN. The unit cell parameters were compressed isotropically. However, the change in the unit cell dimensions at ~4.2 GPa deviates from the trends, where there are sudden changes in *b* and *c* axes. This is due to artefact of deteriorated data as the measurement was carried out at a pressure higher than the hydrostatic limit of PTM. Nevertheless, based on the pressure-dependent structural change of 4CzIPN, the decrease in the volume could be attributed to the decrease in intermolecular interactions, with the additional tert-butyl groups in the carbazole of the 4CzIPN-$^{t}Bu_8$ caused a preferably isotropic contraction.

8.3.2.2 High-Pressure Steady-State Electronic Spectroscopy

The UV-vis absorption spectra were obtained from a crystal with ~20μm thickness. The spectra were collected up to 4.26 GPa. The absorption spectra in various pressure are summarised in **Figure 8.18**. The absorption peak could not be observed; therefore, the absorption spectrum red edge was used to quantify the shift. The absorption red edge was determined from the absorbance at half-maximum of the spectrum. The absorption red-edge in various pressures are summarised in **Table 8.8**.

The fluorescence emission spectra were measured up to 3.95 GPa, and is also shown in **Figure 8.18**. The fluorescence peak is used to quantify the shift. The fluorescence peaks at various pressures are listed in and **Table 8.9**. The change in absorption red-

edge and emission spectrum peak as a function of pressure also illustrated in **Figure 8.19**.

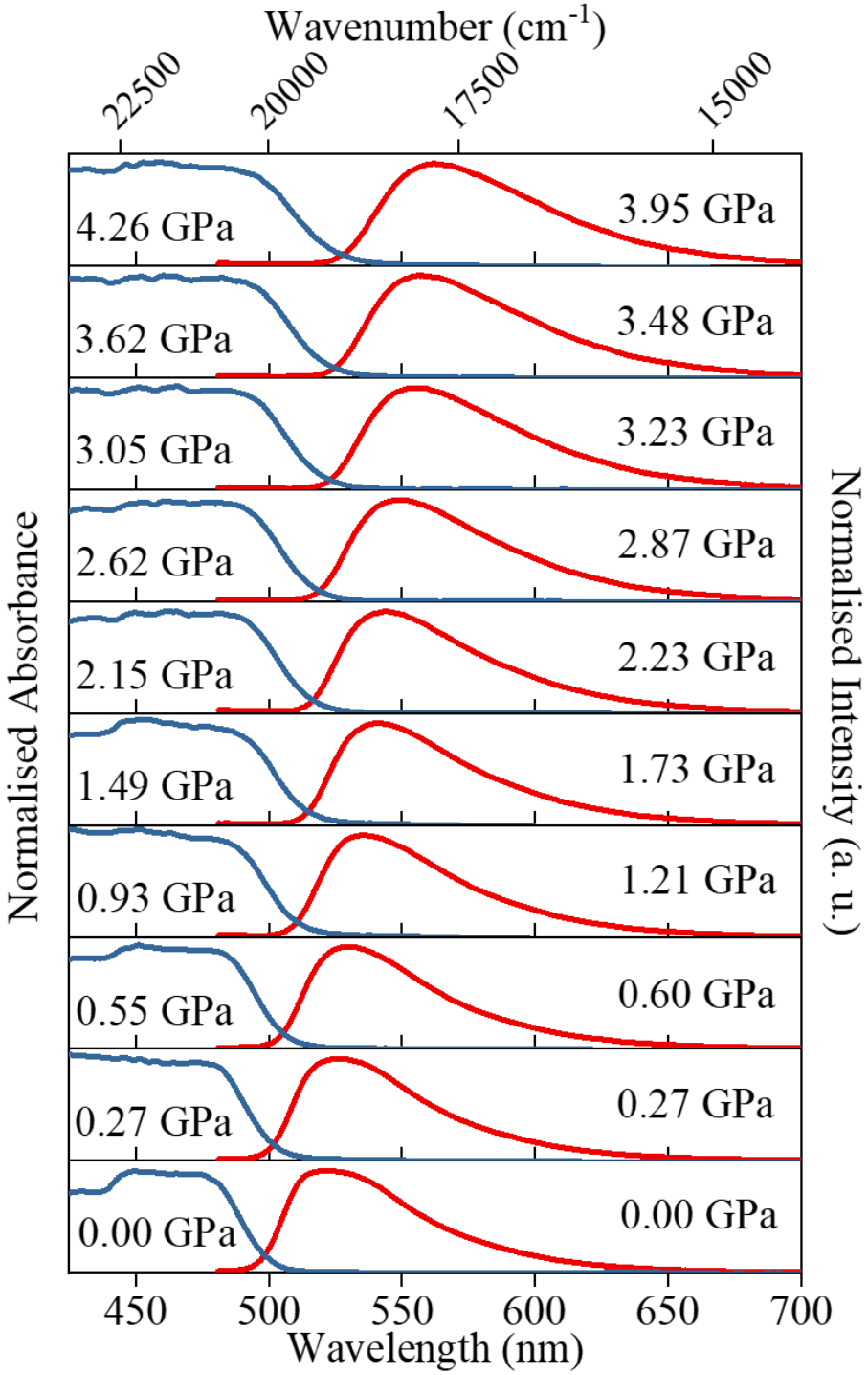

Figure 8.18. Normalised UV-vis Absorption (blue) and fluorescence emission (red) spectra of the 4CzIPN-$^{t}Bu_8$ in various pressure.

Table 8.8. Summary of the wavelength and wavenumber of UV-vis absorption red-edge of the 4CzIPN-$^{t}Bu_8$ in various pressure.

Pressure / GPa	Absorption Edge / nm	Absorption Edge / cm^{-1}
0.00	490	20400
0.27	492	20320
0.55	496	20170
0.93	499	20020
1.49	503	19900
2.15	504	19840
2.62	505	19810
3.05	507	19720
3.62	508	19670
4.26	510	19620

Table 8.9. Summary of wavelength and wavenumber of fluorescence emission peak of 4CzIPN-$^{t}Bu_8$ in various pressure.

Pressure / GPa	Emission Peak / nm	Emission Peak / cm^{-1}
0.00	521	19180
0.27	527	18970
0.60	530	18870
1.21	535	18700
1.73	541	18470
2.23	544	18380
2.87	549	18200
3.23	554	18050
3.48	556	17980
3.95	562	17790

From **Figure 8.19**, it could be seen that both absorption and emission spectra were redshifted as a function of pressure. However, the absorption spectra redshift at ~4 GPa (~780 cm^{-1}) is almost half smaller than that of the fluorescence (~1400 cm^{-1}). At

0 GPa, the Stokes shift could be calculated as 1220 cm^{-1} but getting more significant to 1830 cm^{-1} at ~4 GPa. The absorption and emission shift proportionality appeared to be broken at ~0.8 GPa, where the absorption spectra shift appeared to be stagnated, while the fluorescence spectra continued to shift linearly. This suggests that the Franck-Condon structure became more distinct to the relaxed excited-state structure with increasing pressure. In other words, while the S_0-S_1 energy gap stagnated, the S_1^*-S_0 energy gap keeps decreasing at a pressure higher than ~0.8 GPa. This could be a sign of the change in S_1^*-T_1 energy gap.

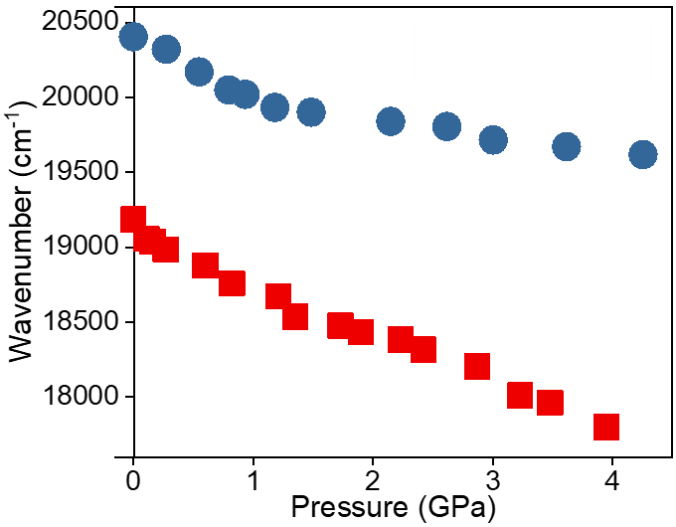

Figure 8.19. The absorption red-edge (blue circle) and fluorescence peak (red square) of 4CzIPN-^{t}Bu$_8$ as a function of pressure.

8.3.2.3 High-Pressure Time-Resolved Fluorescence Emission Spectroscopy

The time-resolved fluorescence emission spectra were collected at 0 GPa, 0.1 GPa, 0.29 GPa, 0.8 GPa, 1.16 GPa, 1.46 GPa, 2.22 GPa, 3.14 GPa, and 3.87 GPa. A second measurement was also carried out at 0 GPa, 0.2 GPa, 0.85 GPa, 1.35 GPa, 1.8 GPa, 2.61 GPa, 3.74 GPa and 4.5 GPa. As has been observed in the steady-state measurement, the time-resolved emission spectrum of the 4CzIPN-^{t}Bu$_8$ also experienced redshift with increasing pressure. The emission spectra in several delayed time at various pressure are shown in **Figure 8.20**. At each pressure, the spectra were essentially unchanged as a function of delayed time. Therefore, it is implied that the emission arises from a single species. The integrated intensity was fitted with stretched mono-exponential decay function a mono-exponential decay function as comparison.

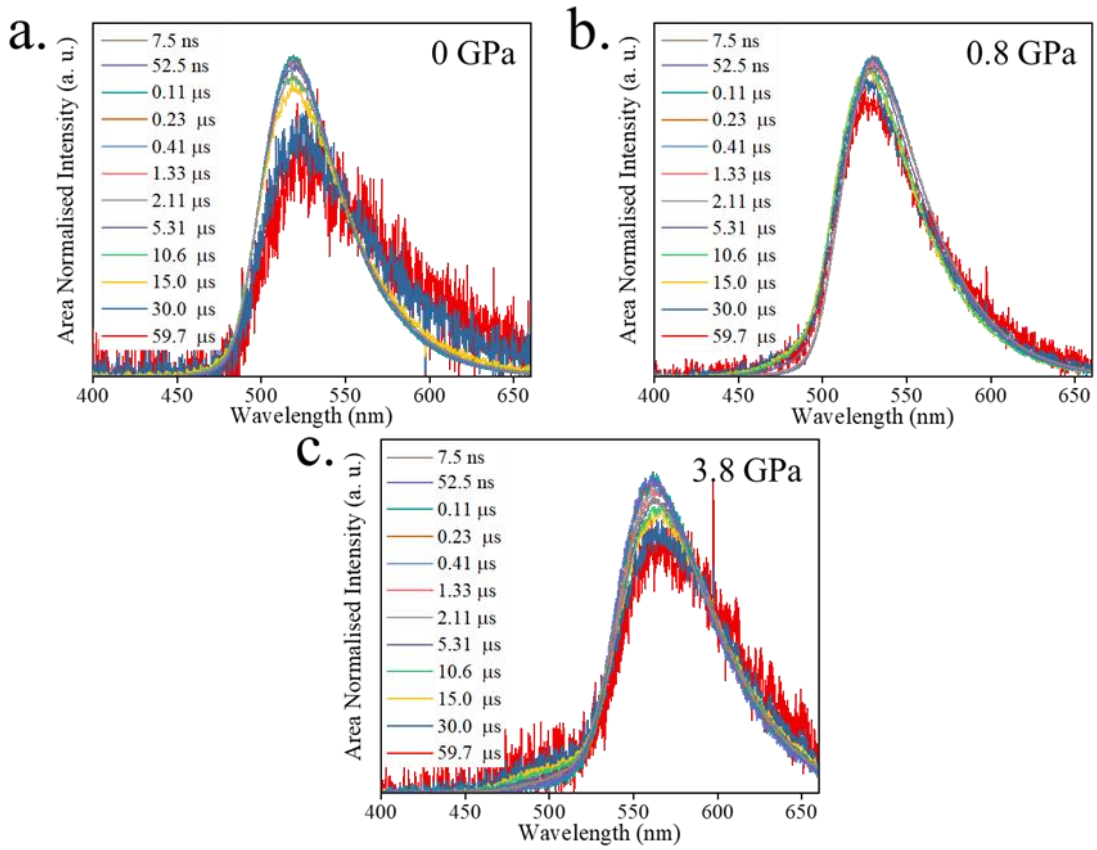

Figure 8.20. The spectra of 4CzIPN-^{t}Bu$_8$ at (a) 0 GPa, (b) 0.8 GPa and (c) 3.8 GPa at various delayed time.

8.3.2.3.1 Stretched Mono-Exponential Decay Fit

The integrated fluorescence intensity decay fitted with stretched mono-exponential decay function at various pressures are plotted in logarithmic-linear scale, as illustrated in **Figure 8.21 a**. The stretched mono-exponential decay fit is used as the decay show time-dependent lifetime. The intensity decay at 0 GPa can actually be fitted with mono-exponential decay function, but at high pressure (i.e. ~4 GPa), the decay showed more of biexponential decay property.

The pre-exponential factor (A-factor) and delayed lifetime (τ) from the stretched mono-exponential fit are plotted as a function of pressure, as shown in **Figure 8.21 b** and **c**. The fitted parameters are listed in **Table 8.10**.

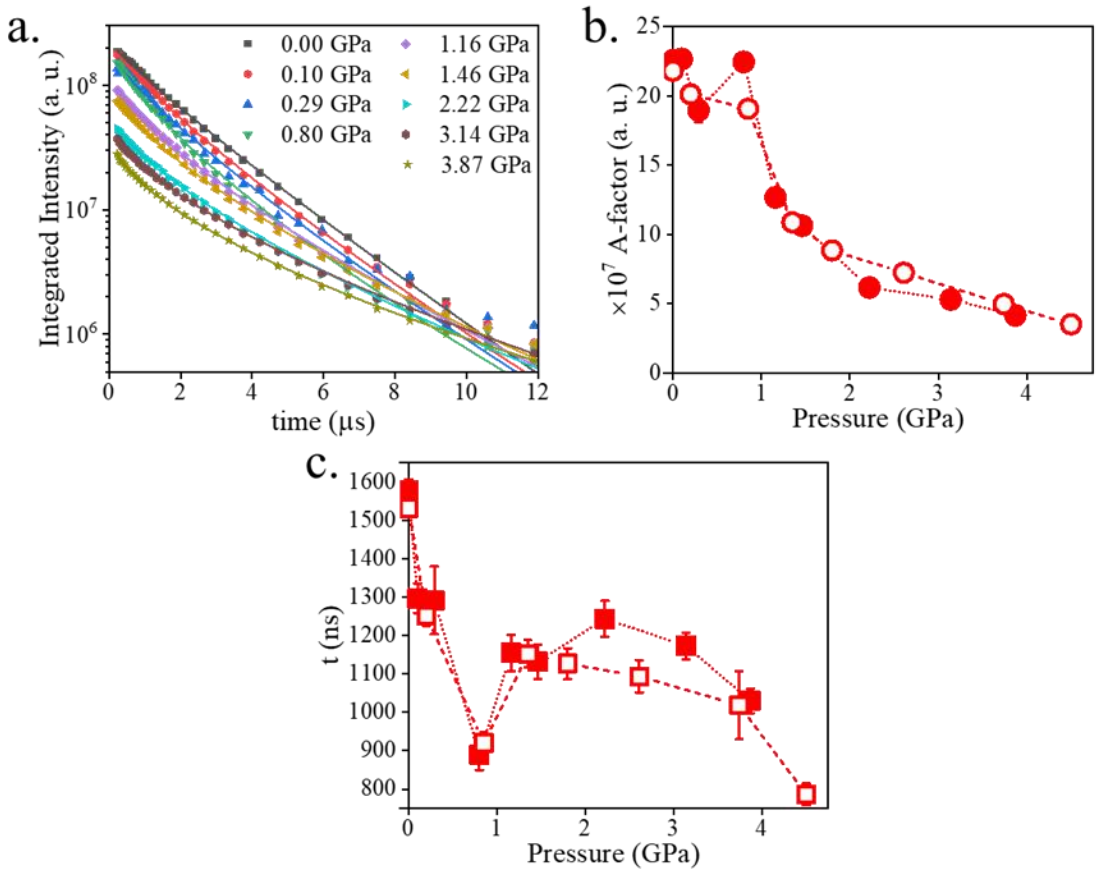

Figure 8.21. (a) the logarithmic-linear plot of integrated fluorescence intensity decay of 4CzIPN-$^{t}Bu_8$ fitted with stretched mono-exponential decay function at various pressure. (b) The A-factor and (c) the lifetime of the fitted fluorescence decay as a function of pressure. The filled and hollow symbols represent the first and second measurements, respectively.

Table 8.10. Summary of fluorescence decay fitted parameters (A-factor and lifetime) of 4CzIPN-^{t}Bu$_8$ fitted with stretched mono-exponential decay function at various pressure.

1st Measurement				2nd measurement			
Pressure / GPa	**A-factor / a. u.**	**τ / ns**	**h**	**Pressure / GPa**	**A-factor / a. u.**	**τ / ns**	**h**
0.00	2.26E8	1578	1.12	**0.00**	2.18E8	1532	1.06
0.10	2.27E8	1297	1.21	**0.20**	2.01E8	1252	1.16
0.29	1.90E8	1292	1.22	**0.85**	1.91E8	920	1.28
0.80	2.25E8	890	1.39	**1.35**	1.09E8	1152	1.29
1.16	1.27E8	1154	1.38	**1.80**	8.85E7	1127	1.35
1.46	1.06E8	1132	1.44	**2.61**	7.24E7	1094	1.45
2.22	6.17E7	1243	1.45	**3.74**	4.98E7	1019	1.66
3.14	5.31E7	1173	1.58	**4.50**	3.52E7	786	1.76
3.87	4.17E7	1030	1.7				

As can be seen from **Figure 8.21 a**, the emission integrated intensity at 200 ns delayed time decreased quite insignificantly at a pressure lower than 0.8 GPa, with a sudden increase in A-factor at 0.8 GPa. A more significant decrease in the intensity (i.e. A-factor) could be seen at higher pressure. On the other hand, the delayed lifetime experienced a significant decrease from ~1.5 μs to only ~0.9 μs up to ~0.8 GPa. This delayed lifetime is close to what has been identified as dimer emission of 4CzIPN (~2 μs) by Etherington *et al*.[19] The delayed lifetime, however, experienced an increase at a pressure higher than 0.8 GPa, before experiencing a decrease at ~2 GPa, while the A-factor continued to decrease.

8.3.2.3.2 Mono-Exponential Decay Fit

The time-dependent emission intensity is also fitted with the mono-exponential decay function, as shown in **Figure 8.22**. The fitted parameters, such as A-factor and delayed lifetime, are also listed in **Table 8.11**.

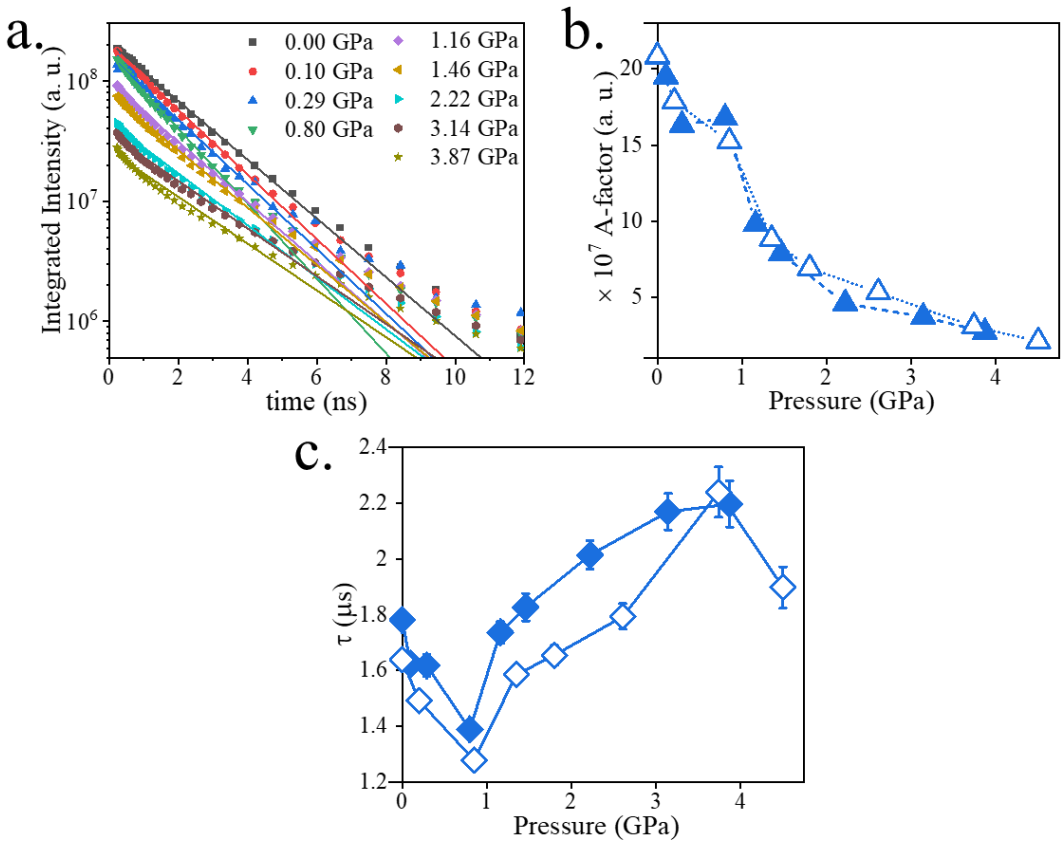

Figure 8.22. (a) the logarithmic-linear plot of integrated fluorescence intensity decay of 4CzIPN-$^{t}Bu_8$ fitted with mono-exponential decay function in various pressure. (b) The A-factor and (c) the lifetime of the fitted fluorescence decay as a function of pressure. The filled and hollow symbols represent the first and second measurements, respectively.

Table 8.11. Summary of fluorescence decay fitted parameters (A-factor and lifetime) of 4CzIPN-$^{t}Bu_8$ fitted with mono-exponential decay function at various pressure.

1st Measurement			2nd measurement		
Pressure / GPa	**A-factor / a. u.**	**τ / ns**	**Pressure / GPa**	**A-factor / a. u.**	**τ / ns**
0.00	2.08E8	1781	**0.00**	2.08E8	1639
0.10	1.95E8	1624	**0.20**	1.79E8	1491
0.29	1.63E8	1618	**0.85**	1.52E8	1279
0.80	1.68E8	1389	**1.35**	8.81E7	1586
1.16	9.79E7	1737	**1.80**	6.90E7	1655
1.46	7.87E7	1827	**2.61**	5.31E7	1794
2.22	4.58E7	2014	**3.74**	3.06E7	2240
3.14	3.69E7	2170	**4.50**	2.09E7	1898
3.87	2.69E7	2197			

The trends of the pressure-dependent A-factor from the stretched mono-exponential and the regular mono-exponential decay function are comparable. The delayed lifetime, however, show very different trends at pressure higher than ~1.2 GPa, where the delayed fluorescence from the mono-exponential fit shows further increases. This could be explained as the heterogeneity factor is increasing with increasing pressure to ~1.7 at ~4 GPa, making the mono-exponential fit fails to represent the intensity decay at higher pressure.

8.3.2.3.3 Decay Fits Comparison

In the case of the 4CzIPN-$^{t}Bu_8$, the emission intensity decay is better fitted with stretched mono-exponential decay as the emission decay is a complex process. As has been mentioned previously, mono-exponential fit can explain the of the delayed fluorescence phenomena at 0 GPa but failed at higher pressure as disorder increase. The use of biexponential fit for emission decay at 0 GPa will result in delayed lifetime of ~6μs, in which the origin is unknown. The use of mono-exponential or biexponential decay fit could result in under- or overinterpretation of the data. Therefore, the change in singlet-triplet energy level is explained with stretched mono-exponential decay function.

At pressure below 0.8 GPa, the A-factor experienced a small decrease followed by stagnation, while the delayed fluorescence experienced a significant decrease with increasing pressure. This could be attributed to the increase in non-radiative decay, caused by the decrease in S_1^*-S_0 and T_1-S_0 energy gaps, without a significant change in the S_1^*-T_1 energy gap (ΔE_{ST}). This scenario is similar to what has been observed in 4CzIPN (see **Figure 8.16),** where the Frack-Condon state, the relaxed excited state and triplet state potential energies were lowered proportionally relative to the ground state.

At a pressure higher than 0.8 GPa, the A-factor experienced a more significant decrease, while the delayed fluorescence showed a sudden increase. This coincides with the stagnation of the steady-state absorption redshift, while the emission spectra redshift continued. This suggests that the S_1^* state potential energy decreased more significantly relative to other states, implying the decrease in the ΔE_{ST}, making a longer-lived emitting species. The decrease of the ΔE_{ST} at ~0.8 GPa can be explained with a simplified Jablonski diagram in **Figure 8.23**. The transition from **Figure 8.23 a** to **b**, shows the stagnation of the excitation energy (Ex) while lowering the emission energy (Em), due to the decrease in the relaxed excited state (S_1^*).

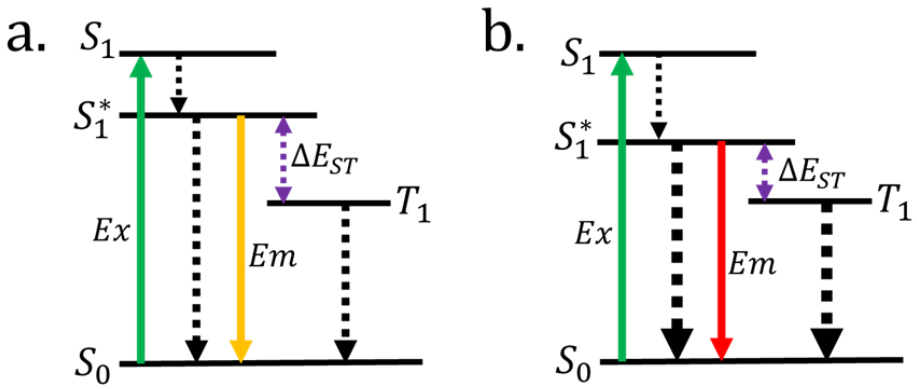

Figure 8.23. The simplified Jablonski diagram of 4CzIPN-^{t}Bu$_8$ at higher than 0.8 GPa. The pressure-induced the shift in energy states from (a) to (b). The black dashed lines represent a non-radiative decay.

At a pressure between ~0.8 GPa and ~2 GPa, the S_1^* potential energy is predicted to keep decreasing relative to other states with increasing pressure, causing the a narrower ΔE_{ST}, indicated by an increase in the delayed lifetime. However, the decrease

in the S_1^* has a consequence in a more substantial non-radiative decay which cause a more significant decrease in the A-factor.

At a pressure higher than ~2GPa, however, the pressure caused a potential energy transition to adopt the scenario of that 4CzIPN. This could be implied from the further decrease in both A-factor and delayed lifetime, which is a sign of an increase in non-radiative decay. It could be implied, therefore, at a pressure higher than ~2 GPa the 4CzIPN-tBu8 did not experience a significant change in $\Delta E_{ST.}$

8.4 Conclusion and Future Work

High-pressure single-crystal diffraction experiment to determine the structure of 4CzIPN has been successfully carried out with the structure could be obtained up to 4.16 GPa. The 4CzIPN crystallises in a triclinic $P\bar{1}$ space group. The unit cell volume was contracted up to ~19% at 4.16 GPa. The crystal experienced an anisotropic contraction, with *a*-axis shrunk by ~10%. From the crystal structure analysis, the pressure caused a significant decrease in the intermolecular carbazoles distances.

Steady-state high-pressure UV-vis absorption and fluorescence emission spectra measurements were also carried out for the 4CzIPN crystal with a custom-built measurement setup up to ~4.3 GPa. At 0 GPa, the stokes shift could be obtained as ~1210 cm^{-1}, indicating a structural relaxation from the Franck-Condon structure to the relaxed excited state. With increasing pressure, the stokes shift appeared to be slightly decreased to ~860 cm^{-1}, indicating a more similar structure between the Franck-Condon and relaxed excited states. This cause by more packed arrangement of molecules in crystal at higher pressure.

Time-resolved high-pressure fluorescence emission spectra measurements were also carried out for 4CzIPN crystal up to ~4.3 GPa using the modified custom-built setup, coupled with Nd:YAG laser and a streak camera. The intensity decays were fitted with bi-exponential decay function. At 0 GPa, the delayed lifetime was found to be ~500 ns and ~2μs, identified as the delayed emission from monomer and dimer species, respectively. The delayed emissions are decreasing with increasing pressure, along with emission intensity, which attributed to the increase in non-radiative decay due to a proportional decrease in S_1^*-S_0 and T_1-S_0 energy gap, without an appreciable decrease in S_1^*-T_1 energy gap (ΔE_{ST}).

The high-pressure single-crystal structure diffraction was also carried out for the 4CzIPN-$^{t}Bu_8$, up to 4.2 GPa. None of the crystal structure could be solved. However, the unit cell parameters could be identified. The 4CzIPN-$^{t}Bu_8$ crystal crystallised in the triclinic $P\bar{1}$ space group. The crystal appeared to be compressed isotropically, with an anomaly at 4.2 GPa, caused by worsening of data.

Steady-state high-pressure UV-vis absorption and fluorescence emission spectra measurements were also carried out for the 4CzIPN up to 4.26 GPa and 3.95 GPa, respectively. Both UV-vis absorption and fluorescence emission spectra were redshifted, with the absorption spectra shift appeared to be stagnated at around ~0.8 GPa. At 0 GPa, the Stokes shift was found to be 1220 cm^{-1}, very similar to the 4CzIPN. The Stokes shift is rather constant up to ~0.8 GPa but getting larger at higher pressure. At ~4 GPa, the Stokes shift was found to be ~1830, significantly more than that of at 0 GPa. This indicates that at a pressure higher than 0.8 GPa, the relaxation of the structure at Franck-Condon state is getting more significant with increasing pressure.

Time-resolved high-pressure fluorescence spectra measurement were carried out up to ~4 GPa, with integrated intensity decays were fitted with stretched mono-exponential function. At 0 GPa, the delayed fluorescence was found to be ~1.5 μs, resembling the delayed fluorescence of the dimer in 4CzIPN. At pressure lower than 0.8 GPa, the delayed fluorescence appeared to be decreased to ~0.9 μs with increasing pressure, along with the decrease in A-factor, which could be attributed to the proportional decrease in S_1^*-S_0 and T_1-S_0 energy gap, without an appreciable decrease in ΔE_{ST}. At a pressure higher than 0.8 GPa; however, the A-factor experienced a sudden large decrease, while delayed fluorescence appeared to be increased. This could be attributed to the decrease in ΔE_{ST}. However, at a pressure higher than ~2 GPa, the delayed fluorescence started to decrease, indicating a more substantial non-radiative decay with no further decrease in ΔE_{ST}.

To concludes, the high-pressure experiments could reveal different phenomena that were found in the 4CzIPN and 4CzIPN-$^{t}Bu_8$, in terms of its crystal structure and electronic energy response to pressure. Follow-up experiments, such as high-pressure low-temperature measurements on both steady-state and time-resolved fluorescence

emission spectra, could be carried out to measure the pressure-dependent value of (ΔE_{ST}) directly.

8.5 References

1. Birks, J. B., *Rep. Prog. Phys.* **1975,** *38* (8), 903-974.
2. Birks, J. B., *Photophysics of aromatic molecules*. Chichester Wiley-Interscience: Chichester, **1970**.
3. Dos Santos, P. L.; Etherington, M. K.; Monkman, A. P., *J. Mater. Chem. C* **2018,** *6* (18), 4842-4853.
4. Eng, J.; Penfold, T. J., *Chem. Rec.* **2020,** *20* (8), 831-856.
5. Yang, Z.; Mao, Z.; Xie, Z.; Zhang, Y.; Liu, S.; Zhao, J.; Xu, J.; Chi, Z.; Aldred, M., *Chem. Soc. Rev.* **2017,** *46* (3), 915-1016.
6. Liu, Y.; Chen, Y.; Li, H.; Wang, S.; Wu, X.; Tong, H.; Wang L., *ACS Appl. Mater. Inter.* **2020,** *12* (27), 30652-30658.
7. Will, P. A.; Reineke, S., Organic light-emitting diodes. In *Handbook of Organic Materials for Electronic and Photonic Devices*, Elsevier: **2019**; pp 695-726.
8. Kim, S. Y.; Jeong, W. I.; Mayr, C.; Park, Y. S.; Kim, K. H.; Lee, J. H.; Moon, C. K.; Brütting, W.; Kim, J. J., *Adv. Func. Mater.* **2013,** *23* (31), 3896-3900.
9. Adachi, C., *Jpn. J. Appl. Phys.* **2014,** *53* (6), 060101.
10. Uoyama, H.; Goushi, K.; Shizu, K.; Nomura, H.; Adachi, C., *Nature* **2012,** *492* (7428), 234-238.
11. Reineke, S.; Walzer, K.; Leo, K., *Phys. Rev. B* **2007,** *75* (12).
12. Adachi, C.; Baldo, M. A.; Thompson, M. E.; Forrest, S. R., *J. Appl. Phys.* **2001,** *90* (10), 5048-5051.
13. Lamansky, S.; Djurovich, P.; Murphy, D.; Abdel-Razzaq, F.; Lee, H. E.; Adachi, C.; Burrows, P. E.; Forrest, S. R.; Thompson, M. E., *J. Am. Chem. Soc.* **2001,** *123* (18), 4304-4312.
14. Lee, D. R.; Kim, M.; Jeon, S. K.; Hwang, S. H.; Lee, C. W.; Lee, J. Y., *Adv. Mater.* **2015,** *27* (39), 5861-5867.
15. Liu, H.; Li, J.; Chen, W. C.; Chen, Z.; Liu, Z.; Zhan, Q.; Cao, X.; Lee, C. S.; Yang, C., *Chem. Eng. J.* **2020,** *401*, 126107.
16. Zou, S. J.; Shen, Y.; Xie, F. M.; Chen, J. D.; Li, Y. Q.; Tang, J. X., *Mater. Chem. Front.* **2020,** *4* (3), 788-820.

17. Xuan, T.; Xie, R. J., *Chem. Eng. J.* **2020,** *393*, 124757.
18. Li, Z.; Qin, A. J., *Natl. Sci. Rev.* **2014,** *1* (1), 22-24.
19. Etherington, M. K.; Kukhta, N. A.; Higginbotham, H. F.; Danos, A.; Bismillah, A. N.; Graves, D. R.; McGonigal, P. R.; Haase, N.; Morherr, A.; Batsanov, A. S.; Pflumm, C.; Bhalla, V.; Bryce, M. R.; Monkman, A. P., *J. Phys. Chem. C* **2019,** *123* (17), 11109-11117.
20. Kim, H. S.; Park, S.-R.; Suh, M. C., *J. Phys. Chem. C* **2017,** *121* (26), 13986-13997.
21. Lee, K.; Siegel, J.; Webb, S.; Leveque-Fort, S.; Cole, M.; Jones, R.; Dowling, K.; Lever, M.; French, P., *Biophys. J.* **2001,** *81* (3), 1265-1274.
22. Raišys, S.; Juršėnas, S.; Simon, Y. C.; Weder, C.; Kazlauskas, K., *Chem. Sci.* **2018,** *9* (33), 6796-6802.
23. Sheldrick, G. M., *Acta Crystallogr. A* **2015,** *71*, 3-8.
24. Dolomanov, O. V.; Bourhis, L. J.; Gildea, R. J.; Howard, J. A. K.; Puschmann, H., *J. Appl. Crystallogr.* **2009,** *42*, 339-341.
25. Betteridge, P. W.; Carruthers, J. R.; Cooper, R. I.; Prout, K.; Watkin, D. J., *J. Appl. Crystallogr.* **2003,** *36*, 1487-1487.
26. Etherington, M. K., Personal Communication. 2020.
27. Macrae, C. F.; Sovago, L.; Cottrell, S. J.; Galek, P. T. A.; McCabe, P.; Pidcock, E.; Platings, M.; Shields, G. P.; Stevens, J. S.; Towler, M.; Wood, P. A., *J. Appl. Crystallogr.* **2020,** *53*, 226-235.
28. Boldyreva, E. V., *J. Mol. Struct.* **2003,** *647* (1-3), 159-179.

Chapter 9
Conclusions

In the 1980s, high-pressure solid-state electronic spectroscopy studies were intensified, with the development of smaller diamond anvil cells (DACs). High-pressure fluorescence emission studies were pioneered by Drickamer, with the main interest on organic and organometallic materials, but there was little work on high-pressure UV-vis absorption spectroscopy and X-ray diffraction measurements.[1] In recent years, high-pressure studies have expanded to include a few studies utilising UV-vis absorption measurements and powder X-ray diffraction, but these have provided limited information on molecular structure and intermolecular interactions.[2, 3] The work described in this thesis has achieved the objective of developing a measurement system to perform both UV-vis absorption and fluorescence emission spectroscopy on crystalline samples at high pressure, in order to combine these measurements with single-crystal high-pressure X-ray crystallography, to directly correlate pressure-induced changes in photophysics with the evolution of the crystal structure.

The measurement of both UV-vis absorption and fluorescence emission spectra is essential to obtain a complete understanding of the photophysics of materials. The UV-vis absorption spectroscopy informs on the electronic transition from the ground state to the Franck-Condon excited state of a system. This energy of this transition can be related to the ground-state structure obtained from the X-ray diffraction. On the other hand, fluorescence emission spectroscopy reveals the energy of the transition from the relaxed excited state to the ground state. Combination of both UV-vis absorption and fluorescence emission spectroscopy is essential to understand the extent of molecular relaxation that occurs in the excited state. With the help of X-ray diffraction, the change in the photophysical behaviour in response to pressure can be linked directly to the change in the crystal structure of the molecule.

In this thesis, it has been revealed that different classes of molecules, namely the Hf-peb MOF, Zr-abdc MOF, molecular rotors, linearly conjugated fluorescent compound and thermally activated delayed fluorescence (TADF) materials show distinct response in their electronic properties, molecular structure, and interactions to increasing hydrostatic pressure,

The study of the Hf-peb MOF, a MOF containing interpenetrating peb^{2-} linker, was the first combined measurement of high-pressure UV-vis absorption, fluorescence emission, and X-ray crystallography to be carried out on a fluorescent MOF. It was revealed that at ambient pressure, two conformers of the linker exist, a coplanar conformer, in which the central phenyl ring coplanar with the terminal phenyl rings, and a twisted conformer, where the central phenyl ring is perpendicular. The twisted conformer had not been reported prior to this study. The fractional population of twisted conformer was found to increase from ~28% at ambient pressure to its exclusive population at 2.1GPa. The two conformers showed distinct emission spectra and the pressure-dependence of their fractional populations could be estimated from the overall fluorescence spectrum. This was in excellent agreement with the pressure-dependent fractional population obtained from crystallography, indicating a very similar fluorescence brightness of both conformers. Examination of the Stokes shift between the absorption and emission spectra showed that there is structural relaxation prior to emission, and the extent of this relaxation is greater for the twisted conformer than for the coplanar one. This work has shown the value of the measurement of fluorescence spectra as a function of pressure in tracking the pressure-induced conformational changes of molecules.

The importance of UV-vis absorption measurement to investigate the photophysics of a non-fluorescent material and its relation to its molecular structure has been demonstrated in the study on Zr-abdc MOF, in which the linker is azobenzene dicarboxylate). Pressure-induced penetration of methanol into the MOF framework produced a hypsochromic shift in the absorption spectrum that could be attributed to the effect of polar solvation on the energy of the $n\pi^*$ transition of the azobenzene chromophore. The use of a non-penetrating hydrostatic medium resulted in a pressure-induced bathochromic shift in the absorption spectrum which, with the aid of TDDFT

calculations, could be related directly to bending of the azobenzene linker with increasing pressure.

The study of the molecular rotors, sym-pentaphenylcyclopentadiene (Ph_5C_5H) and *sym*-heptaphenylcycloheptatriene (Ph_7C_7H) was also the first time that this type of molecule was studied under pressure. For Ph_5C_5H, specific intermolecular inter-phenyl interactions, resembling displaced-stacked benzene dimers, were identified in the ambient-pressure crystal structure. These interactions could be related to the observation of excimer-like emission from the crystal. In contrast, Ph_7C_7H did not show any significant intermolecular inter-phenyl interactions at ambient pressure, but a number of these developed with increasing pressure. Specific inter-phenyl interactions were identified as influencing the pressure-induced changes in the electronic spectra. At the highest pressures, the appearance of new, long-wavelength features in the absorption and emission spectra coincides with the development of stronger displaced-stacked inter-phenyl interactions which are capable of excimer formation. This study has enabled us to directly attribute changes in the photophysics of phenyl-based molecular rotors to the specific intermolecular interactions between the phenyl groups.

Investigation of the electronic spectra of 1,4-bis(4-carbomethoxyphenylethynyl)-benzene (BCPEB) in solution phase showed that its photophysical properties are very similar to the well-known analogue, 1,4-bis(phenylethynyl)benzene (BPEB). The present high-pressure study of BCPEB is the first time that an acetylene π-conjugated system of this type has been studied under these conditions. It was found that, as in solution phase, the electronic spectra in the crystal could be interpreted in terms of torsional isomerism. The pressure-dependence of the spectra could be related to the influence of intermolecular interactions on the torsional mobility of the molecule.

Lastly, pressure-dependent properties were studied for the well-known TADF material 1,2,3,5-Tetrakis(carbazol-9-yl)-4,6-dicyanobenzene (4CzIPN) and its derivative, 4CzIPN-$^tBu_8$. This is also the first pressure-dependent study on the electronic spectra and crystal structure of TADF materials. For the 4CzIPN, the crystal compressed anisotropically with increasing pressure with significant decrease in the intermolecular inter-carbazole distance. This could be correlated to the bathochromic shifts in the

absorption and fluorescence spectra and decreasing lifetime of the TADF emission, as well as a decrease in the intensity of the latter. The results indicated increase in the rate of non-radiative decay with inceasing pressure, without a change in the singlet-triplet energy gap. On the other hand, for the 4CzIPN-$^{t}Bu_8$, the crystal structure compressed isotropically. Moreover, the pressure-dependence of the photophysical properties differed significantly from 4CzIPN. The fluorescence spectrum showed significant bathochromic shift with increasing pressure, whereas the absorption spectrum ceased to shift at pressure higher than ~0.8 GPa. For pressures up to ~0.8 GPa, the TADF lifetime and intensity decreased, in the same manner as the 4CzIPN. However, at pressures higher than ~0.8 GPa, the delayed-fluorescence lifetime started to increase, followed by a sudden decrease in the intensity, which is a sign of the narrowing of singlet-triplet energy gap. At pressure higher than ~2 GPa, the delayed fluorescence lifetime decreased, indicating a further increase in the rate of non-radiative decay. This study has revealed that these two related molecules that were thought to have very similar photophysical properties, actually behave completely different under the influence of pressure, which can be attributed to the observed difference in pressure-induced crystal compression. This insight could only be achieved by the utilisation of both steady-state and time-resolved electronic spectroscopy measurements in combination with X-ray diffraction.

There are many candidates for future studies to gain more knowledge about the effect of pressure on photoactive systems. Some suggestions are made here. The study of simple aromatic molecular crystals, such as benzene, anthracene and phenanthrene, would be useful to understand the effect of pressure on fundamental excitonic properties. Larger aromatic systems such as pyrene and phthalocyanines would also be interesting, since these show a sandwich-type stacking arrangement in the crystal, to gain a better understanding of the excimer formation mechanism. Simpler molecular rotors, such as tetraphenylethylene, would also be interesting to study, to explore inter-phenyl interactions as a function of pressure in terms of the aggregation-induced emission phenomenon. Metal-ligand complexes such as fluorescent Eu-complexes would be excellent candidates in which to study the pressure-dependent efficiency of the antenna effect. Inorganic fluorescent materials such as perovskites would also be great subjects in which study the effect of pressure on the bandgap energy, useful for

photovoltaic applications. The understanding derived from such studies could be used in combination with the techniques and concepts of molecular design to achieve optimum and efficient systems for a variety of applications.

There are several upgrades of the custom-built measurement system could be done in the future to improve its performance. The addition of an automatic pressure adjusting system would be useful to achieve more consistent absorption and emission measurements. Modification of the optics to allow simultaneous measurements of absorption and emission spectra would also be beneficial to get more comparable measurements, eliminating potential sampling error. The development of a system to cool the sample to low-temperature would be useful in the study of TADF materials, to get direct measurement of the singlet-triplet energy gap. Better quality diamonds would extend the measurement capability to shorter wavelengths and would be required to study simple aromatic molecules which absorb and emit in the UV region at wavelengths below ~350 nm.

9.1 References

1. Drickamer, H. G., *Annu. Rev. Mater. Sci.* **1990,** *20,* 1-17.
2. Zhao, D.; Wang, M.; Xiao, G.; Zou, B., *J. Phys. Chem. Lett.* **2020,** *11* (17), 7297-7306.
3. Fu, Z.; Wang, K.; Zou, B., *Chin. Chem. Lett.* **2019,** *30* (11), 1883-1894.s

Appendix I
Crystallographic data of Hf-peb MOF

Table A-1. Abbreviated crystallographic tables of Hf-peb MOF for all structures at 0–0.55 GPa. M_r = 1694.55, Cubic, $Fd\bar{3}m$, Z = 16.

Pressure / GPa	Ambient	0.10	0.23	0.55
Crystal data				
Chemical formula	$C_{72}H_{38}Hf_3O_{16}$	$C_{72}H_{38}Hf_3O_{16}$	$C_{72}H_{38}Hf_3O_{16}$	$C_{72}H_{38}Hf_3O_{16}$
Temperature (K)	299	300	296	296
a (Å)	39.8212 (18)	39.8295 (17)	39.7307 (8)	39.6707 (9)
V (Å^3)	63146 (9)	63185 (8)	62716 (4)	62432 (4)
m (mm^{-1})	2.00	2.00	2.01	2.02
Crystal size (mm)	0.10 × 0.10 × 0.10	0.10 × 0.10 × 0.10	0.10 × 0.10 × 0.10	0.10 × 0.10 × 0.10
Data collection				
T_{min}, T_{max}	0.67, 0.82	0.36, 0.82	0.42, 0.82	0.47, 0.82
No. of measured, independent and observed [I > 2.0s(I)] reflections	94905, 1635, 1287	48173, 1700, 1111	43461, 1481, 988	42979, 1490, 991
R_{int}	0.057	0.094	0.087	0.083
q_{max} (°)	20.9	22.0	20.8	20.9
(sin q/l)$_{max}$ (Å^{-1})	0.503	0.527	0.500	0.501
Refinement				
$R[F^2 > 2s(F^2)]$, $wR(F^2)$, S	0.033, 0.069, 1.05	0.038, 0.080, 1.00	0.042, 0.114, 1.01	0.043, 0.130, 1.00
No. of reflections	1593	1627	1410	1431
No. of parameters	91	90	1	91
No. of restraints	139	133	0	134
H-atom treatment	H atoms treated by a mixture of independent and constrained refinement	H atoms treated by a mixture of independent and constrained refinement	H-atom parameters not refined	H atoms treated by a mixture of independent and constrained refinement
$D\rho_{max}$, $D\rho_{min}$ (e Å^{-3})	0.64, -1.02	1.13, -0.91	1.63, -0.80	1.84, -0.88

Table A-2. Abbreviated crystallographic tables of Hf-peb MOF for all structures at 1.10–2.10 GPa. M_r = 1694.55, Cubic, $Fd\bar{3}m$, Z = 16.

Pressure / GPa	1.10	1.40	1.64	2.10
Crystal data				
Chemical formula	$C_{72}H_{38}Hf_3O_{16}$	$C_{72}H_{38}Hf_3O_{16}$	$C_{72}H_{38}Hf_3O_{16}$	$C_{72}H_{38}Hf_3O_{16}$
Temperature (K)	296	296	296	296
a (Å)	39.6359 (10)	39.5937 (7)	39.5272 (7)	39.4727 (8)
V (Å^3)	62268 (5)	62070 (3)	61757 (3)	61502 (4)
m (mm^{-1})	2.02	2.03	2.04	2.05
Crystal size (mm)	0.10 × 0.10 × 0.10	0.10 × 0.10 × 0.10	0.10 × 0.10 × 0.10	0.10 × 0.10 × 0.10
Data collection				
T_{min}, T_{max}	0.43, 0.82	0.47, 0.82	0.49, 0.82	0.49, 0.81
No. of measured, independent and observed [I > 2.0s(I)] reflections	42213, 1298, 843	42955, 1309, 899	42679, 1483, 1024	42506, 1476, 1018
R_{int}	0.106	0.072	0.072	0.071
q_{max} (°)	20.9	20.9	20.9	20.9
s(sin q/l)$_{max}$ (Å^{-1})	0.501	0.501	0.501	0.501
Refinement				
$R[F^2 > 2s(F^2)]$, $wR(F^2)$, S	0.051, 0.137, 0.88	0.042, 0.108, 1.00	0.033, 0.071, 1.00	0.034, 0.099, 1.00
No. of reflections	1229	1219	1427	1424
No. of parameters	87	91	91	92
No. of restraints	135	134	134	144
H-atom treatment	H atoms treated by a mixture of independent and constrained refinement	H atoms treated by a mixture of independent and constrained refinement	H atoms treated by a mixture of independent and constrained refinement	H atoms treated by a mixture of independent and constrained refinement
$D\rho_{max}$, $D\rho_{min}$ (e Å^{-3})	1.78, -0.88	1.46, -0.91	0.66, -0.87	1.27, -0.68

Appendix II
Input and Relevant Output for Calculation of Absorption to the First Excited State of $abdc^{2-}$ linker

Step 1: Ground-state geometry optimisation, including frequency calculation.

Input:

```
%chk=zrazo0_06gpa.chk
%mem=6GB
%nprocshared=6
#p BHandHLYP/6-311g(d,p) opt freq geom=connectivity

Zr Azo 0.00 GPa opt

-2 1
```

Thermal results from frequency calculation:

```
SCF Done:  E(RBHandHLYP) =  -948.433982060     A.U. after    1 cycles
Zero-point correction=                          0.191364 (Hartree/Particle)
 Thermal correction to Energy=                  0.205280
 Thermal correction to Enthalpy=                0.206224
 Thermal correction to Gibbs Free Energy=       0.145714
 Sum of electronic and zero-point Energies=          -948.242618
 Sum of electronic and thermal Energies=             -948.228702
 Sum of electronic and thermal Enthalpies=           -948.227758
 Sum of electronic and thermal Free Energies=        -948.288268
```

Table A-3. Energy obtained from the DFT optimisation.

Pressure / GPa	Energy / Hartree	Energy / kJ.mol^{-1}	ΔEnergy / kJ.mol^{-1}
0.00	-948.433982060	-2490113.07797	0.0000
0.12	-948.433662935	-2490112.24011	0.8379
0.37	-948.432320327	-2490108.71509	4.3629
0.50	-948.431525220	-2490106.62754	6.4504
0.59	-948.430989629	-2490105.22134	7.8566
1.22	-948.426800032	-2490094.22156	18.8564
1.58	-948.425077104	-2490089.69801	23.3799
1.74	-948.424749970	-2490088.83912	24.2388

Step 2: TD-DFT single point vertical excitation from the ground state.

Input:

```
%oldchk=zrazo0_06gpa.chk
%chk=zrazo0_06gpa_TD.chk
#p BHandHLYP/6-311g(d,p) TD=(Nstates=10,Singlet,Root=1) gfprint
geom=check guess=read

Zr Azo 0.06 GPa TD

-2 1
```

Output:

```
Excited State   1:      Singlet-A      2.9730 eV  417.03 nm  f=0.0000  <S**2>=0.000
     61 -> 71        0.66752
     61 -> 77        0.19093
     69 -> 71       -0.10323
 This state for optimization and/or second-order correction.
 Total Energy, E(TD-HF/TD-KS) =  -948.324724774
 Copying the excited state density for this state as the 1-particle RhoCI density.

 Excited State   2:      Singlet-A      3.8938 eV  318.41 nm  f=1.0242  <S**2>=0.000
     64 -> 71       -0.12199
     70 -> 71        0.68540
```

The absorption of the excited state 1 would be 417.03 nm and the oscillator strength of the transition of 0. With the main orbitals contributing to this transition are 61 → 71. This is the transition of n→π*, examined using the orbital mapping within using the output checkpoint file.

The excited state 2 would be at 318.41 nm with the oscillator strength of the transition of 1.0242. With the main orbitals contributing to this transition are 70 → 71. This is the transition of π→π*.

Appendix III
Crystallographic data of Ph_7C_7H

Table A-4. Crystallographic data for Ph_7C_7H during hydrostatic compression between 0.12 GPa and 2.04 GPa in a Daphne oil 7373.

	0.12 GPa	**0.44 GPa**	**0.98 GPa**	**1.50 GPa**	**2.04 GPa**
Crystal data					
a, *b*, *c* (Å)	9.8731 (12), 10.0827 (18), 19.2541 (19)	9.6994 (13), 9.9444 (16), 18.941 (2)	9.5654 (12), 9.7482 (15), 18.672 (2)	9.4996 (10), 9.5292 (13), 18.5388 (17)	9.4105 (9), 9.4113 (13), 18.3881 (16)
α, β, γ (°)	87.770 14), 90.555 (9), 70.978 (16)	87.411(15), 90.594(10), 70.311 (16)	86.645 (15), 90.144 (10), 69.954 (16)	85.491 (12), 89.348 (8), 70.036 (13)	84.854 (11), 88.795 (8), 69.860 (13)
V (Å^3)	1810.2 (5)	1717.8 (4)	1632.3 (4)	1572.3 (3)	1522.7 (3)
μ (mm^{-1})	0.04	0.04	0.04	0.04	0.04
Crystal size (mm)	0.2 × 0.1 × 0.1	0.2 × 0.1 × 0.1	0.2 × 0.1 × 0.1	0.2 × 0.1 × 0.1	0.2 × 0.1 × 0.1
Data collection					
T_{min}, T_{max}	0.738, 1.000	0.860, 1.000	0.766, 1.000	0.643, 1.000	0.756, 1.000
Measured, independent and observed [$I > 2\sigma(I)$] reflections	7278, 1318, 957	6874, 1235, 962	6844, 1184, 952	6638, 1131, 934	6438, 1083, 922
R_{int}	0.138	0.074	0.076	0.089	0.067
θ_{max} (°)	13.8	13.8	13.8	13.8	13.8
$(\sin \theta/\lambda)_{max}$ (Å^{-1})	0.490	0.490	0.490	0.490	0.490
Refinement					
$R[F^2 > 2\sigma(F^2)]$, $wR(F^2)$, S	0.144, 0.466, 1.81	0.105, 0.297, 1.07	0.102, 0.279, 1.09	0.085, 0.241, 1.08	0.082, 0.227, 1.08
No. of reflections	1318	1235	1184	1131	1083
No. of parameters	113	113	113	113	113
No. of restraints	54	54	54	84	84
$\Delta\rho_{max}$, $\Delta\rho_{min}$ (e Å^{-3})	0.29, −0.23	0.39, −0.33	0.46, −0.29	0.29, −0.19	0.22, −0.23

Table A-5. Crystallographic data for Ph_7C_7H during hydrostatic compression between 2.54 GPa and 5.63 GPa in a Daphne oil 7373.

	2.54 GPa	**3.39 GPa**	**4.68 GPa**	**5.63 GPa**
Crystal data				
a, *b*, *c* (Å)	9.3610 (8), 9.3258 (12), 18.2905 (14)	9.2968 (12), 9.1796 (15), 18.180 (2)	8.986 (10), 9.134 (8), 18.181 (9)	9.19 (9), 9.10 (3), 17.83 (4)
α, β, γ (°)	84.538 (10), 88.427 (7), 69.729 (11)	84.056 (14), 88.039 (10), 69.702 (16)	87.17 (5), 83.03 (7), 69.05 (9)	85.6 (2), 80.9 (4), 68.9 (6)
V (Å^3)	1491.0 (3)	1447.3 (4)	1383 (2)	1374 (16)
μ (mm^{-1})	0.04	0.04	0.04	0.04
Crystal size (mm)	0.2 × 0.1 × 0.1	0.2 × 0.1 × 0.1	0.2 × 0.1 × 0.1	0.2 × 0.1 × 0.1
Data collection				
T_{min}, T_{max}	0.742, 1.000	0.406, 1.000	0.514, 1.000	0.514, 1.000
Measured, independent and observed [$I > 2\sigma(I)$] reflections	11353, 2939, 1553	6002, 1016, 728	706	819
R_{int}	0.099	0.137	n/a	n/a
θ_{max} (°)	22.9	13.8	n.a	n.a
$(\sin\theta/\lambda)_{max}$ (Å^{-1})	0.800	0.490	n/a	n/a
Refinement				
$R[F^2 > 2\sigma(F^2)]$, $wR(F^2)$, S	0.110, 0.369, 1.23	0.123, 0.372, 1.61	n/a	n/a
No. of reflections	2939	1016	n.a	n.a
No. of parameters	197	197	n/a	n/a
No. of restraints	54	54	n/a	n/a
$\Delta\rho_{max}$, $\Delta\rho_{min}$ (e Å^{-3})	0.43, −0.29	0.32, −0.32	n.a	n.a

Appendix IV
Crystallographic data of BCPEB

Table A-6. Crystallographic data for BCPEB during hydrostatic compression between 0.18 GPa and 2.74 GPa in Daphne oil 7373. The crystal has orthorhombic crystal system (*Pbca*).

	0.18 GPa	**0.54 GPa**	**1.31 GPa**	**2.74 GPa**
Crystal Data				
a, *b*, *c* (Å)	7.4006(11) 6.0292(12) 45.91(7)	7.1587(8) 5.9147(9) 45.35(4)	6.9663(7) 5.8281(7) 44.92(3)	6.7257(8) 5.7204(8) 44.36(4)
V (Å^3)	2048.9(3)	1920.4(12)	1824.0(13)	1706.6(15)
μ (mm^{-1})	0.052	0.052	0.052	0.052
Crystal size (mm)	0.2 × 0.1 × 0.1	0.2 × 0.1 × 0.1	0.2 × 0.1 × 0.1	0.2 × 0.1 × 0.1
Data Collection				
T_{min}, T_{max}	0.818, 1.000	n/a	n/a	n/a
Measured, independent and observed [$I > 2\sigma(I)$] reflections	987, 389, 293	635, 320, 268	603, 307, 264	574, 292, 219
R_{int}	0.192	0.224	0.279	0.336
θ_{max} (°)	13.64	12.09	12.09	12.09
$(\sin\theta/\lambda)_{max}$ (Å^{-1})	0.4853	0.4309	0.491	0.4309
Refinement				
$R[F^2 > 2\sigma(F^2)]$, $wR(F^2)$, S	0.076, 0.184, 1.16	0.067, 0.152, 1.14	0.071, 0.211, 1.13	0.104, 0.330, 1.43
No. of reflections	389	320	307	292
No. of parameters	53	50	50	50
No. of restraints	13	31	31	42
$\Delta\rho_{max}$, $\Delta\rho_{min}$ (e Å^{-3})	0.18, −0.19	0.18, −0.19	0.18, −0.21	0.34, −0.38

Table A-7. Crystallographic data for BCPEB during hydrostatic compression between 3.51 GPa and 5.96 GPa in Daphne oil 7373. The crystal has orthorhombic crystal system (*Pbca*).

	3.51 GPa	**4.28 GPa**	**5.96 GPa**
Crystal Data			
a, *b*, *c* (Å)	6.6475(8) 5.6727(8) 44.05(4)	6.6102(11) 5.6588(10) 43.65(5)	6.4844(9) 5.608(1) 43.26(4)
V (Å^3)	1661.1(15)	1632.7(17)	1573.1(16)
μ (mm^{-1})	0.053	0.053	0.053
Crystal size (mm)	0.2 × 0.1 × 0.1	0.2 × 0.1 × 0.1	0.2 × 0.1 × 0.1
Data Collection			
T_{min}, T_{max}	0.306, 1.000	0.701, 1.000	0.509,1.000
Measured, independent and observed [$I > 2\sigma(I)$] reflections	562, 294, 217	553, 248, 171	531, 282, 219
R_{int}	0.188	0.525	0.149
θ_{max} (°)	12.09	12.09	12.08
$(\sin\theta/\lambda)_{max}$ (Å^{-1})	0.4309	0.4309	0.4307
Refinement			
$R[F^2 > 2\sigma(F^2)]$, $wR(F^2)$, S	0.094, 0.307, 1.13	n/a	n/a
No. of reflections	294	n/a	n/a
No. of parameters	50	n/a	n/a
No. of restraints	31	n/a	n/a
$\Delta\rho_{max}$, $\Delta\rho_{min}$ (e Å^{-3})	0.25, −0.43	n/a	n/a

Appendix V
Crystallographic data of 4CzIPN

Table A-8. Crystallographic data for 4CzIPN during hydrostatic compression between 0.08 GPa and 2.53 GPa in Daphne oil 7373. The crystal has triclinic crystal system ($P\bar{1}$).

	0.08 GPa	0.58 GPa	1.24 GPa	1.55 GPa	2.00 GPa	2.53 GPa
Crystal data						
a, *b*, *c* (Å)	9.0601(7) 19.7246(19) 24.126(2)	8.7428(6) 19.2806(16) 23.668(2)	8.5345(6) 19.0304(7) 23.449(2)	8.4736(5) 18.9639(14) 23.3904(18)	8.3736(5) 18.8449(15) 23.284(19)	8.2743(5) 18.7086(14) 23.1889(19)
α, β, γ (°)	77.837(8) 83.707(8) 89.9269(8)	77.927(7) 84.827(7) 89.809(6)	78.103(7) 85.580(7) 89.736(6)	78.144(7) 85.820(7) 89.730(6)	78.245(7) 86.196(7) 89.706(6)	78.265(7) 86.522(6) 89.680(6)
V (Å^3)	4188.3(7)	3885.0(5)	3715.4(5)	3668.5(5)	3589.1(5)	3508.1(4)
μ (mm^{-1})	0.04	0.04	0.04	0.04	0.04	0.04
Crystal size (mm)	0.2 × 0.1 × 0.1	0.2 × 0.1 × 0.1	0.2 × 0.1 × 0.1	0.2 × 0.1 × 0.1	0.2 × 0.1 × 0.1	0.2 × 0.1 × 0.1
Data collection						
T_{min}, T_{max}	0.635, 1.000	0.660, 1.000	0.602,1.000	0.783,1.000	0.690,1.000	0.837,1.000
Measured, independent and observed [$I > 2\sigma(I)$] reflections	7389, 2690, 1826	6832, 2532, 1897	7396, 2729, 1972	6417, 2342, 1876	6304, 2262, 1757	6167, 2225, 1682
R_{int}	0.174	0.105	0.133	0.098	0.101	0.121
θ_{max} (°)	13.25	13.25	13.81	13.25	13.25	13.25
$(\sin\theta/\lambda)_{max}$ (Å^{-1})	0.4717	0.4717	0.491	0.4717	0.4717	0.4717
Refinement						
$R[F^2 > 2\sigma(F^2)]$, $wR(F^2)$, S	0.128, 0.395, 1.52	0.108, 0.314, 1.09	0.132, 0.418, 1.73	0.117, 0.328, 1.73	0.128, 0.428, 1.93	0.1305, 0.422, 1.83
No. of reflections	2690	2532	2729	2342	2262	2225
No. of parameters	282	281	281	281	281	281
No. of restraints	66	92	92	92	92	92
$\Delta\rho_{max}$, $\Delta\rho_{min}$ (e Å^{-3})	0.33, −0.31	0.32, −0.37	0.37, −0.50	0.33, −0.39	0.44, −0.48	0.49, −0.45

Table A-9. Crystallographic data for 4CzIPN during hydrostatic compression between 3.23 GPa and 7.42 GPa Daphne oil 7373. The crystal has triclinic crystal system ($P\bar{1}$).

	3.23 GPa	3.76 GPa	4.16 GPa	5.71 GPa	7.42 GPa
Crystal data					
a, *b*, *c* (Å)	8.2173(5) 18.6072(15) 23.099(2)	8.1553(5) 18.4739(14) 23.0273(19)	8.1480(8) 18.453(2) 23.023(3)	8.054(3) 18.168(6) 23.137(7)	7.9588(12) 17.843(2) 22.626(3)
α, β, γ (°)	78.323(7) 86.738(7) 89.728(6)	78.377(7) 86.932(6) 89.773(6)	78.365(11) 86.986(11) 89.841(9)	78.70(3) 86.98(3) 89.95(3)	79.343(14) 87.57(2) 90.264(15)
V (Å^3)	3453.1(5)	3393.1(4)	3385.6(7)	3315.4(19)	3154.5(8)
μ (mm^{-1})	0.04	0.04	0.04	0.04	0.04
Crystal size (mm)	0.2 × 0.1 × 0.1	0.2 × 0.1 × 0.1	0.2 × 0.1 × 0.1	0.2 × 0.1 × 0.1	0.2 × 0.1 × 0.1
Data collection					
T_{min}, T_{max}	0.640, 1.000	0.860, 1.000	0.371, 1.000	0.585, 1.000	0.539, 1.000
Measured, independent and observed [$I > 2\sigma(I)$] reflections	6070, 2183, 1649	5969, 2136, 1595	5963, 2108, 1204	5837, 2022, 1595	27661, 5848, 930
R_{int}	0.126	0.134	0.294	0.541	0.848
θ_{max} (°)	13.25	13.25	13.25	13.25	23.05
$(\sin\theta/\lambda)_{max}$ (Å^{-1})	0.4717	0.4715	0.4717	0.4716	0.4716
Refinement					
$R[F^2 > 2\sigma(F^2)]$, $wR(F^2)$, S	0.126, 0.424, 1.83	0.134, 0.427, 1.83	0.155, 0.443, 1.45	n/a	n/a
No. of reflections	2183	2136	2108	n/a	n/a
No. of parameters	281	281	281	n/a	n/a
No. of restraints	92	92	92	n/a	n/a
$\Delta\rho_{max}$, $\Delta\rho_{min}$ (e Å^{-3})	0.47, −0.39	0.47, −0.47	0.46, −0.38	n/a	n/a

Matlab Code for Emission Spectrum Integration

The MATLAB code was written by Dr Marc K. Etherington of University of Northumbria based on an earlier code by David Graves of Durham University.

```
function [coeffs,resnorm]= weightedFit
[filename,pathname,filterindex]=uigetfile('Input file & directory.txt');
fileID = fopen(fullfile(pathname,filename));
file=fullfile(pathname,filename);
delimiterIn ='\t';
headerlinesIn = 1;
Data= importdata(file,delimiterIn,headerlinesIn);
fclose(fileID);

%starting frame number
% Locate and subtract the background
% Takes mean of selected baseline
for k = 2:size(Data.data,2)-1
    Data.data(:,k)              =              Data.data(:,k)              -
mean(Data.data(1200:1300,k));%Subtract baseline
    mean(Data.data(1200:1300,k))
end

%Import the ex15 file
exfile = 'EX15_newCCD_corr_Marc_15.txt';
spacer = '\t';
EX = importdata(exfile,spacer);
xaxis = EX(1:size(Data.data,2)-1,1)+0.5.*EX(1:size(Data.data,2)-1,2); %old
time978.2;%NdYAG Trigger

% Integrate spectra
intwindow = EX(1:size(Data.data,2)-1,2).^-1;
B = 0.24*Data.data(:,2:size(Data.data,2));
C = sum(B).*intwindow';% Adds up each column, giving integration

transpose = C';
yaxis = transpose(1:size(Data.data,2)-1);
time = [xaxis,yaxis];

new_y=yaxis;
new_x=xaxis;

%Plot PL transient
p1=loglog(new_x,new_y,'x','color','black','linewidth',2);
hold on
xlabel('Time (ns)')
ylabel('Intensity (arb. u.)')
ax = gca; %get current axis %gcf get current figure %cla clears axes %clf
clear current figure
set(gca,'XLim',[0 1E8]);
set(gca,'XMinorTick','on','YMinorTick','on');
ax.FontSize = 14;
ax.FontWeight = 'bold';
ax.LineWidth = 2;
new_y=new_y;
 D=horzcat(new_x,new_y);
 csvwrite('outout file & directory.csv',D);
end
```